



**Universidade do Estado do Rio de Janeiro**

Centro de Tecnologia e Ciências

Faculdade de Engenharia

Gustavo Charles Peixoto de Oliveira

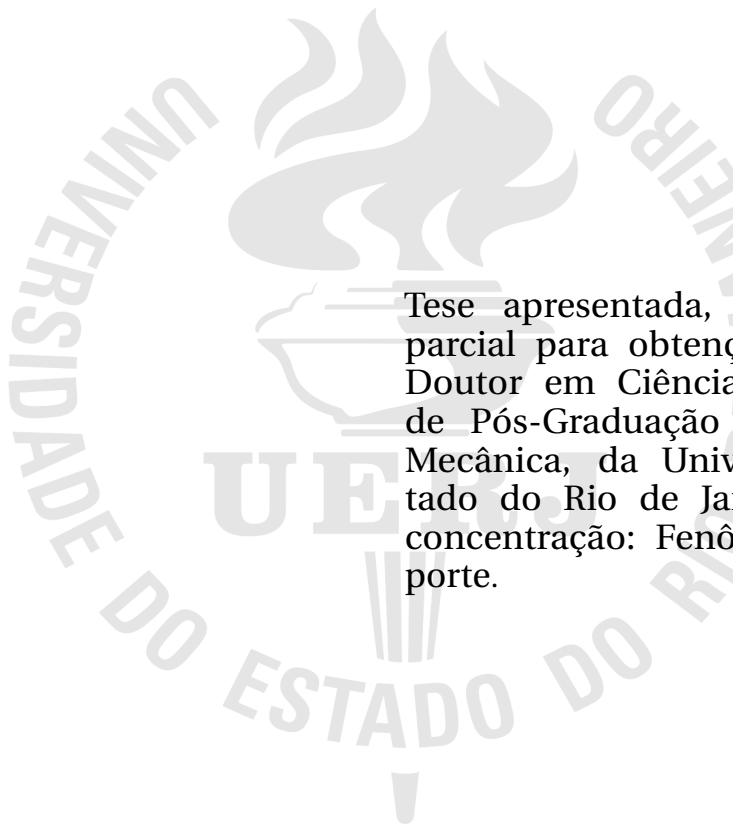
**Drop Jet in Crossflow: ALE/Finite Element  
Simulations and Interfacial Effects**

Rio de Janeiro

2015

Gustavo Charles Peixoto de Oliveira

# **Drop Jet in Crossflow: ALE/FEM Simulations and Interfacial Effects**



Tese apresentada, como requisito parcial para obtenção do título de Doutor em Ciências, ao Programa de Pós-Graduação em Engenharia Mecânica, da Universidade do Estado do Rio de Janeiro. Área de concentração: Fenômenos de Transporte.

Advisor: Prof. Ph.D. Norberto Mangiavacchi

Rio de Janeiro

2015

CATALOGAÇÃO NA FONTE  
UERJ / REDE SIRIUS / BIBLIOTECA CTC/B

O48

Oliveira, Gustavo Charles Peixoto de.

Drop jet in crossflow: ALE/finite element simulations and interfacial effects / Gustavo Charles Peixoto de Oliveira. – 2015.  
218 f.

Orientador: Norberto Mangiavacchi.

Tese (Doutorado) – Universidade do Estado do Rio de Janeiro, Faculdade de Engenharia.

1. Engenharia Mecânica. 2. Mecânica dos fluidos – Teses. 3. escoamento bifásico – Teses. 4. Método dos elementos finitos – Teses.  
I. Mangiavacchi, Norberto. II. Universidade do Estado do Rio de Janeiro. III. Título.

CDU 532

Autorizo, apenas para fins acadêmicos e científicos, a reprodução total ou parcial desta dissertação, desde que citada a fonte.

---

Assinatura

---

Data

Gustavo Charles Peixoto de Oliveira

**Drop Jet in Crossflow: ALE/Finite Element Simulations  
and Interfacial Effects**

Tese apresentada, como requisito parcial para obtenção do título de Doutor em Ciências, ao Programa de Pós-Graduação em Engenharia Mecânica, da Universidade do Estado do Rio de Janeiro. Área de concentração: Fenômenos de Transporte.

Aprovado em: 20 de fevereiro de 2015

Banca Examinadora:

---

Prof. Ph.D. Norberto Mangiavacchi (Orientador)  
Faculdade de Engenharia - UERJ

---

Prof. Ph.D. Carlos Antonio de Moura  
Instituto de Matemática e Estatística - UERJ

---

Prof. Ph.D. Leonardo Santos de Brito Alves (Co-orientador)  
Universidade Federal Fluminense

---

Prof. D.Sc. Álvaro Luiz Gayoso de Azeredo Coutinho  
Universidade Federal do Rio de Janeiro

---

Prof. D.Sc. José Henrique Carneiro de Araújo  
Universidade Federal Fluminense

Rio de Janeiro

2015

## DEDICATION

I dedicate this thesis to God, my *Abba* and manly father, who has bestowed upon me this laurel, even after the most thoughtful mind inquires why; to the sovereignty of the Brazilian science, even though my labour only sows a mere mustard seed.

## ACKNOWLEDGMENTS

To God, loyal scholar, primer of all my ever-lacking science, for assisting me during this long and laborious journey, conceiving me a bit more of knowledge, and battling beside me. Only by Him I can go further beyond. Be Thou praised!

To LTCM staff at Ecole Polytechnique Fédérale de Lausanne while I was an internship doctoral student, especially to Prof. John R. Thome, a hallmark in my career. I am very propelled to send grateful votes to: Mrs. Nathalie Matthey and Cécile Taverney, for an outstanding administrative support; Dr. Jackson Martinichen, for a Brazilian camaraderie among multiple tongues and nations; Dr. Marco Milan, Dr. Sepideh Khodaparast, and Nicolas Antonsen, for sharing an harmonious, silent, and quite serious office; Dr. Ricardo Lima, Dr. Brian d'Entremont, Dr. Sylwia Szczukiewicz, Dr. Tom Saenen, Houxue "The Tiger" Huang, Giulia Spinato, Luca Amalfi, Hamideh Jafarpoorchekab, and Nicolas Lamaison, for joyful and festive days.

To Dr. Mirco Magnini, especially, for his priceless help since the first days at LTCM (*Grazie mille per la vostra collaborazione!*); to Dr. Gustavo Anjos, for a long road of exchanged information and namesake grace (*Obrigado por toda força!*), and to Dr. Bogdan Nichita, for pleasant times beneath an unforgettable jingle: *today, what time?*

To Prof. Peter Monkewitz, for convivial moments and nobility of a wiser person.

To Prof. Anna Renda, *par sa guidance à travers des beautés et des inspirations de la langue française.*

To Prof. Norberto Mangiavacchi and Prof. Leonardo Alves, my advisors in Brazil, whom I could grasp a mix of benefits: friendship, instruction, and motivation.

To Prof. José Pontes, perennial friend, but in likeness of fatherhood, for all the prevailing ages and epochs, undoubtedly.

To my coworkers at GESAR lab and at the old LMP lab. Altogether, for funny and smiling days: behold here, Sonia Nina, Mariana Rocha, Cristiane Pimenta, Jorge Martins, Rachel Lucena, Eduardo Vitral, Melissa Mabuias, and Ana Polessa; behold there, Renan Teixeira, Flávio Santiago, and Ricardo Dias.

To closer friends who surrounded me along this trajectory, for too many special moments: Luís Otávio Olivatto, for being a great fellow under a single faith; Ruben and Sonia

Quaresma, for helping me to see new life elements while walking together with The Eternal; Márcia Oliveira, for giving me hopeful words during lasting trouble times.

To some doctors, who were precious in determined times: Fabio Bolognani, Monica Lima, Gualter Braga, and Gilberto Campos.

To my family and my grandmother, all of them cultivated somewhere inside the seasons' orchard.

To my source of poetry - much more than the years could spell again and again as girlfriend - Viviane Penna, who, beside me, has acquired patience, perseverance, hope, and love. Thank you, 1 ! Also, my kind regards to her parents and relatives.

To State University of Rio de Janeiro, the Mechanical Engineering Program staff, my classmates, and mainly to Prof. Rogério Gama and Prof. Carlos de Moura, for empathic academic lectures.

To Prof. Álvaro Coutinho, whose esteem and respect I shall keep.

To Billy Pinheiro and Damares, on behalf of many other brethren, for a helper arm of faith.

To CNPq-Brazil and the program "Science Without Borders", *sine qua non* elements that provided me with resources to the enrichment of my professional formation.

To CAPES-Brazil, for sponsoring this doctoral research.

Let my teaching drop as the rain, my speech distill as the dew, as the droplets on the fresh  
grass and as the showers on the herb. (The Song of Moses)

*Deuteronomy 32:2*



## RESUMO

**OLIVEIRA**, Gustavo Charles P. de *Drop Jet in Crossflow: ALE/Finite Element Simulations and Interfacial Effects*. 218 f. Tese (Doutorado em Engenharia Mecânica) - Faculdade de Engenharia, Universidade do Estado do Rio de Janeiro (UERJ), Rio de Janeiro, 2015.

Um código computacional para escoamentos bifásicos incorporando metodologia híbrida entre o Método dos Elementos Finitos e a descrição Lagrangeana-Euleriana Arbitrária do movimento é usado para simular a dinâmica de um jato transversal de gotas na zona primária de quebra. Os corpos dispersos são descritos por meio de um método do tipo *front-tracking* que produz interfaces de espessura zero através de malhas formadas pela união de elementos adjacentes em ambas as fases e de técnicas de refinamento adaptativo. Condições de contorno periódicas são implementadas de modo variacionalmente consistente para todos os campos envolvidos nas simulações apresentadas e uma versão modificada do campo de pressão é adicionada à formulação do tipo “um-fluido” usada na equação da quantidade de movimento linear. Simulações numéricas diretas em três dimensões são executadas para diferentes configurações de líquidos imiscíveis compatíveis com resultados experimentais encontrados na literatura. Análises da hidrodinâmica do jato transversal de gotas nessas configurações considerando trajetórias, variação de formato de gota, espectro de pequenas perturbações, além de aspectos complementares relativos à qualidade de malha são apresentados e discutidos.

Palavras-chave: Jato Transversal; Lagrangeano-Euleriano Arbitrário; Elementos Finitos; Escoamento Bifásico; Condições de Contorno Periódicas.

## ABSTRACT

A two-phase flow computational code taking a hybrid Arbitrary Lagrangian-Eulerian description of movement along with the Finite Element Method is used to simulate the dynamics of an incompressible drop jet in crossflow in the primary breakup zone. Dispersed entities are described by means of a front-tracking method which produces zero-thickness interfaces through contiguous element meshing and adaptive refinement techniques. Periodic boundary conditions are implemented in a variationally consistent way for all the scalar fields involved in the presented simulations and a modified version of the pressure field is added to the “one-fluid” formulation employed in the momentum equation. Three-dimensional direct numerical simulations for different flow configurations of immiscible liquids pertinent to experimental results found in literature. Analyses of the hydrodynamics of the drop jet in crossflow in these configurations considering trajectories, drop shape variations, spectrum of small disturbances, besides additional aspects relating to mesh quality are presented and discussed.

Keywords: Jet in Crossflow; Arbitrary Lagrangian-Eulerian; Finite Element; Two-Phase Flow; Periodic Boundary Conditions.

## LIST OF FIGURES

Figure 1	Images from internet sites exemplifying physical conditions in which JICF configurations are detected .....	31
Figure 2	Descriptive sectioning of the jet in crossflow issued normally to the free stream.	32
Figure 3	Model of the jet in crossflow depicting the entrainment effect caused by the free stream. ....	33
Figure 4	The jet in crossflow highlighting its vortical structures. ....	33
Figure 5	Diagram of jet breakup for a gas-liquid pair. ....	42
Figure 6	Experimental observation of breakup regimes of a round liquid jet in stagnant gas. ....	43
Figure 7	Breakup of a capillary water jet at the most unstable mode. ....	43
Figure 8	Breakup modes for a liquid jet injected into an immiscible liquid. ....	44
Figure 9	Primary breakup regime map for nonturbulent round liquid jets in gaseous crossflow. ....	45
Figure 10	Crossflow membrane emulsification process. ....	46
Figure 11	Drop formation and breakup of a calcia/alumina slag jet at high temperature.	47
Figure 12	Scheme representing the descriptions of movement. ....	50
Figure 13	Mathematical representation of the descriptions of movement through homeomorphisms. ....	51
Figure 14	Outlook of the molecular imbalance in the surroundings of an arbitrary gas-liquid interface. ....	56
Figure 15	Uniform distribution of the surface tension over an infinitesimal area and principal radii of curvature. ....	58
Figure 16	Generalized domain including periodic boundaries for a two-phase flow modelling. ....	60
Figure 17	Mesh elements comprising the region around the interface region and effect of transition. ....	61
Figure 18	3D mesh for an arbitrary two-phase flow configuration containing three dispersed spherical elements confined into a microchannel. ....	63
Figure 19	3D mesh for a two-phase slug flow configuration. ....	64

Figure 20	Representative behaviour of the Heaviside function over a two-dimensional surface. ....	71
Figure 21	SL method in a spatio-temporal context over a two-dimensional triangular finite element mesh.....	79
Figure 22	Different two-dimensional compositions of elements.....	81
Figure 23	Two-time representation of a continuous interface $\Gamma^1$ . Dashed: time $t_0$ ; thick: time $t$ ; dotted: trajectory. ....	84
Figure 24	Two-time representation of a piecewise linear interface $\Gamma_h^1$ . Dashed: time $t_0$ ; thick: time $t$ ; dotted: trajectory.....	84
Figure 25	Adaptive refinement strategies applied at interfaces and neighborhoods: (a) criterion based on constant distance; (b) criterion based on distance from the extrema points. ....	86
Figure 26	MINI element 3D highlighting the sites for the degrees of freedom of velocity and pressure. ....	95
Figure 27	Representations of the star $S(i)$ of the node $i$ . ....	98
Figure 28	Possible range of geometrical operations for the discrete interface. ....	99
Figure 29	Sketch of topological mappings for generic geometries. ....	102
Figure 30	Geometrical sketch of the PBC implementation for a 3D periodic finite element mesh. ....	103
Figure 31	Displacement of “leaked” departure points and Semi-Lagrangian correction. ....	116
Figure 32	Periodic domain of simulation for a Taylor vortex flow. ....	117
Figure 33	Relative error in $\mathcal{L}^2$ -norm of the velocity profile for the Taylor vortex flow. ...	119
Figure 34	Taylor vortex’s velocity profile $v_x$ ....	120
Figure 35	Taylor vortex’s velocity profile $v_y$ . ....	121
Figure 36	Taylor vortex’s periodic pressure profile $\tilde{p}$ . ....	122
Figure 37	Scalar $\phi$ being carried by fluid flow. ....	123
Figure 38	Arrangement of the unconfined in-line bubble plume: (a) extended plume model; (b) detail of the periodic cell.....	125
Figure 39	Augmented view of mesh displaying adaptive refinement strategies: circumferential, at the bubble’s surface; azimuthal, at the cylindrical wrap region of radius $R_c$ surrounding it.....	126

Figure 40	Computational mesh highlighting the bubble region: cut plane parallel to the axis of rising of the plume. ....	127
Figure 41	Computational mesh highlighting the adaptive refinement provided by the cylindrical wrap: top-view. ....	127
Figure 42	Dimensionless rising velocities $u_{bc}(t)$ for three different configurations of an air bubble rising immersed into a aqueous sugar solution. ....	129
Figure 43	Elongation ( $\phi$ ) and flatness ( $\psi$ ) ratios of the rising bubbles. ....	129
Figure 44	Bubbles' spatial motion relative to the reference frame moving upwards along with the center of mass. ....	131
Figure 45	FFT-based spectrum of disturbance energy for the ten first harmonic modes relative to the aspect ratios profiles.....	133
Figure 46	Dimensionless rising velocities $u_{bc}(t)$ over the bubble's reference frame for the cases B1 and B2. ....	134
Figure 47	Velocity field and bubble shape for the case B1: plane $yx$ . ....	135
Figure 48	Velocity field and bubble shape for the case B1: plane $zx$ .....	136
Figure 49	Velocity field and bubble shape for the case B2: plane $yx$ . ....	137
Figure 50	Velocity field and bubble shape for the case B2: plane $zx$ .....	138
Figure 51	Configuration of the drop jet in crossflow.....	139
Figure 52	Relation between fixed and moving reference frames in the DJICF flow.....	140
Figure 53	Descriptive scheme of the moving frame technique for a drop in crossflow....	142
Figure 54	Past cylinder flow velocity profile as initial condition for the DJICF simulation.	145
Figure 55	Meshes used for the DJICF simulations. ....	147
Figure 56	$u_c(t)$ -component of drop velocity - MS. ....	148
Figure 57	$v_c(t)$ -component of drop velocity - MS. ....	149
Figure 58	$w_c(t)$ -component of drop velocity - MS. ....	149
Figure 59	$u_c(t)$ -component of drop velocity - WL.....	150
Figure 60	$v_c(t)$ -component of drop velocity - WL. ....	150
Figure 61	$w_c(t)$ -component of drop velocity - WL. ....	151
Figure 62	Streamlines and drop's rims at $t \approx 0.30$ - test ( $MS, 2.0, 1.5$ ).....	152
Figure 63	Streamlines and drop's rims at $t \approx 0.25$ - test ( $MS, 2.0, 3.0$ ).....	153
Figure 64	Streamlines and drop's rims at $t \approx 0.50$ - test ( $MS, 2.0, 5.0$ ).....	154
Figure 65	Streamlines and drop's rims at $t \approx 0.37$ - test ( $WL, 2.0, 1.5$ ).....	155

Figure 66	Streamlines and drop's rims at $t \approx 0.25$ - test (WL, 2.0, 3.0).....	156
Figure 67	Streamlines and drop's rims at $t \approx 0.47$ - test (WL, 2.0, 5.0).....	157
Figure 68	$xy$ -plane drop trajectory - MS.....	158
Figure 69	$xz$ -plane drop trajectory - MS.....	159
Figure 70	$xy$ -plane drop trajectory - WL.....	160
Figure 71	$xz$ -plane drop trajectory - WL.....	160
Figure 72	Drop shape variation - (MS, ·, 1.5). .....	162
Figure 73	Drop shape variation - (MS, ·, 3.0). .....	162
Figure 74	Drop shape variation - (MS, ·, 5.0). .....	162
Figure 75	Drop shape variation - (WL, ·, 1.5). .....	163
Figure 76	Drop shape variation - (WL, ·, 3.0). .....	163
Figure 77	Drop shape variation - (WL, ·, 5.0). .....	163
Figure 78	FFT-based spectrum (MS, ·, 1.5).....	165
Figure 79	FFT-based spectrum (MS, ·, 3.0).....	166
Figure 80	FFT-based spectrum (MS, ·, 5.0).....	166
Figure 81	FFT-based spectrum (WL, ·, 1.5). .....	167
Figure 82	FFT-based spectrum (WL, ·, 3.0). .....	167
Figure 83	FFT-based spectrum (WL, ·, 5.0). .....	168
Figure 84	Skinny triangles: needle and cap elements. ....	171
Figure 85	Skinny tetrahedra: needle, cap and sliver elements. ....	171
Figure 86	Histograms $\mathcal{J}(t)_{tet}$ for group MS. ....	173
Figure 87	Histograms $\mathcal{J}(t)_{tet}$ for group WL. ....	173
Figure 88	Flowchart I: pre-processing stage.....	181
Figure 89	Flowchart II: processing stage. ....	182
Figure 90	Flowchart III: post-processing stage.....	183
Figure 91	UML partial diagram of the in-house femSIM2D/3D code. ....	184
Figure 92	Scheme for the calculation of the curvature.....	194
Figure 93	Example of a process of verification to detect errors in codes. ....	196

## LIST OF TABLES

Table 1	ALE meshing parameters for surface operations. ....	100
Table 2	Physical parameters of the Taylor vortex flow. ....	118
Table 3	Physical property values for the numerical simulations: tests R1-R3. ....	128
Table 4	Physical property values for the numerical simulations of the rising bubble plume tests. ....	130
Table 5	Parameters of simulation according to the experiment no. 5 of Meister and Scheele. ....	146
Table 6	Parameters of simulation according to the fluid combination no. 1(c) of natural jet of Webster and Longmire. ....	147
Table 7	Maximum disturbance energies and dominant modes of the spectral analyses. ....	169
Table 8	FFT sampling ranges and disturbance attenuation thresholds for the spectral analyses. ....	170
Table 9	Mesh quality indicators relative to the statistical histograms. ....	174

## LIST OF SYMBOLS

### Acronyms

ALE	Arbitrary Lagrangian-Eulerian
CAD	Computer-Aided Design
CFD	Computational Fluid Dynamics
CIP	Cubic Interpolated Profile
CK	Chemical Kinetics
CSF	Continuum Surface Force
CVP	Counter-Rotating Vortex Pair
DBC	Dirichlet Boundary Conditions
DJICF	Drop Jet in Crossflow
DOFs	Degrees of Freedom
FE	Finite Element
FEM	Finite Element Method
FFR	Fixed Frame Reference
FFT	Fast Fourier Transform
JICF	Jet in Crossflow
KH	Kelvin-Helmholtz
LBB	Ladyzhenskaya-Babuska-Brezzi
LSA	Linear Stability Analysis
LS	Level-Set
MAC	Marker-and-Cell



MFR Moving Frame Reference  
NBC Neumann Boundary Conditions  
OBC Open Boundary Conditions  
PBC Periodic Boundary Conditions  
RT Rayleigh-Taylor  
VOF Volume of Fluid

### **Greek letters**

$\beta_1$  mesh parameter: pure Lagrangian motion  
 $\beta_2$  mesh parameter: neighbourhood-based velocity smoothing  
 $\beta_3$  mesh parameter: elastic-based velocity Laplacian smoothing  
 $\alpha$  backward displacement vector  
 $\chi$  position in the reference domain  
 $\delta$   $\delta$  function  
 $\delta_\zeta$  distribution over an interface  
 $\eta$  distance to interface, or interface node  
 $\Gamma$  boundary  
 $\gamma_1$  mesh parameter: tangent interface velocity magnitude  
 $\gamma_2$  mesh parameter: elastic-based velocity node relocation  
 $\iota$  cardinality of nodes  
 $\iota_p$  cardinality of pressure/scalar points  
 $\iota_v$  cardinality of velocity points  
 $\kappa$  curvature  
 $\lambda$  barycentric coordinate, or jet-to-crossflow velocity ratio

$\mu$	dynamic viscosity
$\nu$	kinematic viscosity
$\Omega$	domain
$\omega$	frequency
$\overline{\Omega}$	closure of $\Omega$
$\phi$	arbitrary scalar quantity
$\phi$	mapping function from referential domain to the spatial domain
$\Psi$	mass concentration
$\psi$	flatness ratio
$\Psi$	mapping function from referential domain to the material domain
$\rho$	density
$\sigma$	surface tension
$\Sigma$	surface tension matrix
$\tau$	time
$\lambda$	second viscosity
$\mu$	viscosity ratio
$\phi$	elongation ratio
$\rho$	density ratio
$\varphi$	shape function
$\varphi$	mapping function from material domain to spatial domain
$\omega$	circulation
$\rho$	mass diffusivity coefficient
$\xi$	Lagrangian interface point

$\zeta$  continuous surface

### **Roman letters**

$A$  area

$a$  wave amplitude, or peak

$B$  body

**bc** boundary condition discrete vector

$F$  abstract source vector of fluid variables

$\Phi$  abstract unknown vector of fluid variables

$X$  particle pathline

**b** body force, or discrete vector, or binormal vector

$\check{v}$  particle velocity in the referential domain

**c** relative velocity between the fluid and the mesh

$d$  differential

**D** discrete divergent matrix

$e$  element index, or arbitrary function

**E** discrete pressure-related matrix

**e** error

$F$  face of element

$f$  frequency

**F** tensor, or force

**f** interfacial force

$g$  gravity

**G** discrete gradient matrix

<b>g</b>	gravity field
<i>H</i>	Heaviside function
<b>h</b>	Heaviside function discrete vector
<b>I</b>	identity tensor or matrix
<b>j</b>	flux of mass concentration
<i>k</i>	wave number
<b>K</b>	discrete viscosity-related matrix
<i>l</i>	line element, or edge length
<i>L</i>	length
<i>m</i>	dimension
<b>M</b>	mass matrix
<b>n</b>	normal unit vector
<b>o</b>	origin of fixed reference frame
<i>p</i>	hydrostatic pressure
$\tilde{\mathbf{p}}$	discrete periodic pressure vector
<b>p</b>	“pull” vector, or discrete pressure vector
<b>r</b>	right hand side discrete vector
<i>s</i>	curve element
<b>s</b>	surface force
<i>T</i>	simplex, or triangle, or tetrahedron
<i>t</i>	time instant
$\tilde{p}$	periodic pressure
<b>T</b>	tensor

$\mathbf{t}$	tangent unit vector
$u$	arbitrary function
$U$	velocity
$\mathbf{v}$	fluid velocity
$\mathbf{v}_e$	“elastic” velocity
$\hat{\mathbf{v}}$	mesh velocity
$w$	arbitrary weight function
$\mathbf{w}$	weight function discrete vector, or arbitrary vector
$\mathbf{X}$	position in the material domain
$\mathbf{x}$	position in the spatial domain

### Superscripts

$(\cdot)^1$	dispersed phase
$(\cdot)^2$	continuous phase
$(\cdot)^\#$	intermediary, or provisional
$(\cdot)^i$	indexing
$(\cdot)^m$	dimension
$(\cdot)^n$	iterative time step
$(\cdot)^p$	interpolation order
$(\cdot)^r$	integration order
$(\cdot)^\sigma$	relative to surface tension
$(\cdot)^*$	dimensionless
$(\cdot)^T$	transpose

### Subscripts

- (·)<sub>0</sub> initial condition, or compact support
- (·)<sub>1</sub> arbitrary index, or relative to dispersed phase
- (·)<sub>2</sub> arbitrary index, or relative to continuous phase
- (·)<sub>A</sub> relative to area
- (·)<sub>a</sub> arrival
- (·)<sub>β</sub> relative to pressure gradient
- (·)<sub>c</sub> relative to center of mass, or centroid
- (·)<sub>corr</sub> correction
- (·)<sub>crit</sub> critical
- (·)<sub>D</sub> Dirichlet
- (·)<sub>d</sub> departure
- (·)<sub>e</sub> element, or elementary
- (·)<sub>f</sub> final
- (·)<sub>h</sub> relative to refinement
- (·)<sub>#</sub> provisional
- (·)<sub>I</sub> relative to interface
- (·)<sub>i,j</sub> node or point indexing
- (·)<sub>L</sub> relative to lumped
- (·)<sub>λ</sub> relative to jet-to-crossflow velocity ratio
- (·)<sub>m</sub> mean, or intermediary
- (·)<sub>mov</sub> moving
- (·)<sub>N</sub> Neumann
- (·)<sub>NS</sub> relative to Navier-Stokes

- $(\cdot)_P$  periodic
- $(\cdot)_\partial$  relative to boundary
- $(\cdot)_\phi$  relative to elongation
- $(\cdot)_\Psi$  relative to mass concentration
- $(\cdot)_\psi$  relative to flatness
- $(\cdot)_{ref}$  reference
- $(\cdot)_{rel}$  relative
- $(\cdot)_\rho$  relative to phase
- $(\cdot)_t$  relative to time, or compact support

### **Symbols**

- $A_{\mathcal{T}}^{max}$  number of tetrahedra of maximum quality
- \* interelement Neumann contributions
- interelement Neumann contributions
- interelement Neumann contributions
- $Ca$  Capillary number
- $\mathcal{A}$  periodic copying matrix-model
- $\mathcal{B}$  “bubble” function space
- $\mathcal{E}$  error in modulus
- $\mathcal{H}$  Sobolev space
- $\mathcal{L}$  Lebesgue space
- $\mathcal{M}$  MINI element’s function space
- $\mathcal{N}$  set of the vectors normal to a body’s surface
- $\mathcal{O}$  order

$\mathcal{P}$	space of polynomial functions
$\mathcal{Q}$	space of trial functions for pressure
$\mathcal{R}$	space of weight functions
$\mathcal{S}$	space of trial functions for velocity
$\mathcal{U}$	periodic copying vector-model
$\mathcal{V}$	space of weight functions
$\mathcal{X}$	set of the points on a body's surface
$\mathcal{Y}$	set of nodal variables ( <i>ipsis litteris</i> : degrees of freedom)
$\cdot$	inner product
$CFL$	Courant-Friedrichs-Lewy number
$:$	tensor inner product
$dA$	infinitesimal area
$\delta_{,i}$	Kronecker's delta
$\Delta t$	discrete time step
$\delta t$	infinitesimal time
$\Delta \tau$	continuous time interval
$\Delta \mathbf{x}$	displacement
$\diamond$	interelement Neumann contributions
$\dim$	dimension
$\nabla \cdot$	divergent operator
$dl$	infinitesimal line
$\frac{D}{D\tau}$	material derivative operator



$\frac{D}{Dt}$	material derivative operator
$\doteq$	“equivalent by input argument to”
$dV$	infinitesimal volume
$Eo$	Eötvös number
$Eu$	Euler number
$\mathbf{e}_i$	canonical unit vectors of $\mathbb{R}^3$
$\mathbf{e}_p$	unit vector of periodic direction
$\Im$	imaginary part of a complex number
$(\cdot, \cdot)$	inner product, or bilinear form, or ordered pair
$\nabla^2$	Laplace operator
$\rightsquigarrow$	“is associated to”
$\mathcal{I}_{(T)}$	radius ratio quality measure of $T$
$\mathcal{T}_h$	tessellation, or triangulation, or tetrahedralization
$\mathring{\Omega}$	interior of $\Omega$
$E$	disturbance maximum energy
$L$	differential operator
$P, Q$	projection operators
$R$	fixed reference frame
$\hat{R}$	moving reference frame
$N$	Archimedes number
$\nabla$	gradient operator
$Oh$	Ohnesorge number

$\oplus$	direct sum
$\otimes$	tensor product
$\partial$	partial derivative, or boundary
$Pe$	Peclét number
$\mathcal{O}_\%$	mesh quality percentage at a fixed time
$R_1, R_2$	principal radii of curvatures
$\Re$	real part of a complex number
$Re$	Reynolds number
$\mathbb{R}^m$	$m$ -dimensional real vector space
$\nabla \times$	curl operator
$Sc$	Schmidt number
$St$	Strouhal number
$\star$	interelement Neumann contributions
$\mathcal{T}_h^\Gamma$	discrete surface mesh
$\mathcal{T}_h^\Omega$	discrete volume mesh
$\Delta$	interelement Neumann contributions
$\vee$	logical XOR (exclusive “or”)
$Fr$	Froude number
$We$	Weber number

## CONTENTS

	<b>INTRODUCTION</b> .....	28
1	<b>LITERATURE REVIEW</b> .....	30
1.1	<b>Jet in crossflow: physics and models</b> .....	30
1.2	<b>Jet in crossflow: a summary</b> .....	34
1.3	<b>Selected research milestone</b> .....	35
1.3.1	<u>Issues on linear stability</u> .....	35
1.3.2	<u>Other references</u> .....	39
1.4	<b>Instability and breakup in two-fluid jets</b> .....	40
1.5	<b>Purposes of this thesis</b> .....	48
2	<b>TWO-PHASE FLOW MODELLING: TOOL SUITE AND OVERVIEW</b> .....	49
2.1	<b>Arbitrary Lagrangian-Eulerian: a hybrid movement description</b> .....	49
2.2	<b>Short review on numerical methods</b> .....	53
2.3	<b>Interface and surface tension</b> .....	55
2.4	<b>Meshing art and generalities</b> .....	59
3	<b>GOVERNING EQUATIONS</b> .....	65
3.1	<b>Principles</b> .....	65
3.1.1	<u>Mass conservation</u> .....	65
3.1.2	<u>Linear momentum</u> .....	66
3.1.3	<u>Advection-diffusion equation</u> .....	68
3.1.4	<u>The “one-fluid” formulation</u> .....	70
3.2	<b>Applied methods</b> .....	73
3.2.1	<u>Projection method</u> .....	73
3.2.2	<u>Semi-Lagrangian method</u> .....	76
4	<b>FINITE ELEMENT PROCEDURES IN TWO-PHASE FLOWS</b> .....	80
4.1	<b>Historiography and theory of the classical FEM</b> .....	80
4.2	<b>FEM for incompressible two-phase flows</b> .....	83
4.2.1	<u>Explicit representation of interfaces</u> .....	84
4.2.2	<u>Adaptive refinement: determination of thresholds</u> .....	85

4.3	<b>Variational formulation of the governing equations</b>	86
4.3.1	<u>Primitive variables</u>	86
4.3.2	<u>Fluid variables</u>	93
4.3.3	<u>The stable MINI element 3D</u>	94
4.4	<b>Dynamic mesh control and ALE parametrization</b>	96
4.4.1	<u>Dynamic control techniques</u>	97
4.4.2	<u>Geometrical operations and remeshing techniques</u>	98
4.5	<b>Solvers and preconditioning</b>	99
5	<b>PERIODIC BOUNDARY CONDITIONS</b>	101
5.1	<b>Introductory remarks</b>	101
5.2	<b>Design of periodic meshes and their pre-processing</b>	102
5.3	<b>Periodic decomposition via the transformed variable approach</b>	104
5.4	<b>FE/PBC implementation</b>	107
5.4.1	<u>Variational formulation in periodic domains</u>	107
5.4.2	<u>Computational implementation</u>	110
5.4.3	<u>Repair of the backward-in-time Semi-Lagrangian search</u>	115
6	<b>CODE VALIDATION</b>	117
6.1	<b>Taylor vortex in highly viscous fluid</b>	117
6.1.1	<u>Spatial validation of PBC</u>	117
6.1.2	<u>Scalar transport with PBC</u>	119
6.2	<b>Air bubble plume rising in quiescent water</b>	124
6.2.1	<u>Periodic array of in-line rising bubbles</u>	124
6.2.2	<u>Mathematical model</u>	124
6.2.3	<u>Mesh generation and adaptive refinement</u>	126
6.2.4	<u>Validation tests</u>	127
6.2.5	<u>Rising velocity, aspect ratios, trajectories and spectra</u>	129
6.2.6	<u>Wake effects and near-field velocity</u>	132
7	<b>THE DROP JET IN CROSSFLOW</b>	139
7.1	<b>Problem posing</b>	139
7.2	<b>Moving frame reference technique</b>	141
7.2.1	<u>Computation of averaged quantities</u>	144

7.3	<b>Direct numerical simulations</b> .....	144
7.3.1	<u>Initial condition</u> .....	144
7.3.2	<u>Study of DJICF cases: hydrodynamics and discussion</u> .....	146
7.4	<b>Trajectory curves, drop shape variations and spectrum analyses</b> .....	158
7.4.1	<u>Trajectory curves</u> .....	158
7.4.2	<u>Drop shape variations</u> .....	161
7.4.3	<u>Spectrum analyses</u> .....	164
7.5	<b>Mesh quality assessment</b> .....	171
	<b>CONCLUSION</b> .....	175
	<b>APPENDIX A - CODE FLOWCHARTS</b> .....	180
	<b>APPENDIX B - GMSH SCRIPT SAMPLE (PERIODIC SURFACE)</b> .....	185
	<b>APPENDIX C - EQUATIONS OF THE PBC FORMULATION</b> .....	190
	<b>APPENDIX D - CURVATURE AND FRÉNET'S FRAME</b> .....	192
	<b>APPENDIX E - VERIFICATION &amp; VALIDATION</b> .....	194
	<b>APPENDIX F - VITA</b> .....	198
	<b>APPENDIX G - PUBLICATIONS</b> .....	198
	<b>REFERENCES</b> .....	201

## INTRODUCTION

Jets in crossflow (JICFs) arise abundantly in diverse technological apparatuses and natural phenomena that range from mixture microdevices, propulsion systems to gaseous plumes in volcanic eruptions. The main feature of JICFs is their empowerment to provide mixture and dilution of substances, which are processed as the jet is issued into an ambient flow either normal or tilted to it.

In engineering and aerodynamics, some applications of JICFs are the following: in airbreathing turbines, the control of gas emissions is achieved by varying the air-fuel mixture ratio through transverse air jet injection in the primary zone of gas turbine combustors; in scramjets, air at supersonic speeds enters in its combustion chamber and the fast reaction process requires rapid transverse fuel penetration, mixing with crossflow, ignition, and sustainment of combustion; thrust vector control, mainly for rocket engines, - inasmuch as the thrust can be altered in direction and, to a limited extent, in magnitude by the deflection of the flow within the rocket engine's nozzle - is caused by the injection of an array of transverse jets; concerning V/STOL aircrafts, such as the Harrier model, an application is concentrated in the "jump" jets, during take-off, hovering, and transition to wing-borne flight in vertical/short take-off and landing.

Concerning environmental purposes, JICFs are observed as smoke plumes exhausting from chimneys in power plants, flare stack gas burners, and effluents pouring into rivers, where the jet is issued tilted to the free stream. JICFs are a model, moreover, for puffs, flames, and turbulent mixing of gases in the atmosphere. Due to the environmental risks, the reduction of pollutant emissions from hydrocarbon-based systems, such as gas turbines and petroleum refineries as well as the lower ejection of nitrogen oxides ( $NO_x$ ), carbon monoxide ( $CO$ ), and soot into the air evoke immediate decision-making for controlled exhaustions, thereby motivating the research in this area.

On the other hand, the dynamics of nonturbulent immiscible liquid-liquid jets is present in many modern applications, thus opening research branches for the study of drop jets in crossflow (DJICF) developing at microscale. The performance of devices in chemical processes, microfluidics and drug delivery, for instance, is closely based on crossflow shear flows along with dripping and jetting regimes. Crossflow membrane emulsification processes in which the dispersed phase is introduced in the continuous phase by pressure through

a membrane containing one or more pores constitute flows with dense drop interactions. In industry, the capillary breakup of jets of molten oxides at high temperatures, as a final example, is investigated in metal production, steelmaking processes and high-precision solder printing technology.

The comprehension of the physical phenomena associated to DJICFs depend on theoretical, computational, and experimental bases. Under these circumstances, this numerical work is intended to present a study of drop jets in crossflow restricted to the primary breakup zone by using an Arbitrary Lagrangian-Eulerian (ALE)/Finite Element methodology. Dynamic meshes along with the consideration of interfacial effects render key tools to deal with the problems arising from the multifluid/multiphase flow scope such as those contained in this thesis.

## 1 LITERATURE REVIEW

Studies about the JICF have a plentiful history and range each of the experimental, theoretical, and numerical branches broadly. This chapter introduces a conspectus of information devoted to this flow and ends up with the formalization of the purposes of this thesis. We begin with a basic presentation of the general physical aspects of JICF. Sequentially, a review of some selected articles that boosted the scientific progress of this field is given in a medially chronological sense, appending important contributions of the current time to JICF's motifs. Lastly, issues on jet instability and breakup in liquid-liquid systems as well as specific applications of drops in crossflow are presented.

### 1.1 Jet in crossflow: physics and models

As illustrations, Figure 1 displays four great facets of JICF in different situations. First of all, a picture of an aircraft model Harrier - label (a) - shows how the process of vertical short take-off and/or landing (V/STOL) is utterly associated to a crossflow interaction. In second place, an atomized liquid jet in crossflow is viewed as a result of refuelling in an aircraft engine. On the other hand, it is noteworthy to point out how indispensable such regime serves for irrigation, aerosol, and spray technologies. As a third example, now related to the oil industry, the JICF appears as a large plume rising up from a fire at an oil rig in the Gulf of Mexico. Similar behaviour is observed in flare stack gas burners at oil refineries and in big chimneys of chemical industries as displayed in the fourth picture. As can be seen, many situations allow the exploration of the research about JICF configurations.

For the physical evaluation pertinent to the JICF, we refer to the presentation by Rajaratnam [5] diagrammed in Figure 2 as a descriptive sectioning of the jet issued normally to the free stream. As explained therein, the stagnation pressure exerted by the free stream is responsible for deflecting the jet. Due to the turbulent mixing developing on the periphery of the jet, the outer layers lose part of their momentum and hence are easily deflected, bringing forth a characteristic kidney shape for the jet. As the jet hits the free stream, there is a central region of relatively shear free flow. This region specified by the length  $OC$  is generally known as the potential core region. When the jet-to-crossflow velocity ratio  $\lambda^{-1} = \frac{U_j}{U_\infty}$  is relatively greater than 4, the point  $C$  is located directly over the center of the jet. For smaller values, the point  $C$  is pushed downwind.





Figure 1: Images from internet sites exemplifying physical conditions in which JICF configurations are detected: (a) an AV-8B Harrier aircraft during vertical taking-off process (from [1]); (b) atomization of an aircraft engine liquid fuel jet in a crossflow (from [2]); (c) a large plume rising up from a fire on an oil rig in the Gulf of Mexico (from [3]), and (d) gas flow being expelled out to the atmosphere from the big chimney of the Esbjerg Power Station, in Denmark (from [4]).

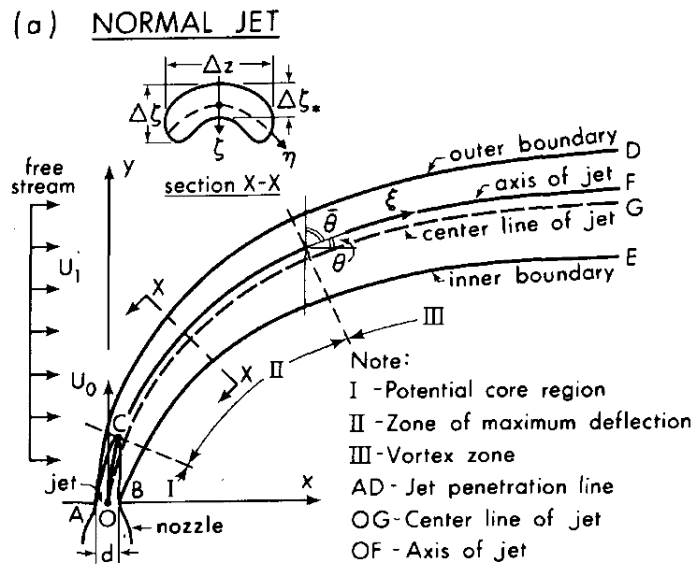


Figure 2: Descriptive sectioning of the jet in crossflow issued normally to the free stream. From [5].

It is known that the length of the potential core varies mainly with the velocity ratio  $\lambda^{-1}$ . Generally, the length of the potential core is less than that of the free jet (*i.e.* the jet in stagnant surroundings) and approaches asymptotically the free jet value for large values of  $\lambda^{-1}$ . From the end of the potential core, the jet suffers a large deflection in a certain length which is known as the zone of maximum deflection, where mixing cores evolve. The remnant portion of the deflected jet is also referred to as the vortex region, where a pair of counter-rotating vortices (CVP) connected by circulation free fluid shed. Apropos the vortical structures developing in the JICF, three other kinds of patterns are recognized in the literature, beyond the CVP before mentioned, namely, shear-layer vortices, horseshoe vortices, and wake vortices.

Several models were introduced in the literature in attempting to tackle the JICF problem. Among them, fundamental references provided geometrical schemes quite representative, such as that of Coelho and Hunt [6], the almost crowned example of the vortical structures supplied by Fric and Roshko [7], and that one of Lim, New, and Luo [8], all of them reproduced in Figure 3 and Figure 4.

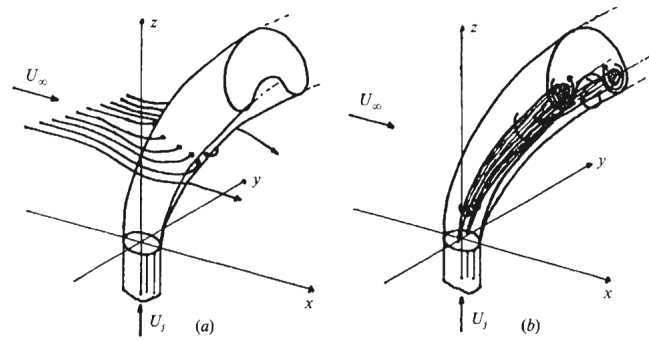
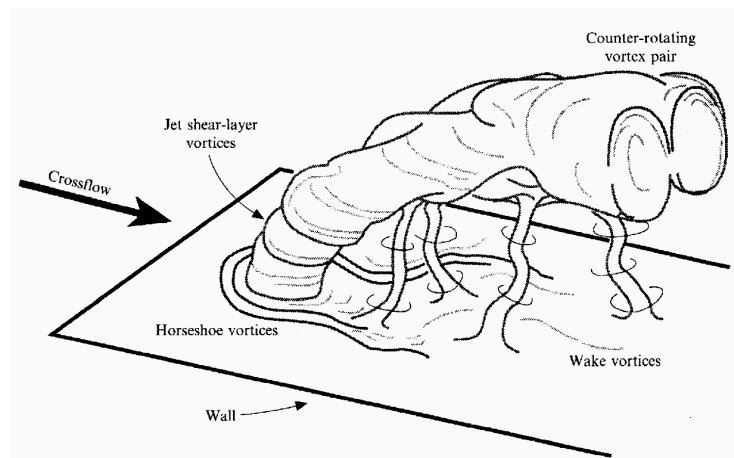
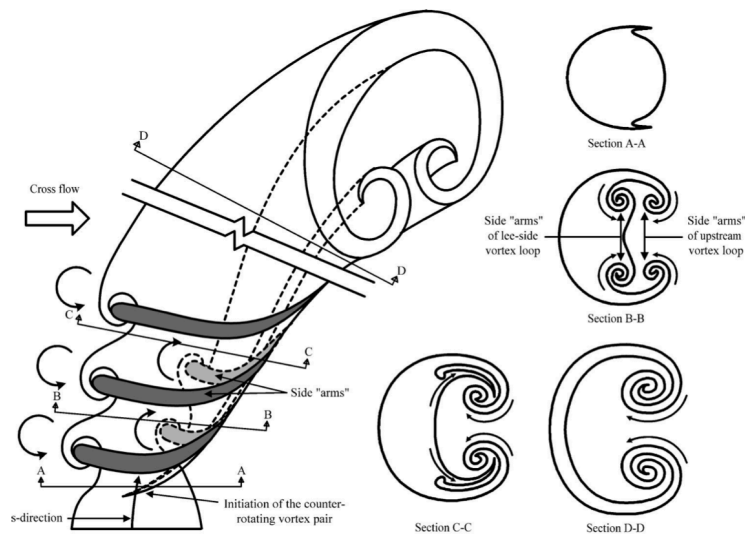


Figure 3: Model of the JICF depicting the entrainment effect caused by the free stream. Extracted from [6].



(a)



(b)

Figure 4: The jet in crossflow highlighting its rich vortical structures: (a) cartoon extracted from the referential work by Fric and Roshko and (b) drawing taken from Lim, New, and Luo.

## 1.2 Jet in crossflow: a summary

Abramovich [9] was one of the pioneers in describing JICF experiments, focusing on the effect of the jet-to-crossflow velocity ratio  $\lambda^{-1}$  on the jet trajectory. Kamotani and Greber [10], and Kelso, Lim and Perry [11], later, advanced on the study of the CVP.

JICF in parallel to thermal plumes were studied by Moussa and Trischka [12], whereas a denser content related to mixture was developed by Smith and Mungal [13]. In this latter article, a scaling criterion was also proposed by establishing three regions for the flow: a vortex interaction region, the near field region and the far field region.

Coelho and Hunt [6] adduced how the momentum transfer, deflection and entrainment occur in the JICF configuration. They studied inviscid vortex-sheet models and pointed out a shortcoming of a widely inviscid 2D model used to describe transverse jets by asserting that the flow within the pipe was not uniform, but affected by the crossflow.

Around the 1990-2000 decades, papers related to jet excitation, better performance of penetration and mixture in crossflows, beyond jet control techniques were conducted by: Johari, Tougas, and Hermanson [14]; Eroglu and Breidenthal [15]; MCloskey *et al.* [16], and Narayanan, Barooah, and Cohen [17]. Such issues involved wave theory and frequencies, whence initiates the comprehension about the sensitivity of the transverse jet to high frequencies.

Theoretical work and numerical simulations of the JICF are also diversified in the literature. Sykes, Lewellen and Parker [18] were among the pioneers in performing 3D numerical simulations of a turbulent jet issued normal to a uniform free stream. In the sequence, Needham, Riley and Smith [19] built 3D models involving concentrations of vorticity for an inviscid incompressible jet issuing skewed into the ambient flow from a semi-infinite pipe. They began to inquire about the cause of deflection of the jet and argued that the influence of the co-flow distorted it asymmetrically.

Minute examinations of the transverse jet through numerical simulations were carried out by Rudman [20]. His jet configuration was flush-mounted into the wall and a compressible code had to be solved with a high Mach number. Even as Rudman had exposed, Hahn and Choi [21] proceed with the study of the effects of computational time step and grid stretching on the numerical solution of a planar jet injected into a laminar boundary-layer.

In regard to the universe of computational techniques, Yuan, Street, and Ferziger [22] were among those who used LES (Large Eddy Simulations) in transverse jet cases, being the

first researchers to deal with and solve the problem of the turbulent boundary-layer appearing in the jet flush-mounted into a wall. Not long ago, Muppidi and Mahesh [23] used DNS (Direct Numerical Simulations) to study the near field of incompressible round jets in crossflow with the goal of obtaining improved correlations for transverse jet trajectories. Additionally, Keimasi, and Taeibi-Rahni [24] came up with techniques based on RANS (Reynolds-Averaged Navier Stokes) equations for the 3D turbulent flow of square jets injected perpendicularly into a crossflow handling several different turbulence models.

Special contents about JICF are found in Karagozian, Cortelezzi and Soldati [25], in a seemingly ceremonial paper by [26], describing a fifty years history about the transverse jet as well as in meticulous synopses organized by Karagozian [27], [28] and Mahesh [29].

### 1.3 Selected research milestone

JICF research is plenteous; hence, it is infeasible and impractical to build a full and unending milestone that wraps each issue in a whole. For this reason, this section will cover a compendium of selected references.

#### 1.3.1 Issues on linear stability

Liquid sheets, stability analysis for inviscid jets and instabilities in viscous jets are issues covered in Lin's book [30], in which we will be anchored to single out important remarks *bis in idem*. Despite its literary worth, other good references about shear flows such as the books by Chandrasekhar [31] and by Schmid and Henningson [32] should be appreciated, though this latter lacks in text about jets. Huerre and Monkewitz [33] is one of the most known papers on local and global instabilities, where spatially developing open shear flows are carefully reviewed.

Batchelor and Gill [34] considered temporally growing disturbances to perform a LSA of the parallel free jet and were followed by Michalke [35], who obtained Strouhal numbers for different momentum thickness of the free jet – the Strouhal number gives a sight of the sensitiveness of open shear flows to perturbations and noises and it is defined by  $St = f_{ref} L_{ref} / U_{ref}$ . Michalke's results relied on a hyperbolic-tangent velocity profile widely known in literature. In others papers [36], [37], [38] he examined the instability mechanism occurring in mixing layers and concluded that spatially growing disturbances were responsible for it.

When studying mixing singular problems with the free jet under the nonparallel flow hypothesis, Morris [39] included viscous effects in his LSA. For the circular jet, Michalke and Hermann [40] described that the incidence of an increasing external co-flow velocity onto the jet decreased the growth rates of the most unstable disturbance but, at the same time, the Strouhal number increased. For this case, they performed an inviscid LSA and made a simple modification of the free jet hyperbolic-tangent profile. Michalke [41] also obtained theoretical results concerning the instability of axisymmetric jets.

Alves [42] studied the shear-layer instabilities and vorticity evolution associated with the JICF in order to get a better understanding of them. A computational code was developed to perform numerical simulations in association with a LSA. The main purposes of that work relied on applications already described herein as well as on some keypoints. Firstly, the instability mechanism in vogue was that one characterized by velocity-gradient regions where most of the vorticity is concentrated. In fact, the question interlaced was how the KH instability that leads to a vortex roll-up in a free jet was affected by the presence of a crossflow perpendicular to the free jet base state. Secondly, a LSA which resulted from the first goal was the additional benefit to understand phenomena concentrated to the near field. The analysis could be switched accordingly between the inviscid and viscous transverse jet base flows. In third place, the numerical simulations were supported by the existence of linear and nonlinear instabilities developing in the transverse jet.

The JICF base velocity profile is three-dimensional and has a non-negligible azimuthal dependence. In his thesis, Alves employed a perturbation expansion approach, using the crossflow-to-jet velocity ratio  $\lambda$  as the perturbation parameter in order to take into account the nonparallel effects of that flow field. Such an approach decouples the azimuthal modes being investigated and is used in the LSA of both the inviscid and viscous base flow models for the transverse jet. Furthermore, a new approach that considers several azimuthal modes simultaneously was developed and applied to the LSA of the inviscid base flow. Another fact emphasized by Alves was a global stability analysis avoidance. The explication was rooted in the expensive time to obtain time-averaged DNS data to use as a base flow for a stability analysis, since DNS resolves a transient flow field evolution with length scales down to the Kolmogorov's scale. An unresolved problem incurs thereof: the development and selection of an appropriate base flow for the transverse jet with respect to the stability analysis.

After a little time, Alves, Kelly, and Karagozian [43] published a paper with results

supplied by the stability analysis of the inviscid transverse jet, in which both the jet and co-flow had the same density. A correction was made in the solution of Coelho and Hunt [6] therein because of an error found in one of the second-order kinematic conditions derived by the authors. Through this correction, the main conclusions of Alves were that positive and negative helical modes for the transverse jet had slightly different growth rates, implying a lack of symmetry for the KH instability arising in the transverse jet. Such an approach was affirmed to be the first mathematical verification that even low-level crossflows can produce weak asymmetries in the transverse jet.

In a two-piece paper series, Megerian *et al.* [44] and Alves *et al.* [45] showed both experimental and theoretical studies upon the transverse jet. Megerian's study provided a detailed exploration of the near field shear-layer instabilities associated with the transverse jet. Jet injection from nozzles which are flush as well as elevated with respect to the tunnel wall were explored experimentally for jet-to-crossflow velocity ratios  $\lambda^{-1}$  in the range  $1 \leq \lambda^{-1} \leq 10$  and with jet Reynolds numbers of 2000 and 3000. The results indicated that the nature of the transverse jet instability is significantly different than that of the free jet, and that the instability changes in character as the crossflow velocity is increased. They proposed explanations for the differences previously observed in transverse jets controlled by strong forcing in order to improve techniques for the transverse jet penetration control, mixing, and spread. On the other hand, Alves presented a local LSA for the subinterval  $\lambda^{-1} > 4$  using two different base flows for the transverse jet and predicting the maximum spatial growth rate for the disturbances through a expansion in powers of  $\lambda$ . This way, the free jet results could be reached as  $\lambda^{-1} \rightarrow \infty$ . His results matched accordingly to Megerian's experiments, thus suggesting that the convective instability occurs in ratios above 4 and that the instability is strengthened as  $\lambda^{-1}$  is decreased. Consistency of his findings with experiments provided powerful evidence of the dominance of the convectively unstable axisymmetric mode, at least in the regime  $\lambda^{-1} > 4$ .

Still considering the expansion in  $\lambda$ , Kelly and Alves [46] reached a uniformly valid asymptotic solution for the transverse jet. This exercise was accompanied by a LSA in which the inviscid vortex sheet analysis of Coelho and Hunt was extended so including asymptotic analysis of the viscous shear layers that formed along the boundaries of the jet. The instability that gives rise to the near field vortices after developing an asymptotic solution for the three-dimensional base flow was investigated and its validity for large values of the Reynolds number

and small  $\lambda$  was pointed out. By using asymptotic methods, they derived a solution of the NS equations valid under some conditions for the transverse jet near field. This achievement led to a more accurate description of the basic flow.

Until now the citations were entwined in the sense of a local stability analysis. Some contributions on global stability analysis, in turn, are mentioned forth. Bagheri *et al.* [47], at first glance, went ahead in taking up a simulation-based global stability analysis of the viscous three-dimensional JICF considering a steady exact solution to the NS equations, which showed that the JICF is characterized by self-sustained global oscillations for a jet-to-crossflow velocity ratio of 3. By suppressing global instabilities by selective frequency damping, they asserted that the JICF is, in fact, globally unstable and must be placed into this category of flows. They verified that not only the most unstable global modes with high frequencies are compact and represent localized wave packets on the CVP, but also that the existence of global eigenmodes justifies the global stability approach as an appropriate tool to describe the inherent and dominant dynamics of the JICF.

Davitian *et al.* [48] studied the transition of the transverse jet shear layer to global instability in the near field by quantifying the growth of disturbances at several locations along and about the jet shear layer. Moreover, frequency tracking and response of the transverse jet to very strong single-mode forcing were applied. It was evidenced that the flush transverse jet's near field shear layer becomes globally unstable when  $\lambda^{-1}$  is within or below a critical range near 3. According to the authors, this work is characterized as a support tool to improve strategies for the transverse jet control, since this field has been widely developed.

Ilak *et al.* [49] published a brief comment on the DNS of a jet in crossflow at low values of the jet-to-crossflow velocity ratio  $\lambda^{-1}$ , in which they mention the observation of hairpin-like vortices. A part of this paper is sustained by results from Schlatter's *et al.* work [50]. In the latter, the jet is studied numerically by considering the maximum velocity of the parabolic profile. Their modelling imposed an inhomogeneous boundary condition at the crossflow wall and the results showed that two fundamental frequencies – a high one and another low one – are present in the flow tied to self-sustained oscillations. They used nonlinear DNS, modal decomposition into global linear eigenmodes, and proper orthogonal decomposition modes.

In a recent publication, Ilak *et al.* [51] analyzed a bifurcation found from DNS at low values of the jet-to-crossflow velocity ratio  $\lambda^{-1}$ , precisely occurring at  $\lambda^{-1} = 0.675$ . As



$\lambda^{-1}$  increased, it was showed that the flow evolved from simple periodic vortex shedding (a limit cycle) to more complicated quasi-periodic behaviour before coming into turbulence. Additionally, a LSA was also performed to predict qualitative data about the dynamics of the nonlinear effects.

### 1.3.2 Other references

New, Lim and Luo [52] reported the results of an experimental investigation on the effects of jet velocity profiles on the flow field of a round JICF using laser-induced fluorescence and digital particle-image velocimetry techniques (DPIV). Though top hat and parabolic jet velocity profiles with the mass ratios ranging from 2.3 to 5.8 were considered, in the case of the shear-layer associated to a parabolic profile of JICF, there was an increase in jet penetration and a reduction in the near-field entrainment of crossflow fluid.

DNS was used by Muppidi and Mahesh [53] to study a round turbulent jet in a laminar crossflow. Turbulent kinetic energy budgets were computed for this flow and it was shown that the near field is far from a state of turbulence. Additionally, it was observed in the near field that the peak of kinetic energy production was close to the leading edge, while the peak dissipation was observed toward the trailing edge of the jet. Velocity and turbulent intensity profiles from the simulation were also compared to some profiles obtained from experiments, and a good agreement was exhibited. Emphatic points in that treatise was the observation that past the jet exit, the flow is not close to established canonical flows on which most models appear to be based.

One year later, Muppidi and Mahesh [54] used DNS to study passive scalar transport and mixing in a round turbulent jet, in a laminar crossflow. In this case, the Schmidt number rose up naturally as a nondimensional parameter. The scalar field was used to compute entrainment of the crossflow fluid by the jet. It was shown that the bulk of this entrainment occurs on the downstream side of the jet and the simulations were used to comment on the applicability of the gradient-diffusion hypothesis to compute passive scalar mixing in the flow field.

Denev *et al.* [55] followed a similar path using DNS for the flow with transport of passive scalars and chemical reactions when studying phenomena and chemical reactions in a JICF. Instantaneous mixing of structures and laminar to turbulent flow transition were compared to experimental data with good agreement.

Many others fields of application of JICF have been provided with scientific research in recent years, which are out of scope of this thesis. However, some references to further contents are listed here: pulsed jets are discussed by Muldoon *et al.* [56], Sau and Mahesh [57] and Coussement *et al.* [58]; jet penetration and injection into subsonic and supersonic crossflow are studied by Lee *et al.* [59] and Rana, Thornber and Drikakis [60], respectively; applications like oil flare stacks, pollutant dispersion, soot emissions and flame stabilization are cited by Grout *et al.* [61] and Marr *et al.* [62]; finally, acoustic excitation and atomization are topics related by Hsu and Huang [63] and Herrmann [64].

#### 1.4 Instability and breakup in two-fluid jets

This section is devoted to bring forth the overall differences among the physical mechanisms encompassing gas-liquid and liquid-liquid jet configurations by emphasizing the drop formation stage in order to narrow the review to the purposes of this thesis. The physics of jets in its entirety is widely discussed by [65], whose major points relate to small perturbations, breakup, spray formation and non-Newtonian effects.

Several studies about jet instabilities found in literature have their fundamentals upon gas-liquid configurations unlike a minor parcel dedicated to liquid-liquid interfaces. The historical development of the LSA applied to liquid jets issued into another immiscible liquid starts from Tomotika [66], who has extended the inviscid LSA previously done by Rayleigh [67]. Although the explanation of Rayleigh pointed that the two main causes of jet instabilities were the operation of the capillary force, whose effect is to render the jet an unstable form of equilibrium and favour its disintegration into detached drops, and those due to the dynamical character of the jet, his investigations were concentrated in liquids issued into calm air.

Tomotika's equation, in turn, was a surmise to guide newer findings, among which Meister and Scheele's [68], [69], who have developed a drop formation theory through experimental studies with 15 liquid-liquid systems and determined the jet length from which breakup occurs. Later, Kitamura [70] found experimentally that the Tomotika's theory described precisely the size of the droplets when the surrounding fluid and the main fluid moved with the same velocity. Attempts to include the relative motion of both the liquids in the LSA were conducted by Bright [71] and [72], for instance.

These pioneer studies about the stability of free jets followed the traditional approach

that defines the disturbances of the jet interface  $\eta$  by

$$\tilde{\eta} = ae^{i(kx - \omega t)}, \quad (1.1)$$

where  $x$  is the axial direction. Such form is initialized over the liquid surface as a result of pressure fluctuations. Weber [73], for example, solved the NS equation for a viscous liquid jet to obtain a characteristic equation which found the most unstable dimensionless growth rate and wave number being, respectively

$$\Re\{\omega\}^* = \frac{1}{2(1 + 3Oh_1)} \quad \text{and} \quad k^* = \frac{1}{\sqrt{2(1 + 3Oh_1)}}, \quad (1.2)$$

where  $Oh_1$  is the Ohnesorge number of the dispersed phase. The Ohnesorge number relates the rate between viscous forces to inertial and surface tension forces and it is written as  $Oh = \mu_{ref} / \sqrt{\rho_{ref} \sigma_{ref} L_{ref}}$ , or, in a different view, as  $Oh = \sqrt{We} / Re$ .

Because of its unstable behaviour, a jet cannot escape the fate of breakup, which takes place in two major regimes, *viz.* the period of large drop formation and the spray formation. The rupture of a continuous jet in drops is motivated by a couple of applications where it occurs, such as in combustion chambers, bioprocesses, chemical emulsions, and ink jet printing. In microfluidic devices, particularly, one resorts to crossflow T-junction geometries for lubrication, enhanced mixture, among others, for which dripping regimes are intended.

The breakup stages in a gas-liquid pair are explored in Figure 5. The distance elapsed from the jet's launching station until the first drop pinches off is called *intact length*, or *breakup length*. Then, as the jet's velocity increases, the intact length tends to achieve a maximum value from which drops are formed. This point lies on somewhere between the points A and B, whereas the quasi-linear uprise marked by the points before A indicates the dripping, end of dripping and jet formation stages. Such sudden changes subsist until drops whose radii measure almost twice the jet's emerge. Between the points B and C, the drops have their radii equivalent to the jet's. Beyond the point C, droplets strip off the surface, thereby shaping a locally atomized regime. As the depth of surface dripping renders deeper, the average droplet radius become smaller so that the jet achieves the completely atomized regime after the point D, *i.e.* the spray regime. At this regime, the droplets' radius decreases with the inlet jet velocity.

Lin and Reitz [74] wrote a review focused on the physical mechanisms that cause the

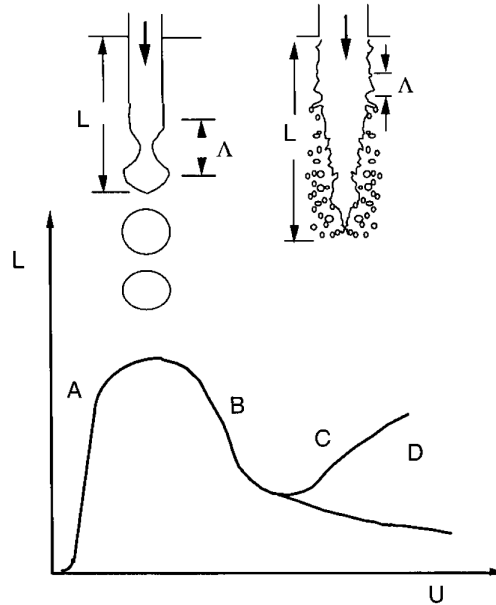


Figure 5: Diagram of the jet breakup length  $L$  vs. jet velocity  $U$ . Extracted from [30], p. 104.

onset of the jet breakup at gas-liquid interfaces. They describe four main breakup regimes corresponding to different flow properties, namely: the Rayleigh breakup regime; first wind-induced regime; second wind-induced regime and the atomization regime. By experimental observations (see Figure 6), it was verified that the breakup drop sizes are on the order of the jet diameter in the Rayleigh and first wind-induced regimes and much less in the second wind-induced and atomization regimes. Furthermore, issues about the way how pressure fluctuations around the interface from inside and outside the jet, capillary pinching with wind assistance and surface tension relate to breakup were explained. The criteria defining these breakup regimes are based on ranges of the  $We$  and  $Oh$  numbers. They are considered manifestations of convective instability and are well organized in the summary developed by [75], whose experimental results studying the Rayleigh breakup in capillary water jets have Figure 7 as an example. It describes the breakup length of a jet at its most unstable mode for different  $We$  numbers.

Richards [76] *et al.*, in their study about breakup in liquid-liquid systems asserted that the nontrivial effects due to the continuous phase outside the jet render the liquid-liquid dynamics more complicated than gas-liquid dynamics for which, most of time, the air is considered the inviscid continuous phase or hypothesized as vacuum. Such difficulties are associated to viscous, buoyancy, surface tension, inertial forces, besides jet contraction, velocity profile relaxation, and relative motion of the continuous phase. In their studies,

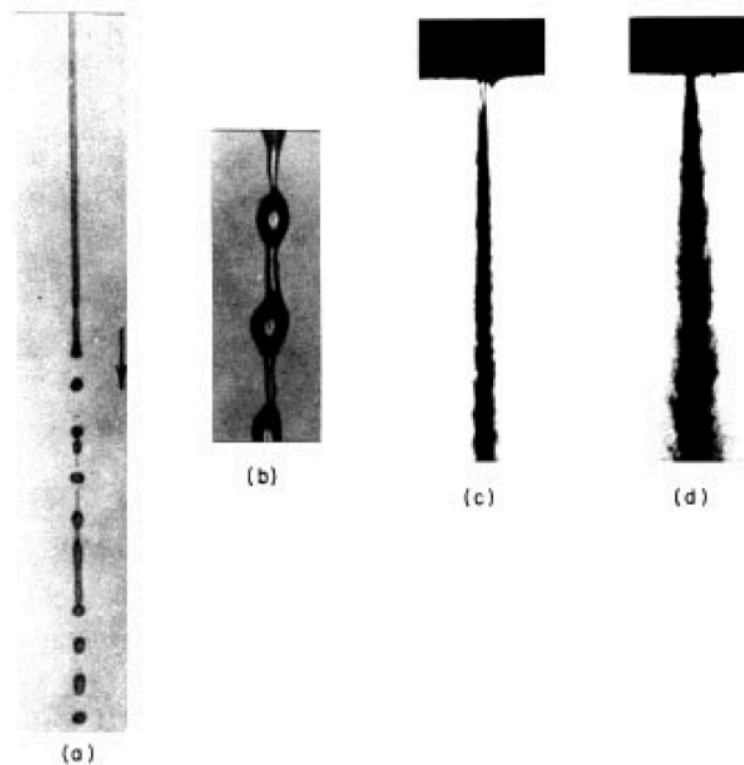


Figure 6: Experimental observation of the four breakup regimes occurring after the issuing of a round liquid jet in stagnant gas: a) Rayleigh breakup; b) first wind-induced regime; c) second wind-induced regime; d) atomization regime. Extracted from [74].

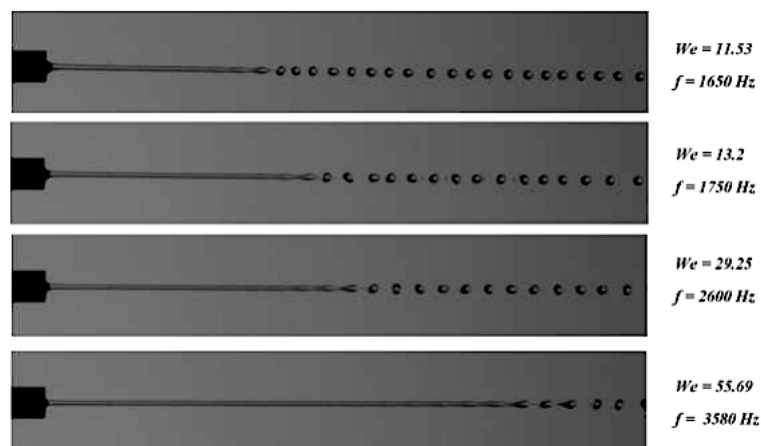


Figure 7: Breakup of a capillary water jet at the most unstable mode. Taken from [75], p. 46.

laminar flow, constant properties (e.g. viscosity, density, surface tension) and axisymmetric disturbances formed the set of hypotheses. The VOF model was applied to predict the jet length, shape, size of formed droplets through numerical simulations and comparisons with experimental data were done as well. Following a similar approach based on VOF, Homma *et al.* [77] studied breakup modes for a liquid jet injected into another immiscible liquid. They found good accordance by contrasting experimental data with their numerical code

and identified three physical breakup modes, *viz.* dripping, jetting with uniform droplets and jetting with nonuniform droplets, although they mentioned the limitation of their code to a certain range of parameters. These breakup modes are depicted in the diagram of Figure 8. For low injection velocities, droplets are formed periodically at the jet nozzle and no jet is observed, thereby featuring the breakup mode called *dripping*. With the increase of the jet velocity, the *jetting* mode appears. Further beyond, the jet is completely broken due to the growth of asymmetric disturbances, so that the jet intact length decreases to define the mode of *atomization*.

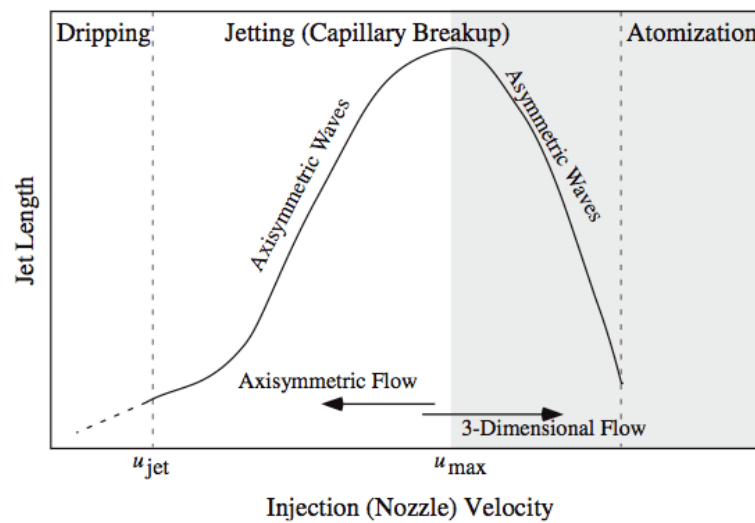


Figure 8: Breakup modes for a liquid jet injected into another immiscible liquid. Taken from [77].

Physical forces play a dominant role in each breakup regime, whose importance is measured by the Weber number, Reynolds number, Froude number, Mach number, density ratios, and velocity of the fluids involved. Despite of the regimes aforementioned, it is possible to find classifications even more detailed in literature. Figure 9, for instance, is a map of the primary breakup regime for liquid jets in gaseous crossflow as a function of the Weber number and the Ohnesorge number. It suggests that the Weber and Ohnesorge numbers govern breakup regime transitions according to certain situations as follow: for conditions where viscous forces are small, gasdynamic forces (or drag) on the liquid jet must be stabilized by surface tension forces, which implies that deformation and breakup regime transitions correspond to particular critical Weber numbers  $We_{crit}$  that are constant; for conditions where surface tension forces are small, on the other hand, gasdynamic forces (drag) on the liquid jet must be stabilized by liquid viscous forces, which implies that critical crossflow

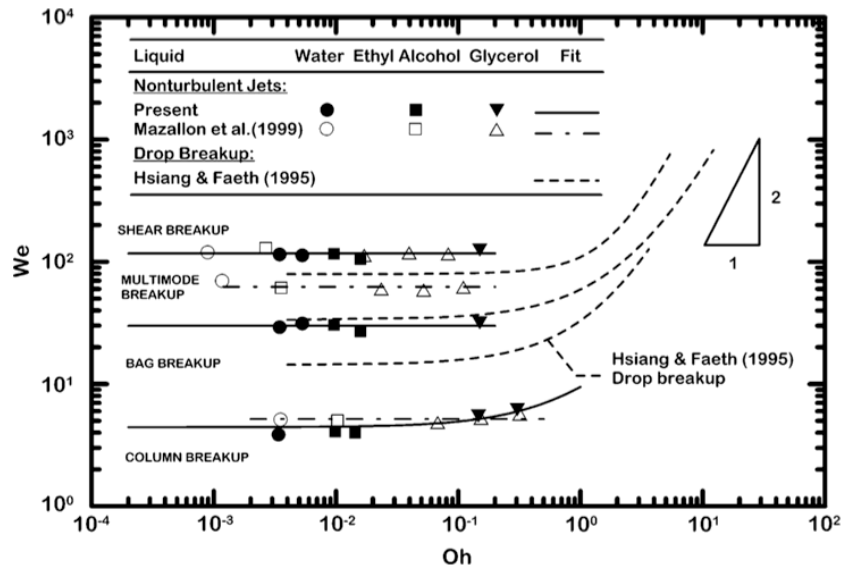


Figure 9: Primary breakup regime map for nonturbulent round liquid jets in gaseous crossflow. Extracted from [78].

Weber numbers are proportional to the square of the Ohnesorge number, *i.e.*  $We_{crit} = \mathcal{O}(Oh^2)$ . As described in the map, specific for some substances, four primary breakup regimes can be described as the Weber number increases, namely: the column (or liquid-column) breakup, bag breakup, multimode (or bag/shear) breakup and shear breakup. According to [79] in their experiments for  $Oh < 1$  (small liquid viscosity), these regimes can be described as the crossflow velocity increases. These regimes are discussed briefly next. The column (or liquid-column) breakup results, at first, from the deformation of the liquid column normal to the crossflow to yield an ellipsoidal cross section which is caused by a reduction of the gas pressure near the side of the jet and ensuing acceleration of the gas over the liquid column. The drag forces due to the flattened shape of the column, in turn, enhance the tendency of the liquid to deflect toward the streamwise direction. As the liquid column deflects, thickened regions (the nodes) appear along the column and shed into drop-like structures with thinner interconnecting liquid column regions. Finally, the breakup occurs by the Rayleigh-like breakup of these filaments. As crossflow velocity increases, the bag-breakup arises after the liquid column is sufficiently flattened so that bag-like structures develop. Such bags result from the deformation of the central portion of the liquid column downstream due to the higher pressure of the stagnating gas flow on the upstream side of the flattened liquid column. With increasing distance along the liquid column, the bags grow, achieve a maximum size and begin to break beginning at their tip due to a Rayleigh-like breakup of the formed

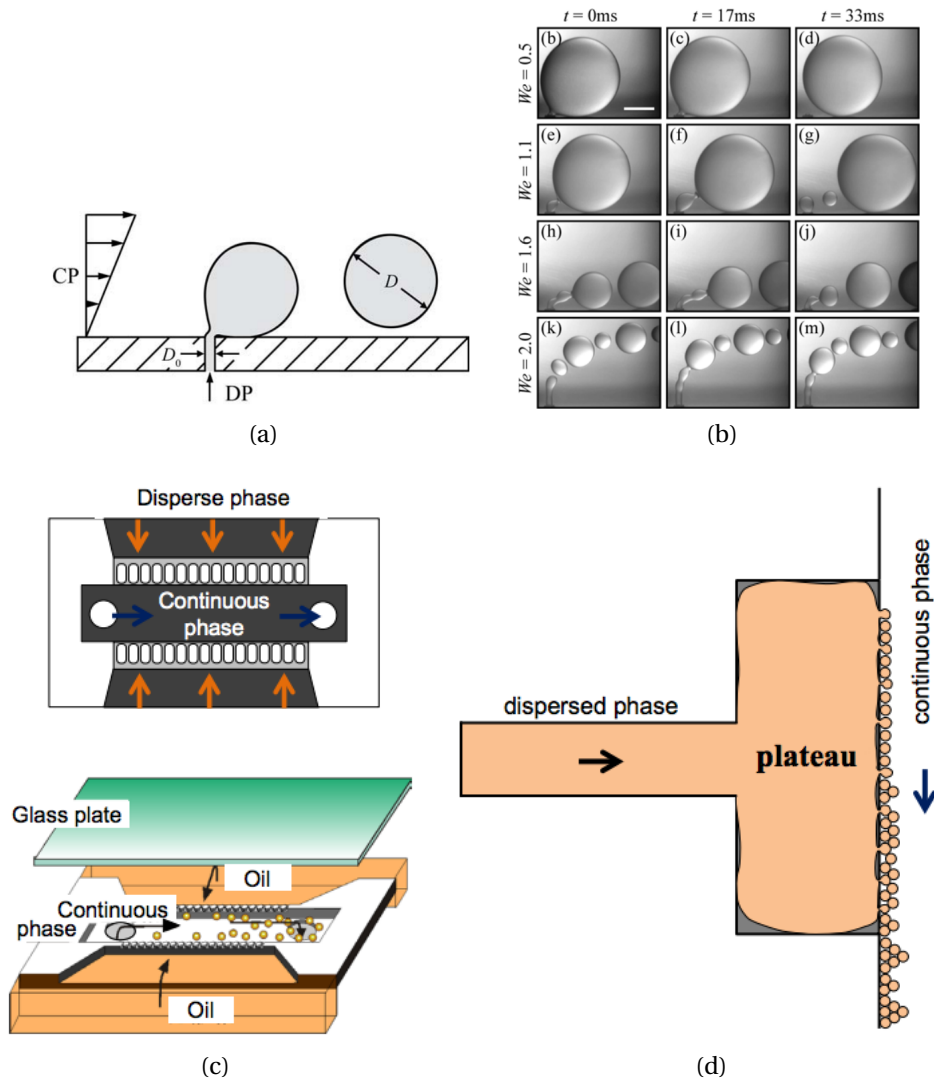


Figure 10: Crossflow membrane emulsification process: (a) diagram, (b) emulsification process (from [80]); (c) microchannel module; (d) multiple droplet generation device (from [81]).

liquid sheet as well. The multimode (or bag/shear) breakup is a complex regime which is a combination of the bag breakup and shear breakup, to be described next. In this stage, both bag-like structures, due to penetration of the liquid column, and liquid ligaments, due to the shearing of liquid from the periphery of the liquid column appear together almost at the same time. Breakup, henceforth, follows after the rupture of the bag-like and ligament structures aforementioned. Lastly, the shear breakup arises similar to the bag and multimode breakup with the largest crossflow velocity. The process begins by deflection of the liquid column toward the crossflow direction followed by distortion of the column into a flattened shape, appearing of wavelike disturbances in the upstream side of the liquid column, formation of ligaments and subsequent detachment of these ligaments. While sheet-like regions might



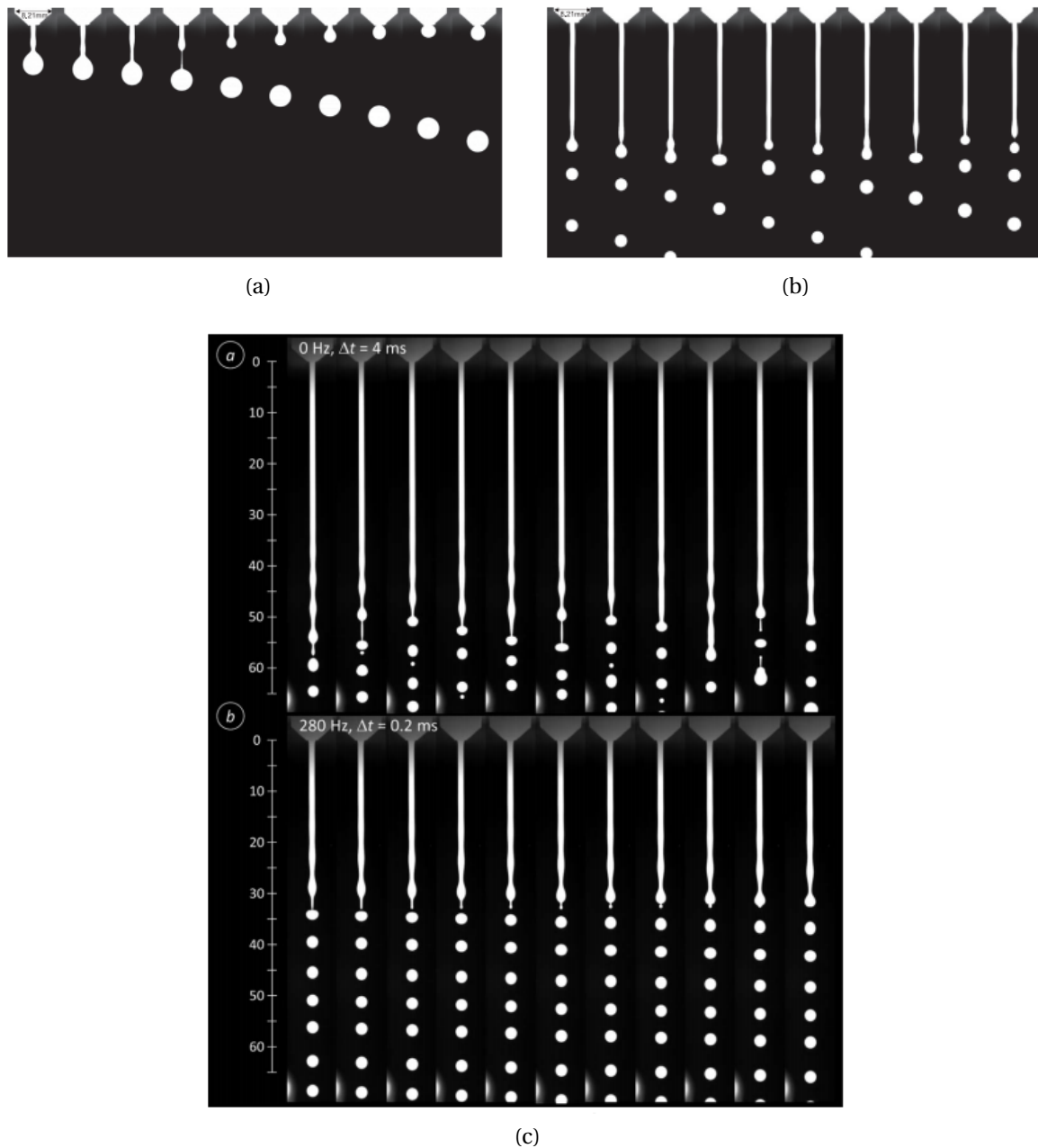


Figure 11: Drop formation and breakup of a calcia/alumina slag jet at high temperature: (a) jet formation (imagery every 5 ms), (b) developed jet (from [82]); (c) jet excited periodically (from [83]).

evolve within the ligament structures, convex bag shapes enclose them at the sides.

All things considered, it is convenient to mention some recent developments regarding drop formation in liquid-liquid systems. The performance of many modern devices in chemical processes, microfluidics and drug delivery, for instance, is closely based on crossflow shear flows along with dripping and jetting modes (see [84] and references therein). Figure 10, for instance, shows how crossflow membrane emulsification processes work. The dispersed

phase (DP) is introduced in the continuous phase (CP) by pressure through a membrane containing one or more pores. In turn, it is driven by the crossflow over the membrane's surface. The capillary breakup of jets of molten oxides (slags) at high temperatures rely on the investigation of metal production, steelmaking processes and high-precision solder printing technology. Figure 11 is an example of the formation and breakup of calcia/alumina slag jets.

### 1.5 Purposes of this thesis

Under the motivational aspects previously reviewed, the contribution of this thesis relies on the numerical simulation of liquid-liquid dynamics, particularly focused on the drop regime and its purposes are:

- to use an Arbitrary Lagrangian-Eulerian Finite Element Method two-phase flow code to simulate a nonturbulent liquid jet in crossflow by considering surface tension effects,
- to apply a unit cell-based model that resorts to periodic boundary conditions along with the moving frame reference technique to follow the jet, and
- to perform an analysis of the flow hydrodynamics in the primary breakup zone of drop formation based on experimental liquid-liquid pairs.

## 2 TWO-PHASE FLOW MODELLING: TOOL SUITE AND OVERVIEW

This thesis encompasses many different attributes as regards computational modelling. By this reason, the gist of this chapter is to accommodate an all-in excerpt about basilar concepts that will be used along the forthcoming chapters. Any order of preference is taken into account herein since each topic is viewed independently when converging to a self-content framework. Section 2.1 centers around the ALE description of movement, an useful tool to deal with flows whose interfaces are highly mobile; Section 2.2, in turn, revises some important advances in two-phase flow modelling along the years organizing a brief history of well-known numerical methods; sequentially, Section 2.3 discourses to some extent about the physicochemical behaviour of interfaces. Lastly, Section 2.4 brings up a few procedures of CAD design, pre-processing, and setting of FE meshes.

### 2.1 Arbitrary Lagrangian-Eulerian: a hybrid movement description

Roots of the ALE methodology stem from pioneer studies like Hirt's [85] and Chan's [86]. Nonetheless the second author proposed a generalized technique to manipulate sharp interfaces in incompressible flows, the treatment of free-surface flows and material interfaces through ALE methods continued to be envisioned by many others. Löhner [87], for instance, points out some modern examples of interactions occurring between fluids and rigid bodies, such as off-shore structures submerged in water, military torpedoes launched in the atmosphere, and rapid trains slithering through the air while entering tunnels. Generally, wetted bodies partially or totally submerged as well as deformable surfaces fall into the class of the best examples.

In the Eulerian description, an observer watches with time what happens at a fixed point in space and around it while fluid particles pass over that locus. On the other hand, in the Lagrangian description an observer is attached to a particle and travels with it undergoing all the changes concomitantly as time elapses. Under a computational point of view, both descriptions can be used to deal with several physical problems and the reasons to opt between them should be based on suitability criteria because of their advantages and drawbacks. Next, a brief analysis of their attributes concerning the mixed ALE description will be done. We will follow substantially the writings by [88] and [89], although [90] is enlightening as a further reference and [91] a more recent text which discusses generalities of moving domains.

A fundamental step to develop a CFD code is to decide which kinematic description to use. A positive point of the Lagrangian description is to allow an easy tracking of free surfaces and interfaces between different materials, but it is unskillful to follow large distortions of the computational domain without requiring frequent remeshing operations. On the other hand,

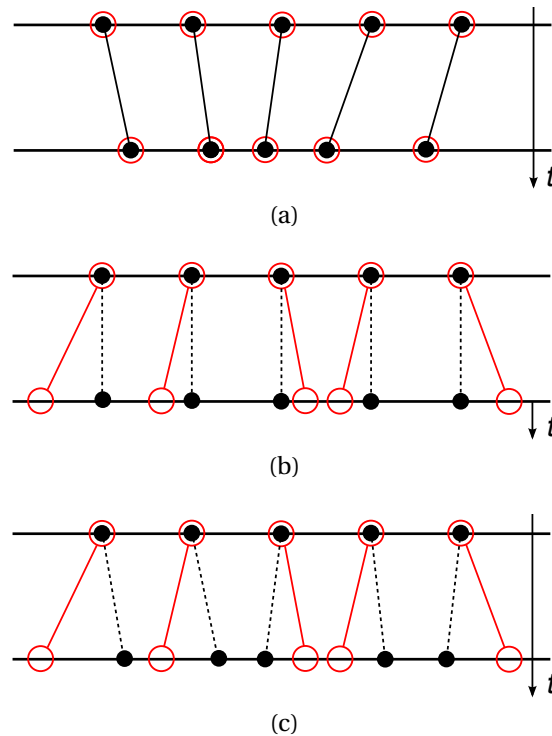


Figure 12: Scheme representing the descriptions of movement: (a) Lagrangian; (b) Eulerian; (c) ALE (hybrid).

although the Eulerian description handles large distortions in the continuum motion with relative easiness, it generally requires higher computational cost to define interfaces precisely, i.e. with high resolution of the flow's details. In order to avoid the shortcomings deriving from a methodology purely Lagrangian or uniquely Eulerian, ALE/FE meshes try to grasp and combine qualities of these two methodologies to produce a better one. When the ALE description is used, some arbitrariness is permitted to the mesh nodes to move freely. Alternatively, they either remain stopped as if governed by an Eulerian fashion, or move together with the fluid, or even walk to a specified direction. These different behaviours are depicted in Figure 12. The dark points identify the mesh nodes, whereas the red circles represent material points. This freedom of movement enables a continuous rezoning functionality so that larger distortions are redressed with good resolution.

To reach its objective, the ALE methodology establishes an “intermediary” domain to bridge an interplay between the material and spatial domains used to map the movement,

which, in the ALE literature, is called the *referential domain*. These nomenclatures are suggested to follow a reasoning line, though they might slightly differ than those presented in classical books of Continuum Mechanics like [92], for instance. With a mathematical language, the ALE description can be deduced through the homeomorphisms represented in Figure 13 (a similar version is found in [90]) and ensuing didacticism. Let  $\varphi$  be the function that maps

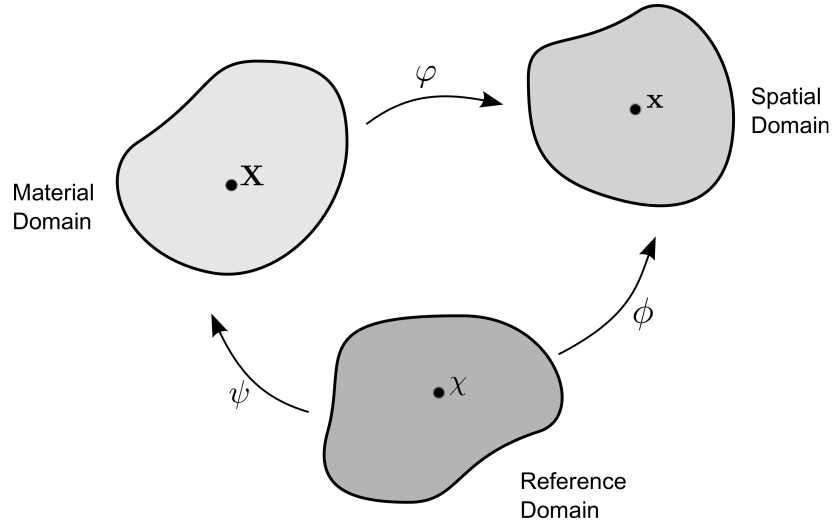


Figure 13: Mathematical representation of the descriptions of movement through homeomorphisms.

the material domain to the spatial domain defined by

$$\begin{aligned} \varphi : B_{\mathbf{X}} \times [t_0, t_f[ &\rightarrow B_{\mathbf{x}} \times [t_0, t_f[ \\ (\mathbf{X}, t) &\mapsto \varphi(\mathbf{X}, t) = (\mathbf{x}, t). \end{aligned}$$

Then, we can write the relation between the material domain and the spatial domain as

$$\mathbf{x} = \mathbf{x}(\mathbf{X}, t).$$

If a notation in the fashion of the Jacobian matrix for  $\varphi$  depending on space and time is used, a compact form to express derivatives is

$$\frac{\partial[\varphi(\mathbf{X}, t)]}{\partial(\mathbf{X}, t)} = \begin{bmatrix} \frac{\partial \mathbf{x}}{\partial \mathbf{X}} & \mathbf{v} \\ \mathbf{0}^T & 1 \end{bmatrix}, \quad (2.1)$$

where

$$\mathbf{v}(\mathbf{X}, t) = \left. \frac{\partial \mathbf{x}}{\partial t} \right|_{\mathbf{x}} \quad (2.2)$$

is the *fluid velocity* and  $\mathbf{0}^T$  a null row-vector.

In like manner, let  $\phi$  be the function that maps the referential domain to the spatial domain defined by

$$\begin{aligned} \phi : B_{\boldsymbol{\chi}} \times [t_0, t_f[ &\rightarrow B_{\mathbf{x}} \times [t_0, t_f[ \\ (\boldsymbol{\chi}, t) &\mapsto \phi(\boldsymbol{\chi}, t) = (\mathbf{x}, t). \end{aligned}$$

A matrix notation for  $\phi$  is also written as

$$\frac{\partial[\phi(\boldsymbol{\chi}, t)]}{\partial(\boldsymbol{\chi}, t)} = \begin{bmatrix} \frac{\partial \mathbf{x}}{\partial \boldsymbol{\chi}} & \hat{\mathbf{v}} \\ \mathbf{0}^T & 1 \end{bmatrix}, \quad (2.3)$$

where

$$\hat{\mathbf{v}}(\boldsymbol{\chi}, t) = \left. \frac{\partial \mathbf{x}}{\partial t} \right|_{\boldsymbol{\chi}} \quad (2.4)$$

is the *mesh velocity*.

Now, let  $\Psi$  be the function that maps the referential domain to the material domain. Differently than the aforementioned mappings, this one is described by using the inverse function as

$$\begin{aligned} \Psi^{-1} : B_{\mathbf{x}} \times [t_0, t_f[ &\rightarrow B_{\boldsymbol{\chi}} \times [t_0, t_f[ \\ (\mathbf{X}, t) &\mapsto \Psi^{-1}(\mathbf{X}, t) = (\boldsymbol{\chi}, t). \end{aligned}$$

Similarly, a matrix notation for  $\Psi$  is written as

$$\frac{\partial[\Psi^{-1}(\mathbf{X}, t)]}{\partial(\mathbf{X}, t)} = \begin{bmatrix} \frac{\partial \boldsymbol{\chi}}{\partial \mathbf{X}} & \check{\mathbf{v}} \\ \mathbf{0}^T & 1 \end{bmatrix}, \quad (2.5)$$

where

$$\check{\mathbf{v}} = \left. \frac{\partial \boldsymbol{\chi}}{\partial t} \right|_{\mathbf{x}} \quad (2.6)$$

can be interpreted as the *particle velocity in the referential domain*.

From these mappings, a dependence relation among  $\mathbf{v}$ ,  $\hat{\mathbf{v}}$ , and  $\check{\mathbf{v}}$  is viewed by the composition

$$\varphi = \phi \circ \Psi^{-1}, \quad (2.7)$$

which shows a direct influence of the ALE construction on purely Eulerian or purely Lagrangian methods.

A relation among deformation gradients and velocities is better visualized when using Equation (2.1), Equation (2.3) and Equation (2.5) to write the matrix equation

$$\begin{aligned} \begin{bmatrix} \frac{\partial \mathbf{x}}{\partial \mathbf{X}} & \mathbf{v} \\ \mathbf{0}^T & 1 \end{bmatrix} &= \begin{bmatrix} \frac{\partial \mathbf{x}}{\partial \chi} & \hat{\mathbf{v}} \\ \mathbf{0}^T & 1 \end{bmatrix} \begin{bmatrix} \frac{\partial \chi}{\partial \mathbf{X}} & \check{\mathbf{v}} \\ \mathbf{0}^T & 1 \end{bmatrix} \\ &= \begin{bmatrix} \frac{\partial \mathbf{x}}{\partial \chi} \frac{\partial \chi}{\partial \mathbf{X}} & \frac{\partial \mathbf{x}}{\partial \chi} \check{\mathbf{v}} + \hat{\mathbf{v}} \\ \mathbf{0}^T & 1 \end{bmatrix}. \end{aligned} \quad (2.8)$$

This latter identity, however, yields

$$\mathbf{v} = \hat{\mathbf{v}} + \begin{bmatrix} \frac{\partial \mathbf{x}}{\partial \chi} \end{bmatrix} \check{\mathbf{v}}, \quad (2.9)$$

implying that the so-called *convective velocity*  $\mathbf{c}$  defined by

$$\mathbf{c} : \mathbf{v} - \hat{\mathbf{v}} = \begin{bmatrix} \frac{\partial \mathbf{x}}{\partial \chi} \end{bmatrix} \check{\mathbf{v}}, \quad (2.10)$$

works like the relative velocity between fluid and mesh. It is worth to underline that  $\mathbf{c}$  should be used in the equations governing the fluid motion under an ALE approach instead of that velocity figuring in the classical forms. In a word,  $\mathbf{c}$  is the essence of the ALE description.

## 2.2 Short review on numerical methods

Experimentations are by far limited to investigate all the physical effects that are crucial for a two-phase system. Testing out several conditions is highly cumbersome in terms of mounting of facilities and data analysis. For these reasons, computational modelling and numerical simulations are a feasible way to circumvent such limitation.

Many different models were devised along the last decades to deal with multiphase systems, thereby inciting the scientific community to seek methods more and more accurate and capable of capturing the complex dynamics that springs out from these systems. Owing to their difficult modelling, the hypothesis of homogeneity is predominantly held even in the most promising methods. A brief history on the main developments concerning the computational modelling of multiphase flows based on [93] is given hereafter with particular

emphasis to two-phase flows in which mobile interfaces play an important role. A point often overlooked to be noticed here is the slight difference between the *multifluid* and *multiphase* concepts. While the former is linked to the notion of different fluids, the latter is affixed to the idea of *same* fluid, but with different phases. In other words, while a system of kind nitrogen-water is a multifluid one, a system vapour-water falls into a multiphase scope.

Boundary integral techniques started up from the 1950's as tools to simulate the Stokes flow and inviscid potential flows, whereby, later, multiphase flow simulations multiplied. Water waves, evolution of KH and RT instabilities, generation of bubbles and droplets due to coalescence, for example, are some cases to which these methods were applied. Even after five decades, some authors continued to use this approach, as reviewed by [94].

As integral techniques evolved, the MAC method appeared with the contribution of [95]. In the MAC method the fluid is identified by marker particles distributed all over the fluid region and the governing equations solved on a regular grid that covers both the fluid-filled part and the empty part of the domain. From the MAC method, new methods arose in the course of time. Replacing the marker particles with a marker function was the fundamental idea to create the VOF method, which began to be widely disclosed after [96]. The advection of the marker function, however, was a known problem due to the numerical diffusion resulting from working with cell-based averaging. Although the representation of the fluid interface per cell was improved, the accuracy of surface tension computation remained a problem to be tackled.

In 1992, the CSF model introduced by [97] was the ground-breaking method found to perform the calculation of surface tension, when they showed that the curvature as well as the surface tension could be computed by taking the divergence of the discrete version of the marker function. Next, [98] developed a conservative form of the CSF model. In the sequence, improvements and extensions of the VOF were developed by [99], [100], and [101], to cite only a few articles.

New approaches derived from the MAC and VOF models appeared in the decade of 1990. Unverdi and Tryggvason [102] introduced the front-tracking method in which the interface was marked by connected marker points used to advect the material properties of the interface and compute the surface tension. This method succeeded to a large set of problems. At the same epoch, other methods came into sight, namely: the LS method by [103] (see also [104] for an extended review), soon promulgated by [105]; the CIP method



by [106], and the phase-field method by [107], also explained in more details by [108] and reviewed by [109]. In the LS method, the interface is identified with the zero contour of a continuous level-set function. The material properties of the flow are reconstructed thereof through a marker function constructed from the level-set function. This approach opposes to the VOF's, in which a discontinuous marker function is advected with the flow. Differently, the CIP method seeks to describe the transition at the interface by a cubic polynomial. The phase-field method modifies the governing equations so that the region between the fluids can be described by a thermodynamically consistent way.

As seen, many methods were devised to face the numerical difficulties arising in the multiphase universe. In spite of their characteristics, the so-called “one-fluid” formulation has been being featured in modern codes because of its ability to treat the different fluids or phases as a unique domain, a reason why it is also employed in this thesis. With this in mind, it was preferred to postpone the discussion of this topic in order to introduce it, especially, on the pages devoted to the equations roster in Section 3.1.

### 2.3 Interface and surface tension

The very thin region created when two phases of matter come into contact is called interface. To be maintained, we should suppose that both the phases have different properties, which, at molecular level, work oppositely one another to retain the physical equilibrium. By considering the three states of the matter – plasma interfaces are not discussed here –, the possible types of interfaces are: gas-liquid, gas-solid, liquid-liquid, liquid-solid and solid-solid. Owing to the proposals of this thesis, we will shorten the essay to comment on fluids only. According to Adamson [110], a general prerequisite for the stable existence of an interface between two phases is that the free energy of formation of the interface be positive. Otherwise, the interface would be expanded and dispersed, thereby leading the phases to mix. In turn, any change provoked by one phase is felt by the other while they are separated by the interface. As an illustration, Figure 14 (adapted from [110]) clarifies the molecular imbalance observed near an arbitrary interface of a gas-liquid system. The color gradient in the interstice between the shaded stems is an analogy to the density jump at the interface, as it would occur for another physical quantity, whereas  $\eta$  measures the normal distance to the interface.

More complex situations occur when three or more phases give rise to multiple interfaces. This is the case of two fluids that, beyond being in contact each other, rest together

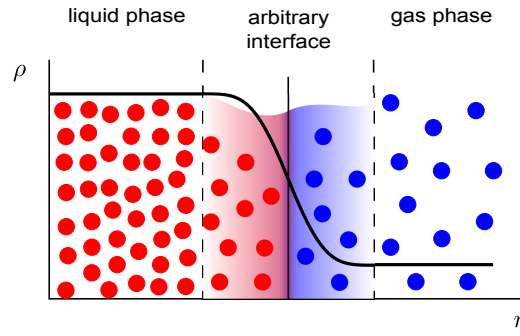


Figure 14: An outlook of the molecular imbalance in the surroundings of an arbitrary gas-liquid interface.

upon a solid wall as to create a third interface, for instance. With the development of new technologies guided by multiphase systems, such class of problems frequently correspond to big challenges in industrial, chemical and biological applications. This scenario is responsible to wage resources in studies about interface phenomena. A more accurate glimpse on interface and surface tension are given next.

We can represent the interface between two fluids through an equation that describes a surface  $\zeta$  immersed in space. In the most general case, this surface is assumed to vary with time. Hence, it can be written by a relation given by  $\zeta(\mathbf{x}, t) = 0$ . If we consider that  $\zeta$  is moving with velocity  $\mathbf{v}$ , each of its points undergoes an infinitesimal displacement  $\delta\mathbf{x} = \mathbf{v}\delta t$  after a time interval  $\delta t$  so that the new equation describing  $\zeta$  is written as

$$\zeta(\mathbf{x} + \delta\mathbf{x}, t + \delta t) = \zeta(\mathbf{x} + \mathbf{v}\delta t, t + \delta t) = 0. \quad (2.11)$$

But, with  $\mathbf{v} = (v_x, v_y, v_z)$ ,  $\delta\mathbf{x} = (v_x\delta t, v_y\delta t, v_z\delta t)$  reads for the displacement of each coordinate. By applying a Taylor expansion on two variables (space and time), we can linearly approximate any change of  $\zeta$ . Therewith, we are conducted to a material displacement

$$\zeta(x + \delta x, y + \delta y, z + \delta z, t + \delta t) = \zeta(x, y, z) + \delta x \frac{\partial \zeta}{\partial x} + \delta y \frac{\partial \zeta}{\partial y} + \delta z \frac{\partial \zeta}{\partial z} + \delta t \frac{\partial \zeta}{\partial t}, \quad (2.12)$$

or

$$\zeta(x + \delta x, y + \delta y, z + \delta z, t + \delta t) = \zeta(x, y, z) + (v_x\delta t) \frac{\partial \zeta}{\partial x} + (v_y\delta t) \frac{\partial \zeta}{\partial y} + (v_z\delta t) \frac{\partial \zeta}{\partial z} + \delta t \frac{\partial \zeta}{\partial t}, \quad (2.13)$$

which gives rise to the material derivative applied to  $\zeta$

$$\frac{D\zeta}{Dt} = \frac{\zeta(x + \delta x, y + \delta y, z + \delta z, t + \delta t) - \zeta(x, y, t)}{\delta t} = v_x \frac{\partial \zeta}{\partial x} + v_y \frac{\partial \zeta}{\partial y} + v_z \frac{\partial \zeta}{\partial z} + \frac{\partial \zeta}{\partial t}, \quad (2.14)$$

provided that  $\delta t$  is assumed small and the linearity assumption used. Hence, the well-known compact form of the operator  $\frac{D}{Dt}$  applied to  $\zeta$  is written as

$$\frac{D\zeta}{Dt} = \frac{\partial \zeta}{\partial t} + \mathbf{v} \cdot \nabla \zeta. \quad (2.15)$$

This derivation comes after [111]. *De facto*, as registered by [93], the condition

$$\frac{D\zeta}{Dt} = 0, \quad \text{at } \zeta = 0 \quad (2.16)$$

is the so-called *kinematic boundary condition*, which says that if a particle is on the interface at a particular time  $t_0$  it will be always there for all  $t > t_0$  since the interface is a material surface.

Interfaces that are sufficiently mobile to assume an equilibrium shape (e.g. meniscus, drops and thin films) stick to the matter of *capillarity*, a vein of Thermodynamics. It deals with the macroscopic and statistical behaviour of interfaces rather than with the details of the molecular structure. Notwithstanding, the concept of surface tension, although surrounded by the physical sense of attractive and repulsive forces, plays a relevant role for the former topic.

In [110], it is discussed that the surface tension can be interpreted dually. On one hand, as a free energy per unit area; on the other hand, as a force per unit length. Furthermore, the author declares that the name *surface free energy* is preferable to *surface tension* in view of a misunderstanding to which we might come across when interpreting its physical meaning. However, despite of conceptual divergences, both of the aforementioned terms are used interchangeably. Figure 15 depicts an infinitesimal element  $dA$  as well as the tangential distribution of the surface tension  $\sigma$  upon it.

In this thesis, effects of contaminants or surfactants due to gradients of surface tension – namely, Marangoni effects – are absent. In this manner,  $\sigma$  is uniform along any curve immersed in the surface. The blue dashed curves intersecting at the center of the infinitesimal element are special, since they determine the principal radii of curvatures  $R_1, R_2$  when the

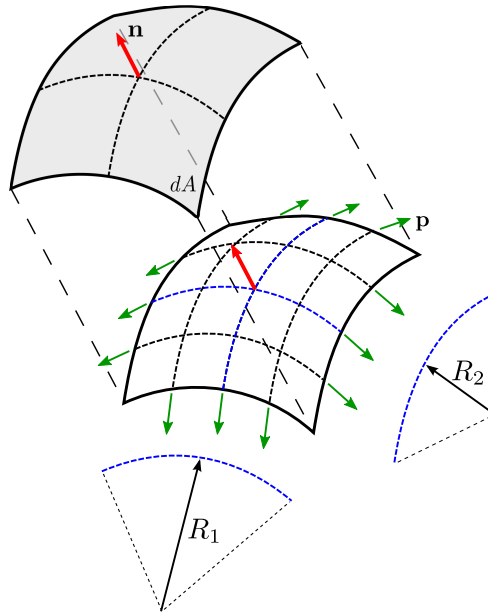


Figure 15: Uniform distribution of the surface tension over an infinitesimal area and principal radii of curvature.

interface slips away from the equilibrium after being perturbed locally. The unit vector  $\mathbf{n}$  helps to quantify curvatures and guides the determination of the capillary pressure taking place at the interface.

Despite of the physical sight about the surface tension, the mechanical point of view is equally enlightening. According to [112], it can be shown that the force on the edge of the element in Figure 15 is written as  $\mathbf{T}_A^\sigma \cdot \mathbf{p}$ , where  $\mathbf{T}_A^\sigma$  is the surface tension tensor and  $\mathbf{p}$  the vector normal to the edge of  $dA$  in a tangent plane. Additionally,  $\sigma$  is an eigenvalue of  $\mathbf{T}_A^\sigma$  so that

$$\mathbf{T}_A^\sigma \mathbf{p} = \sigma \mathbf{p} \Rightarrow \mathbf{T}^\sigma = \sigma \mathbf{I}_A. \quad (2.17)$$

To put another way, since  $\mathbf{n}$  can be obtained by the cross product between the two orthonormal tangent vectors  $\mathbf{t}_1, \mathbf{t}_2$ , it is found that

$$\mathbf{T}_A^\sigma = \sigma (\mathbf{t}_1 \otimes \mathbf{t}_1 + \mathbf{t}_2 \otimes \mathbf{t}_2). \quad (2.18)$$

The force on the element  $dA$  is the integral of the “pull” on its boundary  $\partial A$  (namely, the union of its edges), which is given by

$$\delta \mathbf{F}_\sigma = \oint_{\partial A} \mathbf{T}_A^\sigma \mathbf{p} dl = \int_A \nabla_A \cdot \mathbf{T}_A^\sigma dA, \quad (2.19)$$

whence, after taking the limit up to a point, the surface force per unit area renders

$$\mathbf{f} = \nabla \cdot \mathbf{T}_A^\sigma = \nabla_A \cdot \sigma \mathbf{I}_A = \sigma \nabla_A \cdot \mathbf{I}_A + \mathbf{I}_A \cdot \nabla_A \sigma. \quad (2.20)$$

Thenceforth, it is shown that  $\nabla_A \cdot \mathbf{I}_A = \kappa \mathbf{n}$ , implying the expression

$$\mathbf{f} = \sigma \kappa \mathbf{n} + \nabla_A \sigma, \quad (2.21)$$

in which the second term corresponds to the presence of Marangoni effects, already assumed to be absent here. Hence, it remains

$$\mathbf{f} = \sigma \kappa \mathbf{n}. \quad (2.22)$$

## 2.4 Meshing art and generalities

Mesh generation is the heartwood of the pre-processing stage of any computational code. Along the times, a plethora of software products as well as algorithms to create grids suitable to complex geometries were developed, thus glossing a scenario increasingly compared to a true craftwork. Generally, FE meshes can be created from arbitrary geometries drawn by CAD software, such as the best-known commercial packages for engineering purposes AutoCAD® and SolidWorks®. Currently, CFD tools like Ansys Fluent® and Comsol Multiphysics® - the latter having diverse FE resources - bring built-in CAD capabilities and are engaged to gather all the stages of simulation into an integrated tool. On the other hand, free software devoted to do similar operations are also available. Some tools, such as TRIANGLE [113], TETGEN [114], and GMSH [115] were invaluable for this thesis, from which the meshes were generated. Despite of that, this section aims to present some descriptive tools useful to pave the two-phase framework which all the remain material will be subjected to.

Preliminarily, as a general example, let  $\Omega \subset \mathbb{R}^m$ ,  $m = 2, 3$  be a domain and  $\Gamma$  its boundary, both of which defined as

$$\begin{aligned} \Omega &:= \Omega^1 \cup \Omega^2, \text{ where } \Omega^1 = \bigcup_{g=1}^{nb} \Omega_g^1, \text{ and} \\ \Gamma &:= \Gamma^1 \cup \Gamma^2, \text{ where } \Gamma^1 = \bigcup_{g=1}^{nb} \Gamma_g^1, \Gamma^2 = \Gamma_D \cup \Gamma_P \end{aligned}$$

respectively, where the subscripts 1,2 indicate, in this sequence, the dispersed and continuous phase of a two-fluid flow,  $\Gamma_D$  ( $\Gamma_P$ ) the Dirichlet (periodic) portion of  $\Gamma^2$ , and  $nb$  the number of elements of the dispersed phase. Also, call  $\mathbf{n}_{12}$  and  $\mathbf{n}_{2,D}$  ( $\mathbf{n}_{2,P}$ ) unit normal vectors pointing from  $\Omega^1$  to  $\Omega^2$  and outward  $\Gamma_D$  ( $\Gamma_P$ ), respectively. Depending on the flow to be analyzed,  $\Gamma^1$  may be made up by impermeable solid walls, open boundaries, or inlets, for instance, while each  $\Gamma_g^2$  may represent bodies with mobile interfaces, such as gas bubbles or liquid drops not coalescing one with another. Particularly,  $\Gamma_P$  will be ascribed suitably with Neumann conditions according to a FE sense – discussed in Chapter 5. Figure 16 sketches a typical domain as described above for a two-phase flow formulation.

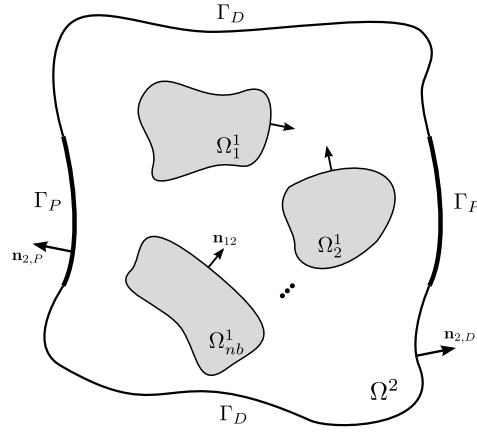


Figure 16: Generalized domain including periodic boundaries for a two-phase flow modelling.

Given a tessellation  $\mathcal{T}_h$  of  $\Omega$ , each simplex  $T \in \mathcal{T}_h$  here either is a triangle ( $m = 2$ ) or a tetrahedron ( $m = 3$ ) with vertices  $\mathbf{x}_j$ ,  $1 \leq j \leq m + 1$ , obeying the classical requirements for a finite element [116], [117]. To describe the mesh structure used to establish the two-fluid nature studied here, a simplistic mathematical description is introduced based on families of discrete parts. Thenceforth, we define

$$\mathcal{T}_{h_1}^{\Gamma^1} := \{T \in \mathcal{T}_h; T \in \text{interface}\}, \quad (2.23)$$

$$\mathcal{T}_{h_2}^{\Gamma^2} := \{T \in \mathcal{T}_h; T \in \text{convex hull}\}, \quad (2.24)$$

$$\mathcal{T}_{h_T}^{\Gamma} := \mathcal{T}_{h_1}^{\Gamma^1} \cup \mathcal{T}_{h_2}^{\Gamma^2} \quad (2.25)$$

$$\mathcal{T}_h^{\Omega^1} := \{T \in \mathcal{T}_h; \dot{T} \subset \Omega^1\}, \quad \rightsquigarrow \blacksquare \text{ (elements)}, \quad (2.26)$$

$$\mathcal{T}_h^{\Omega^2} := \{T \in \mathcal{T}_h; \dot{T} \subset \Omega^2\}, \quad \rightsquigarrow \square \text{ (elements)}, \text{ and} \quad (2.27)$$

$$\mathcal{T}_h^{\Omega} := \mathcal{T}_h^{\Omega^1} \cup \mathcal{T}_h^{\Omega^2}, \quad (2.28)$$

as mesh subsets. The symbol “ $\rightsquigarrow$ ” is used in Figure 17 for a graphical representation of element families sharing an interface in a two-dimensional mesh. Despite of these mathematical definitions, the computational mesh is stored into two data structures only, viz. the *area/volume mesh*  $\mathcal{T}_h^\Omega$ , which accounts for an interior discretization and the *line/surface mesh*  $\mathcal{T}_{h_\Gamma}^\Gamma$ , which discretizes convex hulls and interfaces. Different levels of adaptive refinement  $h$ ,  $h_1$ ,  $h_2$  can be chosen separately for volumes, interfaces and boundaries according to the flow conditions.

Since an interface is traced by edges or faces of the own mesh elements, a sharp thickness is achieved satisfactorily. Therefore, this construction evinces a kind of front-tracking method in which such an interface is identified by evaluating a nodal Heaviside function  $H(\mathbf{x})$  over the elements belonging to  $\mathcal{T}_{h_1}^\Gamma$ . As pointed out by [118], it turns out that the abrupt transition of a property  $\phi$  across the interface can be smoothed with by means of the interpolation

$$\phi(\mathbf{x}) = \phi^1 H(\mathbf{x}) + \phi^2 (1 - H(\mathbf{x})), \quad \forall \mathbf{x} \text{ of } T \in \mathcal{T}_h, \quad \phi^i = \phi|_{\Omega^i}, \quad i = 1, 2. \quad (2.29)$$

Besides, we set forth

$$H(\mathbf{x}_j) := \begin{cases} 0, & \text{if } \mathbf{x}_j \in \mathcal{T}_h^{\Omega^2} \cup \mathcal{T}_{h_2}^{\Gamma^2} \\ 0.5, & \text{if } \mathbf{x}_j \in \mathcal{T}_{h_1}^{\Gamma^1} \\ 1, & \text{if } \mathbf{x}_j \in \mathcal{T}_h^{\Omega^1}. \end{cases} \quad (2.30)$$

for the nodal evaluation. Figure 17 is an overview of elements comprising a neighbourhood of interface highlighting the effect of the interpolation given by 2.29.

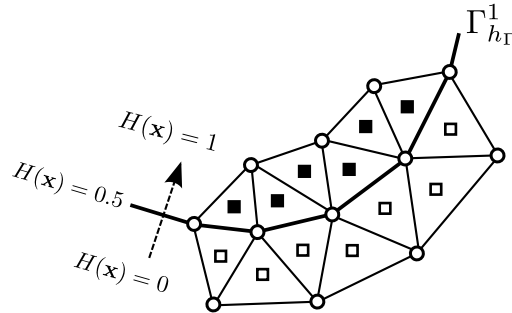
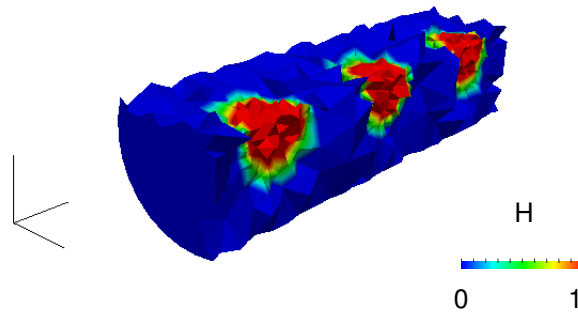


Figure 17: Mesh elements comprising the region around the discrete interface between the fluids and effect of transition caused by interpolation with the Heaviside function.

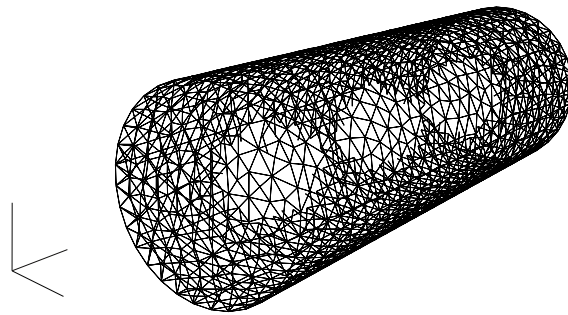
All things considered, the meshing process for the desired two-phase flow configu-

ration is now illustrated in Figure 18 in order to single out how the elements are connected in such a way to create zero-thickness interfaces. The model encompasses three spherical bodies (e.g. bubbles, or drops) dispersed into a medium that is confined inside a truncated microchannel. Such a setup is suitable to study, for instance, the dynamics of bubbles in microscale devices, the breakup and pre-atomization regimes occurring in liquid jets as well as the study of bubble interaction under PBC as will be reported later in Chapter 5. In the same figure, at the top, the quarter of the cylindrical geometry is depicted after the cut by two mutually perpendicular planes to the axis of revolution. As can be seen by the plotting of the Heaviside function  $H(\mathbf{x})$ , the whole domain as well as the interface locus are well represented by the mesh elements. At the bottom, the overview of the entire surfaces is drawn. An additional example for a model of a long capsule-shaped bubble typically encountered in two-phase slug flow regimes is depicted in Figure 19, where  $H(\mathbf{x})$  plays the role as marker function.





(a)



(b)

Figure 18: 3D mesh for an arbitrary two-phase flow configuration containing three dispersed spherical elements confined into a microchannel (a) Heaviside function marking the bulk region, interface locus and inner phase; (b) overview of the equally-spaced spherical bodies in the microchannel.

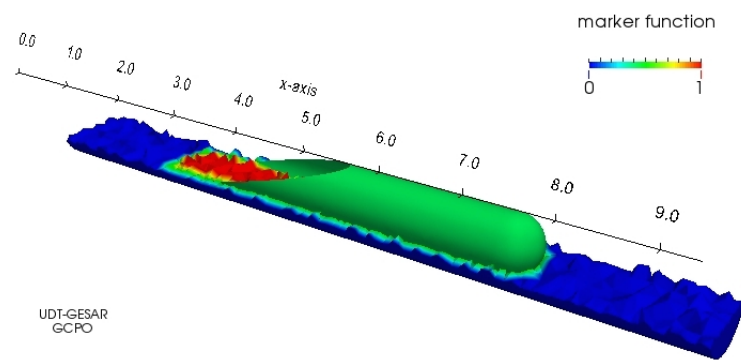


Figure 19: 3D mesh for a long capsule-shaped bubble typically encountered in two-phase slug flow configurations taken from [119].

### 3 GOVERNING EQUATIONS

#### 3.1 Principles

Conservation laws have utter relevance before any thorough study because they gather a set of fundamental hypotheses that drive the behaviour of a physical system. This section presents these main conservation laws and the equations governing the movement of fluids according to the Continuum Mechanics [120]. Integral forms are the starting point in head to a more suitable set of partial differential equations. A summarized writing, however, is preferred instead of a detailed scrutiny upon each principle.

##### 3.1.1 Mass conservation

The terminology *body* is used to specify any limited portion of space with mass  $m$ . If we call such body  $B$ ,  $\rho_t$  its density associated with the time, then,

$$m(B) = \int_B \rho_t dV. \quad (3.1)$$

Moreover, let  $\partial B$  be the boundary of  $B$ ,  $\mathbf{n}$  a unit normal vector pointing outward and  $\mathbf{v}$  the fluid velocity field. By invoking the Divergence Theorem, the equation holds

$$\int_B \nabla \cdot (\rho \mathbf{v}) dV = \int_{\partial B} \rho \mathbf{v} \cdot \mathbf{n} dA. \quad (3.2)$$

For each point  $\mathbf{x} \in B$  at a particular time  $t$ , we establish

$$\int_B \frac{\partial}{\partial t} \rho(\mathbf{x}, t) dV = \frac{d}{dt} \int_B \rho(\mathbf{x}, t) dV. \quad (3.3)$$

By combining Equations (3.2) and (3.3), we write the *Principle of Mass Conservation* for a control volume as

$$\frac{d}{dt} \int_B \rho(\mathbf{x}, t) dV = - \int_{\partial B} \rho(\mathbf{x}, t) \mathbf{v}(\mathbf{x}, t) \cdot \mathbf{n}(\mathbf{x}) dA. \quad (3.4)$$

To put in another way, Equation (3.4) declares that the mass production rate inside  $B$  is numerically equal to the net mass flux flowing out its boundary. Furthermore,

$$\frac{\partial \rho}{\partial t} + \nabla \cdot (\rho \mathbf{v}) = 0, \quad (3.5)$$

holds and it is the *Continuity Equation*. By using the vector identity  $\nabla \cdot (\rho \mathbf{v}) = \mathbf{v} \cdot \nabla \rho + \rho \nabla \cdot \mathbf{v}$ , Equation (3.5) is recast to

$$\frac{\partial \rho}{\partial t} + \mathbf{v} \cdot \nabla \rho + \rho (\nabla \cdot \mathbf{v}) = 0. \quad (3.6)$$

A simplified version of the continuity equation is obtained when one assumes that the density is constant in time, thus evoking the incompressibility hypothesis  $\frac{D\rho}{Dt} = 0$ . Consequently, Equation (3.6) is reduced to the kinematic restriction

$$\nabla \cdot \mathbf{v} = 0, \quad (3.7)$$

### 3.1.2 Linear momentum

When a body  $B$  moves over a continuum, interactions among its particles as well as between  $B$  and its surroundings can take place as distinct manifestations of forces. This system of forces acting upon  $B$  can be written, in turn, as a pair  $(\mathbf{s}, \mathbf{b})$  of functions, such that

$$\mathbf{s} : \mathcal{N} \times \mathcal{X} \longrightarrow \mathbb{R}^m \quad \mathbf{b} : \mathcal{X} \longrightarrow \mathbb{R}^m$$

$\mathbf{s}(\mathbf{n}, \mathbf{x}, t)$ , for  $\mathbf{n} \in \mathcal{N}$ ,  $\mathbf{x} \in \mathcal{X}$  at the time  $t$  are called *surface forces*, whereas  $\mathbf{b}(\mathbf{x}, t)$  are named *body forces*. By assuming that the state of stress at a point  $\mathbf{x}_\partial \in \partial B$  is given by the symmetric tensor  $\mathbf{T}_{\mathbf{x}_\partial}$ , the total surface force on  $B$  is given by

$$\int_{\partial B} \mathbf{T}_{\mathbf{x}_\partial} \cdot \mathbf{n} dA, \quad (3.8)$$

for  $\mathbf{n}$  unitary placed at  $\mathbf{x}_\partial$  and pointing outward  $B$ . Furthermore, since  $\mathbf{b}$  acts upon the interior of  $B$ , the body forces summed up correspond to

$$\int_B \mathbf{b} dV. \quad (3.9)$$

Similarly to the previous section, the net flux of momentum to be considered renders

$$\int_{\partial B} (\rho \mathbf{v} \otimes \mathbf{v}) \cdot \mathbf{n} dA. \quad (3.10)$$

Put together, these forces correspond to the balance of momentum in  $B$ , which corresponds to the equation

$$\int_B \frac{\partial}{\partial t} (\rho \mathbf{v}) dV = - \int_{\partial B} (\rho \mathbf{v} \otimes \mathbf{v}) \cdot \mathbf{n} dA + \int_{\partial B} \mathbf{T}_{\mathbf{x}_0} \cdot \mathbf{n} dA + \int_B \mathbf{b} dV. \quad (3.11)$$

Frequently,  $\mathbf{b} = \rho \mathbf{g}$ , associating to the gravitational field  $\mathbf{g}$ . Now, again through the Divergence Theorem, we obtain, by taking the gravitational field into account,

$$\int_B \frac{\partial}{\partial t} (\rho \mathbf{v}) dV = - \int_B \nabla \cdot (\rho \mathbf{v} \otimes \mathbf{v}) dV + \int_B \nabla \cdot \mathbf{T}_{\mathbf{x}_0} dV + \int_B \rho \mathbf{g} dV. \quad (3.12)$$

In virtue of treating  $B$  infinitesimally, a differential form valid all over stemming from Equation (3.12) is given by

$$\frac{\partial}{\partial t} (\rho \mathbf{v}) + \nabla \cdot (\rho \mathbf{v} \otimes \mathbf{v}) = \nabla \cdot \mathbf{T}_{\mathbf{x}_0} + \rho \mathbf{g}. \quad (3.13)$$

On the other hand, through the identities

$$\nabla \cdot (\rho \mathbf{v} \otimes \mathbf{v}) = (\rho \mathbf{v}) \nabla \mathbf{v} + \mathbf{v} \nabla \cdot (\rho \mathbf{v}) \quad (3.14)$$

and

$$\frac{\partial}{\partial t} (\rho \mathbf{v}) = \frac{\partial \rho}{\partial t} \mathbf{v} + \rho \frac{\partial \mathbf{v}}{\partial t}, \quad (3.15)$$

Equation (3.13) renders

$$\rho \left( \frac{\partial}{\partial t} + \mathbf{v} \cdot \nabla \right) \mathbf{v} + \mathbf{v} \left( \frac{\partial \rho}{\partial t} + \nabla \cdot (\rho \mathbf{v}) \right) = \nabla \cdot \mathbf{T}_{\mathbf{x}_0} + \rho \mathbf{g}. \quad (3.16)$$

Though, Equation (3.5) enforces  $\frac{\partial \rho}{\partial t} + \nabla \cdot (\rho \mathbf{v}) = 0$ , whereby

$$\rho \left( \frac{\partial \mathbf{v}}{\partial t} + \mathbf{v} \cdot \nabla \mathbf{v} \right) = \nabla \cdot \mathbf{T}_{\mathbf{x}_0} + \rho \mathbf{g} \quad (3.17)$$

is a final form for the momentum equation.

Theoretically, it is shown that, for Newtonian fluids – to which we report herein –,  $\mathbf{T}$  is assumed to be a linear function of the rate of strain, namely,

$$\mathbf{T} = (-p + \lambda \nabla \cdot \mathbf{v}) \mathbf{I} + 2\mu \mathbf{D}, \quad (3.18)$$

where the subscript  $\mathbf{x}_\partial$  was dropped out for readability. Above,  $p$  is the pressure,  $\mathbf{I}$  is the identity tensor,  $\mu$  is the viscosity, and  $\mathbf{D} = \frac{1}{2}(\nabla \mathbf{v} + \nabla \mathbf{v}^T)$  is the deformation tensor.  $\lambda$  is the coefficient of second viscosity which, by the Stokes' law, will be determined by assuming a zero bulk viscosity, *i.e.*,  $\lambda + \frac{2}{3}\mu = 0$ . Thereupon, Equation (3.17) rewritten as

$$\rho \frac{D\mathbf{v}}{Dt} = -\nabla p + \nabla \cdot [\mu(\nabla \mathbf{v} + \nabla \mathbf{v}^T)] - \nabla \left( \frac{2}{3}\mu \nabla \cdot \mathbf{v} \right) + \rho \mathbf{g} \quad (3.19)$$

results in the Navier-Stokes equation. Since we will deal with incompressible flows only, Equation (3.7) allows us to attain the simplified form

$$\rho \frac{D\mathbf{v}}{Dt} = -\nabla p + \nabla \cdot [\mu(\nabla \mathbf{v} + \nabla \mathbf{v}^T)] + \rho \mathbf{g} \quad (3.20)$$

At this point, remember that Equation (3.20) should be written considering the ALE referential according to the subject-matter of Section 2.1. In effect, by inserting the convective velocity (cf. Equation (2.10)) into Equation (3.20) and rewriting the advection term of the material derivative, we obtain the ALE form for the momentum equation

$$\rho \left( \frac{\partial \mathbf{v}}{\partial t} + \mathbf{c} \cdot \nabla \mathbf{v} \right) = \rho \left( \frac{\partial \mathbf{v}}{\partial t} + (\mathbf{v} - \hat{\mathbf{v}}) \cdot \nabla \mathbf{v} \right) = -\nabla p + \nabla \cdot [\mu(\nabla \mathbf{v} + \nabla \mathbf{v}^T)] + \rho \mathbf{g} \quad (3.21)$$

### 3.1.3 Advection-diffusion equation

Plentiful phenomena involving the concentration of species occur in nature under the form of binary mixtures or multicomponent systems. Many of them are described by advection-diffusion-reaction equations that take into account all the complex effects arising from the interaction among those substances in space and time. Let us consider  $\Psi$  the mass concentration of an arbitrary chemical species  $\phi$  which is distributed over a body  $B$ . The

principle of conservation for such chemical species over  $B$  is applied as

$$\int_B \frac{\partial \Psi}{\partial t} dV = - \int_{\partial B} \mathbf{j} \cdot \mathbf{n} dA + \int_B f(CK) dV, \quad (3.22)$$

*i.e.* the rate of concentration of the chemical species in  $B$  is equal to the net flux of concentration  $\mathbf{j}$  crossing the body's boundary added by the rate of mass production or destruction as a function of the chemical kinetics  $f(CK)$ . Here, we will consider  $f(CK)$  identically zero. Note, on the other hand, that this equation will be introduced here for future testing purposes only concerning the transport of a scalar passive. Hence, any coupling with the momentum equation is considered.

Thenceforth, by applying the Divergence Theorem to the l.h.s. of Equation (3.22), we obtain

$$\int_B \frac{\partial \Psi}{\partial t} dV = - \int_B \nabla \cdot \mathbf{j} dV, \quad (3.23)$$

whereof

$$\frac{\partial \Psi}{\partial t} = - \nabla \cdot \mathbf{j}. \quad (3.24)$$

By means of the Fick's first law of diffusion, *viz.*  $\mathbf{j} = -\rho \nabla \Psi$ , the previous equation renders

$$\frac{\partial \Psi}{\partial t} - \rho \nabla^2 \Psi, \quad (3.25)$$

for a mass diffusivity  $\rho$ . Additionally, to have a full unsteady description of the diffusive process during the transport of concentration due to a carrying fluid, the convective variation of concentration should be included in Equation (3.25), thus conducting it to

$$\frac{\partial \Psi}{\partial t} + \mathbf{v} \cdot \nabla \Psi - \rho \nabla^2 \Psi = 0, \quad (3.26)$$

or, concisely, in the sense of the material derivative,

$$\frac{D\Psi}{Dt} = \rho \nabla^2 \Psi. \quad (3.27)$$

In order to get the dimensionless form of Equation (3.27), the Péclet number

$$Pe = \frac{U_{ref} L_{ref}}{\varrho_{ref}}, \quad (3.28)$$

measuring the relation between the advective transport rate and the diffusive transport rate of  $\Psi$  is segregated into the product

$$Pe = ReSc, \quad Sc = \frac{\nu_{ref}}{\varrho_{ref}} \quad (3.29)$$

to produce

$$\frac{D^* \Psi^*}{D^* t^*} = \frac{1}{ReSc} \nabla^{*2} \Psi^*, \quad (3.30)$$

or, by removing the asterisk sign, the final form

$$\frac{D\Psi}{Dt} = \frac{1}{ReSc} \nabla^2 \Psi. \quad (3.31)$$

#### 3.1.4 The “one-fluid” formulation

The “one-fluid” formulation seeks to write the momentum equation without appealing to jump conditions at the interface. In this case, the fluids in the different phases apart are treated, in reality, as one sole fluid whose material properties vary abruptly across the interface. Forthwith, the insertion of singular terms into the formulation is required in order to account for the forces acting upon the interface. As declared in [93], this procedure brings up the feasibility of solutions that include generalized functions, such as  $\delta$ -functions or step functions.

In this thesis, the Heaviside function  $H(\mathbf{x})$  plays the role to identify the different fluid regions as well as the interface, *i.e.* the marker function. As pointed out by [118], it turns out that

$$H(\mathbf{x}) = \int_{A_I} \delta(x - x_I) \delta(y - y_I) \mathbf{n} dA_I, \quad \forall \mathbf{x} = (x, y). \quad (3.32)$$

Figure 20 is a sketch of Heaviside function’s behaviour for two-dimensional domains. More-



over, it holds that

$$\nabla H = - \int_{A_I} \delta(x - x_I) \delta(y - y_I) \mathbf{n}_I dA_I = -\delta(\eta) \mathbf{n}, \quad (3.33)$$

where  $\eta$  is the coordinate normal to the interface in a local coordinate system aligned with the interface.

By defining the function  $\delta_\zeta$ , which is concentrated on the interface  $\zeta$  in the same way as the Dirac  $\delta$ -function is concentrated on a point, the following relation holds:

$$\delta_\zeta(\mathbf{x}_I) = \delta(\eta), \quad \mathbf{x}_I \in \zeta. \quad (3.34)$$

However, the function  $\delta_\zeta(\mathbf{x}_I)$  has the property of converting volume integrals into surface integrals so that, for an arbitrary function  $f$ ,

$$\int_V \delta_\zeta(\mathbf{x}_I) f(\mathbf{x}_I) dV = \int_\zeta f(\mathbf{x}) dA_I. \quad (3.35)$$

Due to Equation (3.33), the gradient of the Heaviside function relates to the Dirac  $\delta$ -function as

$$\nabla H = -\delta_\zeta \mathbf{n} = -\delta \mathbf{n}. \quad (3.36)$$

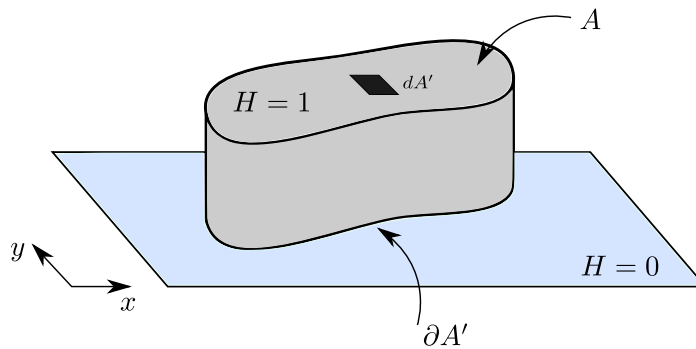


Figure 20: Representative behaviour of the Heaviside function over a two-dimensional surface. Adapted version from [93], p. 35.

Given these considerations, the surface force from Equation (2.22) is added to the

integral form through

$$\mathbf{f}_\zeta \delta_\zeta = \sigma \kappa \mathbf{n} \delta_\zeta, \quad (3.37)$$

whereby, the form

$$\mathbf{f} = \sigma \kappa \nabla H \quad (3.38)$$

gathering the effects of a sharp interface immersed in a arbitrary volume leads to

$$\rho \left( \frac{\partial \mathbf{v}}{\partial t} + (\mathbf{v} - \hat{\mathbf{v}}) \cdot \nabla \mathbf{v} \right) = -\nabla p + \nabla \cdot [\mu (\nabla \mathbf{v} + \nabla \mathbf{v}^T)] + \rho \mathbf{g} + \mathbf{f}. \quad (3.39)$$

In view of the CSF model introduced by Brackbill *et al.* [97], the additional surface force term appended to Equation (3.21) is distributed throughout the volume as a body force.

Additionally, following the standard steps to establish dimensionless quantities (cf. [121]), Equation (3.39) carried to a normalized and dimensionless domain renders

$$\rho^* \left( \frac{\partial \mathbf{v}^*}{\partial t} + (\mathbf{v}^* - \hat{\mathbf{v}}^*) \cdot \nabla^* \mathbf{v}^* \right) = -\nabla p^* + \frac{1}{Re} \nabla^* \cdot [\mu^* (\nabla^* \mathbf{v}^* + \nabla^* \mathbf{v}^{*T})] + \frac{1}{Fr^2} \rho^* \mathbf{g}^* + \frac{1}{We} \mathbf{f}^*, \quad (3.40)$$

with the dimensionless groups

$$Re = \frac{U_{ref} L_{ref}}{\nu_{ref}}, \quad Fr = \frac{U_{ref}}{\sqrt{g_{ref} L_{ref}}}, \quad We = \frac{\rho_{ref} L_{ref} U_{ref}^2}{\sigma_{ref}}. \quad (3.41)$$

The latter variables are measures of reference, whereas the asterisk sign identifies the dimensionless quantities that, without losing the generality, can, henceforth, be dropped out from the equation when referred.

Recalling that the divergence constraint in Equation (3.7) takes the dimensionless form

$$\nabla^* \cdot \mathbf{v}^* = 0, \quad (3.42)$$

after dropping out the asterisk, Equations (3.40) and (3.42) form the set of dimensionless governing equations to be solved for given initial and boundary conditions that set up a well-posed problem. In a reduced form, the set of partial differential equations which we stick

to is given by

$$\mathbf{B}_1(\mathbf{v}, p, \mathbf{f}; \hat{\mathbf{v}}, \rho, \mu, \mathbf{g}) := \rho \frac{\hat{D}\mathbf{v}}{Dt} + \nabla p - \frac{1}{Re} \nabla \cdot [\mu (\nabla \mathbf{v} + \nabla \mathbf{v}^T)] - \frac{1}{Fr^2} \rho \mathbf{g} - \frac{1}{We} \mathbf{f} = \mathbf{0} \quad (3.43a)$$

$$\mathbf{B}_2(\mathbf{v}) := \nabla \cdot \mathbf{v} = 0, \quad (3.43b)$$

$$\mathbf{B}_3(\Psi) := \frac{D\Psi}{Dt} - \frac{1}{ReSc} \nabla^2 \Psi = 0, \quad (3.43c)$$

with

$$\frac{\hat{D}\mathbf{v}}{Dt} = \left( \frac{\partial \mathbf{v}}{\partial t} + (\mathbf{v} - \hat{\mathbf{v}}) \cdot \nabla \mathbf{v} \right), \quad (3.44)$$

so as to compact posterior algorithms.

## 3.2 Applied methods

### 3.2.1 Projection method

Projection methods for incompressible flows have been applied since the late 1960's, when pioneer treatises grounded on time splitting techniques appeared [122], [123]. When these methods are applied to the Navier-Stokes equations, their gist unveils the interpretation of the equations as projections that lie on the Helmholtz-Hodge decomposition [124] (also known as Ladyzhenskaya theorem [125]), which is stated by the following theorem:

**Theorem 3.2.1 (Helmholtz-Hodge decomposition)** *A given vector field  $\mathbf{w}$  is uniquely decomposed in a bounded domain  $\Omega$  with smooth boundary  $\partial\Omega$  as*

$$\mathbf{w} = \mathbf{v} + \nabla \phi, \quad (3.45)$$

where  $\phi$  is a scalar field and  $\mathbf{v}$  a vector field such that  $\nabla \cdot \mathbf{v} = 0$  and  $\mathbf{v} \cdot \mathbf{n} = 0$ , i.e., for any vector  $\mathbf{n}$  normal to  $\partial\Omega$ ,  $\mathbf{v}$  is parallel to  $\partial\Omega$ .

Through this decomposition, velocity and pressure are uncoupled and elliptic equations are solved at each discrete time step. A organized review of projection methods given by Guermond *et al.* [126] separates them into three major classes: pressure-correction methods, velocity-correction methods, and the consistent splitting methods. In this thesis, in evocation to the third ensemble, a canonical splitting method based on exact LU factorization in two

blocks coined by Lee *et al.* [127] as of “type D” is used to tackle the coupling. Before exposing this particular choice, a few words about generalities of the projection method will be imparted next underpinned by Gresho and Sani’s description (cf. [128], Section 3.16.6).

Awhile, we will write the incompressible Navier-Stokes equations in the traditional pressure-velocity version for single-phase flows as

$$\frac{\partial \mathbf{v}}{\partial t} + \nabla p = \mathbf{d} \quad (3.46)$$

$$\mathbf{d} \equiv \nu \nabla^2 \mathbf{v} + \mathbf{g} - \mathbf{v} \cdot \nabla \mathbf{v}. \quad (3.47)$$

Then, from the incompressibility constraint, one verifies that

$$\nabla \cdot \mathbf{v} \Rightarrow \nabla^2 p = \nabla \cdot \mathbf{d}. \quad (3.48)$$

Such Poisson-like equation implies

$$p = (\nabla^2)^{-1} \nabla \cdot \mathbf{d} \quad (3.49)$$

$$\nabla p = \nabla (\nabla^2)^{-1} \nabla \cdot \mathbf{d}, \quad (3.50)$$

which, in turn, renders Equation (3.46) into

$$\frac{\partial \mathbf{v}}{\partial t} = \mathbf{d} - \nabla p \quad (3.51)$$

$$= \mathbf{d} - \nabla (\nabla^2)^{-1} \nabla \cdot \mathbf{d}, \quad (3.52)$$

$$= [\mathbf{I} - \nabla (\nabla^2)^{-1} \nabla \cdot ] \mathbf{d}, \quad (3.53)$$

$$(3.54)$$

Now, two orthogonal projection operators leaping out from the latter equation can be identified, *viz.*

$$P \equiv \mathbf{I} - \nabla (\nabla^2)^{-1} \nabla \cdot \quad (3.55)$$

$$Q \equiv \mathbf{I} - P, \quad (3.56)$$

$$(3.57)$$

so that the projection-like form of the primary Navier-Stokes equations turns into

$$\frac{\partial \mathbf{v}}{\partial t} = \mathbf{P}\mathbf{d}(\mathbf{v}) \quad (3.58)$$

$$= \mathbf{d}(\mathbf{v}) - \nabla p \quad (3.59)$$

$$= \mathbf{d}(\mathbf{v}) - \mathbf{Q}\mathbf{d}(\mathbf{v}) \quad (3.60)$$

with Equations (3.58) and (3.59) delivering the interpretation that the operator  $\mathbf{P}$  removes the gradient part of  $\mathbf{d}$  to reveal its divergence-free part - the acceleration. Insofar that one shows the validity of

$$\nabla \cdot \mathbf{P} = 0 \quad (3.61)$$

$$\nabla \times \mathbf{Q} = 0, \quad (3.62)$$

the complete argument for the projection is sustained by the orthogonal decomposition

$$\mathbf{d} = \mathbf{P}\mathbf{d} + \mathbf{Q}\mathbf{d}, \quad (3.63)$$

i.e, while  $\mathbf{P}$  projects  $\mathbf{d}$  onto the null space of divergent and  $\mathbf{P}\mathbf{d}$  is its divergence-free component,  $\mathbf{Q}$  projects  $\mathbf{d}$  onto the null space of curl and  $\mathbf{Q}\mathbf{d}$  is its curl-free component.

To summarize, the recipe to obtain the solution  $\mathbf{v}$  is stated as follows: guess  $\nabla p$ ; subtract it from  $\mathbf{f}(\mathbf{v})$ ; integrate the result for some length of time coherent to the former guess, and project the final result to the divergence-free subspace. If the guess is perfect, then the divergence-free solution is readily attained; otherwise, a spurious divergence is obtained. In other words, given an incompressible velocity field at an initial time, say  $t = 0$ , that satisfies the boundary conditions imposed, the following steps should be performed:

- i) Guess  $\nabla p(\mathbf{x}, t)$  for  $t \geq 0$ ;
- ii) Solve the momentum equations alone, with  $\nabla p(\mathbf{x}, t)$  acting as another given body force up to a "projection time"  $t = t_m$  at which an appropriate norm of  $\nabla \cdot \mathbf{v}^\#(\mathbf{x}, t_m)$  reaches some acceptable maximum value, where  $\mathbf{v}^\#(\mathbf{x}, t_m)$  is an intermediary velocity not satisfying the divergence-free constraint;
- iii) Project  $\mathbf{v}^\#(\mathbf{x}, t_m)$  onto the nearest divergence-free subspace to obtain  $\mathbf{v}(\mathbf{x}, t_m) = \mathbf{P}\mathbf{v}^\#(\mathbf{x}, t_m)$  and retain  $\mathbf{v}(\mathbf{x}, t_m)$  as the Navier-Stokes velocity, thus finishing one projection cycle.

iv) Restart from the first step.

Because of the uncertainty and fallibility of the guesses, such projection-based methods generally have a considerable degree of sophistication to retrieve the divergence-free solution for the equations. However, several of the proposed techniques not always admit a favourable computational implementation, thus falling back into numerical struggles to deal with the paramount problem of the coupling.

### 3.2.2 Semi-Lagrangian method

The Semi-Lagrangian method gained renown with applications turned to meteorological predictions and climatic phenomena, as seen in [129] and [130]. Having an intrinsic property of allowing numerical simulations managed by long time steps, its benefits to public safety, environment, and economy can be readily recognized. Accurate climatic predictions, for instance, may support urgent decision makings in prospective scenarios of natural disasters, thus helping to mitigate eventual damages, restrain severe losses, and secure an entire population. Historical background and a general review about the method's development in the ambit of the Meteorology is found in [131] and [132].

Aside from its original field, the use of the SL method in other scientific areas had already been advocated [133], so that different names were coined to express it, such as *Method of Characteristics* and *Method Eulerian-Lagrangian* [134]. Concerning its infusion into the finite element's ground, pristine contributions blossomed from [135], at which a numerical algorithm to solve the advection-diffusion equation was intended.

The basis of the SL method focuses on a *backward-in-time* integration whereby the fluid particle trajectories are tracked with the time and can be explained by opting for an advection problem defined on the set  $\Omega \times \tau$ , with  $\tau = \bigcup_{n=0}^{L-1} [nt, (n+1)t]$  being the union of time intervals. If  $\mathbf{x} \in \Omega$  is a spatial position through which the particle  $\chi$  travels and  $\{\mathbf{X}(\tau)\}_{nt \leq \tau \leq (n+1)t}$  is the solution of the differential equation

$$\frac{d\mathbf{X}(\tau)}{d\tau} = \mathbf{v}[\mathbf{X}(\tau), \tau], \quad (3.64)$$

then  $\mathbf{X}(\tau)$  is the trajectory traced by the particle  $\chi$  within the time range  $[nt, (n+1)t]$  -

elsewhere  $t^n, t^{n+1}$  - and also a characteristic of the compact equation

$$\frac{\partial \Phi}{\partial \tau} + \mathbf{v} \cdot \nabla \Phi = \mathbf{F}, \quad (3.65)$$

for  $\Phi = (\Phi_1, \Phi_2, \dots, \Phi_N)$ , the vector of  $N$  fluid variables, and  $\mathbf{F} = (F_1(\Phi), F_2(\Phi), \dots, F_N(\Phi))$ , the vector of  $N$  source terms.

With  $\mathbf{x}$  and  $t$  being parameters for the trajectory, we write  $\mathbf{X}(\tau) = \mathbf{X}(\mathbf{x}, t; \tau)$ . By defining  $\mathbf{x}_\# = \mathbf{X}(\mathbf{x}, nt; \tau)$  as the position occupied by the particle at the instant  $\tau = nt$  and  $\mathbf{x}_a = \mathbf{X}(\mathbf{x}, (n+1)t; \tau)$  as the position occupied by the particle at the instant  $\tau = (n+1)t$ , the goal of the SL method is achieved when the point  $\mathbf{x}_d$ , an approximation to the true departure point  $\mathbf{x}_\#$ , is found after integrating Equation (3.65) backward-in-time. Precisely, the determination of  $\mathbf{x}_d$  obeys a relation such that

$$(\mathbf{x}_d, nt; \tau) \approx (\mathbf{x}_\#, nt; \tau) = (\mathbf{x}_a, (n+1)t; \tau) - \int_{nt}^{(n+1)t} \mathbf{v}(\mathbf{X}(\mathbf{x}, \tau)) d\tau, \quad (3.66)$$

*i.e.*, the observed particle reposes exactly on the site  $\mathbf{x}_a$  at the time  $\tau = (n+1)t$ . Furthermore, it holds (e.g., see Eq. 4 of [133])

$$\Phi(\mathbf{x}_a, (n+1)t; \tau) = \Phi(\mathbf{x}_d, nt; \tau) + \int_{\mathbf{X}} (d\mathbf{x} - \mathbf{v}d\tau) \cdot \nabla \Phi + \int_{\mathbf{X}} \mathbf{F} d\tau. \quad (3.67)$$

Over the years, the numerical development of the SL method spreaded variably. The first approximations for the trajectories, however, were based on simple straight lines. Thereafter, high-order time-splitting schemes arose [136] [137]. In this thesis, the material derivative in the form of Equation (3.65) is approximated by

$$\frac{D\Phi}{D\tau} = \frac{\partial \Phi}{\partial \tau} + \mathbf{v} \cdot \nabla \Phi \approx \frac{\Phi(\mathbf{x}_a, (n+1)t; \tau) - \Phi(\mathbf{x}_d, nt; \tau)}{\Delta t}, \quad (3.68)$$

where  $\Delta t$  is the time step. In such format, the gradient  $\nabla \Phi$  is suppressed on the computations, meaning that the temporal rate of change plus the convective rate of change occur instantaneously in a combined effect. In turn,  $\mathbf{x}_d$  is obtained through

$$(\mathbf{x}_d; \tau) = (\mathbf{x}_a; \tau) - \alpha.$$

Here,  $\alpha$  depends on a known velocity at a previous time step which is computed through the

linear approximation

$$\boldsymbol{\alpha} = \Delta\tau \mathbf{c}(\mathbf{x}_a, nt; \tau) = \Delta\tau (\mathbf{v} - \hat{\mathbf{v}})(\mathbf{x}_a, nt; \tau). \quad (3.69)$$

Generally, such approximations result in departure points that do not match any mesh point. Therefore,  $\Phi(\mathbf{x}_a, nt; \tau)$  must be calculated by means of some interpolation. For these reasons, trajectory integration and interpolation are the constitutive elements of any SL scheme [134]. With the increasing development of high-order methods, theoretical error analyses as well as optimization factor reports related to SL methods were published, of which a known expression for the order of the advection average error of the method was derived, namely,

$$\mathcal{O}\left(\Delta t^r + \frac{\Delta \mathbf{x}^{p+1}}{\Delta t}\right),$$

where  $r$  and  $p$  here stand for the order of trajectory integration and of interpolation, respectively [138].

Although this study is based on an ALE context, the SL methodology might seem abstruse due to its peculiarities. On the one hand, the location of the departure point through the backward calculation Equation (3.69) uses the relative velocity  $\mathbf{c}$  for the advective regression so as to gather both the Lagrangian and Eulerian effects as desired. On the other hand, the velocity interpolated near the foot of the trajectory carries a purely Lagrangian contribution that feeds back the iterative process of the computational code within each time step only. In other words, one observes the existence of an abstract mesh which distorts at each discrete time interval. Figure 21, adapted from [139] enlightens these events inside a spatio-temporal context over a two-dimensional triangular mesh that disregards, for clarity, the mesh movement caused by interference of the ALE dynamics.  $(\mathcal{T}_{\mathbf{X}}^h, (n+1)t)$  and  $(\mathcal{T}_{\mathbf{X}}^h, nt)$  represent two “slices” of the same triangulation at the two time instants analyzed.

The Eulerian mesh is drawn in thick borders, which keeps fixed along the time. The Lagrangian mesh, on the other hand, is formed when the isolated points that spread over the Eulerian mesh are joint by abstract edges, as seen through the gray-filled portion drawn on the same plane where the Eulerian mesh lies on. Additionally, the long-dashed lines starting from the points over the Lagrangian mesh at the instant  $\tau = nt$  and arriving at the points of the Eulerian mesh at the time  $\tau = (n+1)t$  represent the particle trajectories. Among them, the trajectory  $\mathbf{X}(\tau)$ , leaving  $\mathbf{x}_\#$  and arriving at  $\mathbf{x}_a$  is highlighted. The isolated



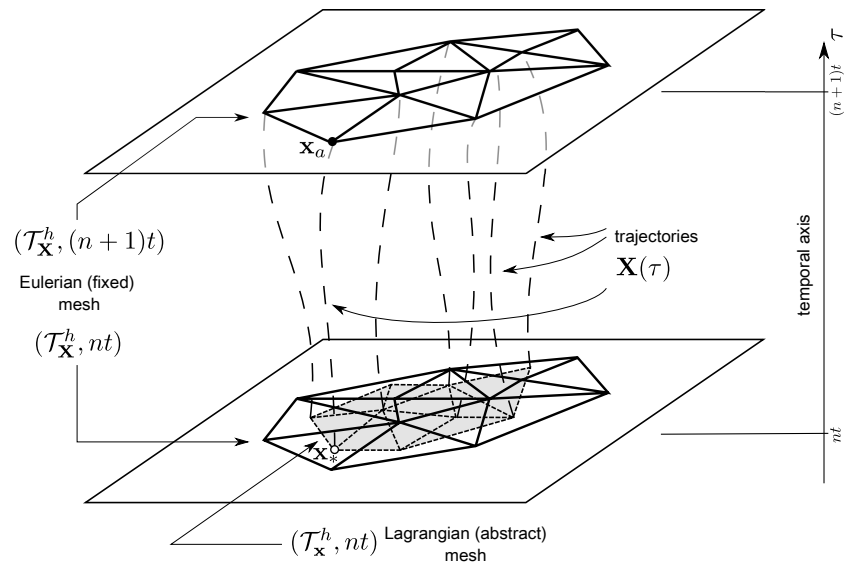


Figure 21: SL method in a spatio-temporal context over a two-dimensional triangular finite element mesh displaying the Lagrangian “abstract” mesh.

points before mentioned are, therefore, the departure points (or “feets”, alternatively) of the characteristic curves already mentioned. This explanation, in turn, just reinforces the concept of an Eulerian-Lagrangian approach, which combines both descriptions.

## 4 FINITE ELEMENT PROCEDURES IN TWO-PHASE FLOWS

The purpose of this chapter is to discourse about theoretical and computational aspects of the FEM with special attention to the gas-liquid two-phase flow dynamics and to concepts related to this thesis. A few considerations on the historical background of the method, however, give occasion to divert out from the Fluid Dynamics momentarily for a better clarification. This is, in turn, the object of the opening section, which has by progression a series of theoretical topics studied in developing the FEM. The part of the text corresponding to more applied contents comes soon after in the sequel.

### 4.1 Historiography and theory of the classical FEM

From the birth of the FEM as a numerical method to solve partial differential equations, the Engineering follows its remarkable uprise until the present time by recognizing it as a robust tool capable to branch in many different facets. In reality, the term FEM was coined by Prof. Ray W. Clough in the 1960's after a premature version before known as *Direct Stiffness Method*, although there exist arguments favourable to the FEM's creation dating back the Leibniz's ages between the XVII and XVIII centuries, when the variational methods were being developed. From these early times, the tied union with the Mathematics elevated the scientific community to sovereign levels of rigour and formalism while clothing the FEM in a solid armour. On the other hand, this process caused a bifurcation in the sense of how to interpret the FEM, dissociating the mathematical current from the physical one. While the former was used to see the FEM under a structural/mechanical basis, the latter accustomed the eyes to see the FEM as a functional/variational problem, both of which getting the same results. The analogy of dividing a domain in smaller pieces called "elements", for instance, is not as complete as the mathematical definition, which requires further attention.

In 1943, Courant presented the so-called *Courant element*, which is the fundamental element formed by a triangle equipped with linear piecewise functions. Afterwards, many others arose as byproducts of compositions, such as the family of *Hermite elements*, *Argyris elements* and *Crouzeix-Raviart elements*, all of them derived from a triangular geometry, but differing by the set of degrees of freedom. In this case, they consider nodal evaluations of either only functions, or functions and directional derivatives, or still functions and higher order derivatives. Figure 22, adapted from [140], illustrates a couple of elements. The arrows

in the Argyris element symbolize the normal derivative evaluated at the midpoints of the edges. Similar ideas extend to other dimensions and geometries, producing new elements.

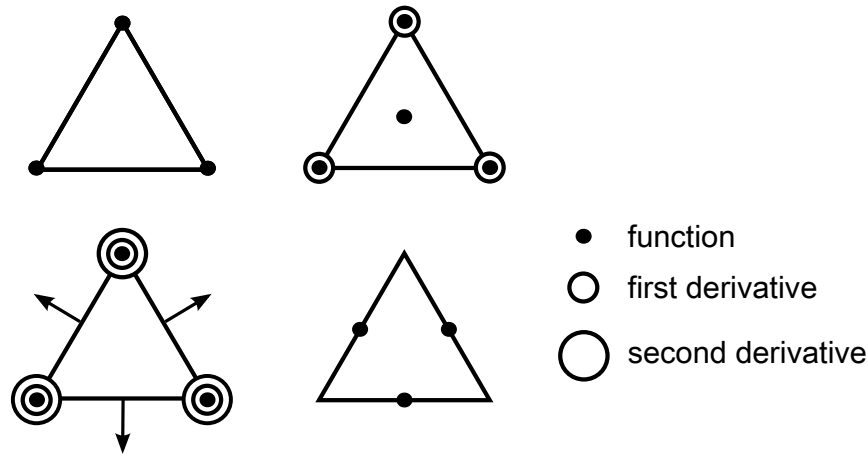


Figure 22: Different two-dimensional compositions: the Courant element, the Hermite element, the quintic Argyris triangle and the nonconforming linear Crouzeix-Raviart triangle (arranged from left to right/top to bottom).

Although the mathematics of FEM flowed independently also with considerable advancements in a functional scope concerning minimization problems and variational forms as previously authored by Ritz and Galerkin in 1910's decade, problems of the structural mechanics boosted the FE research after the period of the II World War, whose interests turned to aircraft engineering, and later, with contributions of renowned corporations, such as IBM, NASA and Boeing. This time was essential to promote the known literature written by Zienkiewicz [141] as well as the ascension of the sovietic influence worldwide with Friedrichs, Petrov and Galerkin's legacy.

In the 1970's, several mathematical books about FEM appeared, including the Strang & Fix's classical book [142]. From this moment on, the most classical FEM acquired variants, such as: the *Generalized FEM (GFEM)* [143], [128], which uses not only polynomial spaces as base functions; the *hp-FEM*, which combines adaptive refinement  $h$  with polynomial orders  $p$  [143]; and the *Extended FEM (XFEM)*, which embeds discontinuous functions to enrich spaces of GFEM [144]. In addition to such a variants, the formulations currently known as *SUPG (Streamline-Upwind Petrov-Galerkin)* [145], *GLS (Galerkin-Least Squares)* [146] and *PSPG (Pressure-Stabilized Petrov-Galerkin)* play a fundamental role in the development of stabilized methods in FE history for both compressible and incompressible dynamics. The so-called *PFEM (Particle-Finite Element Method)* [147] and *NEFEM (NURBS-enhanced finite element method)* [148] also correspond to different branches in the series of FE methods

hitherto.

More recently, emphasis has been given to fluid-structure interaction (FSI) computations, for which several FE-related methods were devised. They include multiscale space-time techniques [149], [150], isogeometric analysis and NURBS (Non-Uniform Rational B-Splines) [151] and ALE methods [152], [153], such as one discusses in this thesis, which also is widely known in FSI problems. For an overview of stabilized methods, see [154]; for future trends and current challenges in FSI modelling, see [155].

A vast list of ancient and modern literature of FEM could not be described here. For brevity, however, the following authors are enough erudite recommendations to know about the multivalency of the FEM, namely, Ciarlet [116], Zienkiewicz & Taylor [156], Reddy [157], Hugues [158], Johnson [159], Wait & Mitchell [160], Girault & Raviart [161], Ern & Guermond [117], [162], among others. This modest bibliography brings up the FEM both theoretically, numerically and computationally. Historical notes about the FEM as summarized here can be found in [163].

Basically, the FEM is directly linked to the search for a function  $u$  that minimizes a given expression of energy. Assuming that the problem to be solved admits a variational formulation which, for an arbitrary differential operator  $L$  and a given function  $f$ , holds an expression like

$$Lu = f, \tag{4.1}$$

for certain initial and boundary conditions, the method can be summarized in the following steps:

- i) Find the variational form of the problem;
- ii) Construct a basis of piecewise polynomial trial functions;
- iii) Assemble and solve the matrix discrete system;
- iv) Estimate the accuracy of the approximation.

To determine the variational or weak form of a finite element problem according to the classical approach, weight functions are used as well as Ritz-Galerkin approximations. Thus, by adjourning details until posterior sections, the weak form of Equation (4.1) reveals in

the form

$$(\mathbf{L}u, w) = (f, w), \quad (4.2)$$

for a given weight function  $w$  and operations of inner products  $(\cdot, \cdot)$  well defined. Thenceforth, function spaces are created to set forth approximations  $u \approx u_h$ ,  $f \approx f_h$ , so that Equation (4.2) is written as

$$(\mathbf{L}u_h, w_h) = (f_h, w_h). \quad (4.3)$$

Such discretized bilinear forms, in turn, are conducted to a  $n$ -dimensional matrix equation in the form

$$\mathbf{L}\mathbf{u}_h = \mathbf{b}, \quad (4.4)$$

of which  $\mathbf{u}_h = \mathbf{L}^{-1}\mathbf{b} \in \mathbb{R}^m$  is the solution. Since  $\mathbf{u}$  would be, indeed, the vector storing the exact values of the solution evaluated pointwise on the discrete domain, the accuracy of the final result must be estimated through an error expression as

$$\mathbf{e} = \|\mathbf{u} - \mathbf{u}_h\|, \quad (4.5)$$

where  $\mathbf{e}$  can have different norm-based definitions.

## 4.2 FEM for incompressible two-phase flows

The list of procedures discussed so far presented the fundamental FEM techniques usually handled in Engineering as a whole. It matters now focusing on the FEM contribution to the field of incompressible two-phase flows, in preparation to the contents to be discussed in the rest of this chapter. Meanwhile, it is instructive to recall the classical definition of a finite element (e.g., see [117], p. 19, or [116], p. 78).

**Definition 4.2.1 (Finite element)** *Let*

*i)  $T \subseteq \mathbb{R}^m$  be a compact, connected, Lipschitz subset with nonempty interior (the element domain);*

*ii)  $\mathcal{P}$  be a vector space of functions  $\varphi : T \rightarrow \mathbb{R}^m$  for some positive integer  $m$  (typically*

$m \leq 3$ ) (the shape functions);

iii)  $\mathcal{Y} = \{\zeta_1, \zeta_2, \dots, \zeta_l\}$  is a basis for  $\mathcal{P}'$ , the dual set of  $\mathcal{P}$  (the nodal variables).

Then,  $(T, \mathcal{P}, \mathcal{Y})$  is called a **finite element**.

Despite of Definition 4.2.1, in Engineering it is common practice to use  $T$  only as the finite element itself.

#### 4.2.1 Explicit representation of interfaces

In Section 2.4, some definitions were established to organize the construction of a two-phase discretized domain with independent mesh subsets, *i.e.* the *surface mesh* and the *volume mesh*. Although this separation is well clarified, the following lines will be dedicated to the discrete representation of the interface, by considering the ALE methodology quoted throughout the text.

Following similar ideas exposed by [164], we seek to characterize the interface by a explicit representation. For this purpose, Figure 23 and Figure 24 will serve as a guide. If  $\mathbf{n}$  is a normal unit vector placed at the interface pointing toward the liquid phase, we consider that the arbitrary motion of a curve is oriented as this vector, having a positive displacement if the local interface velocity points toward the same direction as  $\mathbf{n}$  and negative otherwise.

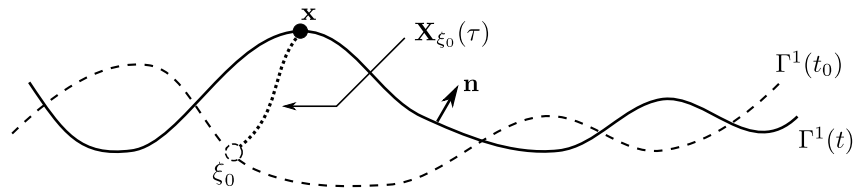


Figure 23: Two-time representation of a continuous interface  $\Gamma^1$ . Dashed: time  $t_0$ ; thick: time  $t$ ; dotted: trajectory.

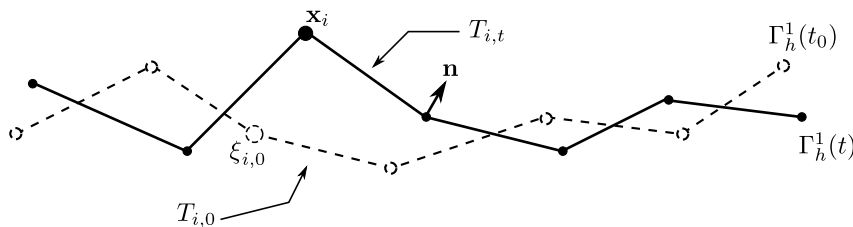


Figure 24: Two-time representation of a piecewise linear interface  $\Gamma_h^1$ . Dashed: time  $t_0$ ; thick: time  $t$ ; dotted: trajectory.

Then, let  $\Gamma^1(t_0), \Gamma_h^1(t_0)$  and  $\Gamma^1(t), \Gamma_h^1(t)$  be the continuous and discrete interfaces at two time instants  $t_0, t, t > t_0$ . As already defined in Section 2.4,  $\Gamma_{h_1}^1$  is a tessellation of the interface

which, in this simpler example, is made up by linear elements. That said, the *interface tracking* methodology relies on the validity of the relation

$$\Gamma(t) \ni \mathbf{x} = \xi_0 + \int_{t_0}^t \hat{\mathbf{v}}(\mathbf{X}_{\xi_0}(\tau), \tau) d\tau, \quad \xi_0 \in \Gamma(t_0), \quad t \geq t_0, \quad (4.6)$$

where  $\mathbf{x}$  is the position at  $t$  reached by a particle that travels with the time  $\tau$  following the trajectory  $\mathbf{X}_{\xi_0}(\tau)$  after the interface is advected with velocity  $\hat{\mathbf{v}}$ . When contrasting the continuous and discrete versions of the illustrations,  $\xi_0$  ( $\xi_{i,0}$ ) means a point of the continuous (discrete) interface at the time  $t_0$ , while  $\mathbf{x}$  ( $\mathbf{x}_i$ ) so is at the time  $t$ . Equation (4.6), hence, exhibits a Lagrangian point of view widely used in numerical methods based on interface tracking. Thus, in fact, due to the mesh movement, it turns out that

$$\Gamma_{h_1}^1(\tau) := \{T(\tau) \in \mathcal{T}_h(\tau); H(\mathbf{x}_i) = 0.5\}, \quad i = 1, 2, \dots, \iota, \quad \tau \in [t_0, t] \quad (4.7)$$

for  $\iota$  mesh nodes. Moreover, this condition is respected everywhere for an interface due to the mesh construction, thus ensuring the perdurable status of thin thickness. In Figure 24, for example, is highlighted the movement of the element  $T_i$ , which has  $\mathbf{x}_i$  as one of its nodes.

#### 4.2.2 Adaptive refinement: determination of thresholds

Given the need of better accuracy in the neighborhood of interfaces as well as in their own representation, some techniques of adaptive refinement are applied here and depicted in Figure 25. The left drawing considers thresholds from which the transition of characteristic size of the elements belonging to  $\mathcal{T}_h^\Omega$  takes place. They are determined by fixing an user-defined distance  $\epsilon$  that establishes the neighborhood  $N_\epsilon[\Gamma_h]$ , which encircles a certain topological region of space (e.g. a strip in 2D; a tube, or sphere, in 3D). On the other hand, the right drawing uses the extrema points of a wambled interface to establish thresholds further above of the maximum absolute or further below of the minimum absolute. In a generalized way, we can write

$$\bar{h}_T = \begin{cases} h_m, & \text{if } T \in N_\epsilon[\Gamma_h] \\ h_M, & \text{if } T \notin N_\epsilon[\Gamma_h] \end{cases},$$

where  $\bar{h}$  is a mean element size. That is to say,  $h_m < h_M$ .

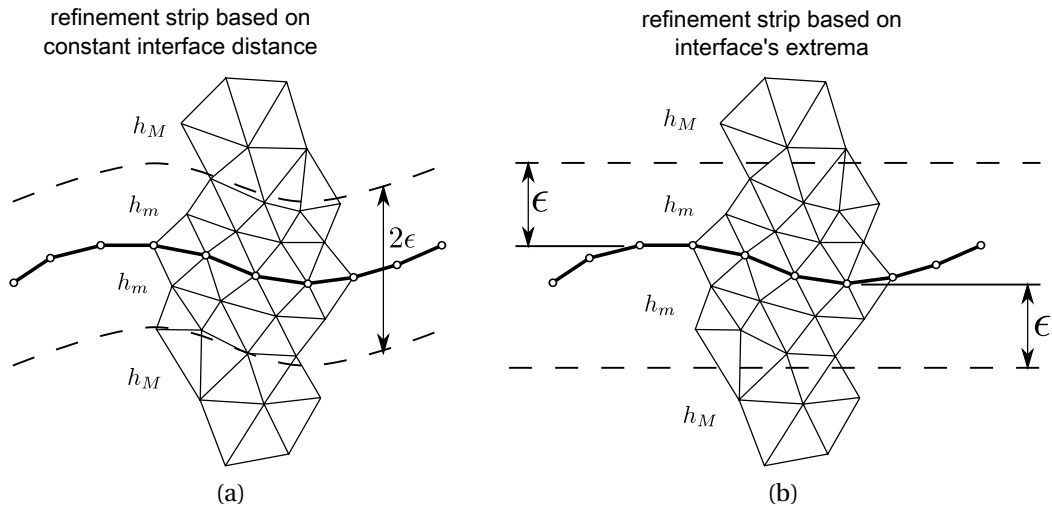


Figure 25: Adaptive refinement strategies applied at interfaces and neighborhoods: (a) criterion based on constant distance; (b) criterion based on distance from the extrema points.

In addition to thresholds, transfinite meshing can be applied for the interfaces through a denser distribution of nodes as depicted in the drawing at right. However, differently than the previous strategy, which can be recalled during the simulation and parametrized over again, this method is used in the pre-processing stage simultaneously with the mesh construction. Together with the first technique, such an approach provides a wide range of adaptive refinement for the control parameter  $h$  relative to the interface mesh.

### 4.3 Variational formulation of the governing equations

#### 4.3.1 Primitive variables

Pioneer researches introducing a variational (or weak) form of the incompressible Navier-Stokes arose some decades ago for the single-phase universe [165]. On the other hand, extensions to two-phase flows based on FE are more juvenile not only by the epoch, but also because of variants arising from the different ways wherewith methods deal with interfaces and curvatures (see, e.g., [166], [167], [121], [153]). The approach used here follows the same derivation for the single-phase dynamics exposed in [168] plus the two-phase increments introduced in [169]. Therefore, most of the algebraic details will be omitted.

A recipe to obtain the weak formulation sought is given in [170] as regards as the *Integrated Method*, which, sealed with the approach of weighted residual, is summarized as follows: to multiply the governing equations by arbitrary test functions; to integrate them



over the domain; to apply partial integration, if necessary, and finally to impose the boundary conditions. Above all, let us define some necessary functional settings on  $\Omega = \Omega^1 \cup \Omega^2$ .

The Sobolev space  $\mathcal{H}^1$  in  $\Omega$  is the set

$$\mathcal{H}^1(\Omega) := \left\{ \mathbf{u} \in \mathcal{L}^2(\Omega); \frac{\partial \mathbf{u}}{\partial x_i} \in \mathcal{L}^2(\Omega), i = 1, 2, \dots, m \right\}.$$

For reasons of application, a simpler writing was preferred instead of the multi-index notation. Above,  $\mathcal{L}^2(\Omega)$  is the set of the square-integrable functions in the sense of Lebesgue [171], defined by

$$\mathcal{L}^2(\Omega) := \left\{ \mathbf{u} : \Omega \rightarrow \mathbb{R}^m; \left( \int_{\Omega} \|\mathbf{u}\|^2 d\Omega \right)^{1/2} < \infty \right\}.$$

The determination of approximation functions over the finite element is sensitive to the construction of a functional basis that can generate a finite dimensional space from an infinite dimensional space called the *trial functions* space. Once the incompressible Navier-Stokes equations have a mixed nature in the sense of coupling velocity and pressure, spaces of trial functions should be chosen conveniently. Then, we include the Sobolev spaces given by

$$\mathcal{S} := \left\{ \mathbf{u} \in \mathcal{H}^1(\Omega); \mathbf{u} = \mathbf{u}_D \text{ in } \Gamma_{D,\mathbf{u}} \subseteq \Gamma_D \right\}.$$

$$\mathcal{Q} := \left\{ q \in \mathcal{L}^2(\Omega); q = q_D \text{ in } \Gamma_{D,q} \subseteq \Gamma_D \right\}.$$

Additionally, the *weight functions* space is defined as:

$$\mathcal{V} := \left\{ \mathbf{w} \in [\mathcal{H}^1(\Omega)]^m; \mathbf{w} = \mathbf{0} \text{ in } \Gamma_D \right\},$$

where  $[\mathcal{H}^1(\Omega)]^m = \mathcal{H}^1(\Omega) \times \dots \times \mathcal{H}^1(\Omega)$  is the  $m$ -times Cartesian product of  $\mathcal{H}^1$ ,  $\mathbf{u}_D$  is the value of the Dirichlet condition over the boundary  $\Gamma_D$ .

From  $\mathcal{S}$ ,  $\mathcal{Q}$ ,  $\mathcal{V}$ , the spaces  $\mathcal{S}^h \subset \mathcal{S}$ ,  $\mathcal{Q}^h \subset \mathcal{Q}$  and  $\mathcal{V}^h \subset \mathcal{V}$  are extracted, both having finite dimension in the sense of a  $h$ -refinement related to the level of mesh discretization [117]. Thus,

$$\mathcal{S}^h := \{ \mathbf{u}^h \in \mathcal{H}^1(\Omega); \mathbf{u}^h = \mathbf{u}_D \text{ in } \Gamma_{D,\mathbf{u}} \subseteq \Gamma_D \},$$

$$\mathcal{Q}^h := \{q^h \in \mathcal{L}^2(\Omega); q^h = q_D \text{ in } \Gamma_{D,q} \subseteq \Gamma_D\}$$

and

$$\mathcal{V}^h := \{\mathbf{w}^h = (w_1^h, w_2^h, \dots, w_m^h) \in [\mathcal{H}^1(\Omega)]^m(\Omega); \mathbf{w}^h = \mathbf{0} \text{ in } \Gamma_D\},$$

Being  $\Gamma$  Lipschitz, a general way of decomposing it reads as

$$\Gamma = \Gamma_D \cup \Gamma_N.$$

$\Gamma_D$  is the *Dirichlet* boundary, or of *essential conditions*, whereas  $\Gamma_N$  is the *Neumann* boundary, or of *natural conditions*, i.e  $\mathbf{u}$  can assume values such that

$$\begin{aligned} \mathbf{u}|_{\Gamma_D} &= \mathbf{u}_D \\ \mathbf{u}|_{\Gamma_N} &:= \mathbf{n} \cdot \nabla \mathbf{u} = \mathbf{u}_N, \end{aligned}$$

where  $\mathbf{n}$  is a unit vector normal to  $\Gamma_N$ . It may be shown that the second condition is satisfied by the own weak formulation, whereby the metonym *natural* is suggested.

Now, by weighting the strong form given by Equations (3.43a) and (3.43b), we get

$$\int_{\Omega} \mathbf{B}_1(\mathbf{v}, p, \mathbf{f}; \hat{\mathbf{v}}, \rho, \mu, \mathbf{g}) \cdot \mathbf{w} d\Omega = \mathbf{0}, \quad \mathbf{w} \in \mathcal{V} \quad (4.8a)$$

$$\int_{\Omega} \mathbf{B}_2(\mathbf{v}) q d\Omega = 0, \quad q \in \mathcal{Q}, \quad (4.8b)$$

which are expanded in the sum of integrals

$$\begin{aligned} & \int_{\Omega} \rho \left( \frac{\partial \mathbf{v}}{\partial t} + (\mathbf{v} - \hat{\mathbf{v}}) \cdot \nabla \mathbf{v} \right) \cdot \mathbf{w} d\Omega + \int_{\Omega} \nabla p \cdot \mathbf{w} d\Omega \\ & - \frac{1}{Re} \int_{\Omega} \nabla \cdot [\mu (\nabla \mathbf{v} + \nabla \mathbf{v}^T)] \cdot \mathbf{w} d\Omega - \frac{1}{Fr^2} \int_{\Omega} \rho \mathbf{g} \cdot \mathbf{w} d\Omega - \frac{1}{We} \int_{\Omega} \mathbf{f} \cdot \mathbf{w} d\Omega, = \mathbf{0} \end{aligned} \quad (4.9a)$$

$$\int_{\Omega} (\nabla \cdot \mathbf{v}) q d\Omega = 0. \quad (4.9b)$$

In turn, the parcels above can be written as bilinear forms defined by means of inner products

as

$$m_\rho \left( \rho; \frac{\hat{D}\mathbf{v}}{Dt}, \mathbf{w} \right) := \int_\Omega \rho \frac{\hat{D}\mathbf{v}}{Dt} \cdot \mathbf{w} d\Omega, \quad (4.10a)$$

$$g(p, \nabla \cdot \mathbf{w}) := \int_\Omega p \nabla \cdot \mathbf{w} d\Omega, \quad (4.10b)$$

$$k(\mu; \nabla \mathbf{v}, \nabla \mathbf{w}) := \int_\Omega \mu (\nabla \mathbf{v} + \nabla \mathbf{v}^T) : \nabla \mathbf{w}^T d\Omega, \quad (4.10c)$$

$$m_\rho(\rho; \mathbf{g}, \mathbf{w}) := \int_\Omega \rho \mathbf{g} \cdot \mathbf{w} d\Omega, \quad (4.10d)$$

$$m(\mathbf{f}, \mathbf{w}) := \int_\Omega \mathbf{f} \cdot \mathbf{w} d\Omega, \quad (4.10e)$$

$$d(\nabla \cdot \mathbf{v}, q) := \int_\Omega (\nabla \cdot \mathbf{v}) q d\Omega. \quad (4.10f)$$

At this point, some comments should be weaved: firstly, the term  $m_\rho \left( \rho; \frac{\hat{D}\mathbf{u}}{Dt}, \mathbf{v} \right)$  relative to the advection is kept in a concentrated form for posterior use of a Semi-Lagrangian approximation for the material derivative; secondly, integrations by parts are implicitly embedded in these forms; lastly, the integrals related to Neumann boundaries vanish due to the natural condition.

Therewith, the weak form of Equations (3.43a) and (3.43b) turns into finding the solution of the system

$$m_\rho \left( \rho; \frac{\hat{D}\mathbf{v}}{Dt}, \mathbf{w} \right) + g(p; \nabla \cdot \mathbf{w}) - \frac{1}{Re} k(\mu; \nabla \mathbf{v}, \nabla \mathbf{w}) - m_\rho(\rho; \mathbf{g}, \mathbf{w}) - \frac{1}{We} m(\mathbf{f}, \mathbf{w}) = \mathbf{0} \quad (4.11a)$$

$$d(\nabla \cdot \mathbf{v}, q) = 0. \quad (4.11b)$$

Nonetheless, the discrete version of Equations (4.11a) and (4.11b) needs to be invoked as

$$m_\rho \left( \rho; \frac{\hat{D}\mathbf{v}_h}{Dt}, \mathbf{w}_h \right) + g(p_h; \nabla \cdot \mathbf{w}_h) - \frac{1}{Re} k(\mu; \nabla \mathbf{v}_h, \nabla \mathbf{w}_h) - m_\rho(\rho; \mathbf{g}_h, \mathbf{w}_h) - \frac{1}{We} m(\mathbf{f}_h, \mathbf{w}_h) = \mathbf{0} \quad (4.12a)$$

$$d(\nabla \cdot \mathbf{v}_h, q_h) = 0. \quad (4.12b)$$

From [160], it is argued that the Galerkin method is the most useful regarding the computational feasibility. In this method, both the trial and weight functions are chosen to dwell in the same space. Furthermore, considering that Equations (4.11a) and (4.11b) are unsteady, a semidiscrete version should be used, *i.e.* the hypothesis is to assume that there are linear combinations of functions for which the coefficients of each shape function depend

on time, while the shape functions themselves vary only with the spatial coordinates. Thus, for a scalar function  $u(\mathbf{x}, t) : (\Omega \times \tau) \rightarrow \mathbb{R}$  and a basis of shape functions  $\{\varphi_i\}, i = 1, 2, \dots, l$ , the global Ritz-Galerkin approximation is given by

$$u(\mathbf{x}, t) \approx u_h(\mathbf{x}, t) := u^D + \sum_{i=1}^l a_i(t) \varphi_i(\mathbf{x}), \quad a_i(t) \in \mathbb{R}, \quad (4.13)$$

where  $u^D = u_h^D \in \mathbb{R}$  is the value of an essential boundary condition imposed on the formulation. That is to say, if  $u|_{\Gamma_D} = u^D \approx u_h^D$ , then, it holds a relation such as

$$\mathcal{S}^h = \mathcal{V}^h \oplus \{\mathbf{u}_h^D\}, \quad \forall \mathbf{u}_h \in [\mathcal{H}^1(\Omega)]^m,$$

for a vector of functions  $\mathbf{u}_h$  consistent with the dimension  $m \leq 3$ .

As aforementioned, the advective term is treated according to a Semi-Lagrangian approach [135] so that

$$\frac{\hat{D}\mathbf{v}_h}{Dt} \approx \frac{\mathbf{v}_h^{n+1} - \mathbf{v}_{h,d}^n}{\Delta t}. \quad (4.14)$$

Such a form stores the advection and ALE effects in a backward-in-time integration of the particle trajectories as explained in Subsection 3.2.2, which has  $\mathbf{v}_{h,d}^n$  as the velocity of the departure point per trajectory. However, the search for the departure point should take into account the mesh movement introduced by the ALE formulation falling over the displacement vector  $\boldsymbol{\alpha}$  (cf. Equation (3.66)) the need of store the contribution provided by the mesh velocity. Thus,

$$(\mathbf{x}_d; \tau) = (\mathbf{x}_a; \tau) - \mathbf{c}_h(\mathbf{x}_a) \Delta t, \quad \mathbf{x}_a \text{ of } T \in \mathcal{T}_h. \quad (4.15)$$

By introducing Equation (4.14) into Equation (4.12a) - safeguarded Equation (4.15) - and considering that Equation (4.13) is implicitly taken into account for both Equations (4.12a) and (4.12b), the semidiscrete version in space and time is given by

$$\begin{aligned} (\rho; \mathbf{v}_h^{n+1}, \mathbf{w}_h) + \frac{\Delta t}{Re} (\boldsymbol{\mu}; \nabla \mathbf{v}_h^{n+1}, \nabla \mathbf{w}_h) + \Delta t (p_h^{n+1}, \nabla \cdot \mathbf{w}_h) = \\ = \Delta t \left[ (\rho; \mathbf{v}_{h,d}^n, \mathbf{w}_h) + \frac{1}{Fr^2} (\rho; \mathbf{g}_h^n, \mathbf{w}_h) + \frac{1}{We} (\mathbf{f}_h^n, \mathbf{w}_h) \right] \end{aligned} \quad (4.16a)$$

$$(\mathbf{v}_h^{n+1}, \nabla \cdot \mathbf{q}_h) = 0 \quad (4.16b)$$

Since Equations (4.16a) and (4.16b) are bilinear forms already discretized, the introduction of a suitable finite element space and ensuing assembling mounting at element-level produces matrices such that, in the respective order, these equations render

$$\mathbf{M}_\rho \mathbf{v}^{n+1} + \frac{\Delta t}{Re} \mathbf{K} \mathbf{v}^{n+1} + \Delta t \mathbf{G} \mathbf{p}^{n+1} = \Delta t \left[ \mathbf{M}_\rho \mathbf{v}_d^n + \frac{1}{Fr^2} \mathbf{M}_\rho \mathbf{g}^n + \frac{1}{We} \mathbf{M} \mathbf{f}^n \right] \quad (4.17a)$$

$$\mathbf{D} \mathbf{v}^{n+1} = \mathbf{0} \quad (4.17b)$$

Concisely, we can write  $\mathbf{B} = \mathbf{M}_\rho + \frac{\Delta t}{Re} \mathbf{K}$  and arrange the equations to give

$$\begin{bmatrix} \mathbf{B} & \Delta t \mathbf{G} \\ \mathbf{D} & \mathbf{0} \end{bmatrix} \begin{bmatrix} \mathbf{v}^{n+1} \\ \mathbf{p}^{n+1} \end{bmatrix} = \begin{bmatrix} \mathbf{r}^n \\ \mathbf{0} \end{bmatrix} + \begin{bmatrix} \mathbf{bc}_1 \\ \mathbf{bc}_2 \end{bmatrix} \quad (4.18)$$

$$\text{with } \mathbf{r}^n = \Delta t \left[ \mathbf{M}_\rho \mathbf{v}_d^n + \frac{1}{Fr^2} \mathbf{M}_\rho \mathbf{g}^n + \frac{1}{We} \mathbf{M} \mathbf{f}^n \right],$$

where  $\mathbf{bc}_1, \mathbf{bc}_2$  are vectors accounting for Dirichlet boundary conditions of velocity and pressure respectively, if any. Recalling that the interfacial force is given by Equation (3.38), in order to obtain its discrete version to accompany the  $We$  number, the following matrix equation is written

$$\mathbf{M} \mathbf{f}^n = \mathbf{\Sigma} \mathbf{G} \mathbf{h}^n, \quad (4.19)$$

where  $\mathbf{\Sigma} = \sigma \kappa(\mathbf{x}_j) \mathbf{I}$  is a diagonal matrix storing the surface tension and curvature effects distributed for all the mesh nodes and  $\mathbf{h}^n$  the discrete vector of the Heaviside function. Consequently, the vector  $\mathbf{r}^n$  in Equation (4.18) takes the form

$$\mathbf{r}^n = \Delta t \left[ \mathbf{M}_\rho \mathbf{v}_d^n + \frac{1}{Fr^2} \mathbf{M}_\rho \mathbf{g}^n + \frac{1}{We} \mathbf{M}_L^{-1} \mathbf{\Sigma} \mathbf{G} \mathbf{h}^n \right],$$

now containing the inverse lumped matrix  $\mathbf{M}_L^{-1}$ .

Taking advantage of the discussion in Subsection 3.2.1, the governing equations are now viewed under a projection-like fully discretized format appropriate to the resulting process derived from the FE intervention,

$$\mathbf{M}_{NS} \mathbf{v}_{NS} = \mathbf{b}_{NS}, \quad (4.20)$$

with

$$\mathbf{M}_{NS} = \begin{bmatrix} \mathbf{B} & -\Delta t \mathbf{G} \\ \mathbf{D} & \mathbf{0} \end{bmatrix}; \quad \mathbf{v}_{NS} = \begin{bmatrix} \mathbf{v}^{n+1} \\ \mathbf{p}^{n+1} \end{bmatrix}; \quad \mathbf{b}_{NS} = \begin{bmatrix} \mathbf{r}^n \\ \mathbf{0} \end{bmatrix} + \begin{bmatrix} \mathbf{bc}_1 \\ \mathbf{bc}_2 \end{bmatrix}, \quad (4.21)$$

whence comes out the following exact LU factorization of  $\mathbf{M}_{NS}$  based on lumping process of the mass matrix  $\mathbf{M}_\rho$  (cf. [127]):

$$\begin{bmatrix} \mathbf{B} & \mathbf{0} \\ \mathbf{D} & \Delta t \mathbf{D} \mathbf{M}_{\rho,L}^{-1} \mathbf{G} \end{bmatrix} \begin{bmatrix} \mathbf{I} & -\Delta t \mathbf{M}_{\rho,L}^{-1} \mathbf{G} \\ \mathbf{0} & \mathbf{I} \end{bmatrix} \begin{bmatrix} \mathbf{v}^{n+1} \\ \mathbf{p}^{n+1} \end{bmatrix} = \begin{bmatrix} \mathbf{r}^n \\ \mathbf{0} \end{bmatrix} + \begin{bmatrix} \mathbf{bc}_1 \\ \mathbf{bc}_2 \end{bmatrix}, \quad (4.22)$$

The lumping technique minimizes the computational cost of inverting  $\mathbf{M}_\rho$ .

Following the straightforward LU scheme, the solution of Equation (4.22) is bipartite.

Firstly, the system

$$\begin{bmatrix} \mathbf{B} & \mathbf{0} \\ \mathbf{D} & \Delta t \mathbf{D} \mathbf{M}_{\rho,L}^{-1} \mathbf{G} \end{bmatrix} \begin{bmatrix} \mathbf{v}^\# \\ \mathbf{p}^{n+1} \end{bmatrix} = \begin{bmatrix} \tilde{\mathbf{b}}_1 \\ \mathbf{bc}_2 \end{bmatrix}; \quad \tilde{\mathbf{b}}_1 = \mathbf{r}^n + \mathbf{bc}_1 \quad (4.23)$$

for the intermediary velocity  $\mathbf{v}^\#$  and the pressure  $\mathbf{p}^{n+1}$  is solved. Chang *et al.* [172] reports that the error due to the splitting process affecting this classic fractional step method is reduced if a unique matrix – in this case,  $\mathbf{M}_{\rho,L}^{-1}$  –, is interspersed in the LU scheme. The shortcoming for the velocity field is corrected posteriorly. Secondly, the system

$$\begin{bmatrix} \mathbf{I} & -\Delta t \mathbf{M}_{\rho,L}^{-1} \mathbf{G} \\ \mathbf{0} & \mathbf{I} \end{bmatrix} \begin{bmatrix} \mathbf{v}^{n+1} \\ \mathbf{p}^{n+1} \end{bmatrix} = \begin{bmatrix} \mathbf{v}^\# \\ \mathbf{p}^{n+1} \end{bmatrix} \quad (4.24)$$

is solved to find the actual values of the fields.

From Equations (4.23) and (4.24), the following routine of calculations can be posed:

$$\text{Solve } \mathbf{B} \mathbf{v}^\# = \tilde{\mathbf{b}}_1; \quad (4.25)$$

$$\text{Solve } \tilde{\mathbf{E}} \mathbf{p}^{n+1} = \tilde{\mathbf{b}}_2; \quad \text{with } \tilde{\mathbf{E}} = \Delta t \mathbf{D} \mathbf{M}_{\rho,L}^{-1} \mathbf{G}; \quad \tilde{\mathbf{b}}_2 = \mathbf{bc}_2 - \mathbf{D} \mathbf{v}^\#; \quad (4.26)$$

$$\text{Correct } \mathbf{v}^{n+1} = \mathbf{v}^\# + \Delta t \mathbf{M}_{\rho,L}^{-1} \mathbf{G} \mathbf{p}^{n+1}. \quad (4.27)$$

However, Anjos [169] generalizes the correction of the intermediary velocity field when gravity forces and interfacial forces are assumed in the modelling of two-phase flows. The incremental

term  $e$ , which comes into the correction equation determines a substep for the projection method resulting in

$$\mathbf{v}_{corr}^\# = \mathbf{v}^\# + \Delta t e(\mathbf{g}, \mathbf{f}, Fr, We) \quad (4.28)$$

and its form depends on the forces  $\mathbf{g}, \mathbf{f}$ , the  $Fr$  and  $We$  numbers as well as on the nature of the flow. For pure single-phase flows without the introduction of the pressure gradient term (discussed in the next chapter),  $\mathbf{v}_{corr}^\#$  reduces to  $\mathbf{v}^\#$ .

#### 4.3.2 Fluid variables

To obtain a variational form for the advection-diffusion equation liable to model the transport of variables immersed in a carrying fluid, we proceed similarly to the previous essay. Then, we begin by introducing the Sobolev space

$$\mathcal{R} := \left\{ r \in \mathcal{L}^2(\Omega); r = 0 \text{ in } \Gamma_D \right\}$$

of weight functions. Therefrom, the finite space  $\mathcal{R}^h \subset \mathcal{R}$ . In turn, we weight the Equation (3.31) to have

$$\int_{\Omega} \frac{D\Psi}{Dt} r dV = \frac{1}{ReSc} \int_{\Omega} \nabla^2 \Psi r dV, \quad r \in \mathcal{R}. \quad (4.29)$$

Then, by analogous reasoning, the bilinear forms coming after using Equation (4.13) for  $u = \Psi$  in the weighted global formulation Equation (4.29) via Galerkin produce the discrete equation

$$m_{\Psi} \left( \frac{\hat{D}\Psi_h}{Dt}, r_h \right) + \frac{1}{ReSc} k_{\Psi}(\varrho; \nabla \Psi_h, \nabla r_h) = 0, \quad (4.30)$$

whereof

$$m_{\Psi} (\Psi_h^{n+1}, r_h) + \frac{\Delta t}{ReSc} k_{\Psi}(\varrho; \nabla \Psi_h^{n+1}, \nabla r_h) = \Delta t m_{\Psi} (\Psi_{h,d}^n, r_{h,p}). \quad (4.31)$$

By writing the matrix form, we have

$$\mathbf{M}_{\Psi} \mathbf{\Psi}^{n+1} + \frac{\Delta t}{ReSc} \mathbf{K}_{\Psi} \mathbf{\Psi}^{n+1} = \Delta t \mathbf{M}_{\Psi} \mathbf{\Psi}_d^n, \quad (4.32)$$

or, with  $\mathbf{B}_\Psi = \mathbf{M}_\Psi + \frac{\Delta t}{ReSc} \mathbf{K}_\Psi$ , the form

$$\mathbf{B}_\Psi \Psi^{n+1} = \mathbf{r}_\Psi^n + \mathbf{bc}_\Psi, \quad (4.33)$$

for

$$\mathbf{r}_\Psi^n = \Delta t \mathbf{M}_\Psi \Psi_d^n \quad (4.34)$$

and  $\mathbf{bc}_\Psi$  a vector containing Dirichlet boundary conditions. Along with Equation (4.18), Equation (4.33), form a system of FE-based ordinary equations as

$$\left\{ \begin{array}{l} \mathbf{B}\mathbf{v}^{n+1} + \Delta t \mathbf{G}\mathbf{p}^{n+1} = \mathbf{r}^n + \mathbf{bc}_1 \\ \mathbf{D}\mathbf{v}^{n+1} = \mathbf{0} + \mathbf{bc}_2 \\ \mathbf{B}_\Psi \Psi^{n+1} = \mathbf{r}_\Psi^n + \mathbf{bc}_\Psi \end{array} \right. \quad (4.35)$$

with a group of generalized discrete initial and boundary conditions

$$\left\{ \begin{array}{l} \mathbf{v}_{i,0} = \mathbf{v}_0, \\ \mathbf{p}_{j,0} = \mathbf{p}_0, \\ \Psi_{j,0} = \Psi_0 \\ \\ \mathbf{v}_i|_{\Gamma_{DvN}^2} = \mathbf{v}_{DvN}^{\Gamma^2} \\ \mathbf{p}_j|_{\Gamma_{DvN}^2} = \mathbf{p}_{DvN}^{\Gamma^2} \\ \Psi_j|_{\Gamma_{DvN}^2} = \Psi_{DvN}^{\Gamma^2} \end{array} \right. \quad (4.36)$$

for  $i = 1, 2, \dots, \iota_v$ ;  $j = 1, 2, \dots, \iota_s$  whose discrete solution for each unknown DOF over the mesh is the triplet  $(\mathbf{v}, \mathbf{p}, \Psi)$ . Here, two remarks are enriching: i) Dirichlet or Neumann boundaries can be chosen provided that they are consistently imposed; ii)  $\dim(\mathbf{v}) = 3\iota_v$ , whereas  $\dim(\mathbf{p}) = \dim(\Psi) = \iota_s$ .

### 4.3.3 The stable MINI element 3D

The Navier-Stokes equations belong to a mixed universe, so that a FE space that deals with the coupling velocity/pressure is required. Moreover, stability criteria need to be satisfied for such space. To attire and complete the theoretical development of Section 4.3,



we call up some information about the Taylor-Hood's family MINI element, which drives the element-level discretization of the presented formulation.

In  $\mathbb{R}^3$ , the MINI element is a tetrahedron containing DOFs at its vertices and at the barycenter (see Figure 26) whose shape functions are similar to “bubbles”. According to the Taylor-Hood approach (cf. [161], p. 174), the velocity field is approximated by a first order polynomial set enriched with functions formed by combining the barycentric coordinates, while the pressure field has only a first-order accuracy. Furthermore, it was proved that the

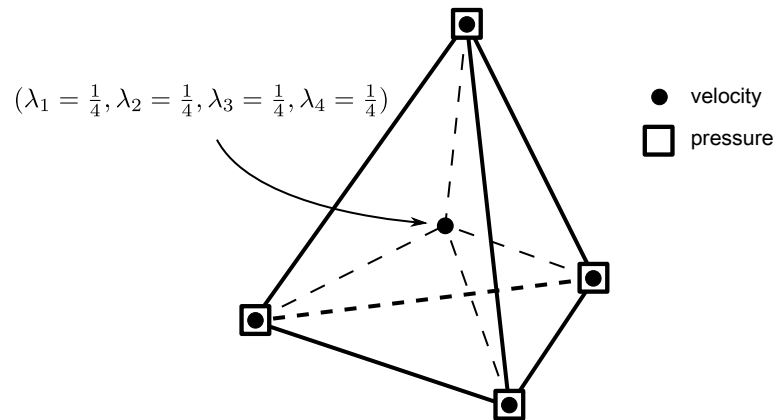


Figure 26: MINI element 3D highlighting the sites for the degrees of freedom of velocity and pressure.

MINI element fulfills the requirements of stability also known as the *LBB* condition [173], [174], [125]. Mathematically, if defined, for  $k \geq 1$  the set

$$\begin{aligned} \mathcal{M}_0^k(\mathcal{T}^h) &= \{\mathbf{v}; \mathbf{v} \in C^0(\Omega), \mathbf{v}|_T \in P_k(T) \quad \forall T \in \mathcal{T}_h\} \\ \dot{\mathcal{M}}_0^k(\mathcal{T}^h) &= \mathcal{M}_0^k(\mathcal{T}^h) \cap \mathcal{H}_0^1(\Omega), \end{aligned}$$

and for  $k \geq 3$  the set

$$\mathcal{B}^k(\mathcal{T}^h) = \{\mathbf{v} | \mathbf{v}|_T \in \mathcal{P}_k(T) \cap \mathcal{H}_0^1(T) \quad \forall T \in \mathcal{T}^h\},$$

when  $k = 3$ , a bubble function proportional to the barycentric coordinates as  $\lambda_1 \lambda_2 \lambda_3 \lambda_4$  lies over the barycenter ( $\lambda_j = \frac{1}{4}, 1 \leq j \leq 4$ ) of the tetrahedron. Then, the MINI element ( $m = 3$ ) uses the FE spaces

$$\begin{aligned} \mathcal{V}^h &= \{(\dot{\mathcal{M}}_0^1) \times (\dot{\mathcal{M}}_0^1) \times (\dot{\mathcal{M}}_0^1)\} \oplus \{\mathcal{B}^3 \times \mathcal{B}^3 \times \mathcal{B}^3\} \\ \mathcal{Q}^h &= \mathcal{M}_0^1 \end{aligned}$$

and evaluates 13 DOFs per element to solve a full system like Equation (4.36). In this case, the DOFs corresponding to the scalar field are evaluated at the vertices of the tetrahedron, just as the DOFs of pressure, forcing the storage of  $3l_v + 2 \times 4l_s = 3l_v + 8l_s$  equations in the computer's memory.

#### 4.4 Dynamic mesh control and ALE parametrization

Many geometrical operations are performed behind the ALE code used in this thesis, mainly due to the dynamic movement of the computational FE mesh. This heavy load of numerical work, namely: displacement, insertion, deletion and rearrangement of nodes; contraction and flipping of edges; smoothing and redistribution of velocity fields, or even mesh quality checking routines require, above all, a physical background upon the flow under examination.

A expression describing the arbitrary movement of a mesh can be given by

$$\hat{\mathbf{v}} = \alpha_1 \mathbf{v} + \alpha_2 \mathbf{v}_e, \quad 0 \leq \alpha_1, \alpha_2 \leq 1, \quad (4.37)$$

for which the real parameters  $\alpha_1, \alpha_2$  balance the mesh velocity to determine intermediary motions that differ from a completely Lagrangian or Eulerian one. Thus, if  $\alpha_1 = 0$  and  $\alpha_2 = 1$ , for instance, a purely elastic motion is achieved, whose interpretation depends on the techniques applied for the mesh treatment. Notwithstanding the free choice of these parameters, higher flexibility is attained when their values are different from zero.

Following the generalized ALE method presented by [169], it is assumed here that the mesh velocity is made up by partial velocities, each of them ascribed according to the flow physics. Given that the computational mesh was defined by Equation (2.23) as the union of two subsets, different mesh operations are allocated for them independently. Thus, the mesh velocity is governed by the following general form:

$$\hat{\mathbf{v}}(\mathbf{x}_j) = \begin{cases} \mathbf{v} - \gamma_1 (\mathbf{v} \cdot \mathbf{t}) \mathbf{t} + \gamma_2 (\mathbf{v}_e \cdot \mathbf{t}) \mathbf{t} & , \text{ if } \mathbf{x}_j \in \mathcal{T}_{h_1}^{\Gamma^1} \\ \beta_1 \mathbf{v} + \beta_2 \mathbf{v}_{I;\epsilon} + \beta_3 \mathbf{v}_e & , \text{ otherwise} \end{cases} \quad (4.38)$$

with  $\mathbf{t}$  being a unit vector on the tangent plane to the interface at  $\mathbf{x}_j = \mathbf{x}_I$ . Apart from any simplicity, this generalized method holds intricate calculations to guarantee an interface

representation highly accurate through nodal scattering. As seen, Equation (4.38) works differently for the mesh subsets. Therefore, a brief description of how each parcel interferes on the scheme is serviceable (cf. [169], ch. 6).

By analyzing the first condition, for interface nodes, we note that  $\hat{\mathbf{v}}$  is made up by the fluid velocity, the tangential component of the fluid velocity and the tangential component of the elastic velocity. More precisely, once the decomposition

$$\mathbf{v}_I = (\mathbf{v} \cdot \mathbf{t})\mathbf{t} + (\mathbf{v} \cdot \mathbf{n})\mathbf{n} \Rightarrow \quad (4.39)$$

$$\mathbf{v}_{I,\mathbf{n}} = \mathbf{v}_I - (\mathbf{v} \cdot \mathbf{t})\mathbf{t}, \quad (4.40)$$

is valid for any interface node, it turns out that the parameter  $\gamma_1$  is associated to the reduction of the tangent interface nodal velocity on the flow so that the two first terms of this condition are combined into one effect, *viz.* of allowing that the interface moves in the normal direction with higher relaxation. Oppositely,  $\gamma_2$  is the parameter responsible for the intensity of mesh smoothing driven by the elastic velocity  $\mathbf{v}_e$ .

On the other hand, the second condition, for volumetric nodes, aggregates components depending on the fluid velocity, the elastic velocity and the additional smoothing velocity  $\mathbf{v}_{I,\epsilon}$  resulting from the contribution of the interface neighbourhood  $\epsilon$ , which we will name “neighbourhood-based velocity”. In turn, it turns out that  $\beta_1$  controls the Lagrangian motion of the volume mesh, whereas  $\beta_2, \beta_3$  manage the intensity of mesh smoothing driven by the neighbourhood-based velocity  $\mathbf{v}_{I,\epsilon}$ , and the elastic velocity, respectively.

#### 4.4.1 Dynamic control techniques

In this thesis, a scheme of Laplacian smoothing is used to relocate the mesh nodes and achieve qualitative elements through volume restriction and aspect ratio control. By considering  $S(i)$  the “star” of the node  $i$  (elements sharing  $i$  as a common vertex), the technique for relocation of points is given by

$$\mathbf{x}_i \rightarrow \hat{\mathbf{x}}_i := \sum_{j \in S(i)}^{#S} w_{ij}(\mathbf{x}_j - \mathbf{x}_i), \quad w_{ij} = l_{ij}^{-1}, \quad (4.41)$$

meaning that  $\mathbf{x}_i$  moves to the new position  $\hat{\mathbf{x}}_i$  within each remeshing operation. Additionally,  $l_{ij}$  is the length of the edge joining the central node  $i$  to each node  $j$  encircling it at the star as

displayed in Figure 27.

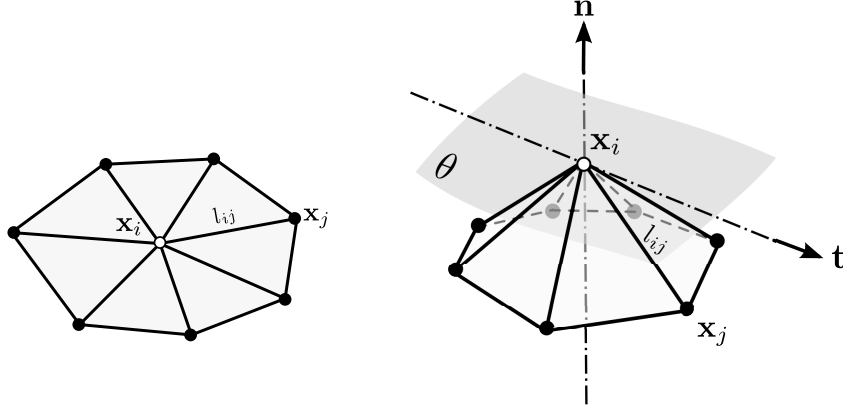


Figure 27: Representations of the star  $S(i)$  of the node  $i$ : 2D version at left and 3D version with the tangent plane  $\theta$  at right.

Both the elastic velocity  $\mathbf{v}_e$  and the neighbourhood-based velocity  $\mathbf{v}_{I;\epsilon}$  play a remarkable role as mesh smoothing appliances. While the former is obtained from an approximation via uniform motion within each discrete time  $\Delta t$ , the latter is computed through the arithmetic mean among the neighbour's velocities which are immersed into the continuous phase, thus taking the near-field dynamics into account for the interface motion. Sequentially, they are defined, for each node  $i$  as

$$\mathbf{v}_e(i) = \frac{1}{\Delta t} \sum_{j \in S(i)} l_{ij}^{-1} (\mathbf{x}_j - \mathbf{x}_i) \quad (4.42)$$

$$\mathbf{v}_{I;\epsilon}(i) = \frac{1}{\#S} \sum_{j \in S(i)} \mathbf{v}_j \quad (4.43)$$

#### 4.4.2 Geometrical operations and remeshing techniques

To gauge harsh topological changes that an interface may undergo in virtue of the hydrodynamics, geometrical operations are performed over the elements of the discrete interface. Among the various techniques of the ALE/FE method discussed here, which are intended to preserve the mesh quality as best as possible, the main operations deserving particular attention are: node insertion ( $\Upsilon^+$ ), node deletion ( $\Upsilon^-$ ), edge contraction ( $\Xi^{\sim}$ ) and edge flipping ( $\Xi^{\emptyset}$ ) as depicted in Figure 28. For each case, a minimal patch of elements is used as model. Such operations, symbolized by  $\Upsilon^+$ ,  $\Upsilon^-$ ,  $\Xi^{\sim}$  and  $\Xi^{\emptyset}$  can be interpreted as functions whose arguments are nodes and/or edges of the interface discrete mesh. In 3D simulations, many topological complications may arise at element-level due to inaccuracies

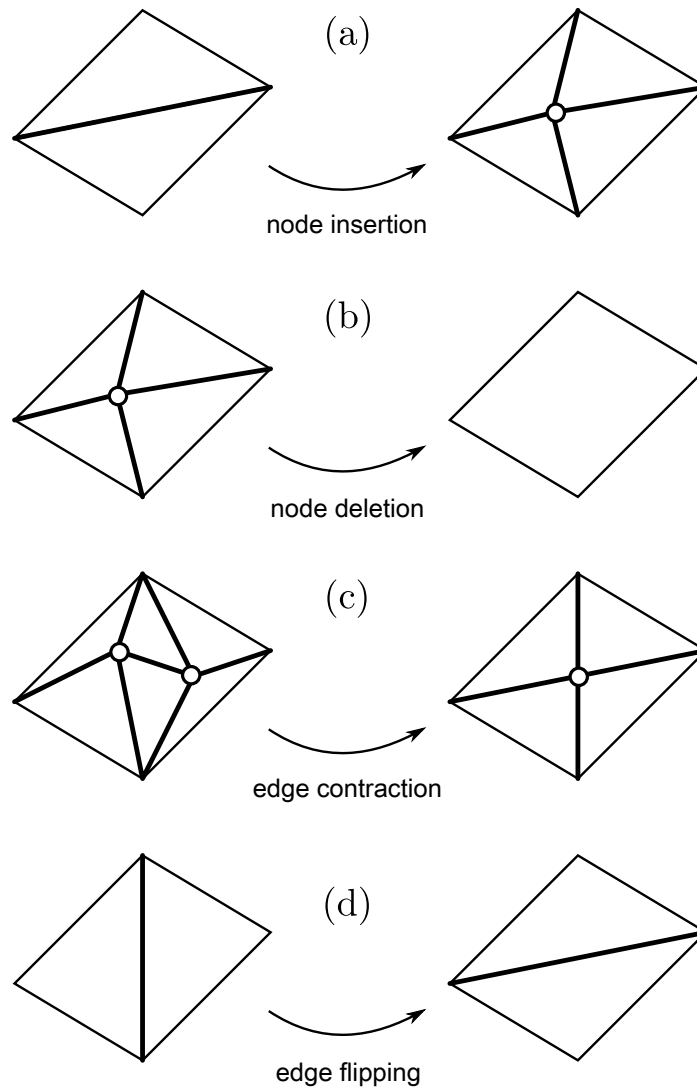


Figure 28: Possible range of geometrical operations for the discrete interface: (a) node insertion; (b) node deletion; (c) edge contraction; (d) edge flipping.

in capturing high curvatures zones or degenerate elements. Due to that wide range of possible configurations for the elements, challenging and exhaustive black-box tests are required to remedy all the potential remeshing failures. In summary, Table 1 gathers the main code objects related to the dynamic mesh control.

#### 4.5 Solvers and preconditioning

Not only due to the ALE remeshing operations, but also the refinement levels imposed over the mesh, the global linear systems generated through FE may render huge, *i.e.* to contain many DOFs. Avoiding time-consuming solutions and sparsity problems is a task which needs optimal combinations between solver/preconditioner. In this thesis, solvers and

Symbol	Description
$\beta_1$	pure Lagrangian motion control
$\beta_2$	neighbourhood-based velocity smoothing
$\beta_3$	elastic-based velocity Laplacian smoothing
$\gamma_1$	tangent interface velocity magnitude control
$\gamma_2$	elastic-based velocity and mesh quality
$\Upsilon^+$	node insertion operator
$\Upsilon^-$	node deletion operator
$\Xi^{\sim}$	edge contraction operator
$\Xi^{\emptyset}$	edge flipping operator

Table 1: ALE meshing parameters for surface operations.

preconditioners based on Krylov spaces from the PETSC library [175] were used. Although a comparative study was not performed to find the better combination, better results were achieved by using Pre-Conjugated Gradient (PCG) solvers together with Incomplete Cholesky (ICC) or Incomplete LU (ILU) preconditioners.

## 5 PERIODIC BOUNDARY CONDITIONS

### 5.1 Introductory remarks

Geometrically periodic configurations arise in many industrial applications and may thenceforward lead fluid flows to some repetitive behaviour. This periodic nature is the basis for several systems, including those operating under a cyclic way. For instance, periodic flows occur in heat exchangers, evaporators, condenser tubes and electronics cooling, at which either arrays of fins or plates are periodically arranged, thus creating sorts of patterns that influence the flow and other system properties.

PBC have been an appreciated tool by researchers in attempting to obtain computational efficiency when either fully-developed or periodic regimes are taken into account. Also, PBC are typically intended to isolate bulk phenomena, when one considers that the boundaries of the real physical system have minor effects. Flows of granular material [176], fluid-particle flows [177], molecular dynamics [178], heat and mass transfer problems [179], and the dynamics of gas-liquid flows in long oil pipelines [180] are some examples of fields where this strategy was used. Some of the references aforementioned use “simulation box”, “unit cell”, or “tiling” as referring to PBC simulations, since the overall flow dynamics is confined into a piece of the domain. Intuitively, the simplest way to idealize the periodicity is to set the same values of an arbitrary quantity on the extremities of the cell.

In regard to a topological point of view, a two-dimensional strip, for instance, can generate a cylinder just as a cylinder can generate a torus by “gluing” their extremities each other. Such topological relations as well as the “tiling” process are depicted in Figure 29 to single out the periodic passage of generic streamlines of a representative in-loop flow. Alike procedure to generate prismatic geometries is done by extrusion of elementary shapes, through which periodic boundaries are identified by geometrical relations, such as reflections or translations. When carrying these operations to the FE context presented here, a few requirements must be fulfilled to avoid degradations and discontinuity of the solution over the elements whose DOFs are under imposition of PBC. In this chapter, the whole strategy to apply PBC on the ALE/FEM context studied is presented in details from the mesh pre-processing stage. Comments on the mathematical formulation through FEM as well as the computational implementation come next.

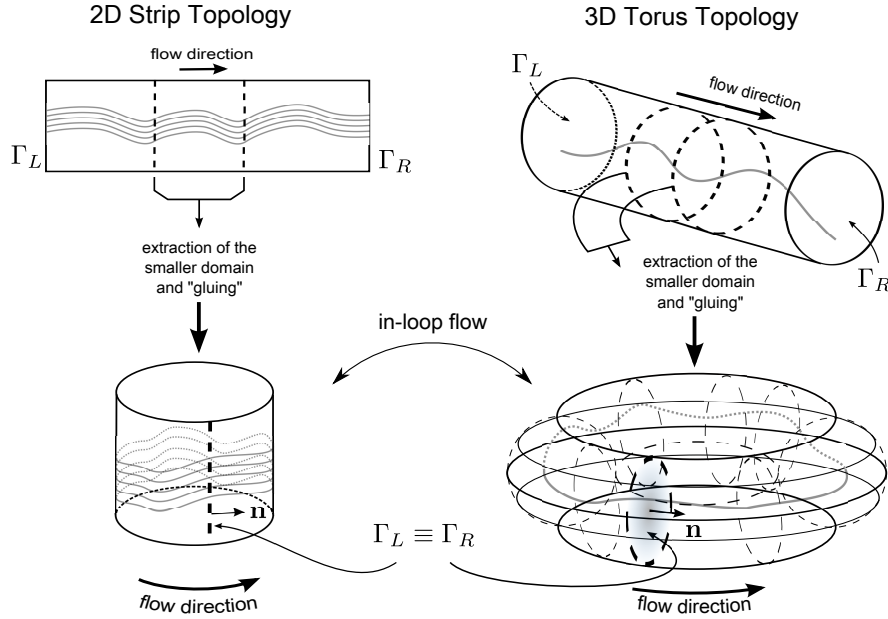


Figure 29: Sketch of the topological mappings, “tiling” process, and in-loop flow settings for generic geometries: 2D strip at left and 3D torus at right.

## 5.2 Design of periodic meshes and their pre-processing

It is assumed here that the PBC implementation depends on meshes that ensure a one-to-one spatial correspondence between each pair of nodes belonging to each periodic boundary chosen *a priori*. The strategy to build periodic meshes - thus termed because of their geometrical construction - is based on both topological and geometrical ideas as before mentioned. In this thesis, the surface mesh  $\mathcal{T}_{h_T}^\Gamma$  is generated through user-defined scripts inserted into the GMSH software during the pre-processing stage. Sequentially, the volume mesh  $\mathcal{T}_h^\Omega$  is created during the code runtime.

Following [181], we will refer to the DOFs of a periodic mesh as: *master*, *slave*, or *internal* according to their spatial location. It is worth to comment that in this context, DOFs and nodes are terminologies used almost interchangeably since the main ideas behind the periodic correspondence are of geometrical nature. The master DOFs will be those placed over the boundary chosen to be at the upstream side of the flow, whereas the slave ones will be their downstream counterparts. All the remnant DOFs, *i.e.* those that are out of the periodic boundaries will be, hence, internal, even if they belong to nonperiodic boundaries. At first, the master and slave nodes have different spatial coordinates over the mesh as regards the period length, but, practically, their independence is changed by an overloading process by which the slave DOFs render “dummy nodes”, thereby matching exactly the sites of the master



DOFs. This numerical artifice eliminates the slave DOFs fictitiously to favour the periodic simulation. Figure 30 (see a two-dimensional version in [182]) sketches the three-dimensional geometrical rudiments to establish the PBC in the FEM. For this specific example, let  $\Gamma_L, \Gamma_R$  be the master and slave periodic boundaries, respectively, and consider  $\mathbf{x}_L = (x_L, y_L, z_L) \in \Gamma_L, \mathbf{x}_R = (x_R, y_R, z_R) \in \Gamma_R$  to be the master and slave nodes holding the DOFs of interest. For  $\iota$  nodes of discretization, the sequences

$$(\mathbf{x}_L; \iota) := \{\mathbf{x}_{L,1}, \mathbf{x}_{L,2}, \dots, \mathbf{x}_{L,\iota}\}$$

$$(\mathbf{x}_R; \iota) := \{\mathbf{x}_{R,1}, \mathbf{x}_{R,2}, \dots, \mathbf{x}_{R,\iota}\}$$

define the geometrical periodicity of the mesh if

$$\mathbf{x}_R = \mathbf{x}_L + L_P \mathbf{e}_P \quad (5.1)$$

for each pair of nodes.

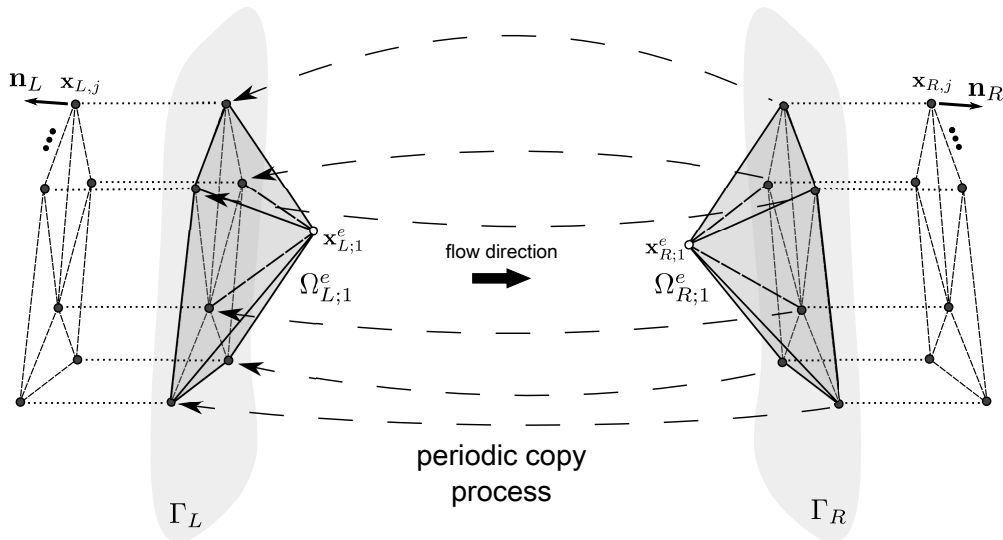


Figure 30: Geometrical sketch of the PBC implementation for a 3D periodic finite element mesh.

In consequence of the geometrical identification, we achieve conformity between the elements sharing the periodic boundaries. For a better view of this, let  $\Omega_{L,1}^e$  and  $\Omega_{R,1}^e$  be the 1-ring neighbours of  $\Gamma_L$  and  $\Gamma_R$ , respectively, where the definition of “ $k$ -rings” here is adapted from that used by [183] to establish the pairing between the two families of periodic elements. In this case, the entity shared with each periodic element is the boundary surface itself. In

other words,

$$\Omega_{d,1}^e := \{\cup_{e=1}^E \Omega_d^e; F_d^e \cap \Gamma_d \neq \emptyset\}, \quad d = L, R. \quad (5.2)$$

Moreover, some elements can also share only nodes rather than an entire edge or face, thus allowing that some  $F_d^e$  is understood as a point only. In this manner, the DOFs that connect edges and faces over the boundaries are prepared to undergo the “gluing” operation by which the contributions of the slave DOFs are cumulative over the master nodes. That is to say, the boundary faces of the elements of  $\Omega_{L,1}^e$  are connected (in a continuous sense) to the internal elements at right the equations relative to the nodes of  $\Gamma_R$  are disregarded in the matrices assembled via the standard FE process, which is discussed in the coming sections. In Figure 30,  $\mathbf{x}_{L,j}, \mathbf{x}_{R,j}$  represent the master and slave nodes, respectively, that seal a periodic pair, whereas  $\mathbf{x}_{L,j}^e, \mathbf{x}_{R,j}^e$  are two nodes underpinning the 1-ring element blocks depicted therein. Such nodes can be more informally recognized as “hooks” of the “umbrella” shape that is formed by these tetrahedra and are excluded from the computational periodicity. Even though, they might be so geometrically since the meshes are always generated with volume restriction, thus enforcing, in this case, quasi-symmetric elements due to the quality tetrahedralization. The unstructured periodic meshes scripts take the built-in command `Periodic Surface` of the GMSH software into account to generate, thereafter, an automatized mechanism that transcribes the surface mesh placed over the master boundary onto the slave boundary. For a sample script about how to generate surface periodic meshes inside a two-phase context (this is the case of Figure 18), see Appendix C.

### 5.3 Periodic decomposition via the transformed variable approach

The imposition of PBC via the transformed variable approach used here follows the physical model introduced by [184] through which the variables of the flow are converted into a cyclic state. According to such a model, the main motivation to be conserved is that of dealing with fully developed flows without having to face computations involving effects of entrance region. Although the simulations presented in this thesis encompass mainly hydrodynamic effects, other physical effects, such as thermal, concentration and electromagnetic fields can be suitably treated through this approach if PBC were equally required (see Subsection 6.1.2).

Since this transformation decouples the flow of the entrance region, some kind of forcing term should be included in the model to compensate the fictitious in-loop domain enforced by the periodicity. As suggested by [184], velocity and pressure should be treated differently in the fully developed regime. While the velocity field obeys a relation of kind

$$\mathbf{v}|_{\Gamma_L} = \mathbf{v}|_{\Gamma_R} \quad (5.3)$$

at the extremities of the periodic cell, the pressure drop is periodic along the cell length, instead of the pressure field itself. For this reason, the approximation

$$\frac{\partial p}{\partial(\mathbf{x} \cdot \mathbf{e}_P)} \approx \frac{\Delta p}{L_P} = \frac{p|_{\Gamma_R} - p|_{\Gamma_L}}{L_P} = \beta \quad (5.4)$$

used for a fluid flowing along the direction  $\mathbf{e}_P$  inside a cell of period  $L_P$ , describes the periodic pressure drop by means of a constant gradient. In this manner,  $\beta$  can be interpreted as a mass flow producer and taken to characterize a decomposition of the pressure field  $p$  of the momentum equation as

$$p = -\beta(\mathbf{x} \cdot \mathbf{e}_P) + \tilde{p}, \quad (5.5)$$

where  $\tilde{p}$  is related to the local motions of the flow, so that holds

$$\tilde{p}|_{\Gamma_L} = \tilde{p}|_{\Gamma_R}. \quad (5.6)$$

As suggested by [185], [179],  $\tilde{p}$  is said to be a *reduced pressure*. With this formulation, the prescription of a pressure gradient is expected, as opposed to a mass flow, or inflow condition. Despite of this interpretation valid for channel flows, for instance, the physical sense of  $\beta$  can take on other facets.

On the other hand, we should bear in mind that Equation (5.5) evokes the hypothesis on unidirectional fully-developed flow and might be the simplest way to settle a forcing term for the periodic problem given the linear pressure drop. Furthermore,  $\beta$  as above is a dimensional value. To be introduced in the dimensionless momentum equation, some suitable form should be found (cf. [186], [187]). Depending on the physical situation to be simulated,  $\beta$  may work as a body force acting on the fluid flow. This is the case, for instance, in a Poiseuille starting flow (cf. Sec. 4 of [188]). For now, by choosing reference quantities for the

Equation (5.5), we will assume that one of its possible representative dimensionless forms is

$$\frac{p}{\rho_{ref}U_{ref}^2} = -\frac{\beta L_{ref}}{\rho_{ref}U_{ref}^2} \frac{(\mathbf{x} \cdot \mathbf{e}_p)}{L_{ref}} + \frac{\tilde{p}}{\rho_{ref}U_{ref}^2} \Rightarrow p^* = -\beta^* (\mathbf{x}^* \cdot \mathbf{e}_p^*) + \tilde{p}^*, \quad (5.7)$$

whose asterisk can be dropped out to have consistency with Equations (3.40) and (3.42).

Therewith, the dimensionless pressure gradient term is given by

$$\beta^* = \frac{\beta L_{ref}}{\rho_{ref}U_{ref}^2} = \left( \frac{\beta}{\rho_{ref}U_{ref}^2} \right) L_{ref}. \quad (5.8)$$

Since the term inside parentheses is the Euler number, we will associate  $\beta^*$  with this dimensionless group by defining

$$\beta^* := Eu_{\beta^*}, \quad (5.9)$$

and calling  $Eu_{\beta^*}$  an Euler number associated to the pressure gradient.

After dropping out the asterisk and inserting Equation (5.7) into Equation (3.43a), the momentum equation takes on the form

$$\begin{aligned} B_{1,p}(\mathbf{v}, \tilde{p}, \mathbf{f}, \hat{\mathbf{v}}, \rho, \mu, \mathbf{g}) := & \rho \left( \frac{\partial \mathbf{v}}{\partial t} + (\mathbf{v} - \hat{\mathbf{v}}) \cdot \nabla \mathbf{v} \right) - Eu_{\beta} \mathbf{e}_1 + \nabla \tilde{p} \\ - \frac{1}{Re} \nabla \cdot [\mu (\nabla \mathbf{v} + \nabla \mathbf{v}^T)] - \frac{1}{Fr^2} \rho \mathbf{g} - \frac{1}{We} \mathbf{f} = & \mathbf{0} \end{aligned} \quad (5.10)$$

being now  $\tilde{p}$  the unknown to be determined.

The periodic boundary conditions resulting therefrom are

$$\mathbf{v}|_{\Gamma_L} = \mathbf{v}|_{\Gamma_R} \quad (5.11)$$

$$\mathbf{n}_L \cdot \nabla \mathbf{v}|_{\Gamma_L} = -\mathbf{n}_R \cdot \nabla \mathbf{v}|_{\Gamma_R} \quad (5.12)$$

$$\tilde{p}|_{\Gamma_L} = \tilde{p}|_{\Gamma_R} \quad (5.13)$$

$$\mathbf{n}_L \cdot \nabla \tilde{p}|_{\Gamma_L} = -\mathbf{n}_R \cdot \nabla \tilde{p}|_{\Gamma_R}. \quad (5.14)$$

These relations express the need for continuity over the periodic boundaries and assure that the primitive variables are identical both in the inlet and outlet, thus closing the connection loop, *i.e.* the fluid should leave the domain just as it comes in. In the FEM context, the Neumann conditions play a relevant role during the assembling process of the elemental matrices

modified for PBC which is explained in the next section. Comini *et al.* [189] underlined that the normal derivative can be prescribed as zero or nonzero, depending if orthogonal or skew incoming flow is desired, but the second case is not examined here.

#### 5.4 FE/PBC implementation

Different methodologies are available to impose PBC through a FE approach both in periodic and non-periodic meshes [190], [181], [191], [192], [193], [194]. Generally, they encompass the enforcement of nodal connectivity through auxiliary lists during the assembling process of the FE global system matrices as well as operations to suppress or sum rows and columns in the global matrices. In this thesis, we have opted by the second strategy, which will be detailed through the next sections.

##### 5.4.1 Variational formulation in periodic domains

Analogous ideas to those presented in Section 4.3 are reused here to set forth a periodic variational formulation for the governing equations. We start by putting together the forms defined in Equations (5.10), (3.43b) and (3.43c) in the system

$$\left\{ \begin{array}{l} \mathbf{B}_{1,P}(\mathbf{v}, \tilde{p}, \mathbf{f}; \hat{\mathbf{v}}, \rho, \mu, \mathbf{g}) = 0 \\ \mathbf{B}_2(\mathbf{v}) = 0 \\ \mathbf{B}_3(\Psi) = 0. \end{array} \right. \quad (5.15)$$

Next, define the following weight function spaces:

$$\mathcal{V}_P := \{\mathbf{w} \in \mathcal{H}_P^1(\Omega); \nabla \cdot \mathbf{w} = 0, \mathbf{w}(\mathbf{x}) = \mathbf{w}(\mathbf{x} + L_P \mathbf{e}_P), \mathbf{x} \in \Gamma_L\}$$

$$\mathcal{Q}_P := \{q \in \mathcal{L}_P^2(\Omega); q(\mathbf{x}) = q(\mathbf{x} + L_P \mathbf{e}_P), \mathbf{x} \in \Gamma_L\}$$

$$\mathcal{R}_P := \{r \in \mathcal{L}_P^2(\Omega); r(\mathbf{x}) = r(\mathbf{x} + L_P \mathbf{e}_P), \mathbf{x} \in \Gamma_L\}.$$

These spaces gather periodic functions used to comply with a variationally consistent formulation of FE with PBC (cf. [191], [195]). Thenceforward, except for the addition of periodic weight functions  $(\mathbf{v}_P, q_P, r_P) \in (\mathcal{V}_P, \mathcal{Q}_P, \mathcal{R}_P)$  in the weak form equations (cf. Equations (4.29),

(4.8a) and (4.8b), the system Equation (5.15) is identical to the original forms. Therefore,

$$\left\{ \begin{array}{l} \mathbf{B}_{1,P}(\mathbf{v}_P, \tilde{p}, \mathbf{f}; \hat{\mathbf{v}}, \rho, \mu, \mathbf{g}) = 0 \\ \mathbf{B}_{2,P}(\mathbf{v}_P) = 0 \\ \mathbf{B}_{3,P}(\Psi_P) = 0 \end{array} \right. \quad (5.16)$$

is the homologous periodic version of Equation (5.15) in the sense of Galerkin. The mesh velocity field  $\hat{\mathbf{v}}$  is not considered periodic since the methodology employed here prevents the motion of  $\mathcal{T}^{\Gamma^2}$ . Consequently, nodes lying on the periodic boundaries are stationary concerning the field  $\hat{\mathbf{v}}$ .

That said, when assigning bilinear forms similar to the standard formulation, the terms expanded from the weighting of Equation (5.16)

$$\left\{ \begin{array}{l} \int_{\Omega} \mathbf{B}_{1,P}(\mathbf{v}_P, \tilde{p}, \mathbf{f}; \hat{\mathbf{v}}, \rho, \mu, \mathbf{g}) \cdot \mathbf{w}_P \, d\Omega = 0 \\ \int_{\Omega} \mathbf{B}_{2,P}(\mathbf{v}_P) \cdot q_P \, d\Omega = 0 \\ \int_{\Omega} \mathbf{B}_{3,P}(\Psi_P) \cdot r_P \, d\Omega = 0 \end{array} \right. \quad (5.17)$$

give rise to the respective discrete equations for the quantities involved:

$$m_{\rho,P}(\rho; \mathbf{v}_{h,P}^{n+1}, \mathbf{w}_{h,P}) + \frac{\Delta t}{Re^{1/2}} k_P(\mu; \nabla \mathbf{v}_{h,P}^{n+1}, \nabla \mathbf{w}_h) + \Delta t g_P(\tilde{p}_h^{n+1}, \nabla \cdot \mathbf{w}_{h,P}) = \Delta t \mathbf{r}_{h,P}^n \quad (5.18a)$$

$$d_P(\mathbf{v}_{h,P}^{n+1}, \nabla \cdot q_{h,P}) = 0 \quad (5.18b)$$

$$\text{with } \mathbf{r}_{h,P}^n = m_{\rho,P}(\rho; \mathbf{v}_{h,d,P}^n, \mathbf{w}_{h,P}) + m_{\rho,P}(\rho; \mathbf{g}_h^n, \mathbf{w}_{h,P}) + \lambda Eu_{\beta} m_P(\varphi_{h,P}^n \mathbf{e}_P, \mathbf{w}_{h,P}) + \frac{1}{We} (\mathbf{f}_{\sigma h}^n, \mathbf{w}_{h,P})$$

with  $\psi_{h,P}^n \mathbf{e}_P, \mathbf{v}_h, \mathbf{w}_h \in \mathcal{V}_P^h \subset \mathcal{V}_P$  and  $\tilde{p}_h, q_{h,P} \in \mathcal{Q}_P^h \subset \mathcal{Q}_P$  for the momentum; and

$$m_{\Psi,P}(\Psi_{h,P}^{n+1}, r_{h,P}) + \frac{\Delta t}{ReSc} k_{\Psi,P}(\varrho; \nabla \Psi_{h,P}^{n+1}, \nabla r_{h,P}) = \Delta t m_{\Psi,P}(\Psi_{h,d,P}^n, r_{h,P}). \quad (5.19)$$

with  $\Psi_{h,P}, r_{h,P} \in \mathcal{R}_P^h \subset \mathcal{R}_P$  for the scalar field.

All the bilinear forms  $P$ -subscripted above can be compared to their counterparts, *viz.* Equations (4.31), (4.16a) and (4.16b). Different than the others, the term  $\lambda Eu_{\beta} m_P(\varphi_{h,P}^n \mathbf{e}_P, \mathbf{w}_{h,P})$  have null contributions in the coordinates transverse to the streamwise periodic flow. In other words,  $\varphi_{h,P}^n \mathbf{e}_P$  are the shape functions relative to the periodic direction  $\mathbf{e}_P$  chosen that

determines

$$(\varphi_{h,P}^n \mathbf{e}_P, \mathbf{w}_{h,P}) = \delta_{iP} (\varphi_{h,P}^n \mathbf{e}_P, \mathbf{w}_{h,P}), \quad 1 \leq i, P \leq 3, \quad (5.20)$$

for the Kronecker's delta  $\delta_{iP}$ , *i.e.* the pressure gradient  $\lambda Eu_\beta$  acts only when  $i = P$ .

In turn, Equations (5.19), (5.18a) and (5.18b) generate the following set of matrix equations:

$$\begin{aligned} \mathbf{M}_{\rho,P} \mathbf{v}_P^{n+1} + \frac{\Delta t}{Re} \mathbf{K}_P \mathbf{v}_P^{n+1} \\ + \Delta t \mathbf{G}_P \tilde{\mathbf{p}}^{n+1} = \Delta t \left[ \mathbf{M}_{\rho,P} \mathbf{v}_{d,P}^n + \mathbf{M}_P \mathbf{b}^n + \frac{1}{Fr^2} \mathbf{M}_{\rho,P} \mathbf{g}^n + \frac{1}{We} \mathbf{M}_P \mathbf{f}^n \right] \end{aligned} \quad (5.21a)$$

$$\mathbf{D}_P \mathbf{v}_P^{n+1} = \mathbf{0} \quad (5.21b)$$

$$\mathbf{M}_{\Psi,P} \Psi_P^{n+1} + \frac{\Delta t}{ReSc} \mathbf{K}_{\Psi,P} \Psi_P^{n+1} = \Delta t \mathbf{M}_{\Psi,P} \Psi_{d,P}^n, \quad (5.21c)$$

with  $\mathbf{b}^n = \lambda Eu_\beta \mathbf{e}_P$ .

Following by analogy to Equation (4.35), eqs. (5.21a - 5.21c) can be written as

$$\left\{ \begin{array}{l} \mathbf{B}_P \mathbf{v}_P^{n+1} + \Delta t \mathbf{G}_P \tilde{\mathbf{p}}^{n+1} = \mathbf{b}_{1,P} \\ \mathbf{D}_P \mathbf{v}_P^{n+1} = \mathbf{b}_{2,P} \\ \mathbf{B}_{\Psi,P} \Psi_P^{n+1} = \mathbf{b}_{3,P}, \end{array} \right. \quad (5.22)$$

for each r.h.s. vector given by  $\mathbf{b}_{i,P}$ ,  $i = 1, 2, 3$ .

Although it is possible to develop a formal essay of the periodic variational formulation – as expressed by Equation (5.22) –, the PBC can be enforced in a more pragmatic manner by spanning directly the nonperiodic operators in the matrices already assembled during the original formulation. The incorporation of the DOFs belonging to the periodic nodes is reached through a pseudounion of the shape functions of the 1-ring neighbour elements of  $\Gamma_L, \Gamma_R$ , which is given by changing the interelement connections in the global matrices. Explanation in details about this procedure is given in [191].

### 5.4.2 Computational implementation

Approaches to implement PBC may fall into a strategy of full reordering of the matrix system by reassembling process. On the other hand, this step may also involve laborious modifications in a large computational code, since all the matrices and vectors would have to be rearranged. Instead performing reassembling operations, it is advisable to pave the entire PBC problem yet during the assembling stage. Segal *et al.* [193] suggest that the global system is previously mounted under PBC restrictions. Nonino and Comini [192] also have worked with similar strategies. This track ends on a system like Equation (5.22). Alternatively, to circumvent this painstaking task of reassembling, we have chosen to take a shortcut to eliminate the DOFs corresponding to the slave periodic boundary. The proposed algorithm runs through the original matrix system by localizing the indices of the connection elements and modifies the elementary submatrices directly, thus avoiding additional memory allocation. A slightly different strategy based on the manipulation of lists is explained, for instance, in [196].

During the elimination process, consider  $(i, j)$  an arbitrary pair of indices identifying the nodes over the periodic boundaries  $\Gamma_L$  and  $\Gamma_R$ , respectively;  $ibL$  a particular index for each node over  $\Gamma_L$  and  $ibR$  a particular index for each node over  $\Gamma_R$ . Let us consider, for  $m = 0, 1, 2$ ,

$$\mathcal{A}(i, j; m)[\cdot] = \begin{array}{c} \begin{array}{cccccccc} & ibL & & ibR & & ibL_N & & ibR_N \\ \begin{array}{c} \ddots \\ \vdots \\ \vdots \\ \vdots \\ \vdots \\ \vdots \\ \vdots \\ \vdots \end{array} & \left| \begin{array}{c} \vdots \\ b_{(i+mv, i+mv)} \\ \vdots \\ 0 \\ \vdots \\ \star \\ \vdots \\ 0 \end{array} \right. & \begin{array}{c} \vdots \\ \vdots \\ \vdots \\ \vdots \\ \vdots \\ \vdots \\ \vdots \\ \vdots \end{array} & \left| \begin{array}{c} \vdots \\ 0 \\ b_{(j+mv, j+mv)} \\ \vdots \\ 0 \\ \bullet \\ \vdots \\ \diamond \end{array} \right. & \begin{array}{c} \vdots \\ \vdots \\ \vdots \\ \vdots \\ \vdots \\ \vdots \\ \vdots \\ \vdots \end{array} & \left| \begin{array}{c} \vdots \\ \vdots \\ \vdots \\ \vdots \\ \vdots \\ \vdots \\ \vdots \\ \vdots \end{array} \right. & \begin{array}{c} \vdots \\ \vdots \\ \vdots \\ \vdots \\ \vdots \\ \vdots \\ \vdots \\ \vdots \end{array} & \left| \begin{array}{c} \vdots \\ 0 \\ \bullet \\ \vdots \\ 0 \\ \vdots \\ \vdots \\ \vdots \end{array} \right. & \begin{array}{c} \vdots \\ \vdots \\ \vdots \\ \vdots \\ \vdots \\ \vdots \\ \vdots \\ \vdots \end{array} \\ & & & & & & & & \end{array} \\ & & & & & & & & \end{array} \begin{array}{l} \\ ibL \\ \\ ibR \\ \\ ibL_N \\ \\ ibR_N \\ \end{array} \end{array} \quad (5.23)$$

a symmetric submatrix-model for the original formulation containing the Neumann in-



terelement contributions according to the FE discretization for the pair  $(ibL, ibR)$ . Above,  $ibL_N, ibR_N$  mark rows (columns) relative to an arbitrary node which is connected to the periodic pair and the symbols at the crossed entries represent nonzero contributions. Hence, this matrix is a substratum of what each global matrix contains on the rows (columns) for the respective dimension. That is, if  $m = 0$ , the matrix is relative to a one-dimensional discretization; if  $m = 1$ , two blocks like the one above should be modified; if  $m = 2$ , the discretization is three-dimensional.

For each pair  $(i, j)$ , with  $i = ibL, ibR, j = ibL, ibR; i, j = 1, \dots, \iota$ , found after algorithmic search,  $\mathcal{A}[\cdot]$  will be modified directly inside the matrices  $\mathbf{B}, \mathbf{D}, \mathbf{G}, \tilde{\mathbf{E}}$  from eqs. (4.25 - 4.27), and  $\mathbf{B}_\Psi$  from Equation (4.33) respecting their dimensions to obtain the periodic counterparts  $\mathbf{B}_P, \mathbf{D}_P, \mathbf{G}_P, \tilde{\mathbf{E}}_P$ , and  $\mathbf{B}_{\Psi,P}$ . Note that  $\tilde{\mathbf{E}}_P$  results of the LU-factorization for the periodic problem by analogy. Besides, since  $\mathbf{D}$  and  $\mathbf{G}$  are nonsquare matrices,  $\mathcal{A}[\cdot]$  must be adapted to be dimensionally consistent. For three-dimensional problems, it turns out that

$$\dim(\mathbf{B}) = \dim(\mathbf{B}_P) = 3\iota_v \times 3\iota_v \quad (5.24a)$$

$$\dim(\mathbf{D}) = \dim(\mathbf{D}_P) = \iota_s \times 3\iota_v \quad (5.24b)$$

$$\dim(\mathbf{G}) = \dim(\mathbf{G}_P) = 3\iota_v \times \iota_s \quad (5.24c)$$

$$\dim(\tilde{\mathbf{E}}) = \dim(\tilde{\mathbf{E}}_P) = \iota_s \times \iota_s \quad (5.24d)$$

$$\dim(\mathbf{B}_\Psi) = \dim(\mathbf{B}_{\Psi,P}) = \iota_s \times \iota_s, \quad (5.24e)$$

so that  $v = \iota_v$  controls the number of DOFs of the velocity field by component, while  $v = \iota_s$  controls the number of DOFs of the pressure and scalar fields.

Thenceforth, the original matrices acquire their periodic version by

- i) summing the row of  $\mathcal{A}[\cdot]$  relative to the periodic node  $ibL$  to the respective row relative to the periodic node  $ibR$ ,
- ii) summing the column of  $\mathcal{A}[\cdot]$  relative to the periodic node  $ibL$  to the respective column relative to the periodic node  $ibR$ ,
- iii) zeroing the row  $ibL$ ,
- iv) zeroing the column  $ibR$  and, finally
- v) adding “1” at the diagonal entries  $(ibL, ibL)$  to avoid indetermination.

This process results in

$$\mathcal{A}_P(i, j; m)[\cdot] = \begin{array}{cccccccc} & \textit{ibL} & & \textit{ibR} & & \textit{ibL}_N & & \textit{ibR}_N \\ \left[ \begin{array}{cccccccc} \ddots & | & \vdots & | & \vdots & | & \vdots & | & \vdots \\ \text{---} & 1 & \text{---} & 0 & \text{---} & 0 & \text{---} & 0 & \text{---} \\ \vdots & | & \ddots & | & \vdots & | & \vdots & | & \vdots \\ \text{---} & 0 & \text{---} & \Sigma_P(i, j; m) & \text{---} & \star & \text{---} & \bullet & \text{---} \\ \vdots & | & \vdots & | & \ddots & | & \vdots & | & \vdots \\ \text{---} & 0 & \text{---} & \star & \text{---} & \Delta & \text{---} & 0 & \text{---} \\ \vdots & | & \vdots & | & \vdots & | & \ddots & | & \vdots \\ \text{---} & 0 & \text{---} & \bullet & \text{---} & 0 & \text{---} & \diamond & \text{---} \\ \vdots & | & \vdots & | & \vdots & | & \vdots & | & \ddots \end{array} \right] & \begin{array}{l} \textit{ibL} \\ \textit{ibR} \\ \textit{ibL}_N \\ \textit{ibR}_N \end{array} \end{array} \quad (5.25)$$

with

$$\Sigma_P(i, j; m) = \mathbf{b}_{(i+mv, i+mv)} + \mathbf{b}_{(j+mv, j+mv)}, \quad i, j = \textit{ibL}, \textit{ibR}; \quad m = 0, 1, 2. \quad (5.26)$$

Accordingly, let

$$\mathcal{U}(i, j; m)[\cdot] = \begin{array}{cccc} \left[ \begin{array}{c} \vdots \\ \mathbf{c}_{(i+mv)} \\ | \\ \mathbf{c}_{(j+mv)} \\ \vdots \\ \square \\ | \\ * \\ \vdots \end{array} \right] & \begin{array}{l} \textit{ibL} \\ \textit{ibR} \\ \textit{ibL}_N \\ \textit{ibR}_N \end{array} & m = 0, 1, 2, & (5.27) \end{array}$$

be a model for the elementary vectors of contribution.  $\mathcal{U}[\cdot]$  will be modified directly inside the vectors  $\tilde{\mathbf{b}}_1, \tilde{\mathbf{b}}_2$  from Equations (4.25) and (4.26), and  $\mathbf{b}_\Psi = \mathbf{r}_\Psi^N + \mathbf{b}\mathbf{c}_\Psi$  from Equation (4.33) respecting their dimensions to obtain the periodic counterparts  $\mathbf{b}_{1,P}, \mathbf{b}_{2,P}$ , and  $\mathbf{b}_{3,P}$  as referred

in Equation (5.22) resulting in

$$\mathcal{U}(i, j; m)[\cdot] = \begin{bmatrix} \vdots \\ 0 \\ | \\ \Sigma_P(i, j; m) \\ \vdots \\ \square \\ | \\ * \\ \vdots \end{bmatrix} \begin{matrix} ibL \\ \\ ibR \\ \\ ibL_N \\ \\ ibR_N \end{matrix} \quad m = 0, 1, 2, \quad (5.28)$$

with, this time,

$$\Sigma_P(i, j; m) = c_{(i+mv)} + c_{(j+mv)}, \quad i, j = ibL, ibR; \quad m = 0, 1, 2, \quad (5.29)$$

and the zeroed component  $ibL$  as opposed to the model-matrix  $\mathcal{U}[\cdot]$ .

The general algorithm of elimination of DOFs for the matrices and vectors of Equation (4.36) according to the previous models reads, for each time step  $t$ , as:

```

for  $t : (0, T]$  do
  for  $i : [1, t]$  do
    for  $m : \{0, 1, 2\}$  do
       $ibL = \mathbf{i}_L(i);$  /*  $\mathbf{i}_L$ : vector of indices  $ibL$  */
       $ibR = \mathbf{i}_R(i);$  /*  $\mathbf{i}_R$ : vector of indices  $ibR$  */
       $\mathcal{A}^t(ibL, \cdot) \leftarrow \mathcal{A}^t(ibL, \cdot) + \mathcal{A}^t(ibR, \cdot);$  /* summing rows */
       $\mathcal{A}^t(\cdot, ibL) \leftarrow \mathcal{A}^t(\cdot, ibL) + \mathcal{A}^t(\cdot, ibR);$  /* summing columns */
       $\mathcal{A}^t(ibR, \cdot) = 0;$  /* zeroing row  $ibR$  */
       $\mathcal{A}^t(\cdot, ibR) = 0;$  /* zeroing column  $ibR$  */
      if  $\mathcal{A}[\cdot] \doteq \mathbf{B}, \tilde{\mathbf{E}}, \mathbf{B}_\Psi$  then
         $\mathcal{A}^t(ibL + mv, ibL + mv) = 1;$  /* filling diagonals */
      end
      if  $\mathcal{U}[\cdot] \doteq \tilde{\mathbf{b}}_1, \tilde{\mathbf{b}}_2, \mathbf{b}_\Psi, (\mathbf{v}, \tilde{\mathbf{p}}, \Psi)$  then
         $\mathcal{U}^t(ibR + mv) = \mathcal{U}^t(ibL + mv);$  /* imposing periodicity */
      end
       $t \leftarrow t + \Delta t$ 
    end
  end
end

```

Observe, however, that  $(\mathbf{v}, \tilde{\mathbf{p}}, \Psi)$  must turn into  $(\mathbf{v}_P, \tilde{\mathbf{p}}, \Psi_P)$  each time step to update the periodic solution of Equation (5.22). This is achieved applying the copying process provided by  $\mathcal{U}$  over these vectors. Besides, for three-dimensional problems, it turns out that

$$\dim(\tilde{\mathbf{b}}_1) = \dim(\mathbf{b}_{1,P}) = 3\iota_v \times 1 \quad (5.30a)$$

$$\dim(\tilde{\mathbf{b}}_2) = \dim(\mathbf{b}_{2,P}) = \iota_s \times 1 \quad (5.30b)$$

$$\mathbf{b}_\Psi = \dim(\mathbf{b}_{3,P}) = \iota_s \times 1 \quad (5.30c)$$

$$\dim(\mathbf{v}) = \dim(\mathbf{v}_P) = 3\iota_v \times 1 \quad (5.30d)$$

$$\dim(\mathbf{p}) = \dim(\tilde{\mathbf{p}}) = \iota_s \times 1 \quad (5.30e)$$

$$\dim(\Psi) = \dim(\Psi_P) = \iota_s \times 1 \quad (5.30f)$$

$$(5.30g)$$

so that, as aforementioned,  $v = \iota_v$  controls the number of DOFs of the velocity field by

component, while  $v = \iota_s$  controls the number of DOFs of the pressure, periodic pressure and scalar fields.

The overloaded equations due to the periodic modification can be better viewed if we write the symbolic equation of the arguments  $(\mathbf{B}_P, \mathbf{v}_P, \mathbf{b}_{1,P})$

$$\mathcal{A}_P(ibL, ibR; 0)[\mathbf{B}_P] \mathcal{U}_P(ibL, ibR; 0)[\mathbf{v}_P] = \mathcal{U}_P(ibL, ibR; 0)[\mathbf{b}_{1,P}], \quad (5.31)$$

the equations for the periodic pair  $(ibL, ibR)$  relative to the  $x$ -component of the velocity field can be extracted:

$$ibL: [1] \times [0] = [0] \quad (5.32)$$

$$ibR: [\mathbf{B}_{(ibL, ibL); P, x} + \mathbf{B}_{(ibR, ibR); P, x}] \times [\mathbf{v}_{ibL; P, x} + \mathbf{v}_{ibR; P, x}] + [\star_x] \times [\square_x] + [\bullet_x] \times [*_x] \quad (5.33)$$

$$(5.34)$$

showing, *de facto*, the gist of the elimination process. The first equation is left out from the computational effort; the second equation, hence, is overloaded, being interpreted as the sum of two parcels: *overload + extra contribution*. Furthermore, in terms of matrices, the previous arguments are embedded into a much bigger system formed by the parts

$$\mathbf{B}_P = \begin{bmatrix} \mathbf{B}_{P,x} & & \\ & \mathbf{B}_{P,y} & \\ & & \mathbf{B}_{P,z} \end{bmatrix}; \quad \mathbf{v}_P = \begin{bmatrix} \mathbf{v}_{P,x} \\ \mathbf{v}_{P,y} \\ \mathbf{v}_{P,z} \end{bmatrix}; \quad \mathbf{b}_{1,P} = \begin{bmatrix} \mathbf{b}_{1,P,x} \\ \mathbf{b}_{1,P,y} \\ \mathbf{b}_{1,P,z} \end{bmatrix} \quad (5.35)$$

The same ideas apply to the other matrices, submatrices, vectors and subvectors making up the system in Equation (5.22).

#### 5.4.3 Repair of the backward-in-time Semi-Lagrangian search

When the approximation of the advective term through the SL method is applied to the nodes near and over the master boundary, the backward-in-time search of the departure points of the particle trajectories may “leak” outward the periodic cell for a higher CFL number. Although the usual manner to correct this deviation is to push them back to the boundary in order to be interpolated, this event has to be repaired by compensating the distance among two correspondent periodic nodes when PBC are implemented.

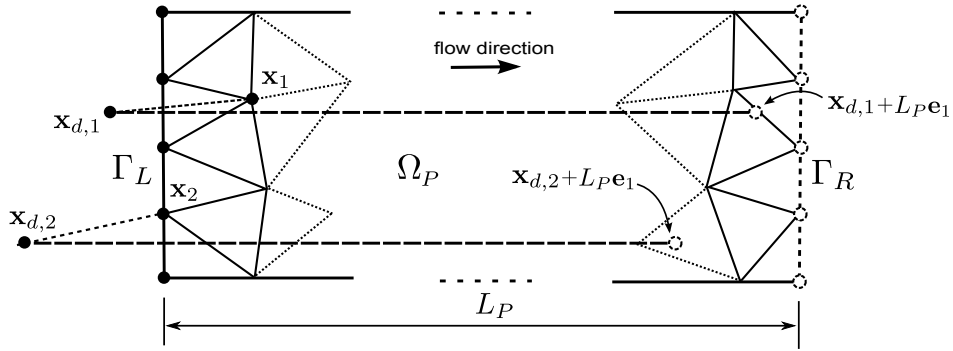


Figure 31: Displacement of the “leaked” departure points to correct the Semi-Lagrangian backward-in-time search in a periodic domain.

Considering that we only deal with parallel boundaries here, this computation is done simply by adding once the length of the domain to the points whose streamwise coordinate value falls outside the domain limits. Through this mechanism, the escaped points along the time are rebounded to the opposite side, thus entering back into the domain. Potential flaws of interelement discontinuities are removed with such repair so that the correctness of the advective interpolation as well as the cyclic behaviour of the simulation are ensured. A two-dimensional schematic representation of this repair is depicted in Figure 31 for  $\mathbf{e}_p = \mathbf{e}_1$ . The condition for the departure points is given by the code snippet below concerning the streamwise  $x$ -direction. Points  $\mathbf{x}_j$  are advected backward-in-time to the departure points  $\mathbf{x}_{j,d}$ , which are displaced toward the flow direction to the points  $\mathbf{x}_{j,d} + L_P \mathbf{e}_1$ .

```

for  $\mathbf{x}_j \in \mathcal{T}_h$  do
  Finds  $\mathbf{x}_{j,d}$ 
  if  $\mathbf{x}_{j,d} \cdot \mathbf{e}_1 < \min\{\mathbf{x}_{j,d} \cdot \mathbf{e}_1\}$  then
    |  $\mathbf{x}_{j,d} \cdot \mathbf{e}_1 \leftarrow \mathbf{x}_{j,d} \cdot \mathbf{e}_1 + L_P$ 
  end
end

```

## 6 CODE VALIDATION

### 6.1 Taylor vortex in highly viscous fluid

#### 6.1.1 Spatial validation of PBC

A single-phase flow manufactured test to verify the spatial DOFs copying process over the periodic boundaries is presented in this section. The domain is a simple cuboid of dimensions  $1.5L_{ref} \times L_{ref} \times 0.2L_{ref}$ , where  $L_{ref}$  is the width as depicted in Figure 32. A Taylor

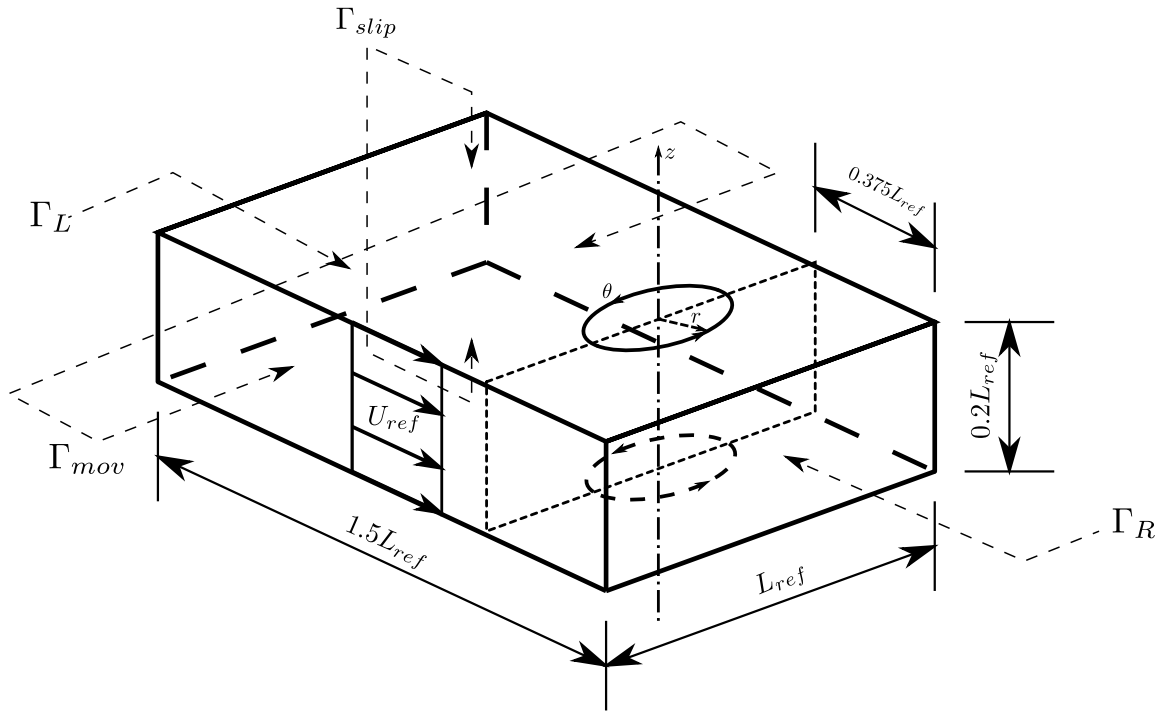


Figure 32: Periodic domain of simulation for a Taylor vortex carried away in a high viscous fluid flow.

vortex, which is an analytical solution of the Navier-Stokes equations [197], is placed over the domain as initial condition to evaluate the numerical error produced by addition of the PBC in the computational code. The vortex's velocity profile is written in dimensionless cylindrical coordinates as

$$v_r(t) = 0 \quad (6.1a)$$

$$v_\theta(t) = \varpi r \exp\left(-\frac{r^2}{4r_c Re^{-1}} t\right) \quad (6.1b)$$

$$v_z(t) = 0 \quad (6.1c)$$

Parameter	Value
$r_c$	$L_{ref}/30$
$U_{ref}$	1
$\varpi$	1
$Re$	35
$Sc$	650
$\Delta t$	0.1

Table 2: Physical parameters of the Taylor vortex flow.

and transformed to Cartesian coordinates as

$$v_x(t) = U_{ref} - v_\theta(t) \sin(\theta) \quad (6.2a)$$

$$v_y(t) = v_\theta(t) \cos(\theta) \quad (6.2b)$$

$$v_z(t) = 0 \quad (6.2c)$$

to work as input data. Above,  $\varpi$  is the circulation,  $r_c$  is the vortex's core radius in the  $v_\theta$ -profile, and  $U_{ref}$  is an increment of tangential velocity added to push the vortex downstream. Once the transient parcel of the tangential velocity decays rapidly with time, the time step  $\Delta t$  as well as the fluid flow properties were selected to produce a qualitative analysis of the vortex's hydrodynamics during this short period of unsteadiness as listed in Table 2.

Besides the enforcement of the PBC for velocity and pressure already expounded in Equations (5.11 - 5.14) over  $\Gamma_L$  and  $\Gamma_R$ , the additional boundary conditions for this test are slip ( $\Gamma_{slip}$ ) for the top and bottom surfaces and of moving walls ( $\Gamma_{mov}$ ) for the lateral surfaces as follows:

$$\mathbf{v} \cdot \mathbf{t} = U_{ref}; \quad \mathbf{v} \cdot \mathbf{b} = \mathbf{v} \cdot \mathbf{n} = 0, \quad \text{at } \Gamma_{mov} \quad (6.3a)$$

$$\mathbf{v} \cdot \mathbf{n} = 0, \quad \text{at } \Gamma_{slip} \quad (6.3b)$$

Observe that  $\mathbf{n}$  points outward the domain's walls and  $\mathbf{b}$  is the binormal vector per wall. To anticipate the periodic passage of the vortex through the walls  $\Gamma_L$  and  $\Gamma_R$ , its center is shifted from the domain's center toward this side.

The relative error of velocity measured in the  $\mathcal{L}^2$ -norm for this test is plotted in Figure



33 and computed as

$$\mathbf{e}_{rel} = \left\{ \int_{\Omega} \frac{(\mathbf{v} - \mathbf{v}_h)^2}{\mathbf{v}_h^2} \right\}^{\frac{1}{2}} \quad (6.4)$$

The error curve limited by  $\mathcal{O}(10^{-3})$  decreases monotonically until getting a minimum. Due to the fast vortex's dissipation observed, the analysis was performed in the range  $0 \leq t < 2.8$ .

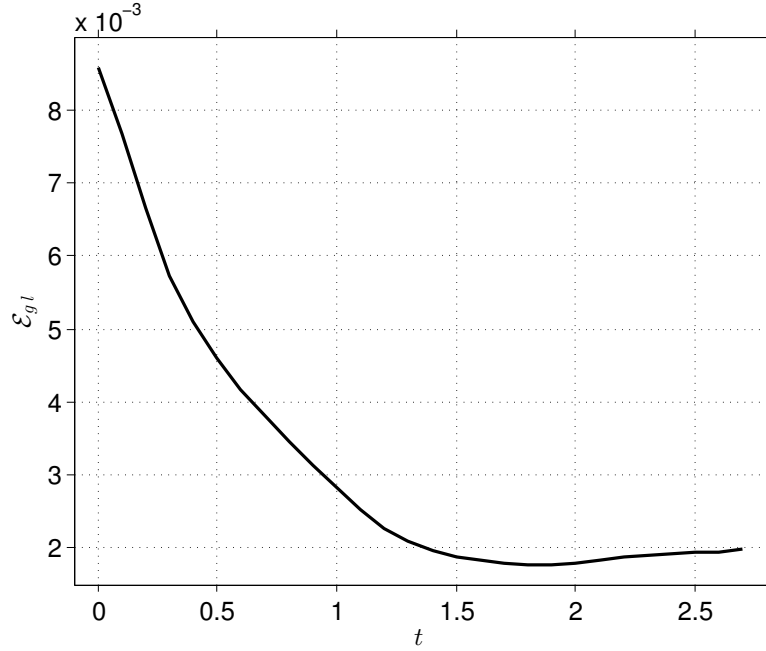
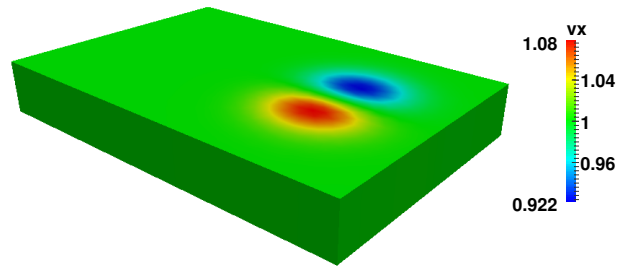


Figure 33: Relative error in  $\mathcal{L}^2$ -norm of the velocity profile for the Taylor vortex flow.

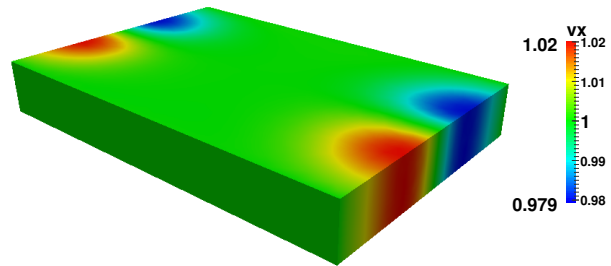
### 6.1.2 Scalar transport with PBC

In addition to the hypothetical viscous fluid being simulated, the Gaussian profile of a scalar quantity described in Equation (6.5) was also distributed initially throughout the domain to verify the compatibility of PBC for cases of a passive scalar transportation with  $Sc \approx 650.0$ . Such conditions can, for instance, describe the spreading of contaminants through sludge flows - provided that the hypothesis of Newtonian fluid is valid -, dissolved salts in industrial mixing as well as represent the advection of low diffusivity chemical agents interspersed in highly viscous liquids.

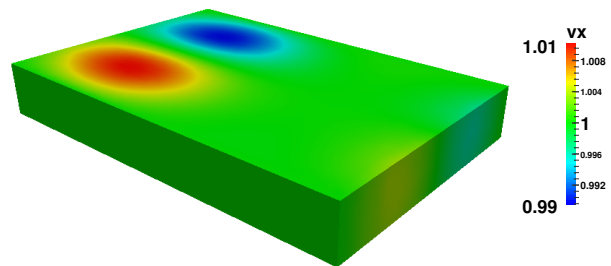
$$\phi(\mathbf{x}) = a \exp \left[ -\frac{(\mathbf{x} \cdot \mathbf{e}_2 - \mathbf{x}_m)^2}{2b^2} \right] \cos(\mathbf{x} \cdot \mathbf{e}_1), \quad b = \frac{1}{2\pi} \quad (6.5)$$



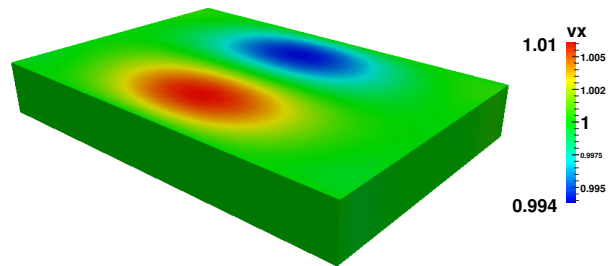
(a)



(b)

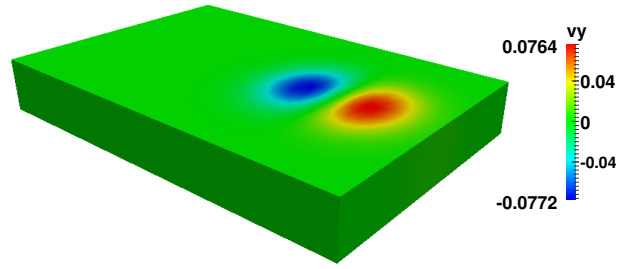


(c)

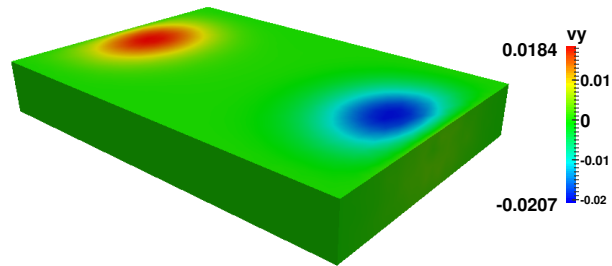


(d)

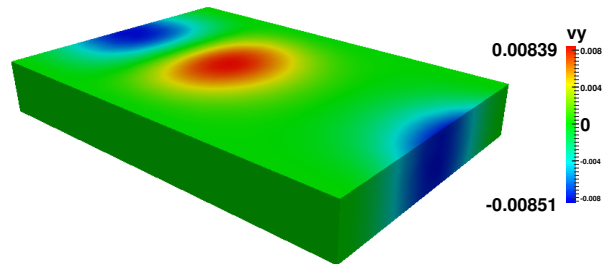
Figure 34: Taylor vortex's velocity profile  $v_x$  : (a)  $t = 0.0$ ; (b)  $t \approx 0.4$ ; (c)  $t \approx 0.8$ ; (d)  $t \approx 1.2$ .



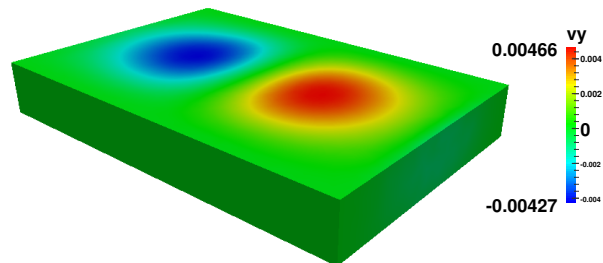
(a)



(b)



(c)



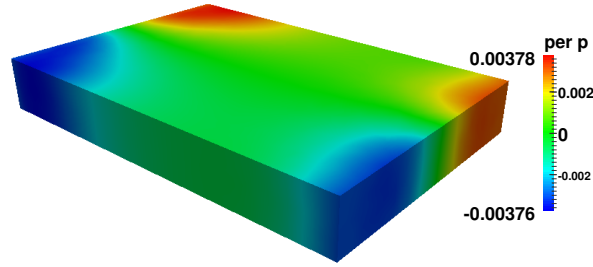
(d)

Figure 35: Taylor vortex's velocity profile  $v_y$ : (a)  $t = 0.0$ ; (b)  $t \approx 0.4$ ; (c)  $t \approx 0.8$ ; (d)  $t \approx 1.2$ .

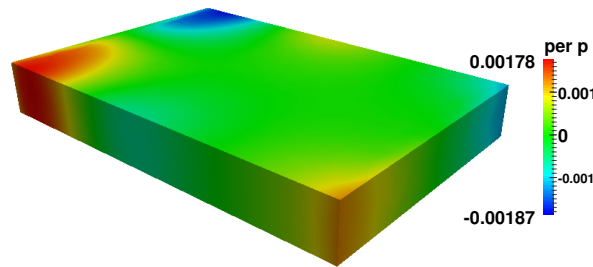
where  $\mathbf{x}_m$  is a point on the central plane parallel to the flow and the peak  $a = 0.8$ . Consequently, the periodic boundary condition

$$\phi|_{\Gamma_L} = \phi|_{\Gamma_R} \quad (6.6)$$

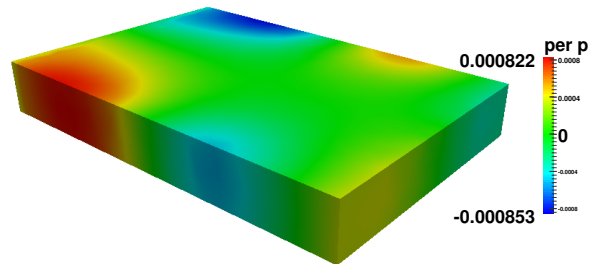
must accompany the Equations (6.3a) and (6.3b). Some pictures of the vortex's streamwise



(a)



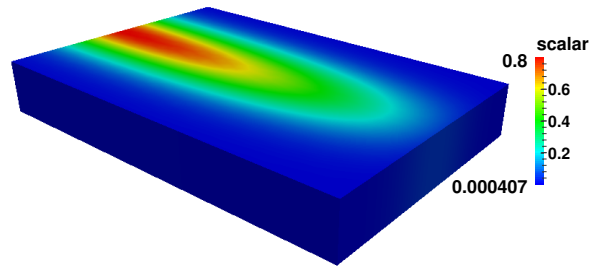
(b)



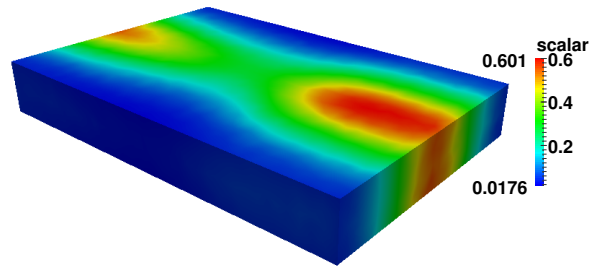
(c)

Figure 36: Taylor vortex's periodic pressure profile  $\tilde{p}$ : (a)  $t \approx 0.4$ ; (b)  $t \approx 0.8$ ; (c)  $t \approx 1.2$ .

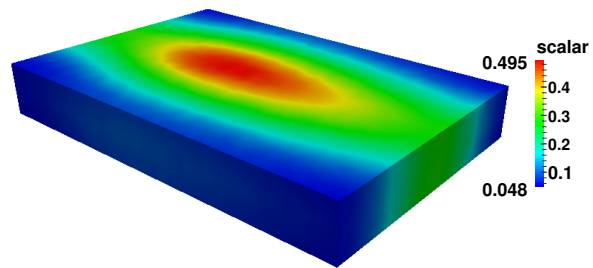
and transverse velocity profiles, periodic pressure field, and scalar field are depicted in Figure 34 and Figure 37 for three time instants, besides the initial condition. As seen, the continuity of the profiles, before, during, and after crossing the periodic walls show the validity of the



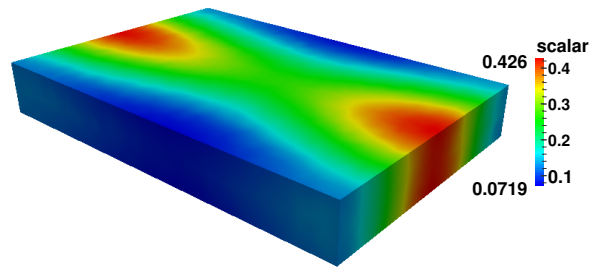
(a)



(b)



(c)



(d)

Figure 37: Scalar  $\phi$  being carried by the fluid flow: (a)  $t = 0.0$ ; (b)  $t \approx 1.1$ ; (c)  $t \approx 2.0$ ; (d)  $t \approx 2.9$ .

copying process embedded in the algorithm. In Figure 36, since the periodic pressure field is zero at the initial instant, the picture was suppressed of the roster. On the other hand, as depicted in Figure 37, the prolonged diffusion of the scalar field allows its observation a little further beyond from the state saturated achieved more rapidly by the velocity.

## 6.2 Air bubble plume rising in quiescent water

### 6.2.1 Periodic array of in-line rising bubbles

Let  $\Omega \subset \mathbb{R}^3$  be the domain depicted in Figure 38 and  $\Gamma$  its boundary defined as  $\Omega = \Omega^1 \cup \Omega^2$  and  $\Gamma = \Gamma^1 \cup \Gamma^2$ , with  $\Gamma^2 = \Gamma^\infty \cup \Gamma^P$ , where the subscripts 1,2 indicate, respectively, the dispersed phase and continuous phase of the flow,  $\Gamma^\infty$  the Dirichlet portion of  $\Gamma^2$ , and  $\Gamma^P$  its supplementary periodic portion. Here,  $\Gamma^\infty$  is placed far from the bubble plume to account for the bulk liquid region where the local interactions are mitigated. This boundary receives a moving wall condition to ensure the well-known MFR technique (cf. Section 7.2), while the PBC are assigned to  $\Gamma^P = \Gamma^T \cup \Gamma^B$ . The surfaces  $\Gamma^T$  and  $\Gamma^B$  satisfy  $\Gamma^T \equiv \mathbf{x} + L\mathbf{e}$ ,  $\forall \mathbf{x} \in \Gamma^B$  for a unit vector  $\mathbf{e}$  as depicted by the element patches in light gray, *i.e.* the upper boundary  $\Gamma^T$  is topologically equivalent to  $\Gamma^B$  by a displacement  $L$ . The extended plume model consists of an arrangement containing spherical bubbles of diameter  $D_b$  equally spaced from above and below (relative to the poles) by a gap length  $s = D_b$  and immersed into a cylinder of diameter  $D \gg D_b$ , whereas the periodic cell considers a slice of this configuration. To take into account the effect of the periodic boundaries on the bubble wake region as well as minimize the effects of the lateral wall, we set  $L = s + D_b$  and  $D = 10D_b$  for the cell's period and diameter, respectively.

### 6.2.2 Mathematical model

A detailed test for the case of an air bubble rising in an aqueous sugar solution considering PBC and the upward force caused by the pressure gradient  $Eu_\beta$  (cf. Section 5.3) was used to check the mathematical model and compared to recently published results [153]. For the bubble plume, the equations valid for both phases separately, are written in the differential

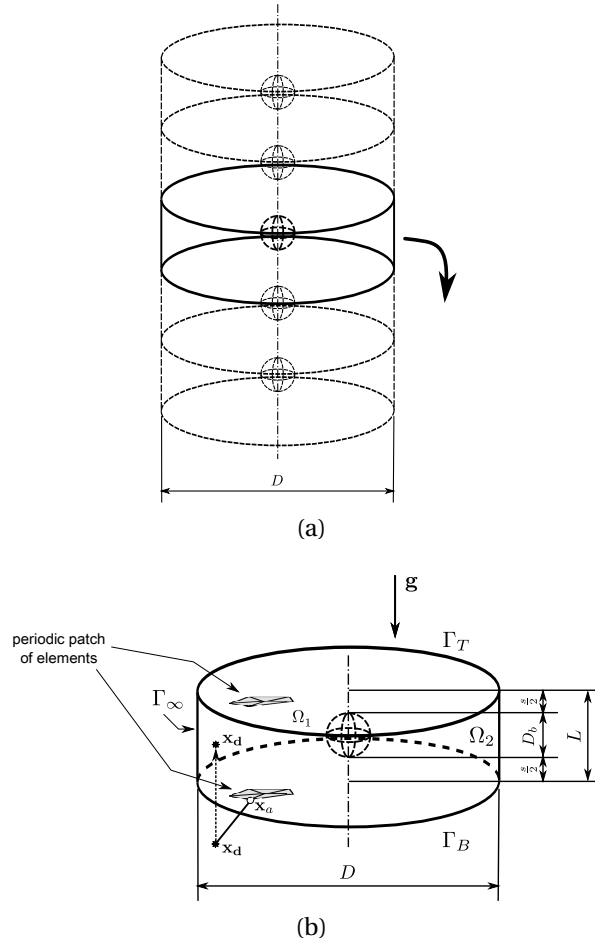


Figure 38: Arrangement of the unconfined in-line bubble plume: (a) extended plume model; (b) detail of the periodic cell.

form as

$$\rho \left( \frac{\partial \mathbf{u}}{\partial t} + (\mathbf{u} - \hat{\mathbf{u}}) \cdot \nabla \mathbf{u} \right) = \lambda E u_{\beta} \mathbf{e} - \nabla \tilde{p} + \frac{1}{Ar^{1/2}} \nabla \cdot [\mu (\nabla \mathbf{u} + \nabla \mathbf{u}^T)] + \rho \mathbf{g} + \frac{1}{Eo} \mathbf{f} \quad (6.7a)$$

$$\nabla \cdot \mathbf{u} = 0, \quad \text{in } \Omega \times t, \quad (6.7b)$$

with the dimensionless parameters  $Ar$  and  $Eo$ , *viz.* the Archimedes and Eötvös numbers, respectively, defined by means of

$$Ar = \frac{g_{ref} D_{ref}^3 \rho_{ref}}{\mu_{ref}^2} \quad Eo = \frac{\rho_{ref} g_{ref} D_{ref}^2}{\sigma_{ref}}, \quad (6.8)$$

take the place of the  $Re$  and  $We$  number in Equation (3.40). In this case,  $D_{ref} = D_b$ ,  $\rho_{ref} = \rho^2$ ,  $\mu_{ref} = \mu^2$ . Moreover, for this analysis, a convenient way to obtain the dimensionless pressure gradient it is to divide Equation (5.5) by  $\rho_{ref} g_{ref} D_{ref}$  and scale the reference velocity

by  $\sqrt{g_{ref}D_{ref}}$ . Thenceforth,

$$p^* = - \left( \frac{\beta_{ref}}{\rho^2 g_{ref}} \right) \left( \frac{L_P}{D_b} \right) (\mathbf{x}^* \cdot \mathbf{e}^*) + \tilde{p}^* \quad (6.9)$$

gives the dimensionless form (the asterisk was dropped out)

$$p = -\lambda Eu_\beta (\mathbf{x} \cdot \mathbf{e}) + \tilde{p}, \quad (6.10)$$

with

$$Eu_\beta = \frac{\beta_0}{\rho^2 g_{ref}}, \lambda = \frac{L_P}{D_b}. \quad (6.11)$$

Since  $\rho_{ref}$  is taken to be the liquid density  $\rho^2$ ,  $Eu_\beta$  can be interpreted this time as the ratio of the upward body force to the gravitational force, which acts to balance the liquid mass contained in the periodic cell. Consequently, at steady state,  $Eu_\beta \approx \mathcal{O}(\rho^2 \mathbf{g} \cdot \mathbf{e}) \approx 1$ .

### 6.2.3 Mesh generation and adaptive refinement

For this study, the periodic mesh was constructed to enable the refinement control at specified regions of the domain and improve the analysis of the flow, since local interactions occurring near the bubble plume can be captured. Adaptive refinement strategies for the array

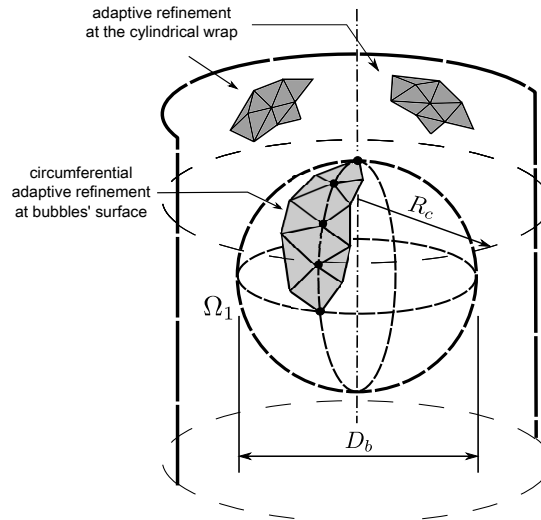


Figure 39: Augmented view of mesh displaying adaptive refinement strategies: circumferential, at the bubble's surface; azimuthal, at the cylindrical wrap region of radius  $R_c$  surrounding it.

of Figure 38 were developed to operate on the bubble's surface as well as over the fluid portion



wrapped by a cylindrical “envelope” of radius  $R_c$  surrounding the bubble, as illustrated in Figure 39. Such strategies afford not only the generation of finer surface meshes that distribute nodes circumferentially on the spherical shells, but also the achievement of smaller elements in the neighbourhood of the plume that produce good aspect ratios.

A view in perspective as well as a top-view of the unstructured mesh used for the bubble plume simulation are displayed, respectively, in Figure 40 and Figure 41 at a particular time instant so as to highlight the higher density of points around the center produced by the adaptive refinement.

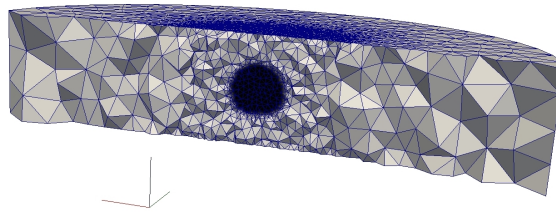


Figure 40: Computational mesh highlighting the bubble region: cut plane parallel to the axis of rising of the plume.

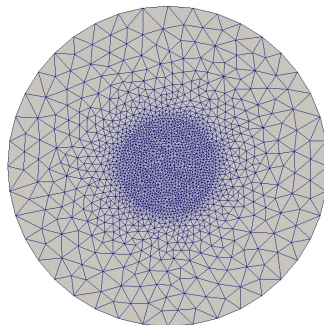


Figure 41: Computational mesh highlighting the adaptive refinement provided by the cylindrical wrap: top-view.

#### 6.2.4 Validation tests

Figure 42 is a plot of the bubble’s center of mass velocity  $u_{bc}(t)$  versus time for three different simulations regarding physics and boundary conditions described as follows: test R1 - rising bubble with no-slip wall conditions everywhere under gravity only (closed boundaries); test R2 - rising bubble with lateral no-slip wall conditions, open boundary conditions at the top/bottom walls under gravity and upward body force; test R3 - rising bubble with lateral moving wall conditions, PBC at the top/bottom walls under gravity and upward body force. Test R1 is discussed in [153] for a parallelepipedal domain and good accordance is attained

Data					
$\mu^1, \mu^2$	$\rho^1, \rho^2$	$\sigma$	$D_b$	$Ar$	$Eu$
1.78e-5, 0.54	1.22, 1350	7.8e-2	2.61e-2	1092	116

Table 3: Physical property values for the numerical simulations: tests R1-R3.

here for a long cylindrical mesh; test R2 was performed to evaluate the balance between the gravity and pressure gradient forces inside the artificial array; test R3, in turn, was carried out to validate the complete PBC formulation coupled with the balance of forces. All of the three tests were carried out over the same computational mesh, whose radius/height are, respectively,  $4D_b/10D_b$ , and the physical property values for them are listed in SI units in Table 3. The time step computation depends on the mesh parameters as well as the other variables related to the ALE model, being updated each iteration (cf. Sec. 5.1 of [153]). For the current tests, an average time step  $\Delta t \approx 0.003$  was determined.

As seen from the  $u_{bc}$  profiles in Figure 42, the tests are in mutual agreement, except for a slight profile discordance over the plateau of terminal velocity for the cases R2 and R3. To measure these deviations in relation to R1, the mean percentage difference within the time of simulation  $[0, t_{max}]$  given by

$$\mathcal{E}_{Rj,R1} = \frac{100\%}{t_{max}} \left( \frac{v_{bc,j}(t) - v_{bc,1}(t)}{v_{bc,1}(t)} \right), \quad j = 2, 3, \text{ with}$$

$$v_{bc,i}(t) = \int_0^{t_{max}} u_{bc,i}(t) dt, \quad i = 1, 2, 3, \quad (6.12)$$

was computed to be  $\mathcal{E}_{R2,R1} = 3.97\%$  and  $\mathcal{E}_{R3,R1} = 3.51\%$ , thus reporting acceptable difference ranges for both cases, being the smallest one reported for the PBC/MFR formulation proposed.

The deviations of R2 and R3 in relation to R1 is due to differences in the problem setups, including effects coming from the boundary conditions and the splitting process used to calculate the velocity field - as explained in Subsection 3.2.1. The tests were sensitive to the time step size chosen, since the addition of the pressure gradient  $Eu_\lambda$  introduced a numerical error of  $\mathcal{O}(\Delta t)$  caused by the imbalance between gravity forces and pressure forces produced by the splitting process.

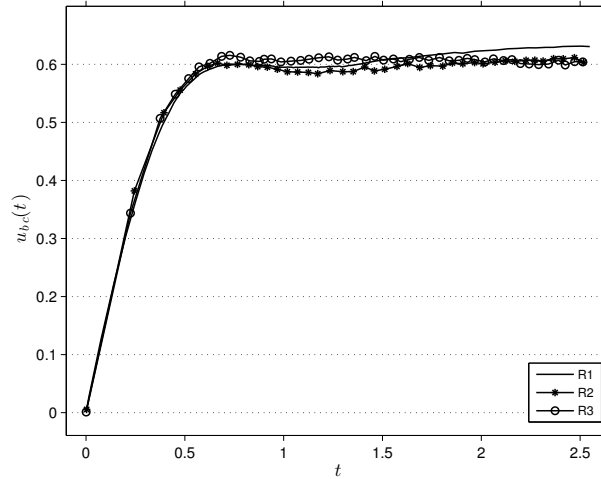


Figure 42: Dimensionless rising velocities  $u_{bc}(t)$  for three different configurations of an air bubble rising immersed into a aqueous sugar solution.

### 6.2.5 Rising velocity, aspect ratios, trajectories and spectra

Bubble deformation and oscillation are intimately linked to flow properties, such as surface tension, bubble size, and inertia effects. The next subsections describe rising velocities, bubble shape and oscillation analyses for two cases of bubble plumes inside the periodic domain of Figure 38 ( $L = 2D_b$ ), whose physical property and parameter values are listed in Table 4. For clarity, the cases are labeled as B1 and B2 and their underlying difference

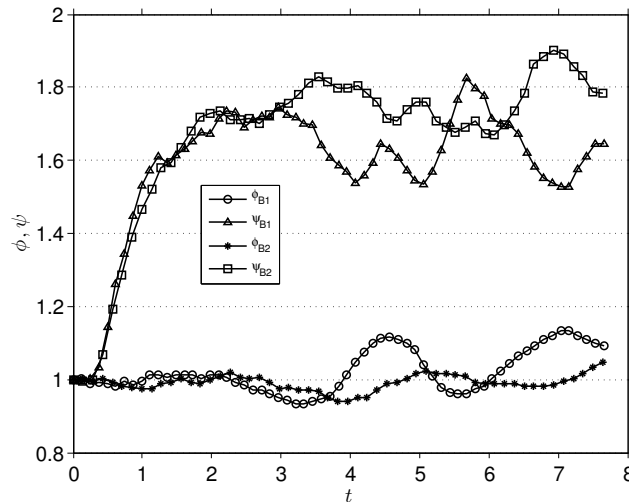


Figure 43: Elongation ( $\phi$ ) and flatness ( $\psi$ ) ratios of the rising bubbles.

is related to the bubble diameter in the periodic cell, namely, 4.0 mm and 5.2 mm, respectively.

Curves of the two bubble shape factors were calculated and plotted in Figure 43, *viz.*

Table 4: Physical property values for the numerical simulations: cases B1 and B2, respectively. (from [198])

Case	$\mu^1, \mu^2$	$\rho^1, \rho^2$	$\sigma$	$D_b$	$Ar^{1/2}$	$EO$
B1	18.2e-6, 958.08e-6	1.205, 998	0.0728	4e-3	824.96	2.15
B2	idem	idem	idem	5.2e-3	1222.8	3.63

the elongation and flatness ratios defined, respectively, as:

$$\phi = \frac{b}{c}; \quad \psi = \frac{c}{a}, \quad (6.13)$$

where  $a, b, c$  are the maximum length of the bubble's principal axes in the streamwise (chosen to be the  $x$  axis) and transverse directions ( $y$  and  $z$  axes). As seen, the initial condition (that is to say  $\phi = \psi = 1$ ) of both the cases vouch for the perfectly spheroidal shape of the bubbles. With the time and the ascent motion of the bubbles, the flattening process dominates over the elongation up to  $t \approx 2.5$ , thus portraying an oblate shape with a dimple underneath the bubble comparable to experimental observations [199]. From this threshold, shape irregularities become more visible as oscillations are felt by the bubbles, without following, however, a defined periodicity. In turn, the shape variations occur freely as far as the end of the simulations, with the elongation profiles less protruded.

Path instabilities, zigzag and spiral motions for gas bubbles rising both in clean water and other liquids are effects recognized in literature and the mechanisms responsible for their appearing have been debated through different points of view (cf. [200], [201], [202], [198], [203]). It is known, however, that the bubble's mobility is deeply affected when impurities are dispersed in the flow. To compare with these results, qualitative behaviours were observed for the cases B1 and B2 in the periodic domain regarding the bubbles' trajectories and its projections as depicted in Figure 44. While in the first test the bubble underwent an off-center wobbling motion marked by acute spots, the second test presented, furthermore, a twist motion around the directrix line erected from the point  $(y_t, z_t) = (0.09, -0.045)$ , approximately between  $t = 2$  and  $t = 4$ , before its full unfolding. Given the millimetric difference of diameters for the two cases, these curves suggest that the effect of the bubbles' wake brought onto themselves - in the sense of a plume made up by equally spaced bubbles - amounts to a path instability which depends on the bubble size and, therefore, on the Eötvös number, in accordance with arguments expressed in the previous citations. Besides, the trajectories tend

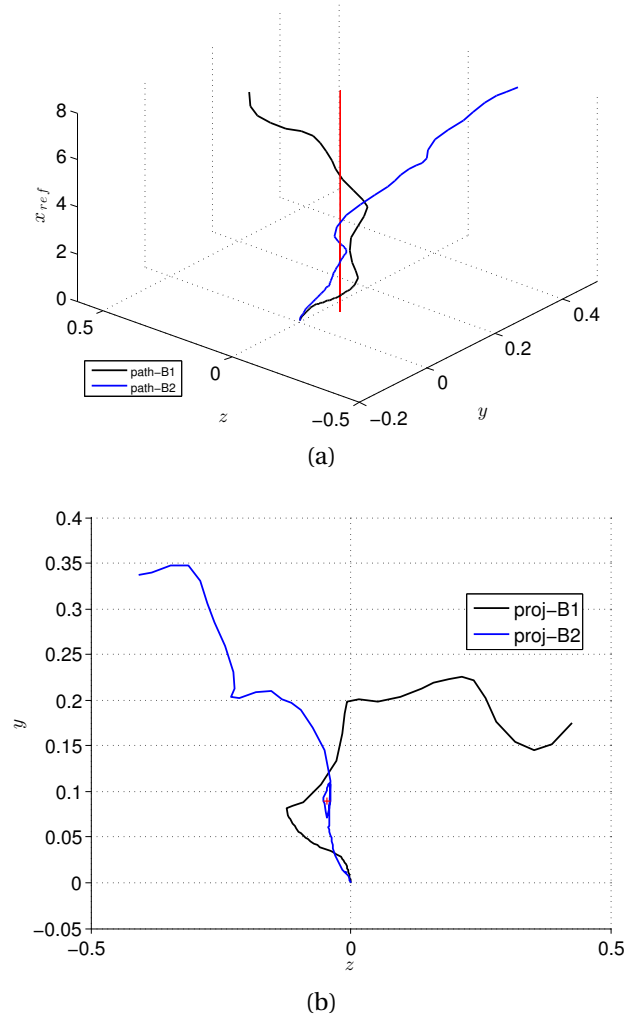


Figure 44: Bubbles' spatial motion relative to the reference frame moving upwards along with the center of mass ( $x_{ref}$  coordinate): (a) path and directrix line of the twist emerged in case B2 (in red); (b) projection of the paths over the  $yz$ - and the directrix's base point  $(y_t, z_t) = (0.09, -0.045)$  (in red).

to develop a seemingly chaotic path.

In attempting to quantify the harmonic modes involved in the oscillatory motion of the bubbles, a spectral analysis based on the fast Fourier transform (FFT) of the signals  $\phi_j(t), \psi_j(t), j = 1, 2$ , was performed. The spectral analysis considered only data on the range given by  $t_S = [2.5, t_{max}]$ , thus disregarding the initial evolution stage. FFT-based spectra of magnitude of disturbance energy computed through the expression

$$|FFT_{Bj}[F(t)]| = FFT[F(t)]\overline{FFT[F(t)]};$$

$$F(t) = \phi_j(t), \psi_j(t), \quad j = 1, 2, \quad (6.14)$$

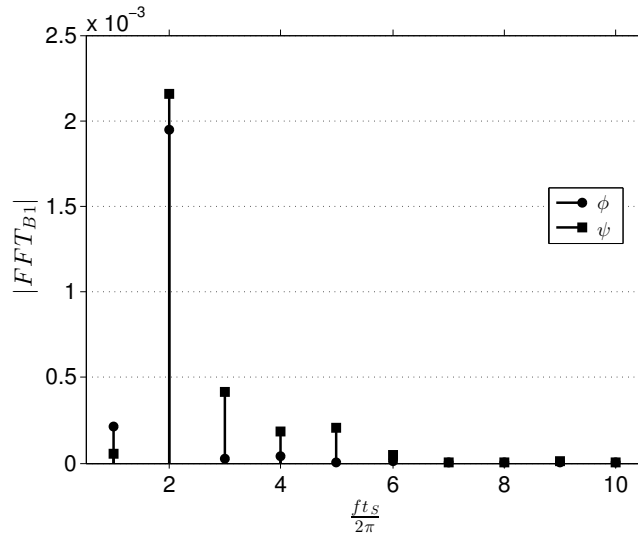
with the overbar meaning complex conjugate, for the ten first harmonic modes,  $1.0 \leq \frac{f t_S}{2\pi} \leq 10.0$ , are depicted for the cases B1 and B2 in Figure 45. The analysis took into account a considerably large quantity of sampling data over the reduced temporal interval  $t_S$ , but it showed that the energies of higher magnitude are noticeable only at the low frequencies of the spectra.

This FFT-based analysis shows that both the cases have their energy peak concentrated in the second harmonic. This value is close to the frequencies associated to the (2,0) and the (2,2) modes reported in [198]. For the case B1 the energy peak associated to the flatness profile is only slightly more intense than the elongation's, while for the case B2 the elongation energy is much larger than the flatness energy. Furthermore, the energy of the case B1 is very concentrated on  $\frac{f t_S}{2\pi} = 2.0$ , whereas that of the case B2 is spread over the frequencies in the range  $1.0 \leq \frac{f t_S}{2\pi} \leq 3.0$ . On the other hand, a slight alternance of intensities between even and odd harmonics can be observed along the range, though the case B1 has a higher overall energy than the case B2. Considering that the spectra are nondimensional, the increased spreading in the frequencies in case B2 is indicative of a more complex behaviour.

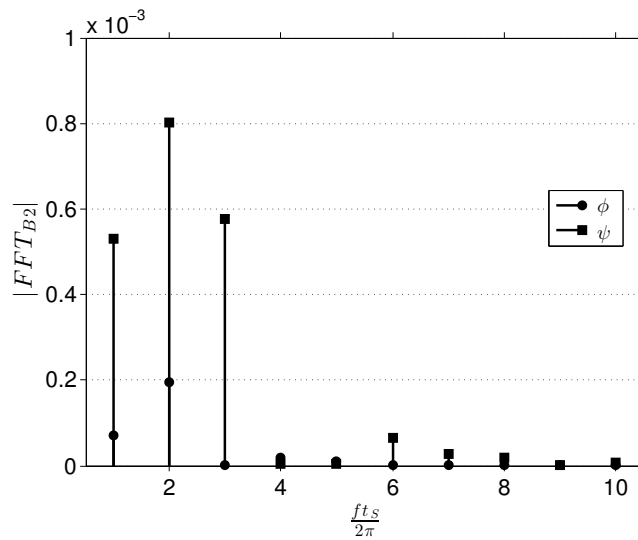
Filtered rising velocity profiles for the cases B1 and B2 are depicted in Figure 46. The need of filtering is firstly justified by the jump of density at the air-water interface, which implies small pressure variations inside the bubble, thus generating higher velocity therein; secondly, to remeshing operations inherent to the numerical method, such as insertion and deletion of nodes, that cause instantaneous variations in the center of mass's position. Consequently, a special treatment of box filtering is required to smooth the influence of short-time spurious oscillations experienced by the bubble while ascending. As seen, the fluctuations of velocity are intensified from  $t \approx 2.5$ , in accordance with the analysis previously reported.

### 6.2.6 Wake effects and near-field velocity

Analyses of the flow in the bubble's surroundings are limited here to a near-field distance, defined to be the periodic cell region below of  $2D_b$  from the nondisplaced bubble's center of mass, and are conducted for each test in this subsection. Due to the complex imaging of the three-dimensional hydrodynamic field evolving around the bubble, two stacks of pictures gathering the velocity field as well as the bubble shape information at four time instants, namely {3.00, 4.50, 5.50, 6.50}, are arranged from Figure 47 to Figure 50 relative to



(a)



(b)

Figure 45: FFT-based spectrum of disturbance energy for the ten first harmonic modes relative to the signals representative of the aspect ratios profiles  $\phi_j(t), \psi_j(t), j = 1, 2$  evaluated in the interval  $t_S = [2.5, t_{max}]$ : (a) case B1; (b) case B2.

an axis whose center is fixed in the initial position of the bubble's center of mass. In the background, the magnitude of the velocity field is plotted over the transverse planes  $yx$  and  $zx$ ; in the foreground, the bubble shape highlighting the zero-thickness finite element surface meshing is overlaid.

The downward flow reflects the imposition of the MFR technique by which the degrees of freedom of the streamwise velocity are subtracted by the center of mass velocity  $-U_{bc}$  which is updated each time step. By comparing the flow evolution vis-a-vis for each pair B1-B2 of projection planes, some inferences about the overall flow can be drawn from the

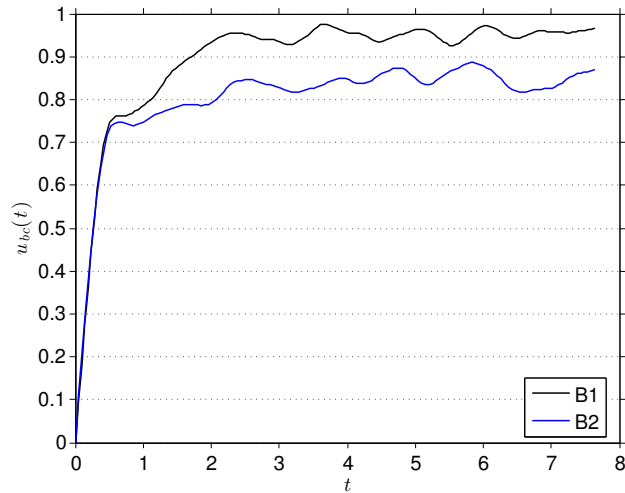


Figure 46: Dimensionless rising velocities  $u_{bc}(t)$  over the bubble's reference frame for the cases B1 and B2.

simulation snapshots. Firstly, the oblate shape persists for a considerable time along the path and it is a common trait in both the cases; so is the wobbling motion, which is boosted up by higher velocity gradients in the bubble's skirt region around  $t = 5.50$ . Off-center motion is seen by contrasting the bubble shape at  $t = 3.00$ , a few instants after the oscillation outset, against  $t = 6.50$ ; for instance, when the drift from the reference center is played by the bubbles. Consecutive inclinations of the bubbles concerning the azimuthal angle formed between their central axis and the streamwise axis are also exhibited on both projection planes concomitantly, thereby confirming the presence of wobbles in the spatial trajectories observed as much in the previous subsection as in the cited references. It is seen, moreover, that the dimple evolution underneath the bubble of the case B1 differs from that arising in B2, which is more restrained during this stage - however unclear from the pictures. Despite of that, the dimple existence can be verified from the smooth reentrant portions of counterflow underneath the bubbles and around their fringes.



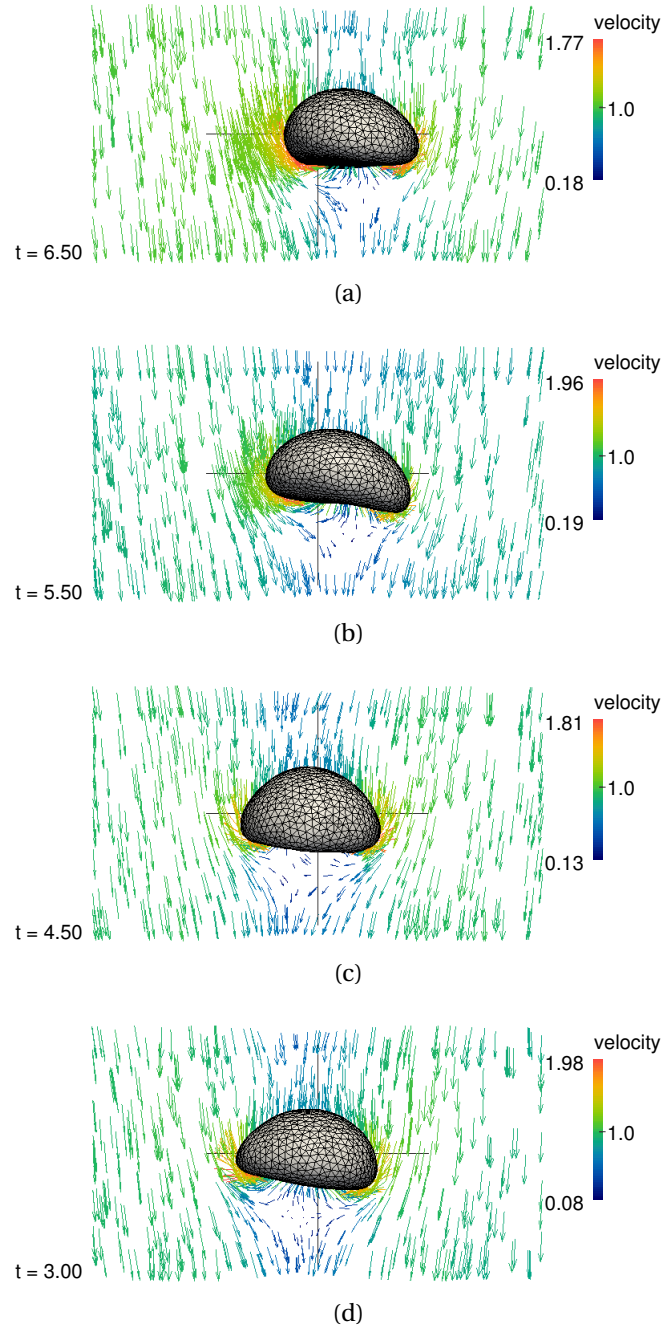


Figure 47: Velocity field and bubble shape for the case B1: plane  $yx$ ; (a)  $t = 3.00$ , (b)  $t = 4.50$ , (c)  $t = 5.50$ , (d)  $t = 6.50$ .

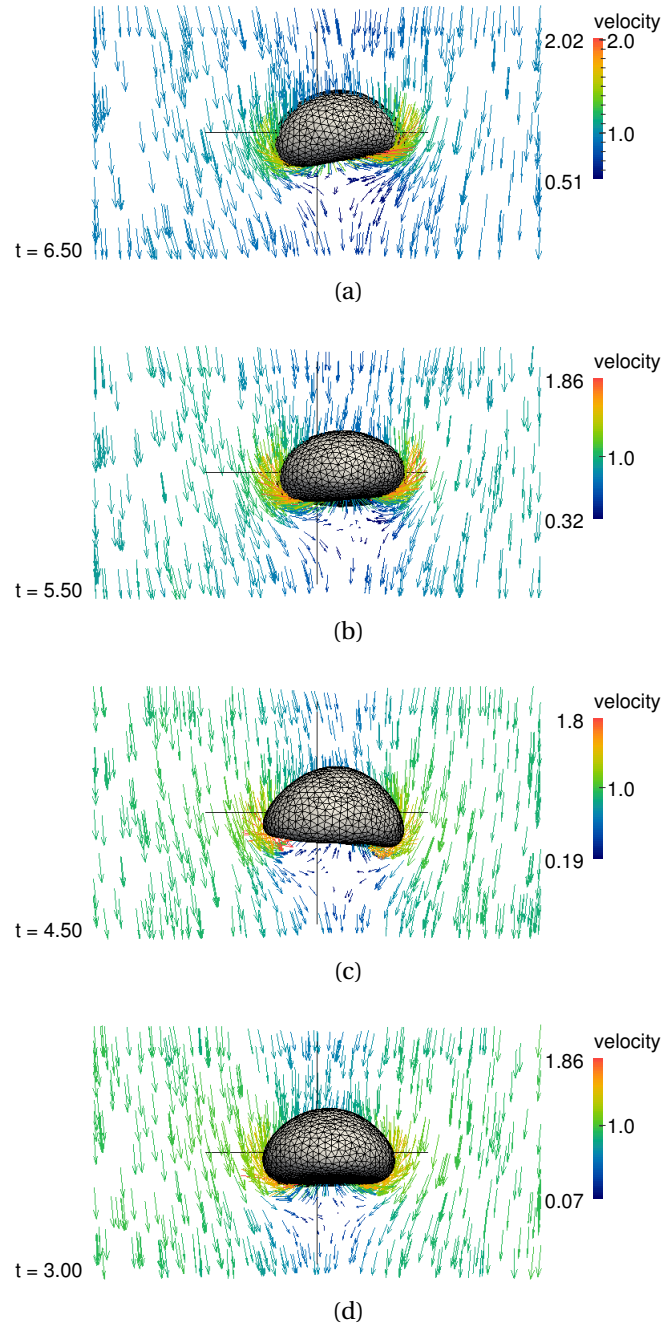


Figure 48: Velocity field and bubble shape for the case B1: plane  $xz$ ; (a)  $t = 3.00$ , (b)  $t = 4.50$ , (c)  $t = 5.50$ , (d)  $t = 6.50$ .

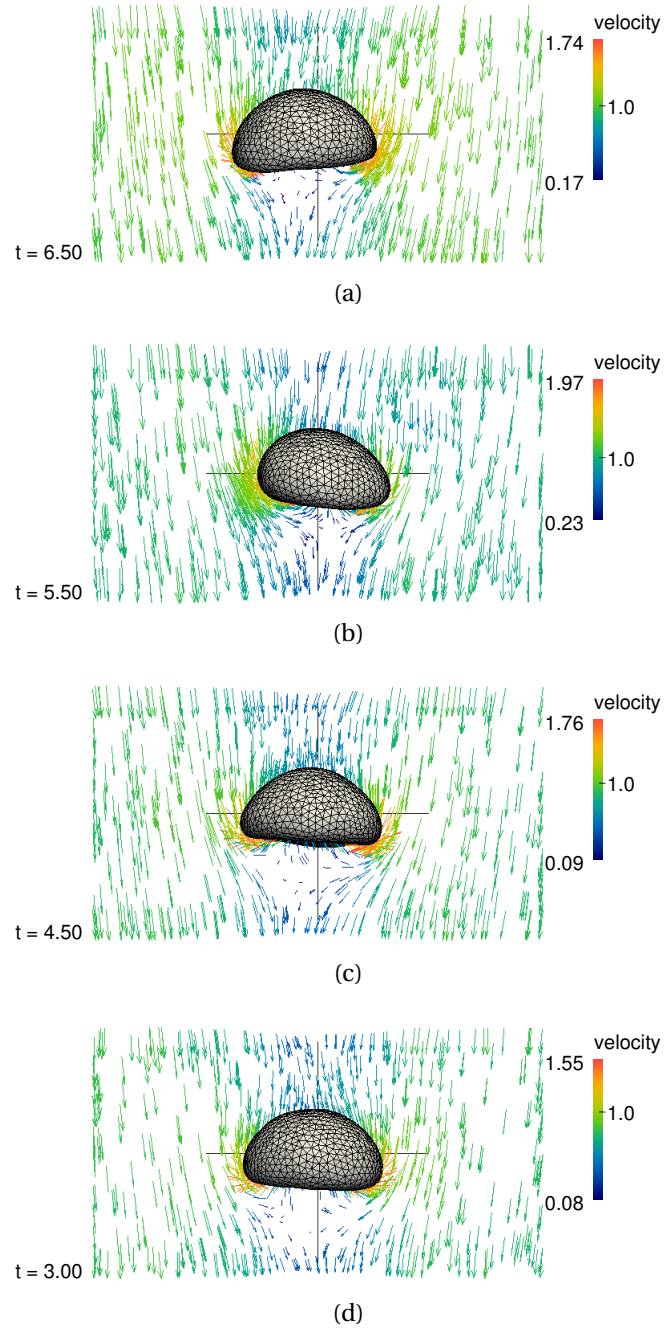


Figure 49: Velocity field and bubble shape for the case B2: plane  $yx$ ; (a)  $t = 3.00$ , (b)  $t = 4.50$ , (c)  $t = 5.50$ , (d)  $t = 6.50$ .

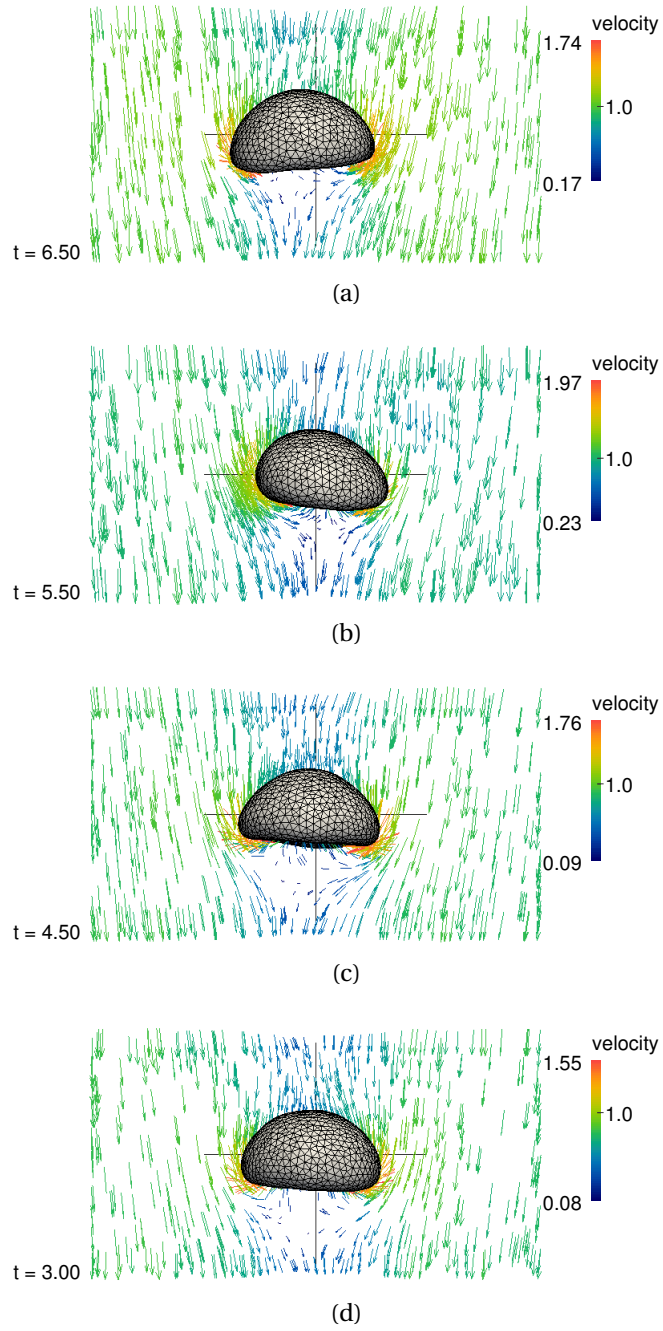


Figure 50: Velocity field and bubble shape for the case B2: plane  $zx$ ; (a)  $t = 3.00$ , (b)  $t = 4.50$ , (c)  $t = 5.50$ , (d)  $t = 6.50$ .

## 7 THE DROP JET IN CROSSFLOW

### 7.1 Problem posing

With a physical meaning similar to the cases reviewed in Chapter 1, the flow of a liquid jet issued into another immiscible liquid portion after breaking in drops is analyzed. We focus on the primary breakup zone after the drop detachment and not on the mechanisms leading to the breakup. To give an insight about the whole description of the problem, we refer to the arrangement of the DJICF studied in this thesis as depicted in Figure 51.

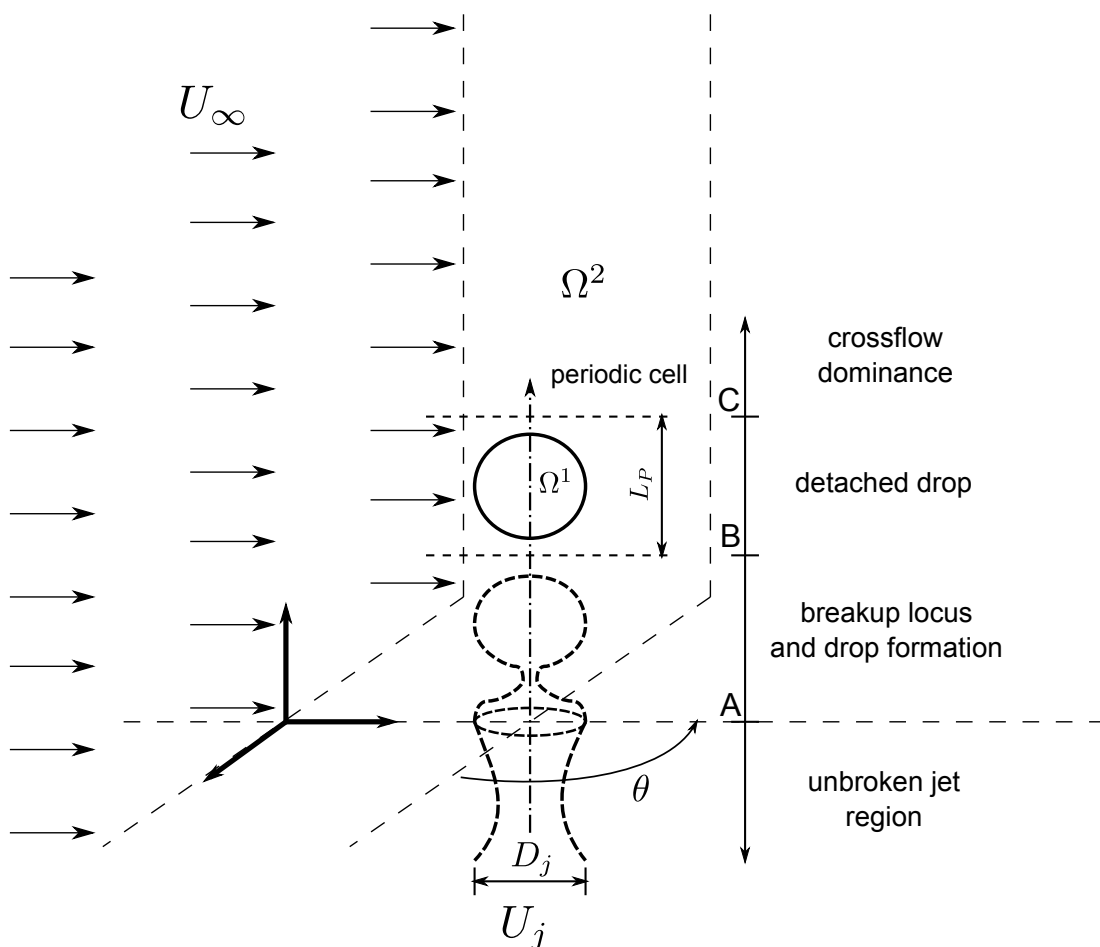


Figure 51: Arrangement of the DJICF.

The cylindrical-shaped jet is considered to expel drops of diameter  $D_j$  with velocity  $U_j$  in a periodic way and perpendicularly into an unconfined liquid portion  $\Omega^2$  whose crossflow velocity is  $U_\infty$ . The unbroken jet region is below the point A. Between the points A and B, a Rayleigh breakup mode is assumed to occur and form the drop. During the short space between B and C, the drop is completely detached off the jet. Beyond the point C, the crossflow

inertia is assumed to dominate over the jet deflecting the drop depending on the crossflow-to-jet velocity ratio  $\lambda$ . As it will be seen forth, the drop is modelled as a spherical body initially which may deform along its trajectory depending on the flow properties, mainly ruled by the  $We$ ,  $Oh$ ,  $Re$  and  $Ca$  numbers, where

$$Ca = \frac{We}{Re} \frac{\mu}{\lambda^{-1}} \quad (7.1)$$

is the *capillary number* here defined according to [84] for the viscosity ratio  $\mu = \mu_1/\mu_2$ . In this preliminary study, gravity effects are not considered, just as the relevance of the  $Fr$  number.

To account for the PBC, the periodic cell is placed around the drop by enclosing it inside a certain period length  $L_P$ . Since this approach imparts a limited treatment of the flow, a MFR technique is additionally incremented in the modelling in attempting to analyze deflection, topological changes and hydrodynamic effects over and surrounding the drop enclosed by this simulation box. The relation between fixed and moving reference frames as well as the collocation of the periodic cell domain and boundary conditions are elucidated by observing Figure 52. In this idealized diagram, the drop, after detaching off the jet, travels in

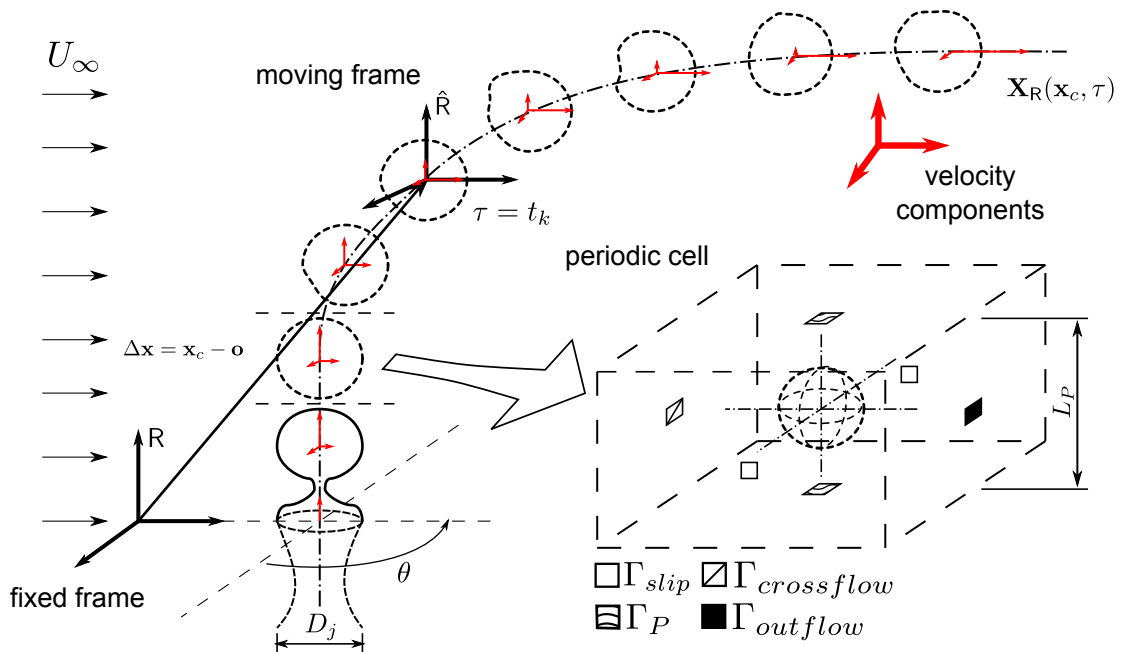


Figure 52: Relation between fixed and moving reference frames in the DJICF flow as well as an overview of the periodic cell domain with the selection of the boundary conditions.

space undergoing the influence of the crossflow. Several configurations of the drop along its trajectory are drawn in dashed lines. The velocity components following the drop's motion are placed at its center of mass  $\mathbf{x}_c$ , which performs the trajectory described by the curve  $\mathbf{X}_R(\mathbf{x}_c, \tau)$ . When establishing the relation between the physical reference frames, the called *fixed frame* is firstly defined by  $R$  which, in this generalized scheme, is placed at a convenient site in the continuous domain  $\Omega^2$ . The second referential, defined by  $\hat{R}$ , is called the *moving frame* and it is placed at the drop's center of mass so that

$$\Delta \mathbf{x} = \mathbf{x}_c - \mathbf{o} \quad (7.2)$$

represents the displacement of the drop's center of mass in relation to the origin  $\mathbf{o}$  of  $R$ . At right, in the same figure, the computational periodic cell is laid out as a cuboid whose boundaries are divided into four groups represented by painted snips, namely,  $\Gamma_{slip}$ ,  $\Gamma_P$ ,  $\Gamma_{crossflow}$  and  $\Gamma_{outflow}$ . More specifically, aside the PBC and NBC, the DBC obey

$$p = 0 \quad \text{at} \quad \Gamma_{outflow} \quad (7.3)$$

$$\mathbf{v} \cdot \mathbf{n} = V_\infty \quad \text{at} \quad \Gamma_{crossflow} \quad (7.4)$$

$$\mathbf{v} \cdot \mathbf{n} = 0 \quad \text{at} \quad \Gamma_{slip}, \quad (7.5)$$

for  $\mathbf{n}$  normal to its respective wall.

## 7.2 Moving frame reference technique

The MFR technique resorts to a strategy based on reference frames while creating a relative context of interaction between Eulerian and Lagrangian descriptions. In this thesis, the MFR approach is used together with the enforcement of PBC in order to reduce the computational cost of the simulations when reducing, mainly, mesh size and number of DOFs (see, e.g. Subsection 6.2.1).

Generally, MFR codes are used to simulate dispersed flows in their several configurations in which the dispersed bodies remain stopped with time whilst the boundaries encircling them are placed in relative motion. Although the idea behind this technique can be extended for other cases, examples of such applications with or without PBC are found, mainly, in simulations of bubble or drop flows, as studied in [204], [205], [206], [207]. Whereas all of these

papers use MFR for unidirectional flows only, this section describes the additional details of implementation of the MFR technique by considering the existence of transverse flows as well. Since this approach is adapted for the DJICF problem, the two-dimensional periodic cell scheme depicted in Figure 53 will be used as an extension of those seen in the previous section. Given that the drop has velocity  $U_j$ , if  $U_\infty \neq U_j$  a curved trajectory is experienced by

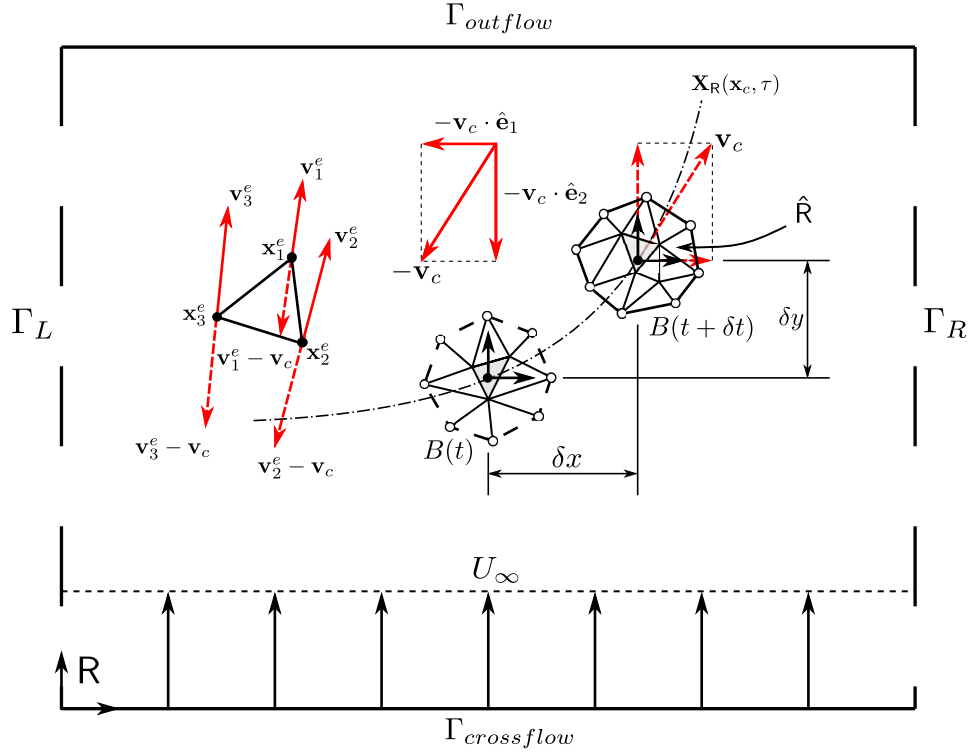


Figure 53: Scheme of the displacement of a drop in crossflow and implementation of the moving frame technique.

the drop even for a minimal displacement. Let us consider, however,  $B(\tau = t), B(\tau = t + \delta t)$  two configurations of an arbitrary dispersed body  $B$  at two time instants. In relation to a Cartesian fixed frame  $R$ , the entire body undergoes an infinitesimal displacement of  $(\delta x, \delta y)$  from left to right with its center of mass traveling according to the Lagrangian trajectory  $\mathbf{X}_R(\mathbf{x}_c; \tau)$ . On the other hand, the moving frame  $\hat{R}$  attached to the body's center of mass  $\mathbf{x}_c$  which follows the body motion in space and time, at first, should remain fixed for all the time at the position of the center of mass identified in space when  $\tau = t$ , thus conveying the dynamics to an Eulerian point of view.

Whilst, physically, the instantaneous velocity

$$\mathbf{v}_{inst} = \lim_{\delta t \rightarrow 0} \frac{\delta \mathbf{x}}{\delta t} \quad (7.6)$$



is responsible for the infinitesimal displacement of the body within  $t \leq \tau \leq t + \delta t$ , numerically, the velocity evaluated at the center of mass is the parameter playing the fundamental role in the discrete time step  $\Delta t$ . Therewith, two numerical steps arise: the computation of the velocity and position of the center of mass and the determination of the body's retardment. The former will be discussed in Subsection 7.2.1; the latter, next.

Since the center of mass' velocity  $\mathbf{v}_c$  is determined for each time instant, all the flow field should undergo a retardment of velocity given by

$$\mathbf{v}_{rel} = \mathbf{v} - \mathbf{v}_c \quad (7.7)$$

to create a relative field so that the body  $B$ , after it has been displaced to  $B(\tau = t + \delta t)$ , be brought back to its position at  $B(\tau = t)$ . The effect of such subtraction of the flow's velocity field is drawn in red lines in Figure 53 as much for the body itself as for an arbitrary element  $e$  of the continuous phase  $\Omega^2$ . That is to say, for each triangular element with vertices  $\mathbf{x}_j^e$ ,  $j = 1, 2, 3$ , the resulting velocity  $\mathbf{v}_c$  is summed to the nodal velocities with opposed sign to give  $\mathbf{v}_{rel;e}^j = \mathbf{v}_j^e - \mathbf{v}_c$ ,  $j = 1, 2, 3$ . As explained by [208], the interplay between inertial and stationary reference frames works as a correction scheme that may suffer the influence of a wave pressure that eventually dissipates during the simulation since the body is forced to go back and forth each time step, thus requiring some numerical artifice. In this thesis, the numerical steps to implement the MFR technique are represented in the algorithm below:

```

for  $t : (0, T]$  do
   $\Delta \mathbf{x}(t) = \mathbf{x}(t) - \mathbf{x}(t = 0)$ ;          /* displacement */
   $\mathbf{v}_{inst}(t) = \mathbf{v}_c(t) + \frac{\Delta \mathbf{x}}{\Delta t}$ ;    /* accumulating instantaneous velocity */
   $\mathbf{v}_R = \mathbf{v}(t) + \mathbf{v}_{inst}$ ;          /* recovering velocity - relative to FFR */
   $\mathbf{x}_R = \mathbf{x}(t) + \mathbf{v}_R \Delta t$ ;          /* recovering position - relative to FFR */
   $\mathbf{v}(\Omega) = \mathbf{v} - \mathbf{v}_{inst}(t)$ ; /* corrected relative velocity - flow field */
end

```

It should be pointed out that such retardment operations require an update not only of the DBC to take the changes of the flow field into account, but also of the code variables that store the velocity values, which are reused in the iterative process.

### 7.2.1 Computation of averaged quantities

As aforementioned, the computation of the velocity and position of the center of mass of a dispersed body is necessary not only for the establishment of the MFR technique, but also for a considerable amount of discrete quantities in the FE ambit. Generally, the center of mass  $\mathbf{x}_c$  is an interior point not matching a mesh node as depicted by the dark points inside the shaded triangular elements in Figure 53. Then, under the numerical point of view, every property  $\phi(\mathbf{x}_c)$  is computed at element level through a global average of elementary nodal values. For the specific case of determining the position and velocity of the center of mass of a dispersed body, the following approximated version of integrals is computed:

$$\begin{aligned} \phi(\mathbf{x}_c^g) &= \left( \frac{\iiint \phi dV}{\iiint dV} \right)_{\Omega_g^1}, \quad g = 1, 2, \dots, nb \\ &= \frac{\sum_{e=1}^E \phi_{c,e}^g V_e^g}{\sum_{e=1}^E V_e^g}; \quad \phi_{c,e}^g = \frac{\sum_{j=1}^{\#J} \phi^g(\mathbf{x}_j^e)}{\#J}, \quad J = m + 1, \end{aligned} \quad (7.8)$$

where  $nb$  is the number of dispersed bodies,  $E$  is the number of simplices making up each dispersed body,  $J$  is the number of vertices of the element and  $V$  stands for volume. These formulae apply for each component separately in  $\mathbb{R}^3$ . Note, additionally, that, if  $m = 2$ , the computations can be performed by replacing the volume integrals by area integrals and doing the necessary modifications.

## 7.3 **Direct numerical simulations**

This section presents the main results of this thesis concerning the full 3D simulations of the DJICF configuration. The liquid-liquid pairs chosen relate to well-known experimental tests.

### 7.3.1 Initial condition

Because of the DJICF problem is based on the MFR technique explained previously, a special initial condition was implemented for the simulations to restrain undesirable overshooting of the velocity field caused by the retardment effect applied to the drop during the first iterative step. For this objective, the imposition of the potential flow around a cylinder

was done to wrap the drop region so as to seem a drop encapsulated by a tube extending along the direction normal to the periodic one. Moreover, such flow tends to cause a slight disturbance on the drop due to the circulations that rise up behind the drop in the nearby wake region. Figure 54 depicts at the top three fluid layers passing around the drop on the

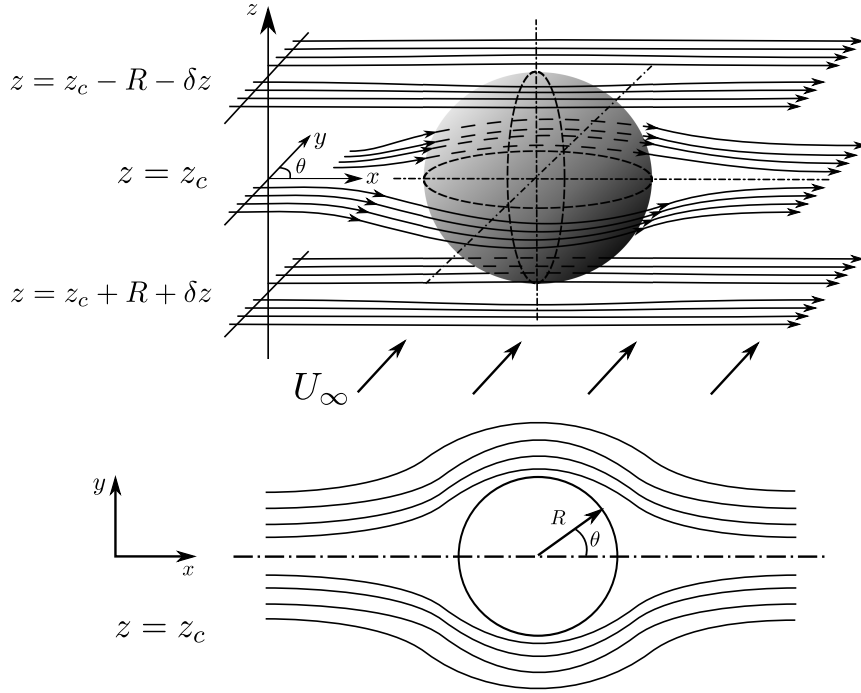


Figure 54: Past cylinder flow velocity profile as initial condition for the DJICF simulation.

planes  $z = z_c$ ,  $z = z_c + R + \delta z$  and  $z = z_c - R - \delta z$ , where  $R$  is the drop's radius and  $\delta z$  a small distance away from the poles; at the bottom is the top view of the flow on the symmetry plane  $z = z_c$ . When imposing such initial condition to the flow field, we intend to provoke a smooth transition from the initial departure of the drop toward its subsequent instants when it will experience the crossflow incidence. The periodicity is allotted to  $x$ -axis, whereas the crossflow condition is assigned to  $y$ -axis.

The velocity profile of this condition is initialized over the computational mesh and written in cylindrical coordinates as

$$v_r = (U_j \cos(\theta) + U_\infty \sin(\theta)) \left[ 1 - \left( \frac{R}{r} \right)^2 \right] + U_{added} \quad (7.9)$$

$$v_\theta = (-U_j \sin(\theta) + U_\infty \cos(\theta)) \left[ 1 + \left( \frac{R}{r} \right)^2 \right] \quad (7.10)$$

$$v_z = 0, \quad (7.11)$$

thus using  $U_j$  and  $U_\infty$  as parameters.

At this point, it should be explained that  $U_{added} = U_j$  is added to the original profile to compensate the difference which will be deduced of the flow immediately afterwards the simulation begin because of the MFR calculation (see the algorithm in Section 7.2) that retards the drop's motion.

### 7.3.2 Study of DJICF cases: hydrodynamics and discussion

Two different pairs of immiscible liquids relating to experiments performed, respectively, by Meister and Scheele [69] (also reproduced by [76]) for a water/*n*-heptane interface and by Webster and Longmire [25] (see p. 226) for a water-glycerin/Dow Corning sylicon-oil interface make up the next simulations, whose physical parameters are presented in Table 5 and Table 6. For convenience, the labels MS and WL will be used as abbreviations of the references cited above to designate the numerical tests. Additionally, two other parameters will determine the simulations, namely the ratio  $\lambda$  and the periodic cell's length  $L_P$ . Hence, the different configurations of tests chosen are expressed by a triple of parameters as

$$(Ref, \lambda, L_P), \text{ for } Ref = MS, WL; \lambda = 1.0, 1.5, 2.0 \text{ and } L_P = 1.5, 3.0, 5.0. \quad (7.12)$$

While different values of  $L_P$  seek to analyze the effect of the PBC by considering different spacing between drops (in the sense of the imposed periodicity), small values of  $\lambda$  seek to add a weak effect to the crossflow so as to ensure small disturbances in the surroundings of the drop and preserve the periodicity with less tendency to deflection. The cuboid-shaped meshes used in the simulations, which differ one another by the length  $L_P$ , are depicted in Figure 55 clipped along the axis of periodicity.

The analysis of the simulations starts from the velocity field  $\mathbf{v}_R(t) = (u_c, v_c, w_c)(t)$ , whose component profiles are organized for each configuration from Figure 56 to Figure 61 as the ratio  $\lambda$ . By observing the curves of  $u_c$  and  $v_c$ , it is noticeable that  $u_c$  decays monotonically from  $U_j = 1.0$  - the dimensionless jet velocity - at the initial instant to zero in the far-field

Data				
$\mu$	$\rho$	$D_j$	$Re$	$We$
2.43	1.45	0.68	1851	2.20

Table 5: Parameters of simulation according to the experiment no. 5 of Meister and Scheele [69].

Data				
$\mu$	$\rho$	$Oh$	$Re$	$We^*$
0.15	1.18	0.013	50	0.80

Table 6: Parameters of simulation according to the fluid combination no. 1(c) of natural jet of Webster and Longmire [25], p. 226. \*  $We = (ReOh)^{0.5}$

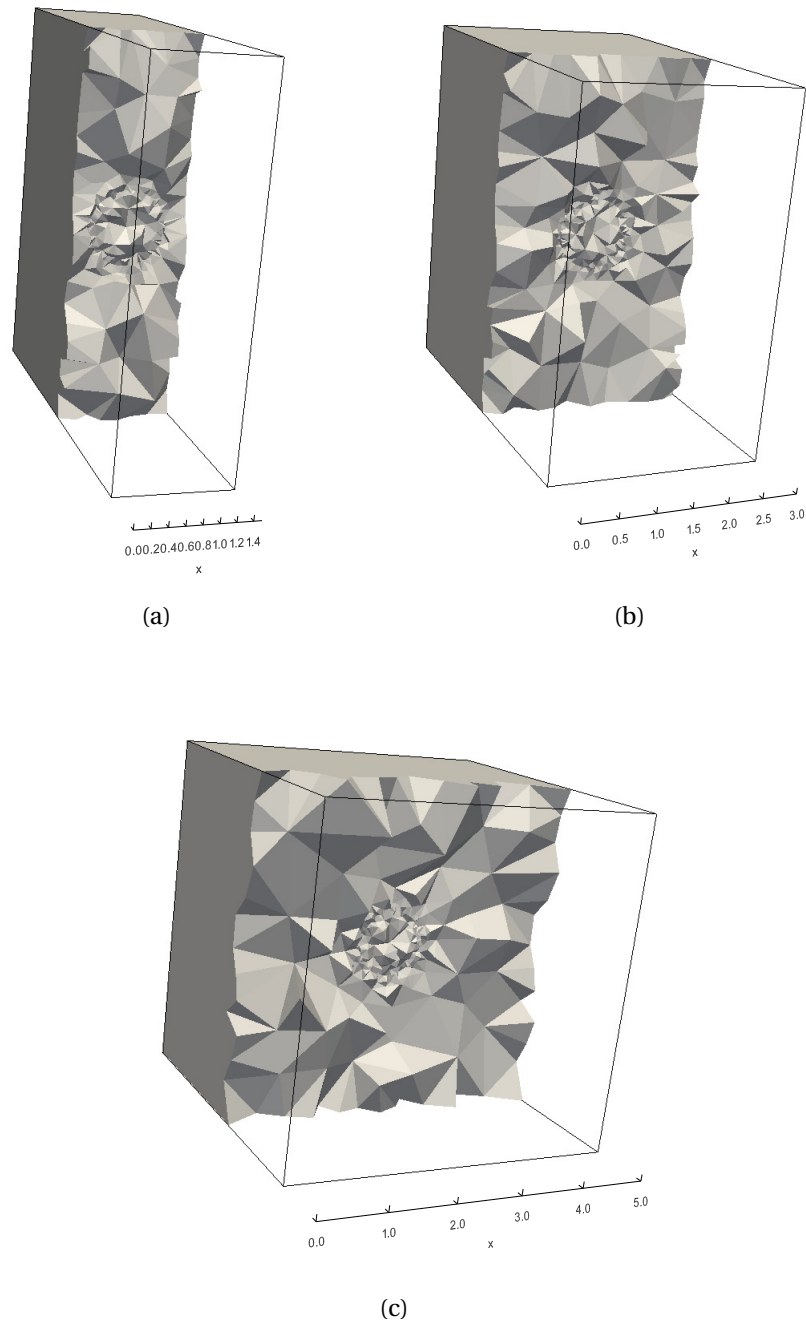


Figure 55: Meshes used for the DJICF simulations: (a)  $L_P = 1.5$ ; (b)  $L_P = 3.0$ ; (c)  $L_P = 5.0$ .

region, whereas  $v_c$  approaches asymptotically  $U_\infty = \lambda U_j$ . It should be noted that the initial condition given by Equation (7.9) was essential to produce these profiles under a MFR scheme as aforementioned.

On one hand, the behaviour of  $w_c$  shows very small variations in comparison to the other profiles during the interval of simulation studied. Except for the cases with  $L_P = 1.5$ ,  $w_c$  describes, at most, a slightly descending motion of the drop downward the crossflow plane, but without following a defined pattern. The highest values of  $w_c$  are observed in the cases  $(MS, \cdot, \cdot)$ , whose upper bounds are of  $\mathcal{O}(10^{-2})$ . On the other hand, the duration of decay of  $u_c$  as well as of rise of  $v_c$  up to their respective final values differ from case to case. Note, for example, how  $u_c$  and  $v_c$  reach their steady state within different times in the  $(WL, \cdot, \cdot)$  group. Even more uncommon is the behaviour of  $u_c$  for  $(WL, \cdot, 1.5)$ , which suggests an inflection of the drop's trajectory backward. Such a behaviour may be related to the influence of the flow nearby the drop which is more prominent due to the PBC and the smaller value of  $L_P$ . The simulations were stopped taking the profile  $v_c$  as reference, *i.e.* when the value of  $\lambda$  was achieved, since it reflects the drop's motion already dominated by the crossflow.

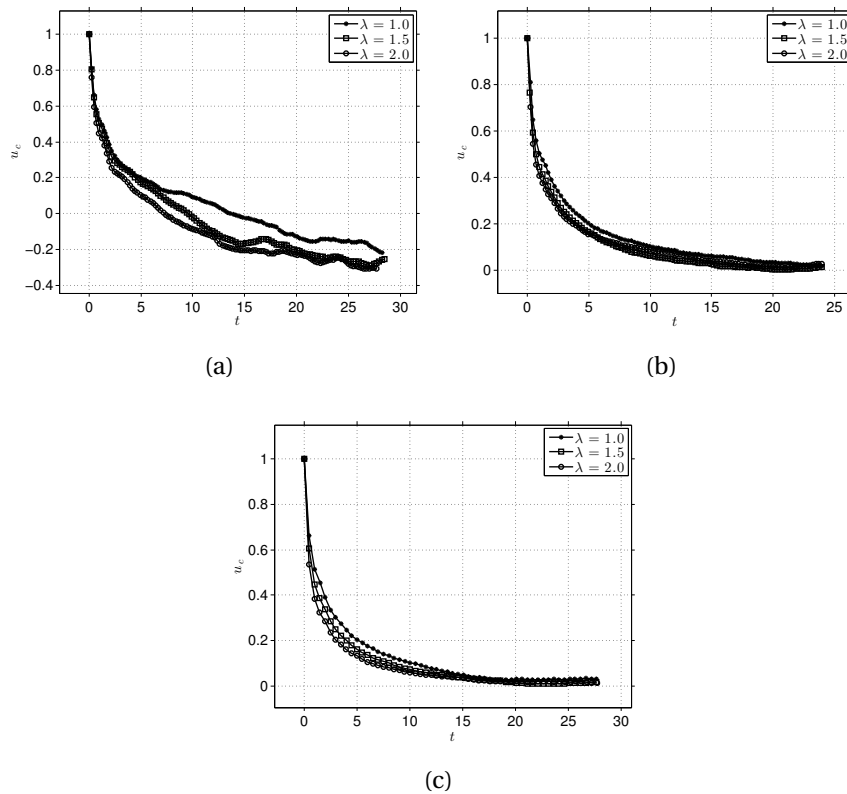


Figure 56:  $u_c(t)$  profile - MS: (a)  $(MS, \cdot, 1.5)$ ; (b)  $(MS, \cdot, 3.0)$ ; (c)  $(MS, \cdot, 5.0)$ .

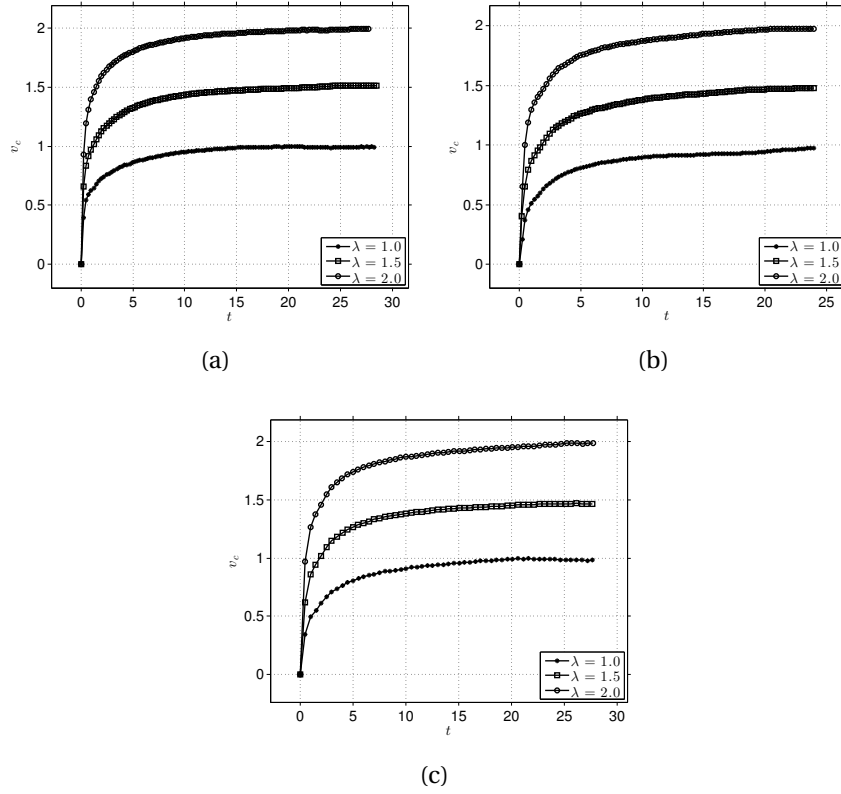


Figure 57:  $v_c(t)$  profile - MS: (a)  $(MS, \cdot, 1.5)$ ; (b)  $(MS, \cdot, 3.0)$ ; (c)  $(MS, \cdot, 5.0)$ .

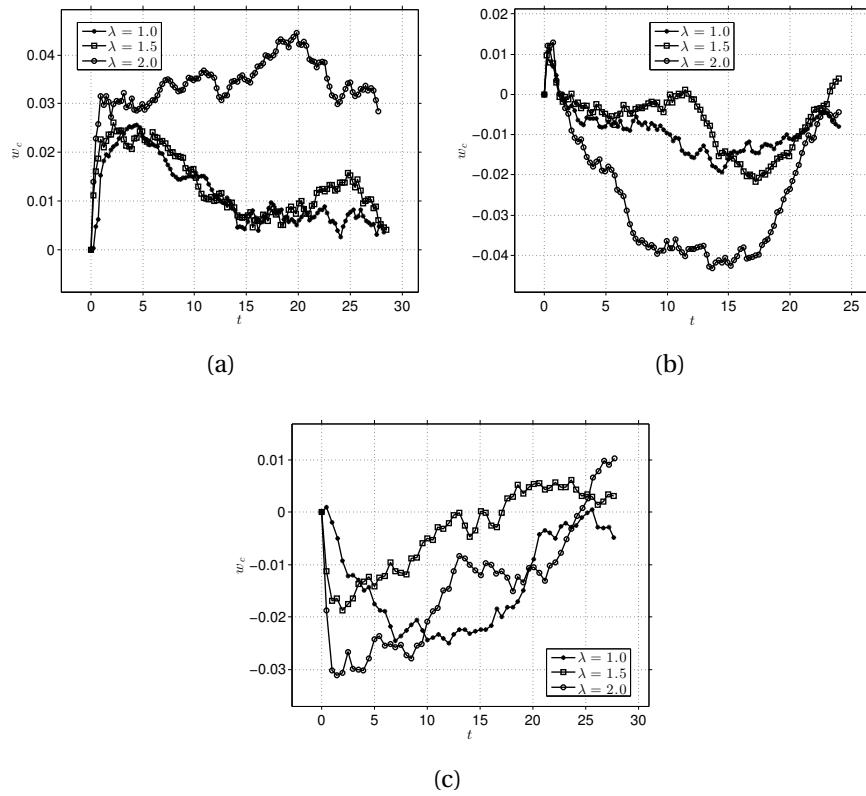


Figure 58:  $w_c(t)$  profile - MS: (a)  $(MS, \cdot, 1.5)$ ; (b)  $(MS, \cdot, 3.0)$ ; (c)  $(MS, \cdot, 5.0)$ .

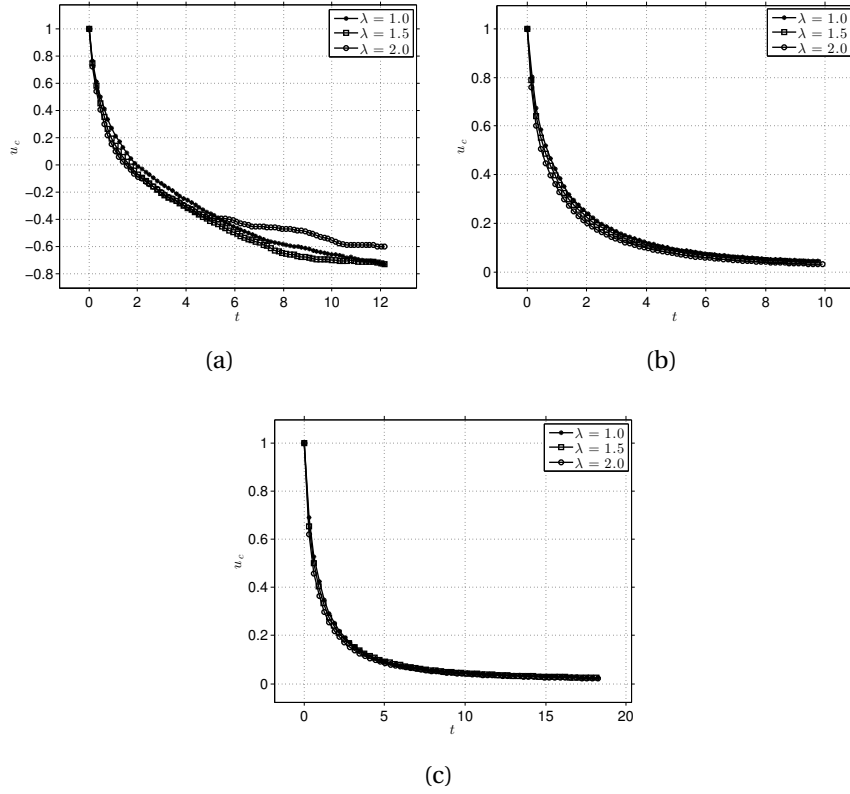


Figure 59:  $u_c(t)$  profile - WL: (a)  $(WL, \cdot, 1.5)$ ; (b)  $(WL, \cdot, 3.0)$ ; (c)  $(WL, \cdot, 5.0)$ .

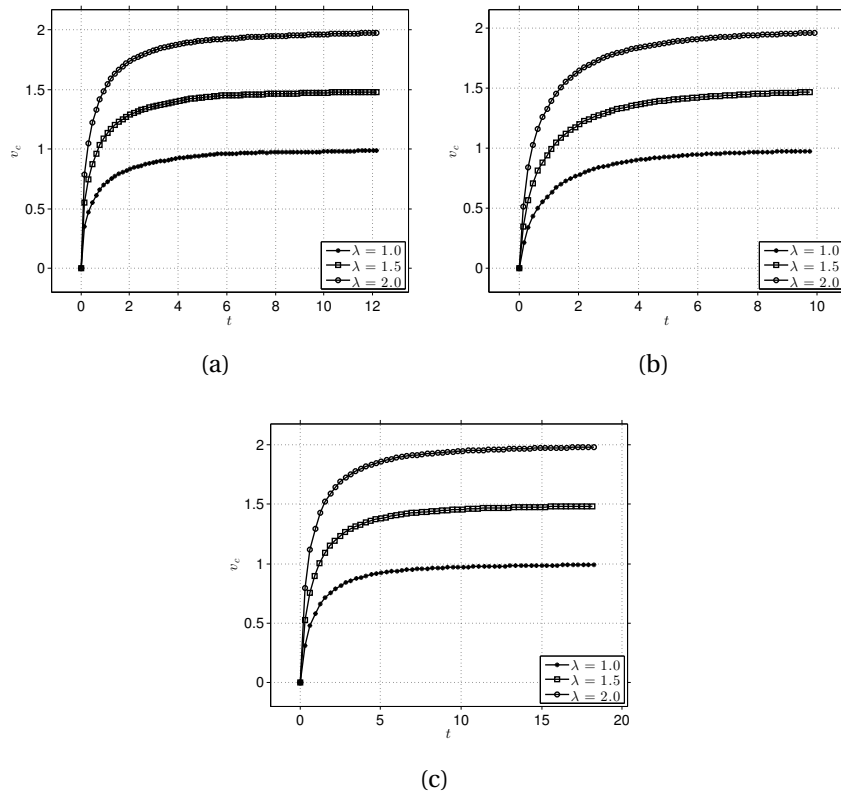


Figure 60:  $\nu_c(t)$  profile - WL: (a)  $(WL, \cdot, 1.5)$ ; (b)  $(WL, \cdot, 3.0)$ ; (c)  $(WL, \cdot, 5.0)$ .



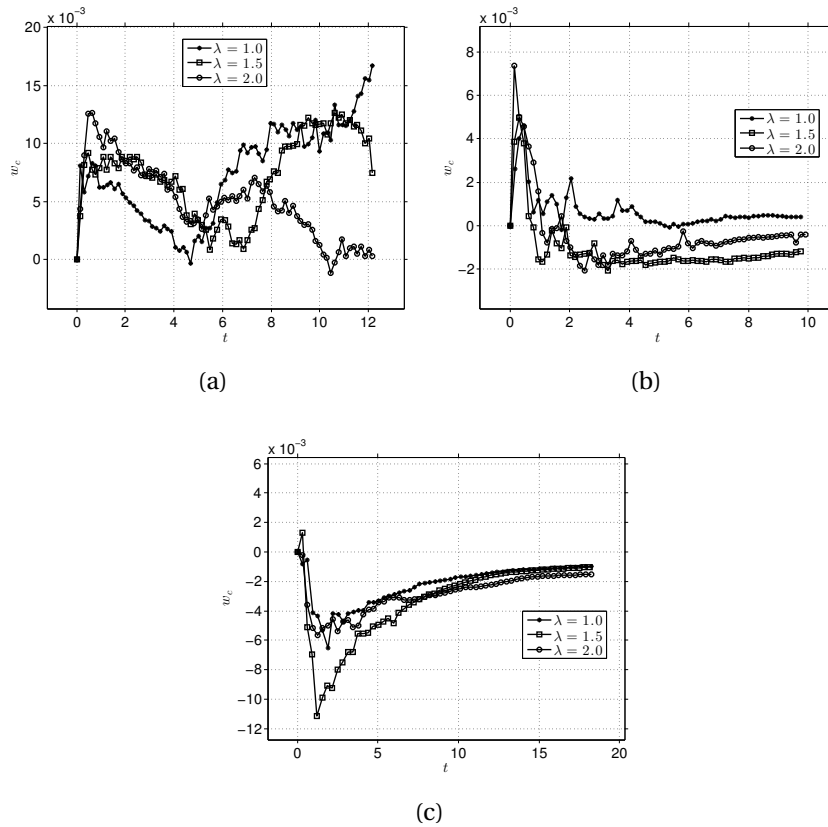


Figure 61:  $w_c(t)$  profile - WL: (a)  $(WL, \cdot, 1.5)$ ; (b)  $(WL, \cdot, 3.0)$ ; (c)  $(WL, \cdot, 5.0)$ .

To illustrate the topological changes undergone by the drop in crossflow, some images containing streamlines and drop shape cuts obtained through the group of simulations  $(\cdot, 2.0, \cdot)$  at specific times are depicted below. The streamlines are seen from behind the drop, encompassing it inside a box equivalent to half of the periodic cell cut by the symmetry plane tangent to the periodic direction. For each image of streamline are associated two others of symmetry planes that cross the drop surface along the regions  $xy$  and  $xz$  so as to characterize the drop's rims. Moreover, vectors of the relative velocity field  $\mathbf{v}_{rel}$  were plotted over the rims to highlight its local effect over the drop. Though the family of tests WL showed moderate deformation, their related shapes were included here for completeness.

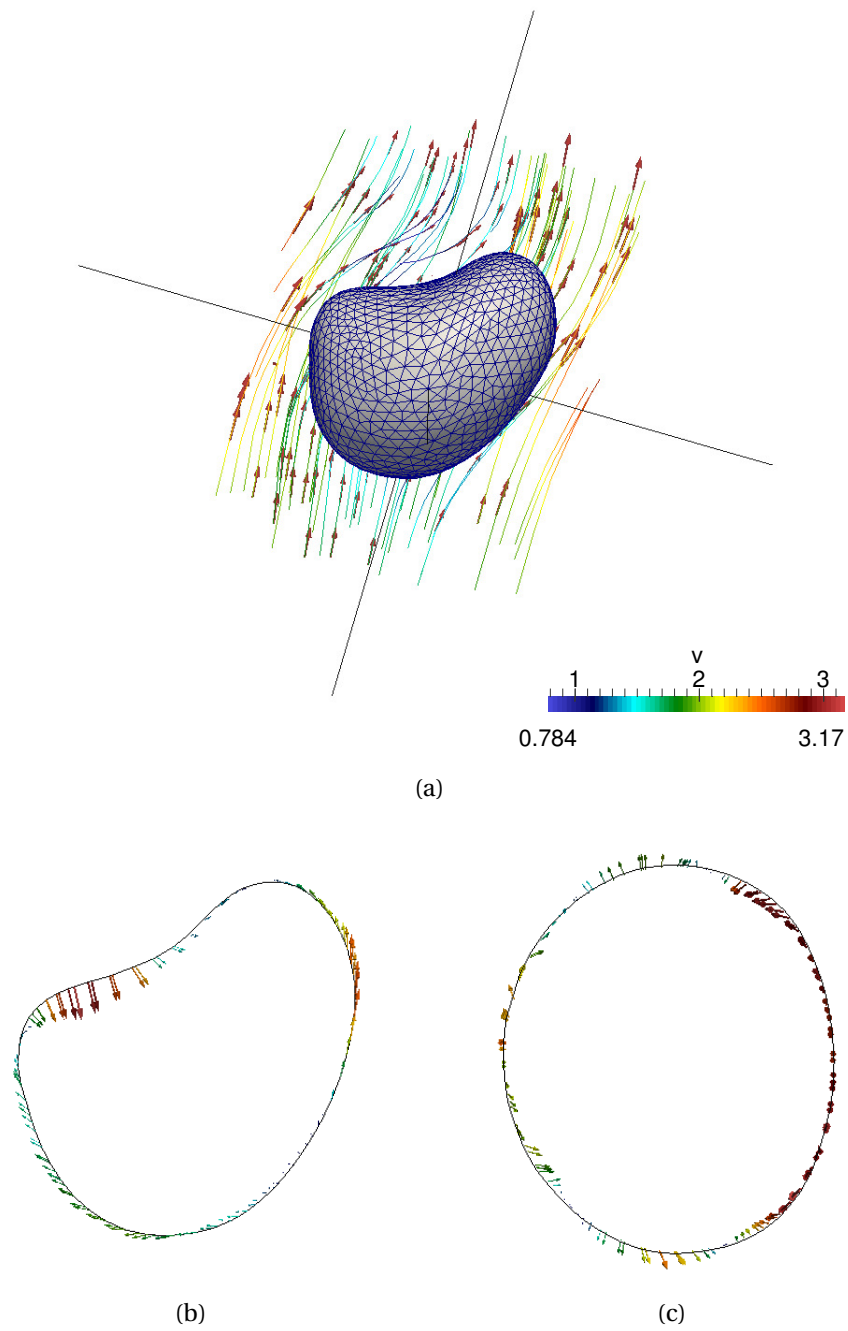


Figure 62: Streamlines and drop's rims at  $t \approx 0.30$  - test (MS,2.0,1.5): (a) streamlines and velocity field; (b) drop's rim on the plane  $xy$ ; (c) drop's rim on the plane  $xz$ .

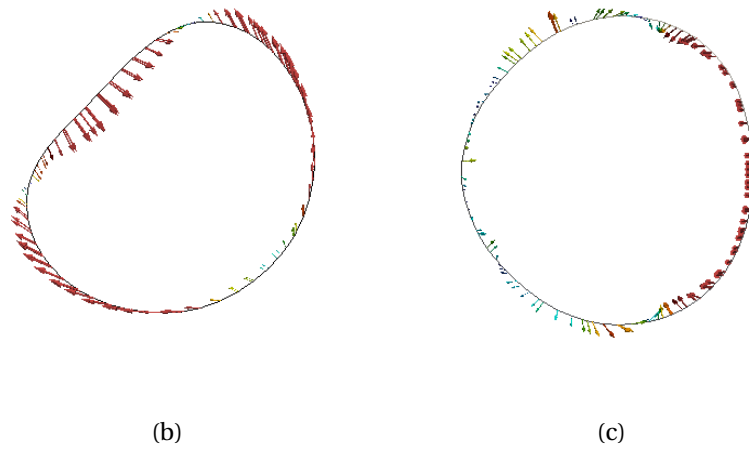
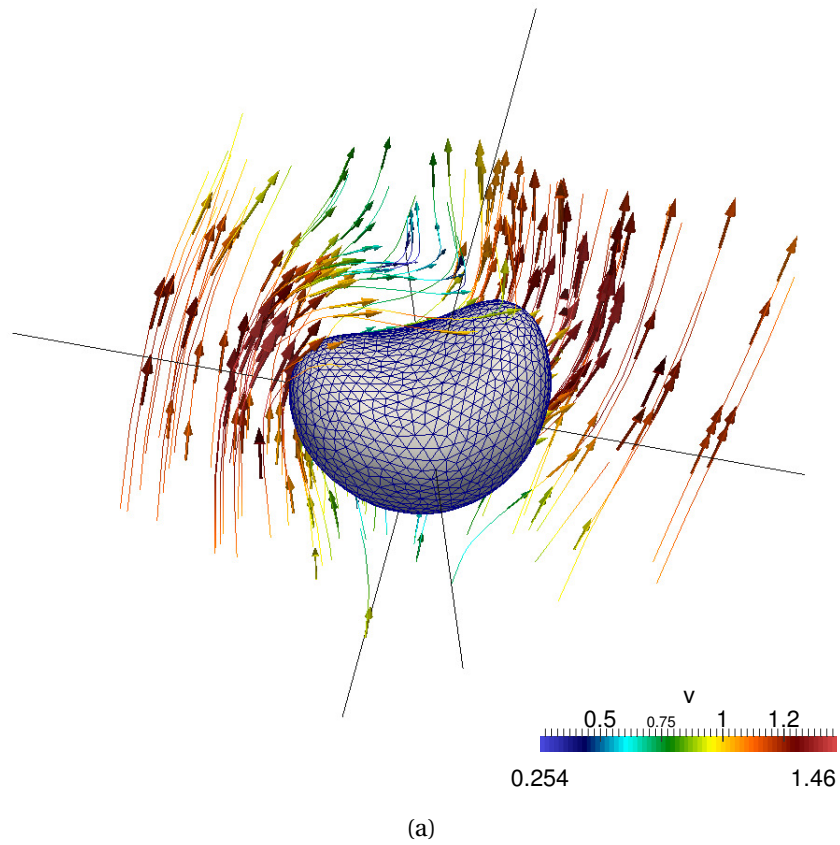


Figure 63: Streamlines and drop's rims at  $t \approx 0.25$  - test ( $MS, 2.0, 3.0$ ): (a) streamlines and velocity field; (b) drop's rim on the plane  $xy$ ; (c) drop's rim on the plane  $xz$ .

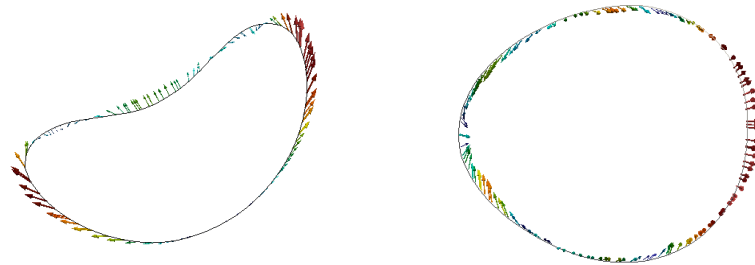
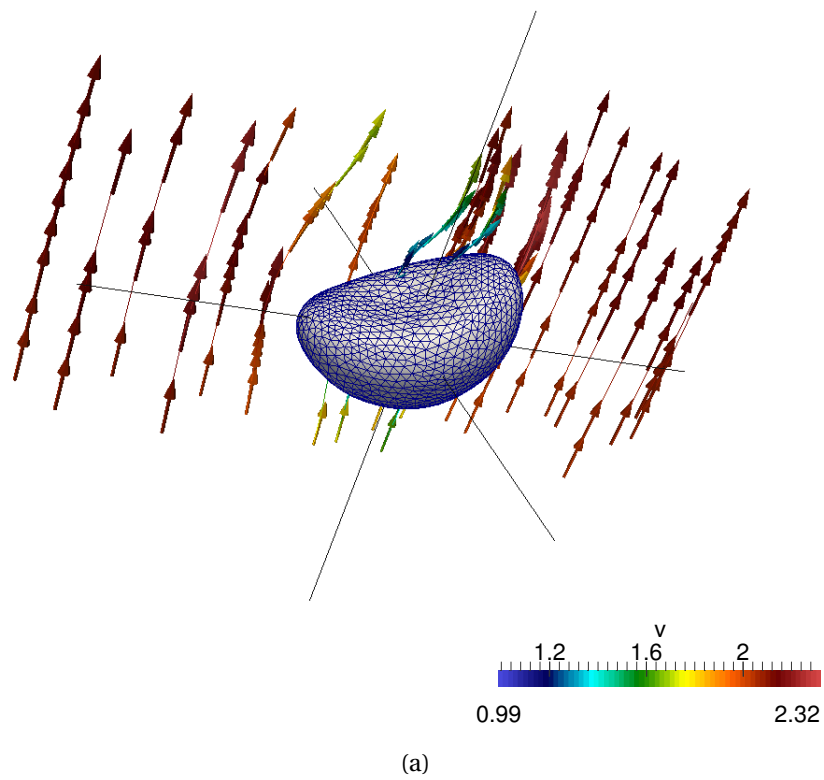


Figure 64: Streamlines and drop's rims at  $t \approx 0.50$  - test ( $MS, 2.0, 5.0$ ): (a) streamlines and velocity field; (b) drop's rim on the plane  $xy$ ; (c) drop's rim on the plane  $xz$ .

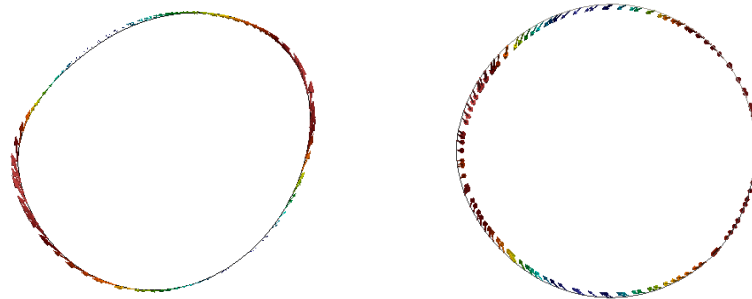
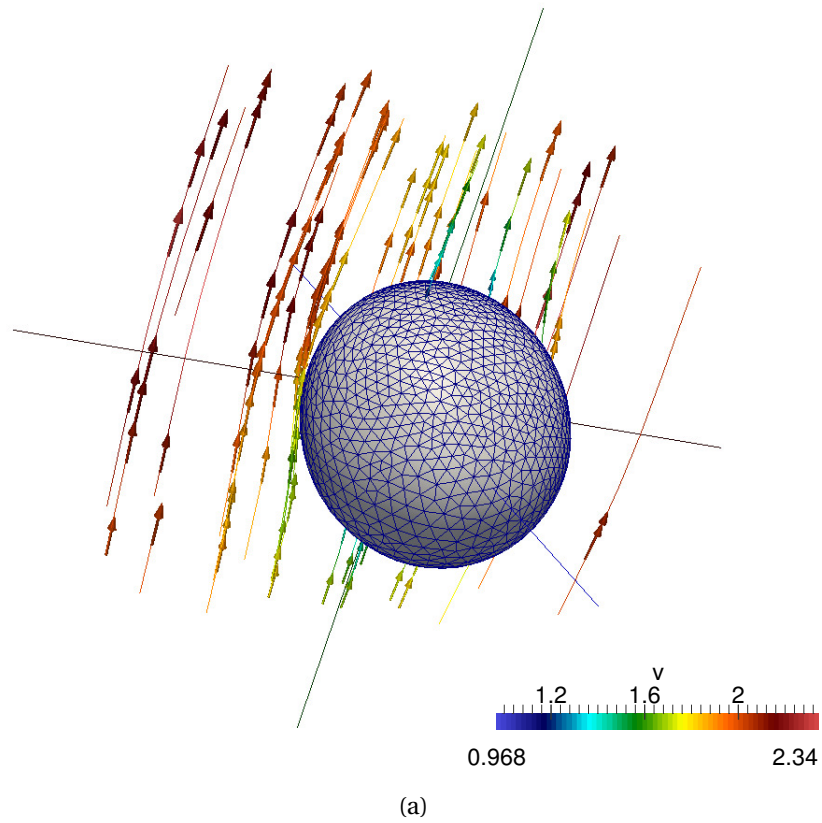


Figure 65: Streamlines and drop's rims at  $t \approx 0.37$  - test  $(WL, 2.0, 1.5)$ : (a) streamlines and velocity field; (b) drop's rim on the plane  $xy$ ; (c) drop's rim on the plane  $xz$ .

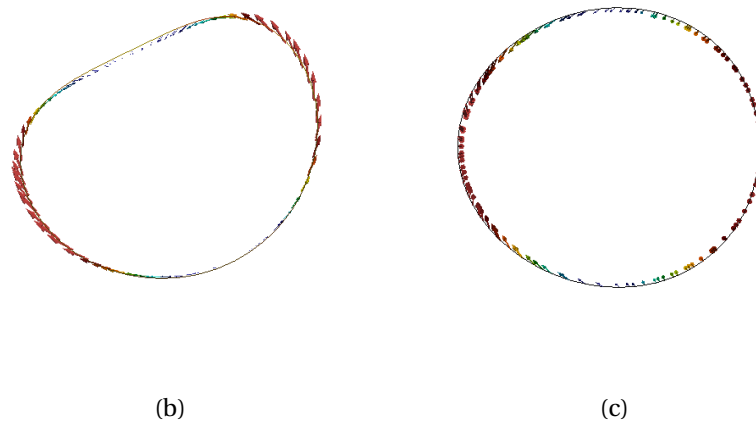
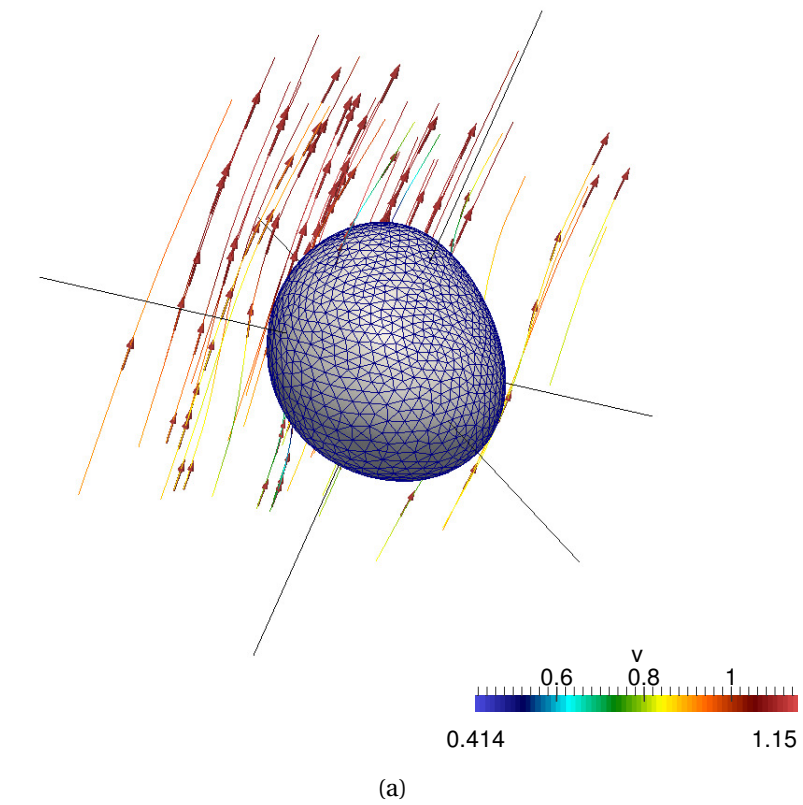


Figure 66: Streamlines and drop's rims at  $t \approx 0.25$  - test ( $WL, 2.0, 3.0$ ): (a) streamlines and velocity field; (b) drop's rim on the plane  $xy$ ; (c) drop's rim on the plane  $xz$ .

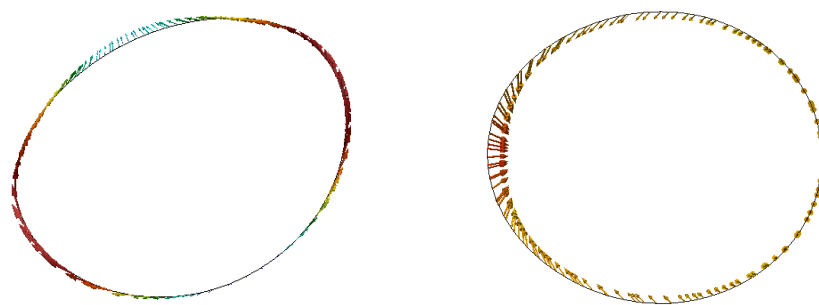
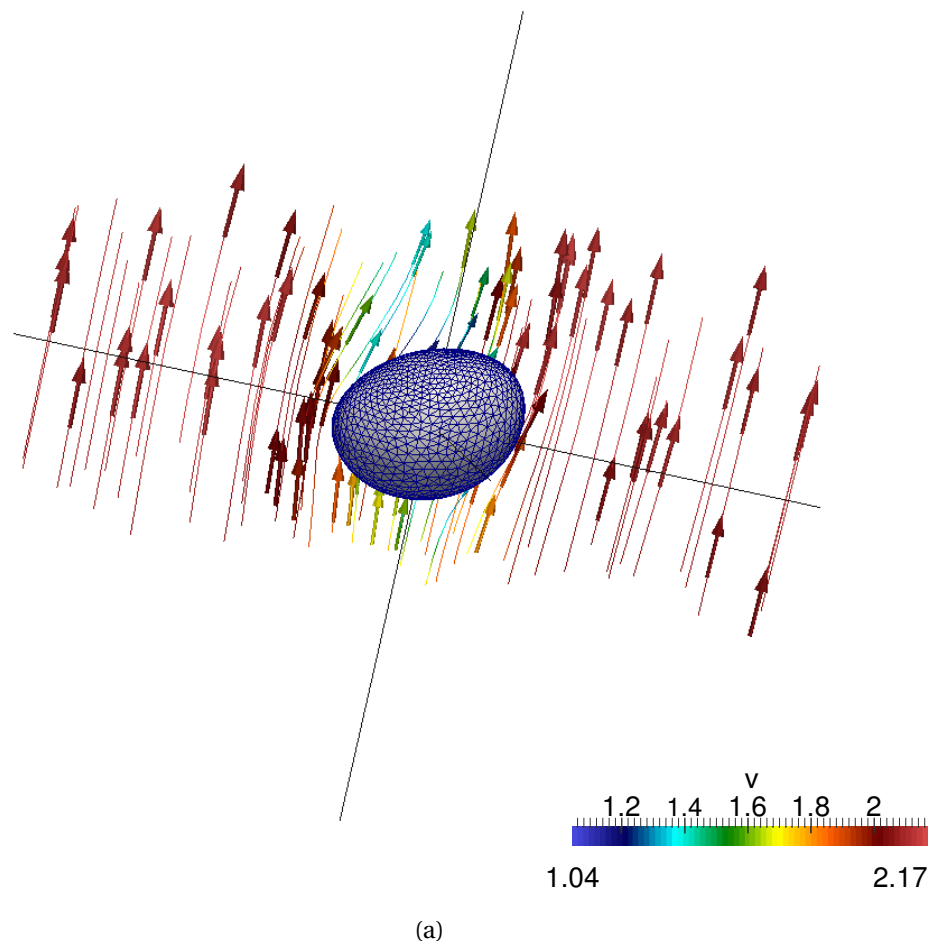


Figure 67: Streamlines and drop's rims at  $t \approx 0.47$  - test ( $WL, 2.0, 5.0$ ): (a) streamlines and velocity field; (b) drop's rim on the plane  $xy$ ; (c) drop's rim on the plane  $xz$ .

## 7.4 Trajectory curves, drop shape variations and spectrum analyses

### 7.4.1 Trajectory curves

The drop's behaviour concerning the trajectory that it experiences by incidence of the crossflow is represented by curves projected onto the planes  $xy$  and  $xz$ . The former class of projections display the deflection caused by the transverse flow; the latter class of projections display the deviation of the drop away from its center of mass' trajectory. Although the trajectory is a three-dimensional curve, spatial variations occurring along the direction normal to the uniform crossflow were found to be of a much smaller order than those due to the deflection. Trajectories for the pair labeled as MS are plotted in Figure 68 and Figure 69, while that Figure 70 and Figure 71 concern the pair labeled as WL. Given the small changes taking place on the plane  $xz$ , we will focus on analyzing the curves traced on the planes  $xy$ .

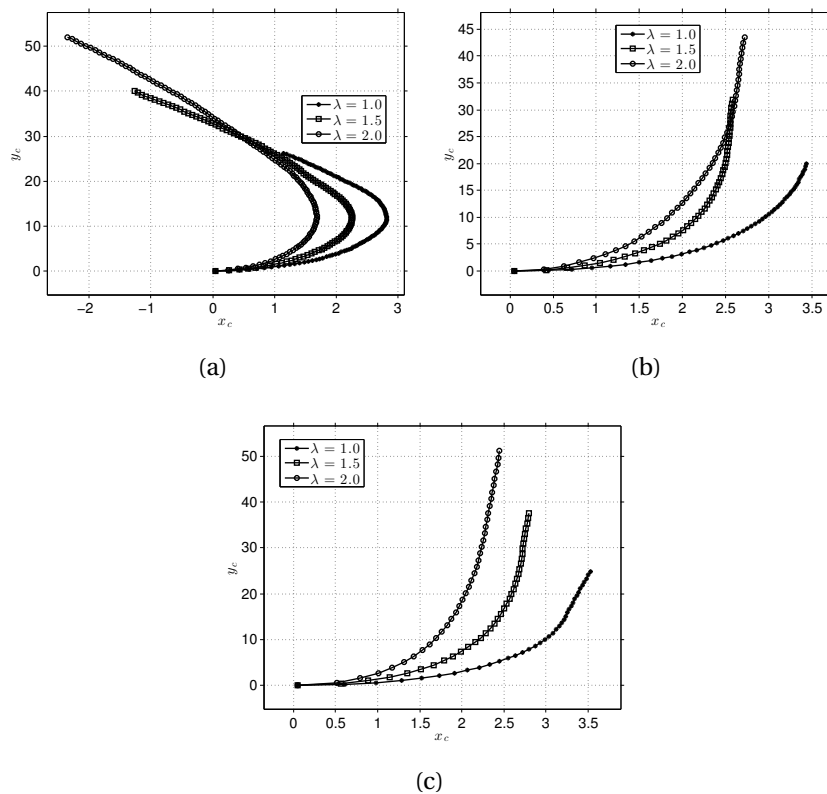


Figure 68:  $xy$ -plane drop trajectory - MS: (a)  $(MS, \cdot, 1.5)$ ; (b)  $(MS, \cdot, 3.0)$ ; (c)  $(MS, \cdot, 5.0)$ .

As expected, the higher is the value of  $\lambda$  the broader is the deflection of the drop jet. This behaviour is consistent for almost all the cases simulated although the scale of displacement between the  $x$  and  $y$  directions varies from 1::14 to 1::17 in these cases, meaning



that the crossflow dominance takes place quickly. The unique exceptions are the curves traced by the drop in the simulations of the group  $(\cdot, \cdot, 1.5)$  which, as mentioned in the previous subsection, suggest that the drop moves oppositely to its initial direction of launch.

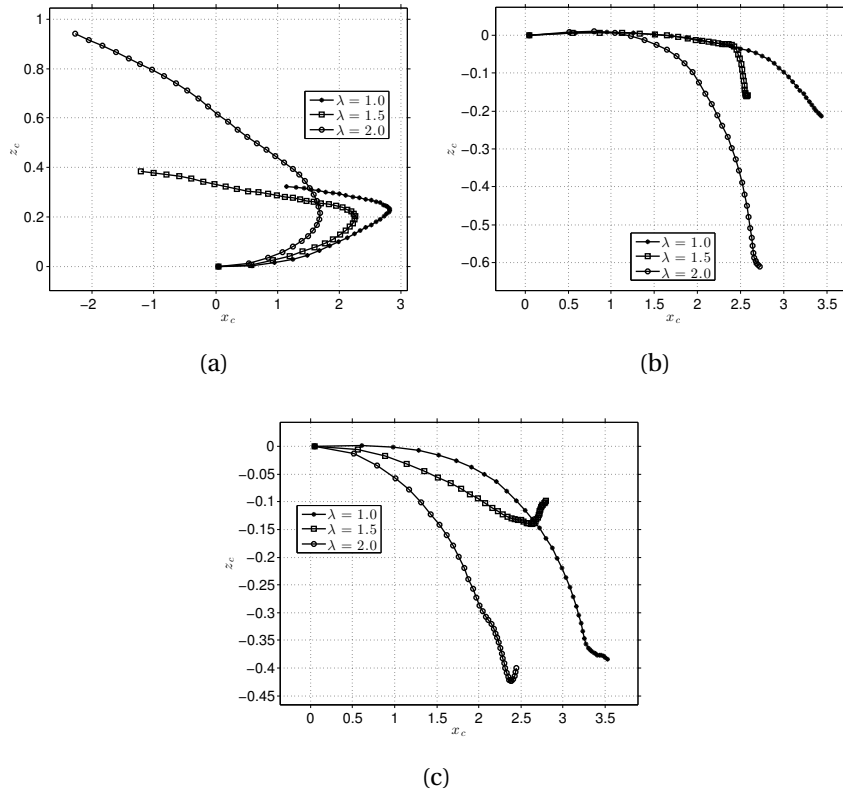


Figure 69:  $xz$ -plane drop trajectory - MS: (a)  $(MS, \cdot, 1.5)$ ; (b)  $(MS, \cdot, 3.0)$ ; (c)  $(MS, \cdot, 5.0)$ .

The cases that describe the most uncommon behaviours are the ones of the family  $(WL, \cdot, 1.5)$ , whose motion backward occurs in a scale 1::4. A possible explanation for this situation may be related to the effect of a  $L_P$  reduced and the consequences coming from the periodic gap among drops declared as follows: the drop jet is launched with velocity  $U_J$ ; due to the constant crossflow, the profile imposed and the momentum exchange, the drop loses velocity and deforms; the drop's deformation at the initial instants is caused by marked flatness that forms a wider surface area which, in turn, eases the crossflow actuation; finally, the crossflow pushes the drop backward. Such a description is coherent with the profile of  $\phi(t)$  for  $L_P = 1.5$  depicted in Figure 73. It is possible to observe that the flatness curve increases to values above 1.0 for  $(WL, \cdot, 1.5)$ , whereas it decreases to values below 1.0 for these cases at the initial stages of motion, thus suggesting that a "lift" is produced. Furthermore, when comparing the profiles of elongation and flatness for the families  $L_P = 1.5$  to their respective profiles for  $L_P = 3.0, 5.0$ , we note that similar effects occur.

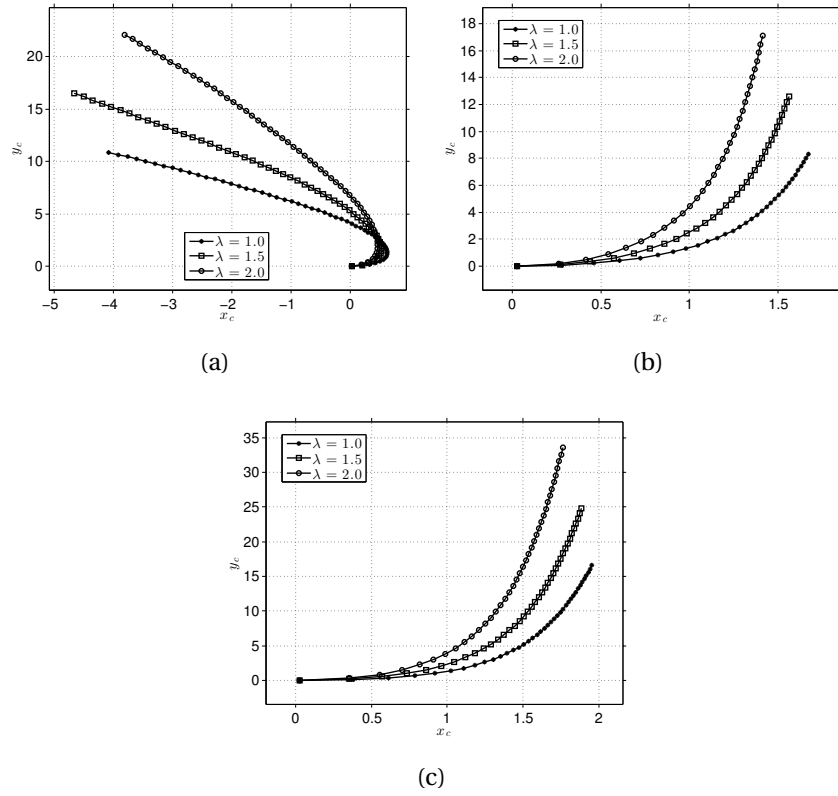


Figure 70:  $x y$ -plane drop trajectory - WL: (a)  $(WL, \cdot, 1.5)$ ; (b)  $(WL, \cdot, 3.0)$ ; (c)  $(WL, \cdot, 5.0)$ .

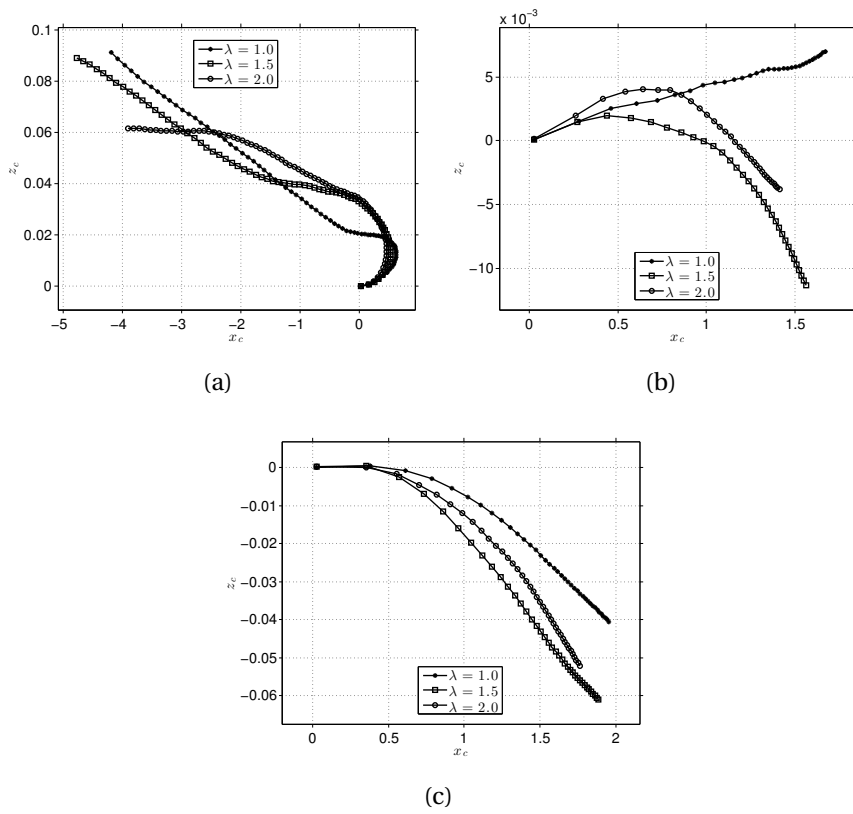


Figure 71:  $x z$ -plane drop trajectory - WL: (a)  $(WL, \cdot, 1.5)$ ; (b)  $(WL, \cdot, 3.0)$ ; (c)  $(WL, \cdot, 5.0)$ .

### 7.4.2 Drop shape variations

To analyze the shape assumed by the drop in the flow considered here, the expressions of aspect ratio for elongation and flatness are revisited from their definition in Equation (6.13), *i.e.*

$$\phi = \frac{b}{c}; \quad \psi = \frac{c}{a}, \quad (7.13)$$

for the principal axes  $a, b, c$ . The curves of  $\phi(t)_\lambda$  and  $\psi(t)_\lambda$  are sketched below for each simulation, by gathering the three different values of the ratio  $\lambda$  and of the length  $L_P$  per plot. The general behaviour for the curves is described by a region of oscillation, when the drop deforms by action of the crossflow, followed by another of damping, when the drop travels steadily. A specific feature that makes the profiles of the family MS differ from the ones of the family WL is the time interval in which some deformation is still evident, which extends up to around  $t \approx 4.5$  for WL and up to  $t \approx 20.0$  for MS. Arguments for having a much larger interval with predominance of deformation for the MS cases rely on the different physical properties of the flows, mainly on the value of the  $We$  number which, being smaller, indicates that the forces due to the surface tension dominate over the inertial forces as well as that the drop is less tolerant to deformation. In this comparison, a caveat should be raised for the cases  $L_P = 1.5$ , that show some level of noise and out-of-phase oscillation for different values of  $\lambda$ , besides being unclear to describe.

Another point to consider about the curves of  $\phi(t)_\lambda$  and  $\psi(t)_\lambda$  concern their amplitude. It is seen that, for all the cases simulated, the maximum and minimum values of flatness are, respectively, higher and lower than elongation's, thus suggesting that there are more shapes with wider surface area projected perpendicularly to the crossflow direction. One concludes, additionally, that the variation of  $\lambda$  causes shape deformations very similar to the drop, with localized discrepancies of phase occurring within the interval  $[0.0, t \approx 2.0]$ .

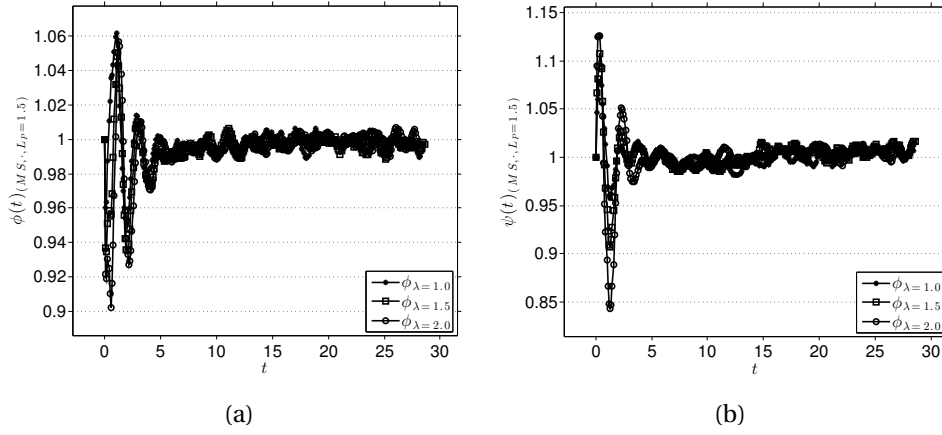


Figure 72: Drop shape variation -  $(MS, \cdot, 1.5)$ : (a)  $\phi(t)$ ; (b)  $\psi(t)$ .

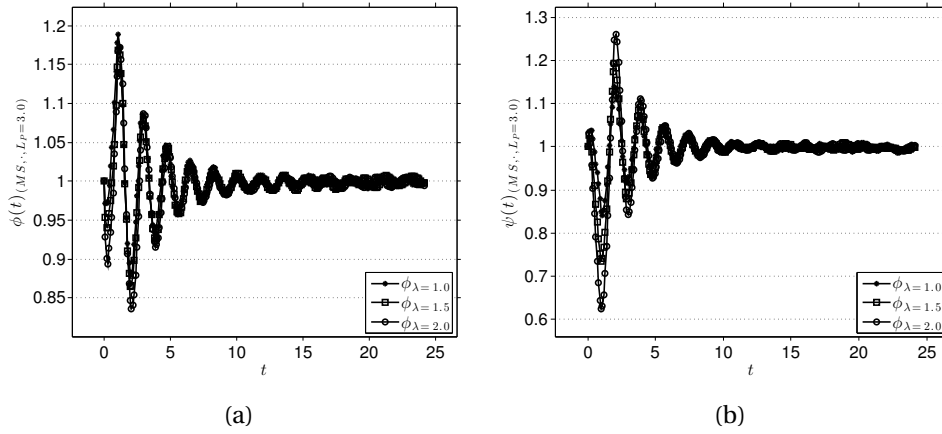


Figure 73: Drop shape variation -  $(MS, \cdot, 3.0)$ : (a)  $\phi(t)$ ; (b)  $\psi(t)$ .

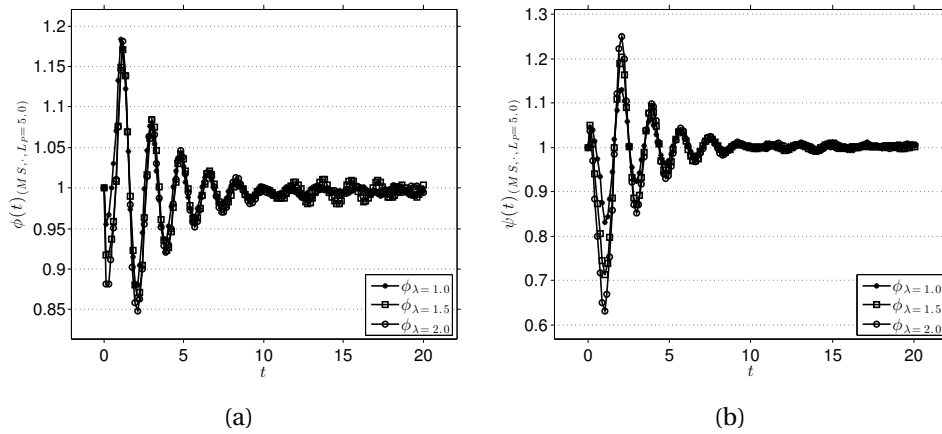


Figure 74: Drop shape variation -  $(MS, \cdot, 5.0)$ : (a)  $\phi(t)$ ; (b)  $\psi(t)$ .

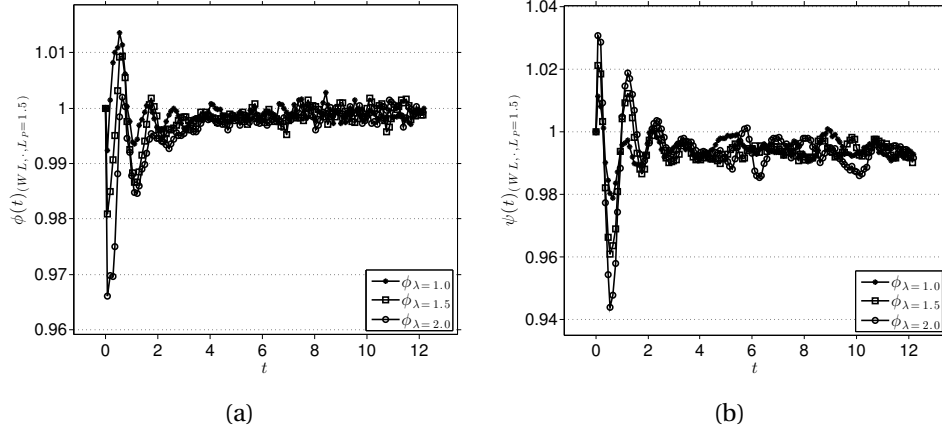


Figure 75: Drop shape variation -  $(WL, \cdot, 1.5)$ : (a)  $\phi(t)$ ; (b)  $\psi(t)$ .

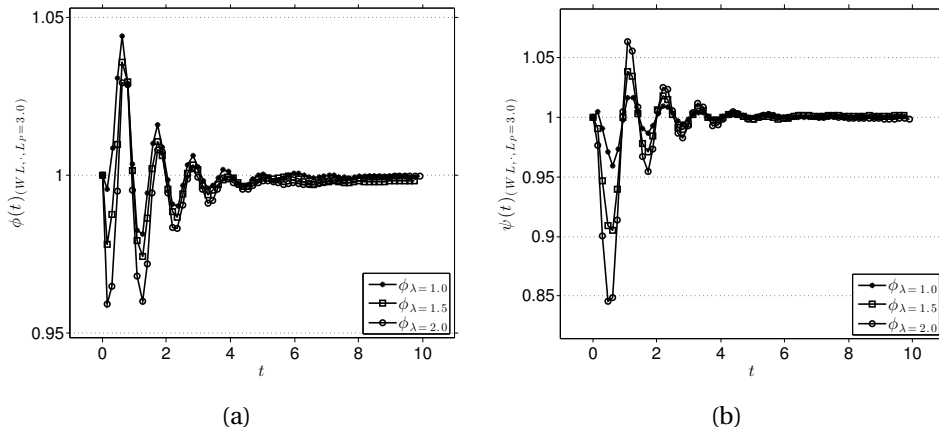


Figure 76: Drop shape variation -  $(WL, \cdot, 3.0)$ : (a)  $\phi(t)$ ; (b)  $\psi(t)$ .

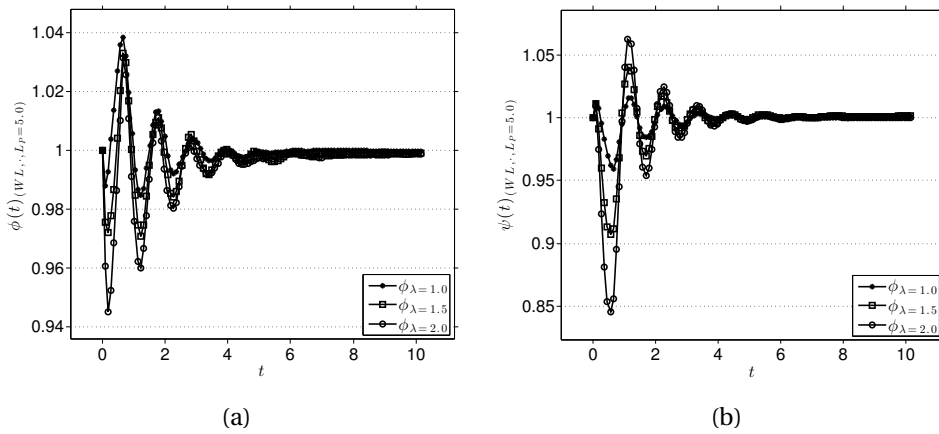


Figure 77: Drop shape variation -  $(WL, \cdot, 5.0)$ : (a)  $\phi(t)$ ; (b)  $\psi(t)$ .

### 7.4.3 Spectrum analyses

From this point on, spectrum analyses for the DJICF configurations studied are presented. The input signals for the FFT calculation correspond to the curves  $\phi(t)_\lambda$  and  $\psi(t)_\lambda$ , which evince disturbances affecting the drop. FFT-based spectra for elongation and flatness are plotted in the figures below separated according to the values of  $\lambda$ . Inasmuch as the spectrum of magnitude of such a disturbances is expressed as given by Equation (6.14), it is convenient to introduce in the following discussion the values given by

$$E_{\phi_\lambda} = \max\{|FFT[\phi(t)_\lambda]|\} \quad \text{and} \quad E_{\psi_\lambda} = \max\{|FFT[\psi(t)_\lambda]|\}, \quad (7.14)$$

which represent, respectively, the maximum disturbance energy achieved with the slight wobbling of the drop relative to the profiles of elongation and flatness, whereas

$$f_\phi^* \quad \text{and} \quad f_\psi^* \quad (7.15)$$

are dimensionless vibration frequencies (or harmonic modes) associated to each of these profiles within a sampling range  $t_s$ . The choice of  $t_s$ , however, was done by truncating the whole time of the simulations into the regions where the small disturbances were more active, thus restraining the interval of analysis. Besides, only the 10 first modes are plotted for each simulation. Spectra for the group MS are plotted from Figure 78 followed by spectra for the group WL plotted from Figure 81.

Table 7 lists the maximum energy values along with their respective most amplified modes associated to  $\phi(t)_\lambda$  and  $\psi(t)_\lambda$  for the testing configurations  $(Ref, \lambda, L_p)$ . Furthermore, note that

$$E_{F(t)} = \max\left\{\left(\Re\{FFT[F(t)]\}^2 + \Im\{FFT[F(t)]\}^2\right)^{0.5}\right\}, \quad F(t) = \phi(t)_\lambda, \psi(t)_\lambda \quad (7.16)$$

evokes the maximum value in modulus of complex modes associated to the shape ratios.

A point to be emphasized is that the output of  $FFT[F(t)]$  requires the sampling time range  $t_s$  to be uniform. Since the selection of the time step  $\Delta t$  may be different for each simulation and vary after remeshing operations (cf. Sec. 5.1 of [153]),  $t_s$  must be modified so

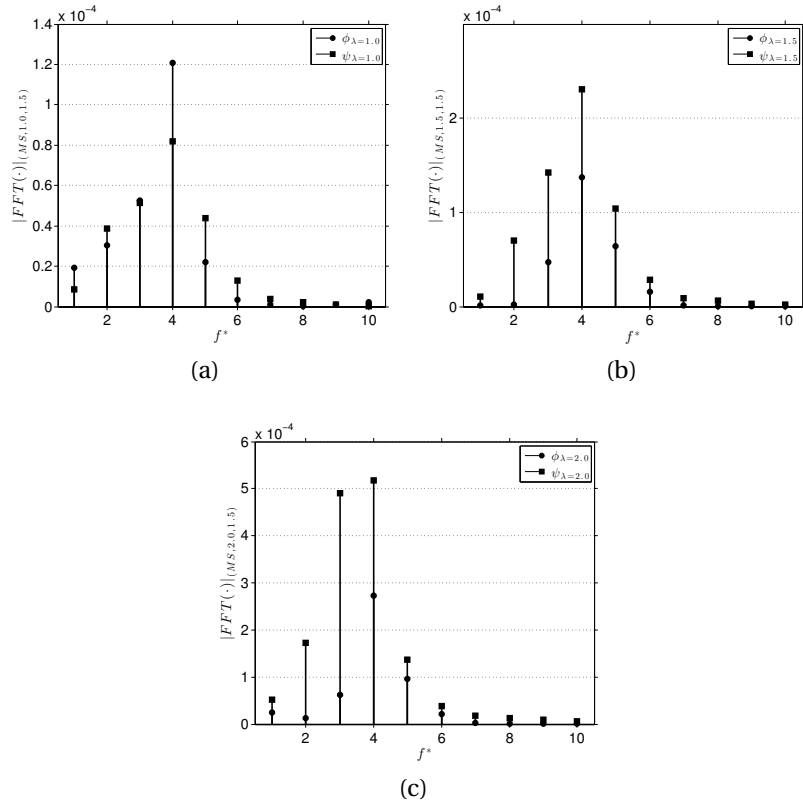


Figure 78: FFT-based spectrum: (a)  $(MS, 1.0, 1.5)$ ; (b)  $(MS, 1.5, 1.5)$ ; (c)  $(MS, 2.0, 1.5)$ .

that this uniformity be ensured. For that objective, the average time step

$$\overline{\Delta t} = \frac{(\Delta t)_n}{N} = \frac{(t^{n+1} - t^n)}{N}; \quad n = 0, 1, \dots, N-1 \quad (7.17)$$

and the function `interp1` from MATLAB® were used to build a new discrete vector  $t_S$  equally spaced from the original one. The sampling ranges specified for each case as well as the approximated thresholds from which the disturbances are attenuated are organized in Table 8.

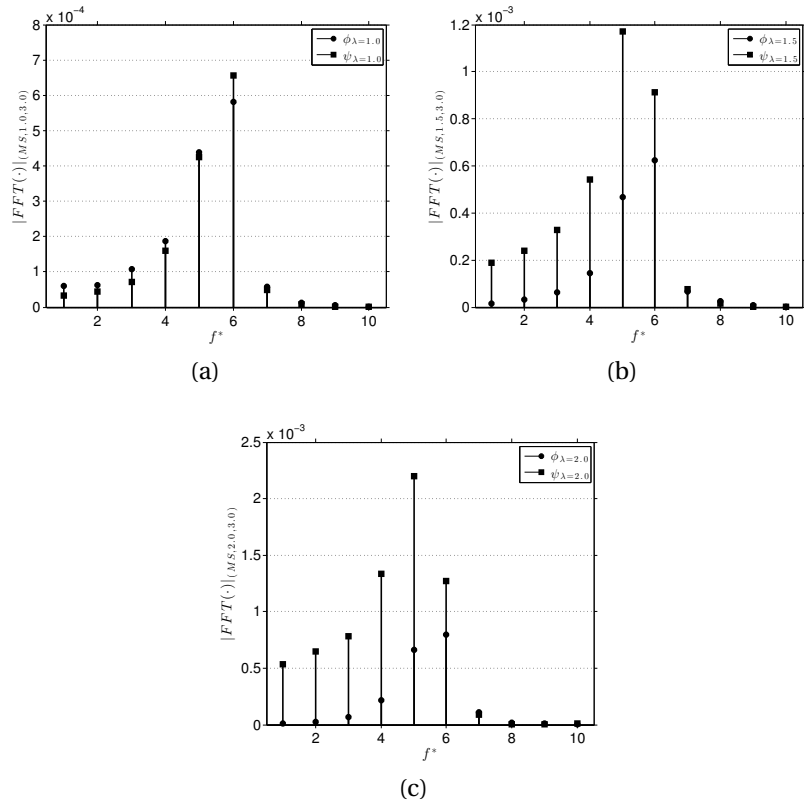


Figure 79: FFT-based spectrum: (a)  $(MS, 1.0, 3.0)$ ; (b)  $(MS, 1.5, 3.0)$ ; (c)  $(MS, 2.0, 3.0)$ .

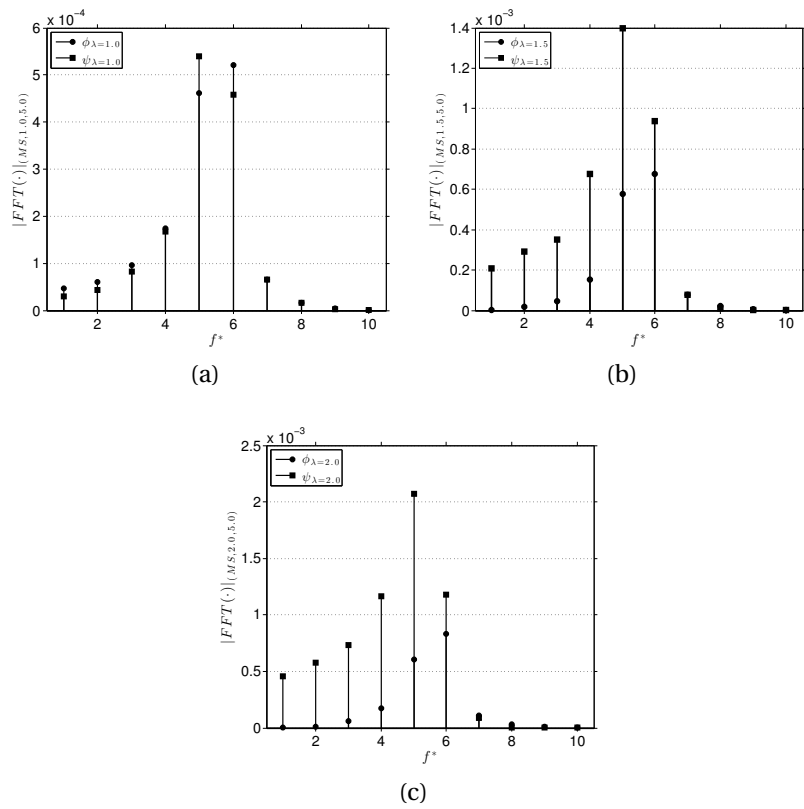


Figure 80: FFT-based spectrum: (a)  $(MS, 1.0, 5.0)$ ; (b)  $(MS, 1.5, 5.0)$ ; (c)  $(MS, 2.0, 5.0)$ .



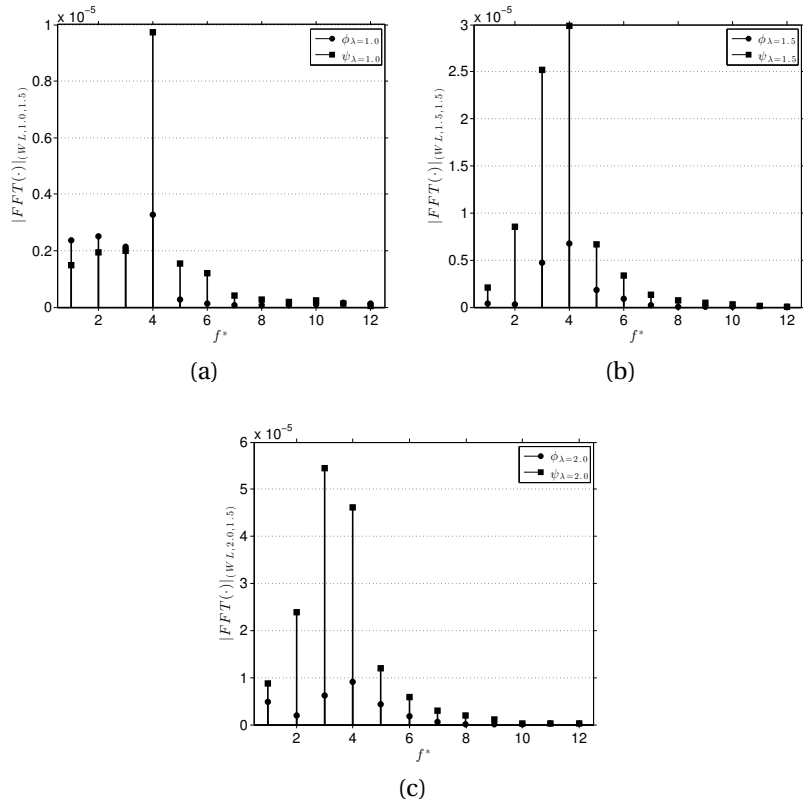


Figure 81: FFT-based spectrum: (a)  $(WL, 1.0, 1.5)$ ; (b)  $(WL, 1.5, 1.5)$ ; (c)  $(WL, 2.0, 1.5)$ .

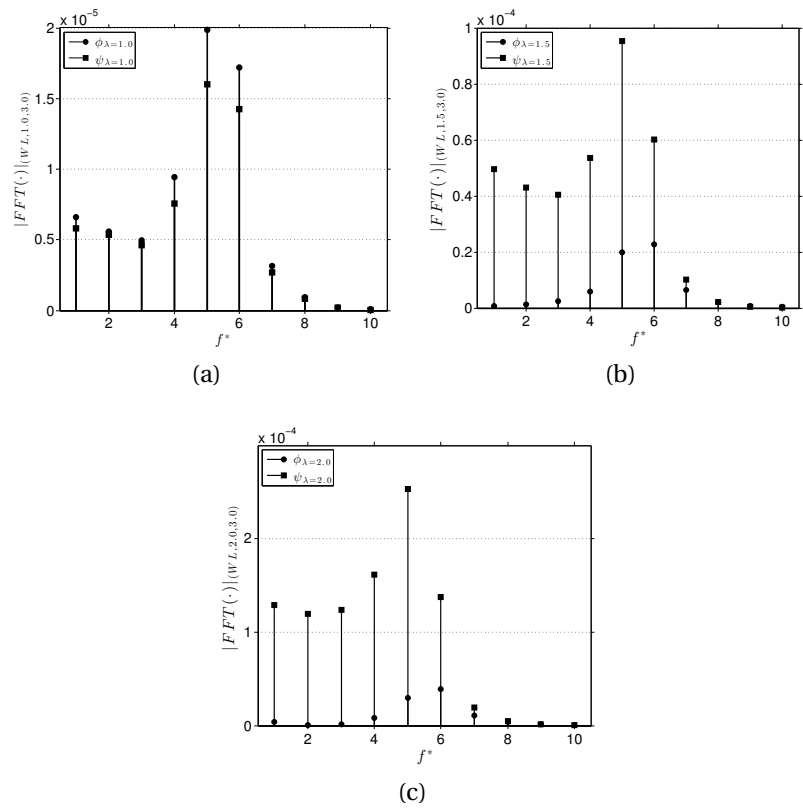


Figure 82: FFT-based spectrum: (a)  $(WL, 1.0, 3.0)$ ; (b)  $(WL, 1.5, 3.0)$ ; (c)  $(WL, 2.0, 3.0)$ .

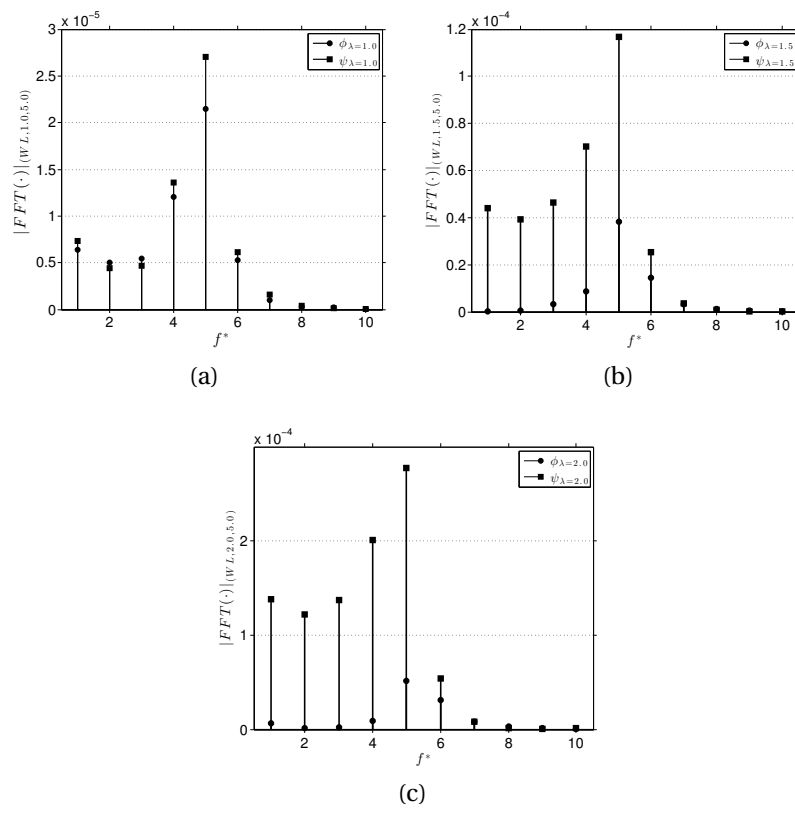


Figure 83: FFT-based spectrum: (a)  $(WL, 1.0, 5.0)$ ; (b)  $(WL, 1.5, 5.0)$ ; (c)  $(WL, 2.0, 5.0)$ .

Test Configuration ( <i>Ref</i> , $\lambda$ , $L_P$ )	Elongation: $\phi$		Flatness: $\psi$	
	$E_\phi$	$f_\phi^*$	$E_\psi$	$f_\psi^*$
( <i>MS</i> , 1.0, 1.5)	0.1209e-03	4	0.8209e-04	4
( <i>MS</i> , 1.5, 1.5)	0.1371e-03	4	0.2307e-03	4
( <i>MS</i> , 2.0, 1.5)	0.2724e-03	4	0.5173e-03	4
( <i>MS</i> , 1.0, 3.0)	0.5823e-03	6	0.6555e-03	6
( <i>MS</i> , 1.5, 3.0)	0.6240e-03	6	1.2000e-03	5
( <i>MS</i> , 2.0, 3.0)	0.7976e-03	6	2.2000e-03	5
( <i>MS</i> , 1.0, 5.0)	0.5204e-03	6	0.5398e-03	5
( <i>MS</i> , 1.5, 5.0)	0.6744e-03	6	1.4000e-03	5
( <i>MS</i> , 2.0, 5.0)	0.8320e-03	6	2.1000e-03	5
( <i>WL</i> , 1.0, 1.5)	0.3273e-05	4	0.9720e-05	4
( <i>WL</i> , 1.5, 1.5)	0.6780e-05	4	2.9883e-05	4
( <i>WL</i> , 2.0, 1.5)	0.9122e-05	4	5.4396e-05	3
( <i>WL</i> , 1.0, 3.0)	1.9835e-05	5	1.5984e-05	5
( <i>WL</i> , 1.5, 3.0)	0.2279e-04	6	0.9535e-04	5
( <i>WL</i> , 2.0, 3.0)	0.3907e-04	6	2.5348e-04	5
( <i>WL</i> , 1.0, 5.0)	2.1435e-05	5	2.7042e-05	5
( <i>WL</i> , 1.5, 5.0)	0.3822e-04	5	1.1677e-04	5
( <i>WL</i> , 2.0, 5.0)	0.5176e-04	5	2.7757e-04	5

Table 7: Maximum disturbance energies and dominant modes of the spectral analyses.

Test Configuration ( <i>Ref</i> , $\lambda$ , $L_P$ )	Sampling Range $t_S$	Threshold $t \approx$
( <i>MS</i> , 1.0, 1.5)	7.5	20.0
( <i>MS</i> , 1.5, 1.5)	7.5	20.0
( <i>MS</i> , 2.0, 1.5)	7.5	20.0
( <i>MS</i> , 1.0, 3.0)	10.0	20.0
( <i>MS</i> , 1.5, 3.0)	10.0	20.0
( <i>MS</i> , 2.0, 3.0)	10.0	20.0
( <i>MS</i> , 1.0, 5.0)	10.0	20.0
( <i>MS</i> , 1.5, 5.0)	10.0	20.0
( <i>MS</i> , 2.0, 5.0)	10.0	20.0
( <i>WL</i> , 1.0, 1.5)	4.0	12.0
( <i>WL</i> , 1.5, 1.5)	4.0	12.0
( <i>WL</i> , 2.0, 1.5)	4.0	12.0
( <i>WL</i> , 1.0, 3.0)	6.0	10.0
( <i>WL</i> , 1.5, 3.0)	6.0	10.0
( <i>WL</i> , 2.0, 3.0)	6.0	10.0
( <i>WL</i> , 1.0, 5.0)	5.5	10.0
( <i>WL</i> , 1.5, 5.0)	5.5	10.0
( <i>WL</i> , 2.0, 5.0)	5.5	10.0

Table 8: FFT sampling ranges and disturbance attenuation thresholds for the spectral analyses.

## 7.5 Mesh quality assessment

High-quality meshes are fundamental to produce accurate results. The poorer the mesh elements are generated, the poorer the solution is computed. Bad elements are those whose shape present certain disproportionalities or degeneracies which affect directly the results since they magnify a series of problems regarding conditioning, discretization and interpolation, for example.

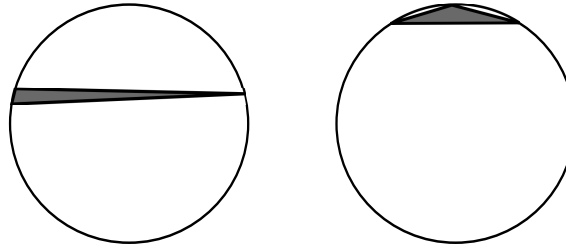


Figure 84: Examples of skinny triangular elements: needle, at left; cap, at right.

According to the literature concerned with mesh generation, such elements are called *skinny* elements. Some classes of bad-quality triangles and tetrahedra are depicted in Figure 84 and Figure 85, adapted from [209]. *Needle* elements have disparate edge lengths; *cap* elements either have an angle near  $180^\circ$  (a triangle) or a large solid angle (tetrahedron); *sliver* tetrahedra have very small circumradius-to-shortest edges ratio, but bad dihedrals. Preventing the existence of these elements while creating a mesh is one of the big challenges of a good mesh generator; so is developing robust dynamic meshing operations.

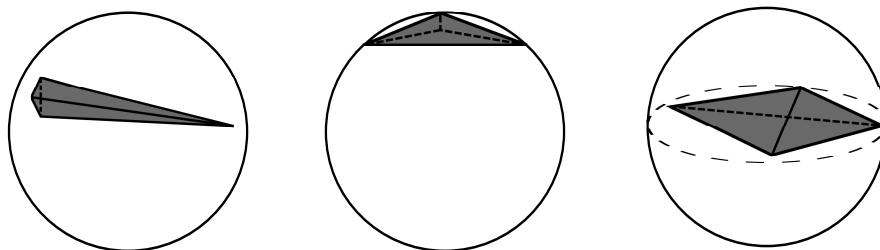


Figure 85: Examples of skinny tetrahedral elements: needle, at left; cap, at center; sliver, at right.

In order to verify the effectiveness of the dynamic meshing provided by the ALE/FE methodology used in this thesis such as reported in Section 4.4, the mesh quality of the simulations was assessed using a quality measure relative to the *ratio radius* of tetrahedra,

which reads as

$$\mathcal{J}_{tet}(t) = \left[ \frac{R_{out}(t)}{3R_{in}(t)} \right]_{tet}, \quad (7.18)$$

with  $R_{in}$  ( $R_{out}$ ) being the inradius (circumradius) of a tetrahedral element. The data analysis is plotted in the form of histograms ( $\mathcal{J}_{tet}(t) \times A$ ), where  $A$  is the number of mesh elements relative to the index  $\mathcal{J}_{tet}$ . That is to say, the better is the quality of an element the closer is  $\mathcal{J}_{tet}$  to 1.0 for this element. Note, furthermore, that  $\mathcal{J}_{tet}$  depends on time due to the arbitrary mesh motion and consequent change of the inradius and circumradius. However, provided that the mesh parameters are combined to produce good aspect ratios as well as fair point distributions as Equation (4.38) rules, it is expected that  $R_{in}$  and  $R_{out}$  do not vary overly with time.

As will be seen through the histograms plotted below, an overall quality measure will be given for the volume mesh. Since higher densities of  $\mathcal{J}_{tet}(t)$  are concentrated by far in the major part of the mesh elements, poor elements are almost absent in the simulations. This observation ensures not only the quality of the method itself, but also of the mesh generator. In the next subsections, the histograms of  $\mathcal{J}_{tri}(t)$  are displayed before those of  $\mathcal{J}_{tet}(t)$  for the MS and WL experimental conditions simulated. The behaviour of the histograms is very similar for all the cases simulated. For this reason, only a few arbitrarily chosen were considered.

The histograms gather data relative to the time instant when the insertion rate due to the dynamical meshing returns the highest amount of elements whose quality is maximum. Besides, the percentage of quality for this specific instant was computed so as to give the maximum order of quality attained in the associated simulation. Table 9 lists the information relative to the mesh quality assessment:  $t_A$  is the time when the mesh reaches the maximum number of tetrahedra;  $A_{\mathcal{J}}^{max}$  is the number of tetrahedra with the highest quality and  $\mathcal{O}_{\%}$  is the percentage of elements whose  $\mathcal{J}_{tet}$  is maximum in relation to the total mesh elements at  $t_A$ . The latter value emphasizes, additionally, the order of quality of the related test. It turns out, therefore, that the high values presented - above 90 % for all the cases except for (MS, 1.5, 3.0) - in the last column allow us to assert that the ALE/FE methodology applied is enough robust.

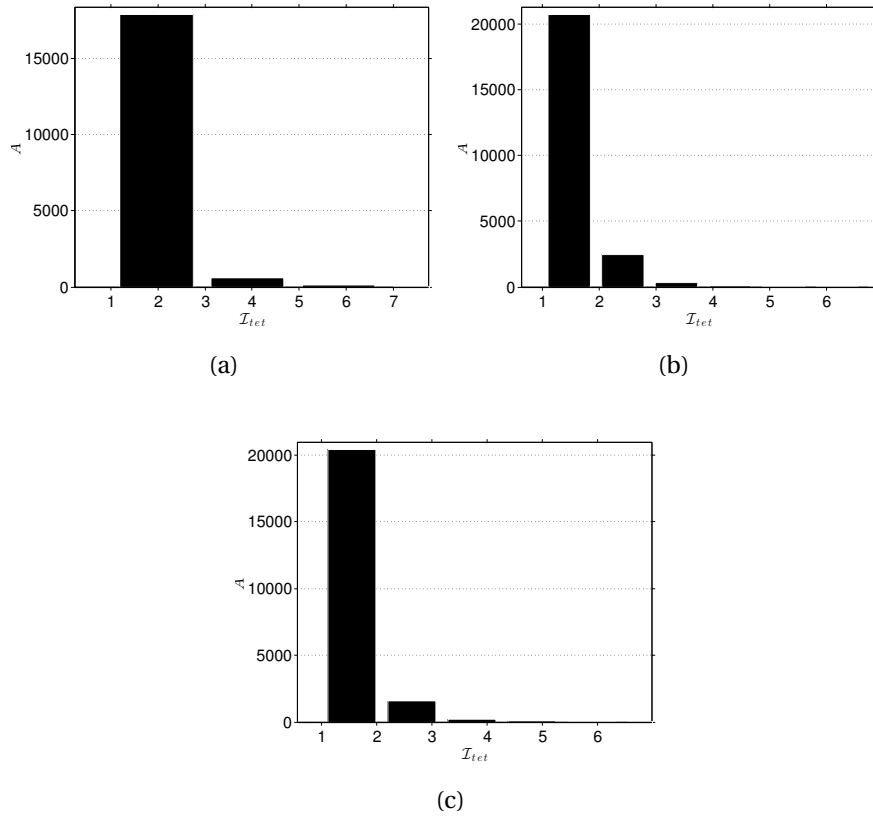


Figure 86: Histograms - group MS: (a) ( $MS, 1.0, 1.5$ ); (b) ( $MS, 1.5, 3.0$ ); (c) ( $MS, 2.0, 5.0$ ).

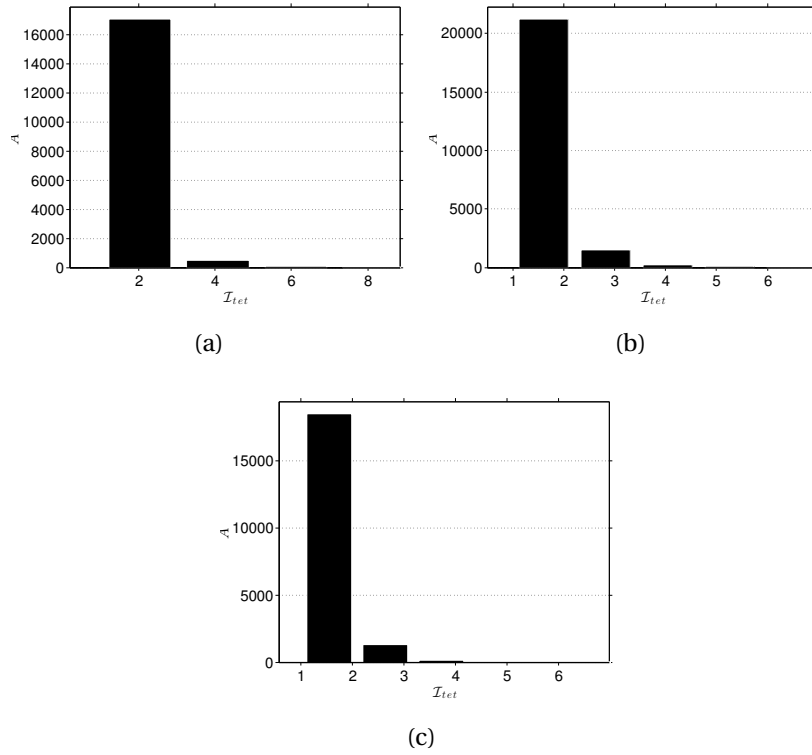


Figure 87: Histograms - group WL: (a) ( $WL, 1.0, 1.5$ ); (b) ( $WL, 1.5, 3.0$ ); (c) ( $WL, 2.0, 5.0$ ).

Test Configuration $(Ref, \lambda, L_P)$	Time Instant $t_A$	Number of Elements $A_{\mathcal{I}}^{max}$	Quality Percentage $\mathcal{O}_{\%}$
$(MS, 1.0, 1.5)$	1.03	17881	95.86
$(MS, 1.5, 3.0)$	8.50	20748	87.42
$(MS, 2.0, 5.0)$	25.47	20421	91.54
$(WL, 1.5, 1.5)$	8.17	17060	96.71
$(WL, 2.0, 3.0)$	9.68	21229	91.88
$(WL, 2.0, 5.0)$	13.22	18479	92.20

Table 9: Quality indicators relative to the statistical histograms  $(\mathcal{I}_{tet}(t) \times A; 10)$ .



## CONCLUSION

This thesis studied the numerical modeling of a particular flow featured by the influence of a crossflow over drops that detach off a continuous jet taking into account a periodic approach. The basis for this research was inspired in the well-known canonical flow of a jet in crossflow, which was dealt with in a nonturbulent scope. Given the large amount of research concerned with strong jet-to-crossflow ratios as well as with vortical structures shedding through gas-liquid mixtures, this study took a different path when investigating weak crossflow ratios in liquid-liquid interfaces. Assumptions were established concerning the focus on the jet's primary breakup zone and the inclusion of periodic boundary conditions into the model. Nevertheless, the computational structure as well as the ideas behind the numerical algorithms demonstrated to be a promising tool in studying other two-phase flow regimes pictured by dispersed bubbles and drops.

In Chapter 2, we addressed the fundamental aspects of the ALE description, introduced a short review on numerical methods available to model two-phase flows, and discussed a few topics of the mechanics with interfaces, such as the jump of properties near an interface and the existence of surface tension. Finally, we established a mathematical description of the meshing structures applied in the computational code used in this thesis to provide organization of the content and resources for better theoretical outlines.

Basic principles used in CFD, governing equations, and the one-fluid formulation were introduced in Chapter 3, by emphasizing the inclusion of the volumetric representation of the surface tension force into the momentum equation and how a marker function is implemented to identify the different fluids or phases making up the flow. Additionally, selected information about the semi-Lagrangian method and the projection method were given.

Chapter 4 along with Chapter 5 provided the detailed description of the FE formulation applied to two-phase flows as used in this thesis, by integrating the variational approach to include periodic boundary conditions into this set. Moreover, they explained the peculiarities of the operational tools that make up this methodology, subsequently applied to validation tests in Chapter 6 that certified the implementations.

The drop jet in crossflow investigated with details in Chapter 7, starting from the configuration of a very particular testing setup for studying different fluid-fluid cases. A

technique based on a moving-frame reference were extended to deal with transverse flows. Despite of using only two fluid pairs of known experimental applicability, several data could be extracted from combinations of parameters defining the jet-to-crossflow ratio and the periodic cell's length, such as analyses of hydrodynamics, drop shape, spectrum and mesh quality so promoting a handful of computational and statistical information fairly complete as regarding the intended goals of this thesis.

Generally, the ALE/FE methodology employed here gathers many advantages since it provides a generalized form to control the mesh motion, besides aggregating functions that enable versatile dynamic meshing operations, such as node addition, node deletion, mesh smoothing and refinement, which ensure a sophisticated level of adaptivity for different flow behaviours. To enforce the usability of the tools developed with this work, analyses of two-fluid configurations under experimental conditions were performed. Qualitative comparisons about the hydrodynamics of bubble and drops immersed in fluids commonly mentioned in literature as well as some contributions about shape factors and energy spectra were presented.

By considering the overall set of technicalities employed in this thesis, a not exhaustive list of issues can be arranged, of which specific problems may derive. Some directions for future work are the following.

- Development of high-order methods: as issues relating to numerical accuracy, not only the interpolation through the semi-Lagrangian method needs an upgrade from its linear capability, but also the projection method applied, which requires better accuracy.
- Algorithm improvement for PBC: although the matrix operations required to enforce the PBC over rows and columns follow a computational approach known as CSR (*Compressed Sparse Row*), which stores only the nonzero entries of the matrices in order to escape memory allocation due to the sparsity, this methodology lacks improvement for column operations. The strategy was implemented for square matrices and well applied for symmetric matrices while taking advantage of the symmetry to produce more compact loops. Nonsquare matrices, however, are not optimized as to column loops. Furthermore, the computation time for PBC operations also require additional observation.

- Selection of boundary conditions: the methodology presented here combines PBC, DBC, and NBC set by selecting boundary physical groups tagged at the pre-processing level. While the formulated problems are well defined with regard to the mathematical point of view, their numerical resolution might be intricate when defining consistent boundary conditions. Running tests showed that the choice among pairs solver-preconditioner may render dependent on the problem. Intersection points, viz. corner points, which share different boundaries worth careful attention and better strategies to select priorities should be achieved.
- Multidimensional periodicity: in this thesis, the periodicity was applied only in one direction. Although this capability enables the simulation of several flows of practical interest, other situations in which multidimensional periodicity occurs need to be covered. The alternative way is to extend the mesh generation for more complex surfaces, obtained by translation or rotation, for instance, and suit the computational code to receive such extra functionality.
- Handling of topological changes: the modelling of physical phenomena associated to the topological changes of dispersed bodies in two-phase configurations, such as acute deformations, breakup and coalescence is not completely solved in the current code. Besides requiring the reordering of the data structures responsible to save the mesh data, such a capability should be assessed so that the physical interactions among the dispersed bodies are respected. Flows whose hydrodynamic effects are complex (e.g. approaching velocity, film thinning and rupture in bubble coalescence) represent a path to be unveiled.
- Coupling of physical mechanisms: diabatic flows inside the scope of heat and mass transfer dynamics together with multidimensional periodicity are a goal to be achieved, since modern applications encompassing two-phase flow regimes, such as bubbly and slug flows, have a big quota of interest in thermo-mechanical applications where ubiquitous temperature variations and heat transfer processes reign.
- Parallel computing: advancing toward data parallelism as well as evaluating the performance of the numerical code across a multi-core stage represents another potential learning curve regarding the current code.

- Curvature and capillary pressure modelling: the curvature computation follows a geometrical idea which is based on the Frénet's relations. Although the results obtained until now are satisfactory for a class of dispersed flows, namely bubbles and drops, other flow regimes, such as annular and jet flows require additional attention because of their prolonged interfaces. Since they may have instabilities, localized high-curvature zones may be generated by peaked nodes that cause unavoidable bad-shaped elements. Therefore, new alternatives for interpolation and capture of numerically uncontrollable curvatures should be developed. Additionally, advancements in the coupling with PBC are necessary as regards to the computation of curvature over the periodic faces over which interface points overlap.
- Marangoni effects: flows subject to Marangoni effects generated by surface tension gradients due to the influence of either contaminants or surfactants as well as reactive flows represent another field of study opened to the numerical code used in this thesis.
- Multifluid interaction: all cases dealt with here take a two-fluid/two-phase flow condition. Although the interaction of too many dispersed elements can be studied in these conditions, the codification required to include three or more substances should be implemented. Surely, this further step will open up several opportunities of study.
- Extensions for the drop jet configuration: the inclusion of gravity is an incremental effect to be considered in the future. Another point to be considered sticks to the imposition of the initial condition of the jet. It is known that disturbances emerge from a drop that detaches off a unbroken liquid jet, which may propagate with the drop's motion. Therefore, the survey on an initial condition that considers such effects is deserves additional study. Concerning the periodic spacing of drops, a condition similar to a "multipole flow" formed by sources and sinks interposed in-line may help to resolve the flow in the gaps between trailing and leading drops whilst also resorts to a disturbed flow around the drops.

To conclude, it should be emphasized that have been arising not only many variants of the classical FEM along the recent decades, but also many opportunities for newer applications. Incompressible two-phase flows, strictly, represent an important portion of this whole and so will be the ongoing tools intended to develop FEM codes. ALE/FEM methods have gained immeasurable proportions in fluid-structure interaction problems, from which other

front-end creative solutions may appear and be adapted for different situations. Moreover, with the ascension of FE-based commercial codes, the state-of-art in developing scientific MCFD codes with robust and uncomplicated programming languages in this field will may be able to become a prosper research line.

**APPENDIX A - Code Flowcharts**

This appendix gathers overview flowcharts of the FE-based in-house code used in this thesis concerning the three basic macro stages of any software turned to Computational Fluid Dynamics as well as a very simple UML partial diagram of the main C++ classes involved in the PBC programming.

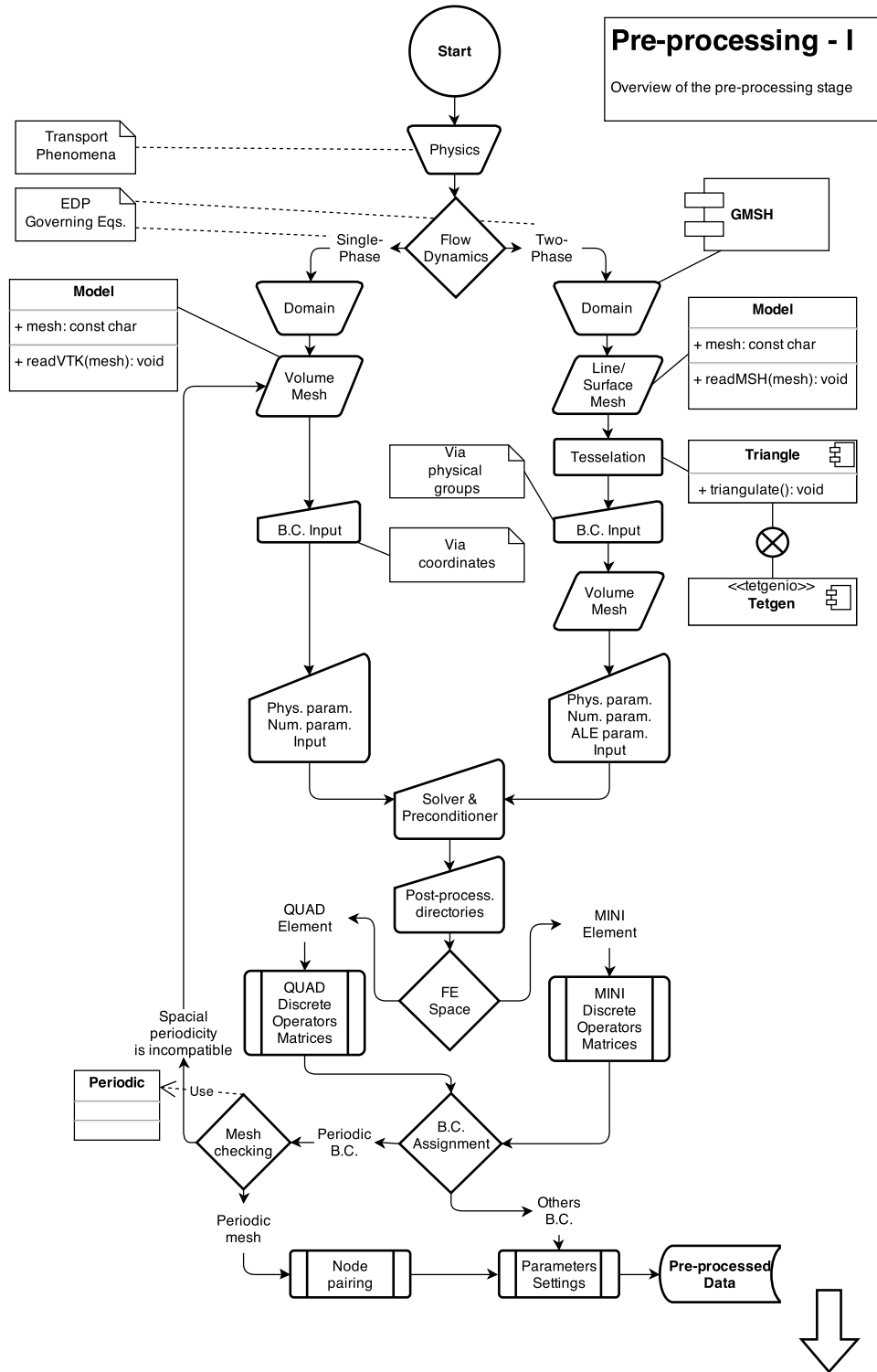


Figure 88: Flowchart I: pre-processing stage.

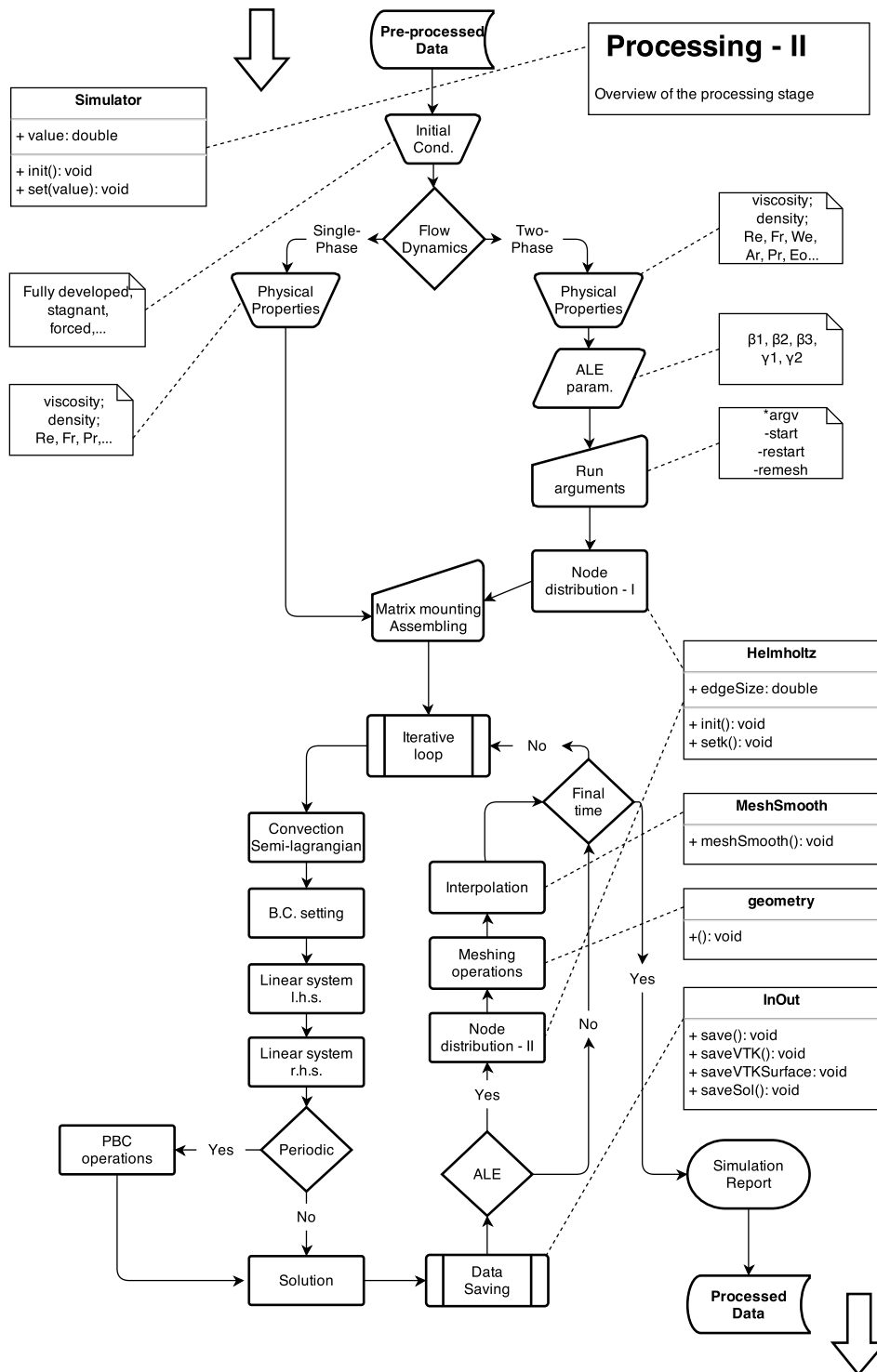


Figure 89: Flowchart II: processing stage.



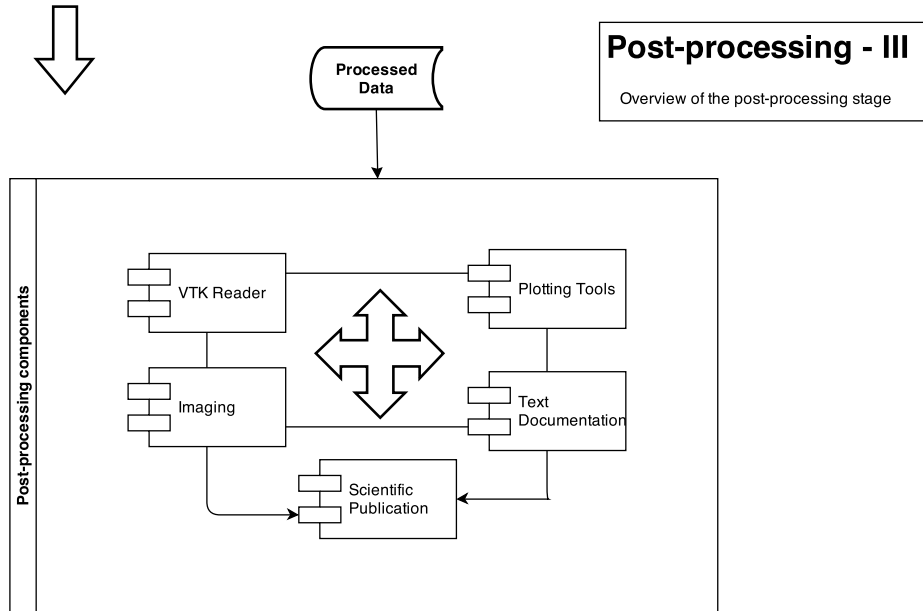


Figure 90: Flowchart III: post-processing stage.

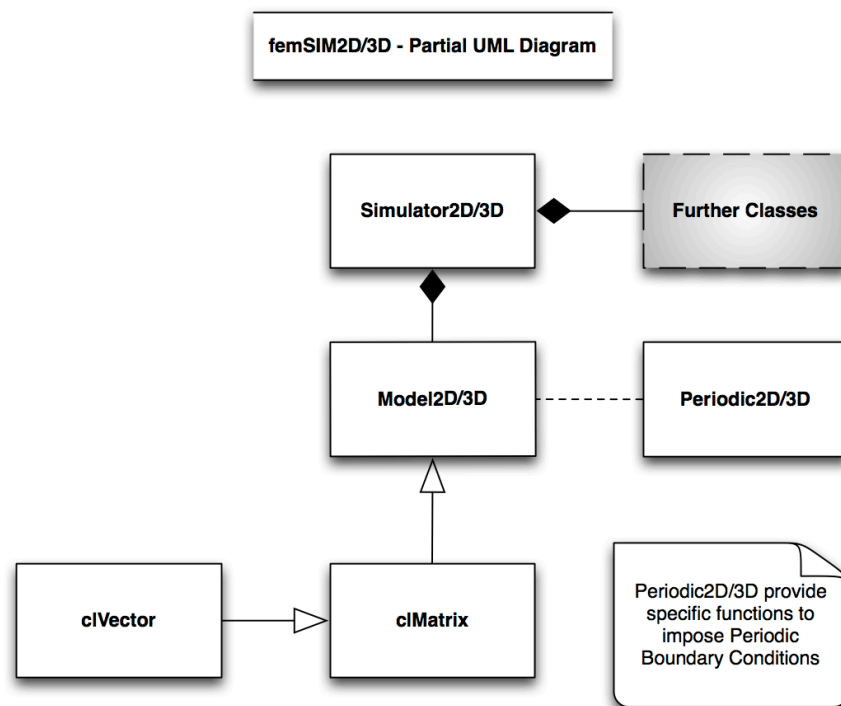


Figure 91: UML partial diagram of the in-house femSIM2D/3D code.

**APPENDIX B - GMSH SCRIPT SAMPLE (PERIODIC SURFACE)**

```

/* File: sample-periodic-surface-thesis.geo
 * Author: Peixoto de Oliveira, Gustavo
 * Date: December 31st, 2013
 * Description: Generates a 3D channel with periodicity
 *      and array of nb equally-spaced spheres.
 */

// Characteristic Lengths
b = 0.08; // bubbles
wp = 0.2; // walls

// Boundary Geometry
xMin = 0;
yMin = 0;
zMin = 0;

r1 = 1; // radius
D = 2*r1; // diameter

// Bubble Parameters
DB = 1; // bubble diameter
rb = DB/2; // bubble radius

g = rb; // gap length
s = 2*g; // slug length

nb = 3; // number of bubbles
LM = nb*DB + (nb - 1)*s; // bubble array
L = LM + 2*g; // channel length

// 1. PERIODIC SURFACES

// left end
p1 = newp;
Point(p1) = {xMin,yMin,zMin,wp}; // center
p2 = newp;
Point(p2) = {xMin,yMin,zMin - r1,wp};
p3 = newp;
Point(p3) = {xMin,yMin + r1,zMin,wp};
p4 = newp;
Point(p4) = {xMin,yMin,zMin + r1,wp};
p5 = newp;
Point(p5) = {xMin,yMin - r1,zMin,wp};

// right end
p6 = newp;
Point(p6) = {xMin + L,yMin,zMin,wp}; // center
p7 = newp;

```

```

Point(p7) = {xMin + L,yMin,zMin - r1,wp};
p8 = newp;
Point(p8) = {xMin + L,yMin + r1,zMin,wp};
p9 = newp;
Point(p9) = {xMin + L,yMin,zMin + r1,wp};
p10 = newp;
Point(p10) = {xMin + L,yMin - r1,zMin,wp};

/* --- BUILDING CIRCLES --- */
// left end
c1 = newc;
Circle(c1) = {p2,p1,p3};
c2 = newc;
Circle(c2) = {p3,p1,p4};
c3 = newc;
Circle(c3) = {p4,p1,p5};
c4 = newc;
Circle(c4) = {p5,p1,p2};

// right end
c5 = newc;
Circle(c5) = {p7,p6,p8};
c6 = newc;
Circle(c6) = {p8,p6,p9};
c7 = newc;
Circle(c7) = {p9,p6,p10};
c8 = newc;
Circle(c8) = {p10,p6,p7};

/* --- BUILDING EXTERNAL LINES --- */
l1 = newl;
Line(l1) = {p2,p7};
l2 = newl;
Line(l2) = {p3,p8};
l3 = newl;
Line(l3) = {p4,p9};
l4 = newl;
Line(l4) = {p5,p10};

// 2. INTERNAL DOMAIN - BUBBLES

// Origin
x0 = xMin;
y0 = yMin;
z0 = zMin;

For i In {1:nb} // BEGIN LOOP

// --- spherical bubble points

```

```

pp9 = newp;
Point(pp9) = {x0 + g + rb + (i - 1)*(DB + s), y0, z0, b};
pp10 = newp;
Point(pp10) = {x0 + g + rb + (i - 1)*(DB + s), y0, z0 - rb, b};
pp11 = newp;
Point(pp11) = {x0 + g + rb + (i - 1)*(DB + s), y0 + rb, z0, b};
pp12 = newp;
Point(pp12) = {x0 + g + rb + (i - 1)*(DB + s), y0, z0 + rb, b};
pp13 = newp;
Point(pp13) = {x0 + g + rb + (i - 1)*(DB + s), y0 - rb, z0, b};
pp14 = newp;
Point(pp14) = {x0 + g + (i - 1)*(DB + s), y0, z0, b};
pp15 = newp;
Point(pp15) = {x0 + g + DB + (i - 1)*(DB + s), y0, z0, b};

// --- BUILDING CIRCLES ---

// x-normal meridian
cc11 = newc;
Circle(cc11) = {pp12,pp9,pp11};
cc12 = newc;
Circle(cc12) = {pp11,pp9,pp10};
cc13 = newc;
Circle(cc13) = {pp10,pp9,pp13};
cc14 = newc;
Circle(cc14) = {pp13,pp9,pp12};

// z-normal meridian
cc15 = newc;
Circle(cc15) = {pp11,pp9,pp14};
cc16 = newc;
Circle(cc16) = {pp14,pp9,pp13};
cc17 = newc;
Circle(cc17) = {pp13,pp9,pp15};
cc18 = newc;
Circle(cc18) = {pp15,pp9,pp11};

// --- DISCRETIZATION (THETA) CIRCLES ---
nt2 = 14; // number of theta points per quarter of circle (total around circle is 4*nt)
//Transfinite Line{cc11,cc12,cc13,cc14,cc15,cc16,cc17,cc18} = nt2 Using Bump 1;

// BUBBLES' SURFACES
// reference: central axis is X-positive and theta counterclockwise

// 0:Pi/2
lb21 = newl;
Line Loop(lb21) = {cc12,cc13,-cc16,-cc15};
sb21 = news;

```

```

Ruled Surface(sb21) = {lb21};

// Pi/2:Pi
lb22 = new1;
Line Loop(lb22) = {-cc18,-cc17,-cc13,-cc12};
sb22 = news;
Ruled Surface(sb22) = {lb22};

// Pi:3*Pi/2
lb23 = new1;
Line Loop(lb23) = {-cc11,-cc14,cc17,cc18};
sb23 = news;
Ruled Surface(sb23) = {lb23};

// 3*Pi/2:2*Pi
lb24 = new1;
Line Loop(lb24) = {cc15,cc16,cc14,cc11};
sb24 = news;
Ruled Surface(sb24) = {lb24};

Printf("Generating dispersed body %g...",i);
Printf("Data bubble: %g",i);
Printf("Bubble's ruled surface - 0:Pi/2 = %g",sb21);
Printf("Bubble's ruled surface - Pi/2:Pi = %g",sb22);
Printf("Bubble's ruled surface - Pi:1.5*Pi = %g",sb23);
Printf("Bubble's ruled surface - 1.5*Pi:2*Pi = %g",sb24);

// DISPERSED PHYSICAL SURFACES
Physical Surface(Sprintf("Dispersed%g",i)) = {sb21,sb22,sb23,sb24};

EndFor

// 4. BUILDING EXTERNAL SURFACES

// left end
l115 = new1;
Line Loop(l115) = {-c4,-c3,-c2,-c1};
s1 = news;
Plane Surface(s1) = {l115};

// right end
l116 = new1;
Line Loop(l116) = {c5,c6,c7,c8};
s2 = news;
Plane Surface(s2) = {l116};

// channel's surfaces

l117 = new1;

```

```
Line Loop(l117) = {-11,c1,l2,-c5};
s3 = news;
Ruled Surface(s3) = {l117};

l118 = new1;
Line Loop(l118) = {-12,c2,l3,-c6};
s4 = news;
Ruled Surface(s4) = {l118};

l119 = new1;
Line Loop(l119) = {-13,c3,l4,-c7};
s5 = news;
Ruled Surface(s5) = {l119};

l120 = new1;
Line Loop(l120) = {-14,c4,l1,-c8};
s6 = news;
Ruled Surface(s6) = {l120};

// --- PERIODIC SURFACES MESHING s1 - Master :: s2 - Slave

Periodic Surface s1 {c1,c2,c3,c4} = s2 {c5,c6,c7,c8};

// 5. BOUNDARY PHYSICAL SURFACES

Physical Surface("PeriodicLeftBoundary") = {s1};
Physical Surface("PeriodicRightBoundary") = {s2};
Physical Surface("NoSlipBoundary") = {s3,s4,s5,s6};

/* End of script */
```

## APPENDIX C - EQUATIONS OF THE PBC FORMULATION

### Enforcement of PBC: mathematical aspects

Let

$$\begin{aligned} \int_{\Omega} \rho \left[ \frac{\partial \mathbf{v}_P}{\partial t} + (\mathbf{v}_P - \hat{\mathbf{v}}) \cdot \nabla \mathbf{v}_P \right] \cdot \mathbf{w}_P d\Omega - Eu_{\beta} \int_{\Omega} \mathbf{e}_P \cdot \mathbf{w}_P d\Omega + \int_{\Omega} \nabla \tilde{p} \cdot \mathbf{w}_P d\Omega \\ - \frac{1}{Re} \int_{\Omega} \nabla \cdot [\mu (\nabla \mathbf{v}_P + \nabla \mathbf{v}_P^T)] \cdot \mathbf{w}_P d\Omega - \frac{1}{Fr^2} \int_{\Omega} \rho \mathbf{g} \cdot \mathbf{w}_P d\Omega \\ - \frac{1}{We} \int_{\Omega} \mathbf{f} \cdot \mathbf{w}_P d\Omega = \mathbf{0}, \quad \mathbf{v}_P, \mathbf{w}_P \in \mathcal{V}_P \end{aligned}$$

be the expanded form of

$$\int_{\Omega} \mathbf{B}_{1,P}(\mathbf{v}_P, \tilde{p}, \mathbf{f}; \hat{\mathbf{v}}, \rho, \mu, \mathbf{g}) \cdot \mathbf{w}_P d\Omega = 0,$$

which is included in Equation (5.17). By using integration by parts in the viscous term and periodic pressure term,

$$\begin{aligned} \int_{\Omega} \nabla \cdot [\mu (\nabla \mathbf{v}_P + \nabla \mathbf{v}_P^T)] \cdot \mathbf{w}_P d\Omega &= - \int_{\Omega} \mu [(\nabla \mathbf{v}_P + \nabla \mathbf{v}_P^T) : \nabla \mathbf{w}_P^T] d\Omega + \\ &+ \int_{\Gamma} \mathbf{n} \cdot [\mu (\nabla \mathbf{v}_P + \nabla \mathbf{v}_P^T) \cdot \mathbf{w}_P] d\Gamma \\ \int_{\Omega} \nabla \tilde{p} \cdot \mathbf{w}_P d\Omega &= - \int_{\Omega} \tilde{p} \nabla \cdot \mathbf{w}_P d\Omega + \int_{\Gamma} \tilde{p} \mathbf{w}_P \cdot \mathbf{n} d\Gamma. \end{aligned}$$

Now, since  $\Gamma = \Gamma_P \cup \Gamma_D$ , the  $\Gamma$ -integrals can be decomposed into

$$\begin{aligned} \int_{\Gamma} \mathbf{n} \cdot [\mu (\nabla \mathbf{v}_P + \nabla \mathbf{v}_P^T) \cdot \mathbf{w}_P] d\Gamma &= \int_{\Gamma_D} \mathbf{n} \cdot [\mu (\nabla \mathbf{v}_P + \nabla \mathbf{v}_P^T) \cdot \mathbf{w}_P] d\Gamma + \\ &+ \int_{\Gamma_P} \mathbf{n} \cdot [\mu (\nabla \mathbf{v}_P + \nabla \mathbf{v}_P^T) \cdot \mathbf{w}_P] d\Gamma \\ \int_{\Gamma} \tilde{p} \mathbf{w}_P \cdot \mathbf{n} d\Gamma &= \int_{\Gamma_D} \tilde{p} \mathbf{w}_P \cdot \mathbf{n} d\Gamma + \int_{\Gamma_P} \tilde{p} \mathbf{w}_P \cdot \mathbf{n} d\Gamma. \end{aligned}$$

However, given that

$$\mathbf{w}_P|_{\Gamma_D} = \mathbf{0},$$



the integrals relate to the Dirichlet boundary vanish, thus remaining

$$\int_{\Gamma} \mathbf{n} \cdot [\mu (\nabla \mathbf{v}_P + \nabla \mathbf{v}_P^T) \cdot \mathbf{w}_P] d\Gamma = \int_{\Gamma_P} \mathbf{n} \cdot [\mu (\nabla \mathbf{v}_P + \nabla \mathbf{v}_P^T) \cdot \mathbf{w}_P] d\Gamma$$

$$\int_{\Gamma} \tilde{p} \mathbf{w}_P \cdot \mathbf{n} d\Gamma = \int_{\Gamma_P} \tilde{p} \mathbf{w}_P \cdot \mathbf{n} d\Gamma.$$

The periodic boundary, in turn, is decomposed by  $\Gamma_P = \Gamma_L \cup \Gamma_R$ , where  $\Gamma_R = \Gamma_L \oplus L_P \mathbf{e}_P$  to give

$$\int_{\Gamma_P} \mathbf{n} \cdot [\mu (\nabla \mathbf{v}_P + \nabla \mathbf{v}_P^T) \cdot \mathbf{w}_P] d\Gamma = \int_{\Gamma_L} \mathbf{n} \cdot [\mu (\nabla \mathbf{v}_P + \nabla \mathbf{v}_P^T) \cdot \mathbf{w}_P] d\Gamma +$$

$$+ \int_{\Gamma_R} \mathbf{n} \cdot [\mu (\nabla \mathbf{v}_P + \nabla \mathbf{v}_P^T) \cdot \mathbf{w}_P] d\Gamma$$

$$\int_{\Gamma_P} \tilde{p} \mathbf{w}_P \cdot \mathbf{n} d\Gamma = \int_{\Gamma_L} \tilde{p} \mathbf{w}_P \cdot \mathbf{n} d\Gamma + \int_{\Gamma_R} \tilde{p} \mathbf{w}_P \cdot \mathbf{n} d\Gamma.$$

Now, the enforcement of the PBC require that

$$\mathbf{v}|_{\Gamma_L} = \mathbf{v}|_{\Gamma_R}$$

$$\mathbf{n} \cdot \nabla \mathbf{v}|_{\Gamma_L} = -\mathbf{n} \cdot \nabla \mathbf{v}|_{\Gamma_R}$$

$$\tilde{p}|_{\Gamma_L} = \tilde{p}|_{\Gamma_R}$$

$$\mathbf{n} \cdot \nabla \tilde{p}|_{\Gamma_L} = -\mathbf{n} \cdot \nabla \tilde{p}|_{\Gamma_R},$$

so that

$$\int_{\Gamma_L} \mathbf{n} \cdot [\mu (\nabla \mathbf{v}_P + \nabla \mathbf{v}_P^T) \cdot \mathbf{w}_P] d\Gamma + \int_{\Gamma_R} (-\mathbf{n}) \cdot [\mu (\nabla \mathbf{v}_P + \nabla \mathbf{v}_P^T) \cdot \mathbf{w}_P] d\Gamma$$

$$\int_{\Gamma_L} \tilde{p} \mathbf{w}_P \cdot \mathbf{n} d\Gamma + \int_{\Gamma_R} \tilde{p} \mathbf{w}_P \cdot (-\mathbf{n}) d\Gamma.$$

cancel out in the formulation because of the opposite sign of the normal vector over  $\Gamma_R$ . Finally, the periodic mesh nodes in the discrete equations are manipulated via rows/columns operations.

## APPENDIX E - CURVATURE AND FRÉNET'S FRAME

### Curvature

Curvature is a scalar function  $\kappa(s)$  that associates a real number to each point of a parametrized curve in  $s$  by a real interval like  $a \leq s \leq b$ . From Differential Geometry [210], one ascertains that the curvature measures “how much the curve is bending at the parametrized point”. This quantity is well understood by comparing it to the role played by a derivative of the velocity vector at a point of a trajectory. However, the concept of curvature extends to smooth surfaces where it turns into a much more intricate matter. For a general surface  $\zeta$ ,  $\kappa(s)$  should satisfy some properties. The most intuitive are:

- $k$  is a smooth map;
- a point with an open neighbourhood contained in a plane has zero curvature;
- if  $\mathbf{p}, \mathbf{q} \in \zeta$  are points such that  $\mathbf{p}$  has a neighbourhood that forms a sharp peak higher than a neighbourhood of  $\mathbf{q}$ , then  $\kappa(\mathbf{p}) > \kappa(\mathbf{q})$ .

### The Frénet's frame

When we consider a curve in  $\mathbb{R}^3$  parameterized in  $s$  by a real interval like  $a \leq s \leq b$ , three vectors are essential to give information about that curve, namely, the normal vector  $\mathbf{n}(s)$ , the tangent vector  $\mathbf{t}(s)$  and the *binormal vector*  $\mathbf{b}(s)$ . This latter vector only makes sense in  $\mathbb{R}^3$ , since it is defined by

$$\mathbf{b} = \mathbf{t} \times \mathbf{n}. \quad (7.19)$$

$\{\mathbf{t}, \mathbf{n}, \mathbf{b}\}$  form an orthonormal basis to  $\mathbb{R}^3$ , which, indeed, is called the *Frénet's frame*.

### Calculation of curvature for one-dimensional interfaces

Another relevant characteristic of the method used here concerns the computation of the curvature  $\kappa$ , which depends on geometrical operations performed over interface elements. With the insertion of the CSF model [97] to estimate the interfacial force that goes along with the Equation (3.39), an accurate retrieval of the curvature is needed. In order to spare

painstaking reproductions of all the geometrical apparatus, we will refer to [169], [211] for further ascertainment.

The discrete process to calculate the unit normal vector in two-dimensional domains takes two properties into account. Firstly, the interface is a curve represented by a set of linear elements and structured. Secondly, the normal vectors for each neighbour element can be obtained by orthogonalizing the unit tangent vectors to each element, which, in fact, are obtained by normalizing the element length itself. In turn, the normal vector for the shared node is evaluated by summing the contributions of the normal elemental vectors. This scheme is depicted in Figure 92. Mathematically, if  $\mathbf{n}(e_{L,i}), \mathbf{n}(e_{R,i})$  are the unit normal vectors evaluated over the neighbour elements respectively at left and at right of the interface node  $\mathbf{x}_i$ , then,

$$\mathbf{n}(e_{L,i}) = \mathbf{R}_{\pi/2} [\mathbf{t}(e_{L,i})], \quad \mathbf{n}(e_{R,i}) = \mathbf{R}_{\pi/2} [\mathbf{t}(e_{R,i})], \quad (7.20)$$

where

$$\mathbf{t}(e_{L,i}) = \frac{\mathbf{x}_{L,i} - \mathbf{x}_i}{\|\mathbf{x}_{L,i} - \mathbf{x}_i\|}, \quad \mathbf{t}(e_{R,i}) = \frac{\mathbf{x}_{R,i} - \mathbf{x}_i}{\|\mathbf{x}_{R,i} - \mathbf{x}_i\|}. \quad (7.21)$$

Above,  $\mathbf{x}_{L,i}, \mathbf{x}_{R,i}$  are the vertices of the neighbour elements not matching the interface node and  $\mathbf{t}(e_{L,i}), \mathbf{t}(e_{R,i})$  their respective unit tangent vectors generated by the rotation matrix  $\mathbf{R}_{\pi/2}$ . Directly from Equations (7.20) and (7.21), one gets

$$\mathbf{n}(\mathbf{x}_i) = \mathbf{n}(e_{L,i}) + \mathbf{n}(e_{R,i}) = \mathbf{R}_{\pi/2} [\mathbf{t}(e_{L,i}) + \mathbf{t}(e_{R,i})]. \quad (7.22)$$

Meanwhile, the curvature  $\kappa(\mathbf{x}_i)$  is evaluated for each interface node by an approximation adapted from a formulae set of the Frénet's frame, or, even more formally, *Frénet-Serret Theorem* - see [210] - for curvature and torsion. 7.23 is the continuous version of one among the Frénet's formulae relating  $\kappa$  and the unit vector tangent  $\mathbf{t}$  to the interface

$$\kappa \mathbf{n} = \frac{\partial \mathbf{t}}{\partial s} \approx \frac{\mathbf{t}(e_{L,i}) - \mathbf{t}(e_{R,i})}{\bar{h}}. \quad (7.23)$$

Since the elements  $e_{L,i}, e_{R,i}$  do not necessarily have the same size, the evaluation of  $\kappa(\mathbf{x}_i)$  is undertaken as an average distribution over the mean length  $\bar{h}$  of the neighbour elements

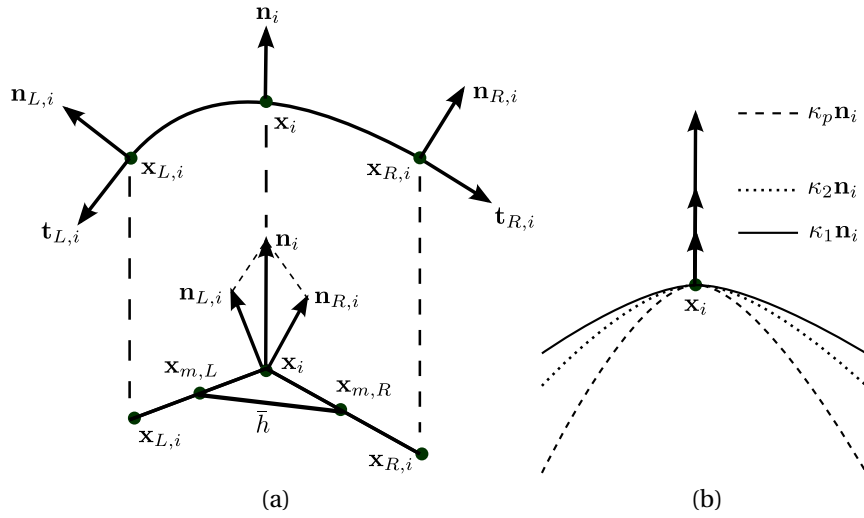


Figure 92: Scheme for the calculation of the curvature: (a) continuous and discrete versions; (b) effect of the curvature upon the normal vector at  $\mathbf{x}_i$ .

given by

$$\bar{h} = \frac{1}{2}(h_L + h_R), \tag{7.24}$$

where  $h_L, h_R$  are the lengths of the neighbour elements. Also depicted in Figure 92 at left, it is seen that  $\bar{h}$  binds the two midpoints  $\mathbf{x}_{m,L}, \mathbf{x}_{m,R}$ . At right, a sketch was added only to illustrate how  $\kappa$  affects the normal vector  $\mathbf{n}_i$  by stretching it. From Equation (7.23), it is inferred that the higher the tangential derivative along the interface, the higher the norm of the vector  $\kappa \mathbf{n}_i$ , because if, for instance, we choose a sequence  $(\kappa_p)$  such that  $\kappa_1 < \kappa_2 < \dots < \kappa_p$ , then

$$\|\kappa_1 \mathbf{n}_i\| < \|\kappa_2 \mathbf{n}_i\| < \dots < \|\kappa_p \mathbf{n}_i\|. \tag{7.25}$$

In other words, high curvatures tend to magnify the normal vector at  $\mathbf{x}_i$ .

## APPENDIX E - VERIFICATION & VALIDATION

The following text contains clippings about the meaning of verification and validation in terms of the CFD's vogue. Such terminologies, sometimes used interchangeably, are discussed here in order to elucidate presumable ambiguities. For a long and detailed review about the topic, refer to [212] and references therein.

### The concept of V&V

**Definition 7.5.1 (Verification)** *The process of determining that a model implementation accurately represents the developer's conceptual description of the model and the solution to the model.*

**Definition 7.5.2 (Validation)** *The process of determining the degree to which a model is an accurate representation of the real world from the perspective of the intended uses of the model.*

Verification provides evidence, or substantiation, that the mathematical model, which is derived from the conceptual model, is solved correctly by the computer code that is being assessed. Verification does not address the issue of whether the mathematical model - defined by a set of partial differential or integro-differential equations along with the required initial and boundary conditions - has any relationship to the real world, e.g., physics. Validation, on the other hand, provides evidence, or substantiation, of how accurately the computational model simulates the real world for system responses of interest. Validation activities presume that the computational model result is an accurate solution of the mathematical model.

### Code verification procedures

Considering the numerical solution of PDEs, code verification comprises the activities of:

1. defining appropriate benchmarks for the evaluation of solution accuracy and
2. determining what constitutes satisfactory performance of the algorithms on the benchmarks.

Code verification relies on the comparison of computational solutions to the "correct answer". The correct answer is provided by highly accurate solutions for a set of well-chosen

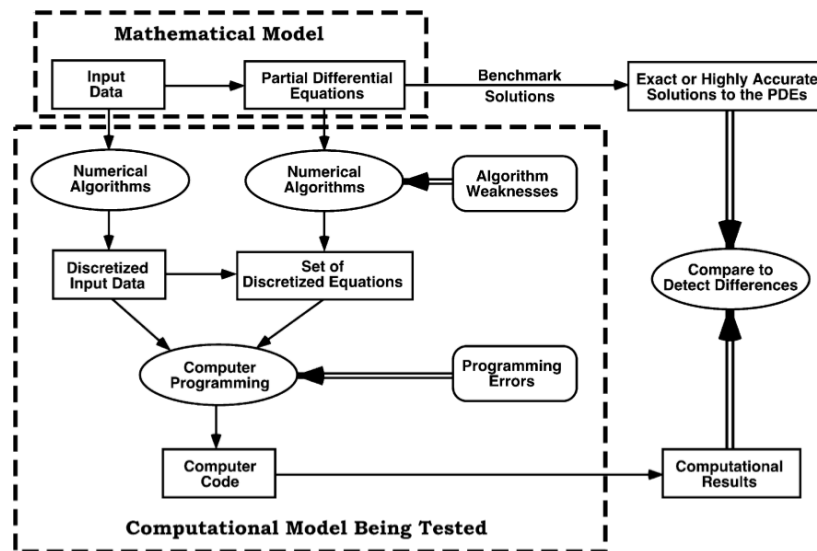


Figure 93: Example of a process of verification to detect errors in codes. Extracted from [212].

benchmarks, and this answer can only be known in a relatively small number of isolated cases. These cases therefore assume a very important role in code verification and should be carefully formalized in test plans that describe how the code will be verified. In code verification, the key feature to determine is the observed, or demonstrated, order of convergence using multiple numerical solutions. An example of method that uses exact or highly accurate solutions to the PDEs to detect numerical algorithm deficiencies and programming errors is illustrated in Figure 93.

The mathematical model is the general model for the application of interest, whereas the exact and highly accurate solutions to the PDEs are special-case solutions of the mathematical model. For these special cases, benchmark solutions can be computed. Four types of highly accurate solutions (from highest to lowest) are recognized:

1. manufactured solutions;
2. analytical solutions;
3. highly accurate numerical solutions to the ODEs and
4. highly accurate numerical solutions to the PDEs.

More specifically, analytical solutions are closed-form solutions to special cases of the PDEs defined in the mathematical model, commonly represented by infinite series, complex integrals, and asymptotic expansions. However, the most significant practical shortcoming of

classical analytical solutions is that they exist only for very simplified physics, material properties, and geometries. Therefore, it is indispensable to use the same modelling assumptions for both the benchmark solution and the code being tested.

**APPENDIX F - VITA**

Gustavo Charles Peixoto de Oliveira was born March 31st, 1987 in Barra do Piraí, Rio de Janeiro, Brazil. He received his Licentiate degree in Mathematics from Federal Fluminense University/CECIERJ in 2008. Decided to pursue an academic career more inclined to applied contexts, moved to the Engineering's atrium, whereby received his M.Sc. degree in Metallurgy and Materials Engineering from Federal University of Rio de Janeiro in 2011 with a two-year grant provided by the governmental Brazilian funding agency CNPq. Meanwhile, he began to work with CFD tools to investigate the hydrodynamic stability of rotating flows occurring in electrochemical cells. He started his Ph.D. trail still in 2011, was a one-year internship Ph.D. visitor at Ecole Polytechnique Fédérale de Lausanne, Switzerland, during 2013, specifically at LTCM - Laboratoire de Transfert de Chaleur et de Masse, supported by the Science Without Borders Program (CNPq/Brazil). There, he worked with gas-liquid two-phase flow dynamics. Back to Brazil, he received the degree of D.Sc. in Mechanical Engineering in 2015 from State University of Rio de Janeiro, also sponsored by the Brazilian agency CAPES with a four-year integral scholarship.



**APPENDIX G - PUBLICATIONS**

- ★ OLIVEIRA, G. P., ANJOS, G. R., PONTES, J., MANGIAVACCHI, N., THOME, J.R. *ALE/finite element modeling of an unconfined bubble plume in periodic domain: bubble shape and oscillation analysis*, accepted for publication by the Journal of the Brazilian Society of Mechanical Sciences and Engineering, 2015.
- ★ PONTES, J., MANGIAVACCHI, N., ANJOS, G. R., LUCENA, R., GAONA, C. M., OLIVEIRA, G. P., FERREIRA, D. *A Survey of Results Concerning Steady Solutions and the Stability of a Class of Rotating Flows*. Proceedings of the 3rd Conference of Computational Interdisciplinary Sciences, Asunción, Paraguay, 2014.
- ★ OLIVEIRA, G.P., MANGIAVACCHI, N., ANJOS, G., PONTES, J., THOME, J.R. *Comparative CFD Simulations of Gas Transport in Slug Flow from Periodic Arrays with Single or Multiple Bubbles*. Proceedings of the 3rd Conference of Computational interdisciplinary Sciences, Asunción, Paraguay, 2014.
- ★ OLIVEIRA, G.C.P., ANJOS, G., PONTES, J., MANGIAVACCHI, N. *Finite Element Analysis of Pressure-Driven Laminar Flow Inside Periodically Staggered Arrays*. Proceedings of the VII Brazilian National Congress of Mechanical Engineering, Belém, Brazil, 2014.
- ★ OLIVEIRA, G.C.P., MANGIAVACCHI, N., ANJOS, G., THOME, J.R. *Numerical Simulation of a Periodic Array of Bubbles*, Mecánica Computacional, v. XXXII, 1813-1824, 2013.
- ★ OLIVEIRA, G.C.P., MANGIAVACCHI, N., ANJOS, G., THOME, J.R. *Topological Remeshing and Locally Supported Smoothing for Bubble Coalescence in Two-Phase Flows*. Proceedings of the 22nd International Congress of Mechanical Engineering, Ribeirão Preto, Brazil, 2013.
- ★ MORAES, E.L.S., OLIVEIRA, G.C.P., ANJOS, G., MANGIAVACCHI, N., PONTES, J. *Semi-Lagrangian Algorithms for Second Order for the Study of Hydrodynamics of Electrochemical Cells*. Proceedings of the 14th Brazilian Congress of Thermal Sciences and Engineering, Rio de Janeiro, Brazil, 2012.
- ★ OLIVEIRA, G.C.P., MANGIAVACCHI, N., PONTES, J. *Semi-Lagrangian High-Order 3D Interpolation: Survey on a Finite Element Z-Type Operator*. Proceedings of the 14th Brazilian Congress of Thermal Sciences and Engineering, Rio de Janeiro, Brazil, 2012.

- ★ OLIVEIRA, G.C.P, MANGIAVACCHI, N., PONTES, J. *High-Order Interpolation Applied to the Modeling of Advective Transport for Incompressible Flows*. Congress of Computational and Applied Mathematics- CMAC/NE, Natal, Brazil, 2012.
- ★ OLIVEIRA, G.C.P, *Hydrodynamic Stability in Electrochemical Cells Through the Finite Element Method*, M.Sc. dissertation, Federal University of Rio de Janeiro, Brazil, 2011.
- ★ OLIVEIRA, G.C.P, MANGIAVACCHI, N., PONTES, J. *A Semi-Lagrangian Scheme for Fluid Flow Simulations with a Zienkiewicz-Type Finite Element Interpolation*. Proceedings of the 21st International Congress of Mechanical Engineering, Natal, Brazil, 2011.

## REFERENCES

- [1] AVIATION Spectator, accessed November 2014, <<http://www.aviationspectator.com/image/photos/military-aircraft/fighters/av-8b-harrier-ii/av-8b-harrier-jet-151>>.
- [2] AMERICAN Physical Society Sites, Division of Fluid Dynamics, accessed November 2014, <<http://www.aps.org/units/dfd/pressroom/gallery/2010/hermann10.cfm>>.
- [3] THINK Progress, accessed November 2014, <<http://thinkprogress.org/climate/2014/03/14/3405801/bp-is-back>>.
- [4] ESJBERG Power Station, RGB Stock, accessed November 2014, <<http://www.rgbstock.nl/photo/o1R0Bxu/Cole+Power+Plant>>.
- [5] RAJARATNAM, N. *Turbulent Jets*. Amsterdam: Elsevier Scientific Publishing Company, 1976.
- [6] COELHO, S.; HUNT, J. The dynamics of the near field of strong jets in crossflows. *Journal of Fluid Mechanics*, Cambridge Univ Press, v. 200, p. 95–120, 1989.
- [7] FRIC, T.; ROSHKO, A. Vortical structure in the wake of a transverse jet. *Journal of Fluid Mechanics*, Cambridge Univ Press, v. 279, p. 1–47, 1994.
- [8] LIM, T.; NEW, T.; LUO, S. On the development of large-scale structures of a jet normal to a cross flow. *Physics of Fluids*, AIP Publishing, v. 13, n. 3, p. 770–775, 2001.
- [9] ABRAMOVICH, G. *The Theory of Turbulent Jets*. Cambridge: MIT Press, 1963.
- [10] KAMOTANI YAND GREBER, I. Experiments on a turbulent jet in a cross flow. *AIAA journal*, v. 10, n. 11, p. 1425–1429, 1972.
- [11] KELSO, R.; LIM, T.; PERRY, A. An experimental study of round jets in cross-flow. *Journal of Fluid Mechanics*, Cambridge University Press, v. 306, p. 111–144, 1996.
- [12] MOUSSA, Z.; TRISCHKA, J.; ESKINAZI, S. The near field in the mixing of a round jet with a cross-stream. *Journal of Fluid Mechanics*, Cambridge University Press, v. 80, n. 01, p. 49–80, 1977.

- [13] SMITH, S.; MUNGAL, M. Mixing, structure and scaling of the jet in crossflow. *Journal of Fluid Mechanics*, Cambridge University Press, v. 357, p. 83–122, 1998.
- [14] JOHARI, H.; PACHECO-TOUGAS, M.; HERMANSON, J. Penetration and mixing of fully modulated turbulent jets in crossflow. *AIAA journal*, v. 37, n. 7, p. 842–850, 1999.
- [15] EROGLU, A.; BREIDENTHAL, R. Structure, penetration, and mixing of pulsed jets in crossflow. *AIAA journal*, v. 39, n. 3, p. 417–423, 2001.
- [16] MCLOSKEY, R. et al. The actively controlled jet in crossflow. *Journal of Fluid Mechanics*, Cambridge University Press, v. 452, p. 325–335, 2002.
- [17] NARAYANAN, S.; BAROOAH, P.; COHEN, J. Dynamics and control of an isolated jet in crossflow. *AIAA journal*, v. 41, n. 12, p. 2316–2330, 2003.
- [18] SYKES, R.; LEWELLEN, W.; PARKER, S. On the vorticity dynamics of a turbulent jet in a crossflow. *Journal of Fluid Mechanics*, Cambridge University Press, v. 168, p. 393–413, 1986.
- [19] NEEDHAM, D.; RILEY, N.; SMITH, J. A jet in crossflow. *Journal of Fluid Mechanics*, Cambridge University Press, v. 188, p. 159–184, 1988.
- [20] RUDMAN, M. Simulation of the near field of a jet in a cross flow. *Experimental Thermal and Fluid Science*, Elsevier, v. 12, n. 2, p. 134–141, 1996.
- [21] HAHN, S.; CHOI, H. Unsteady simulation of jets in a cross flow. *Journal of Computational Physics*, Elsevier, v. 134, n. 2, p. 342–356, 1997.
- [22] YUAN, L. L.; STREET, R. L.; FERZIGER, J. H. Large-eddy simulations of a round jet in crossflow. *Journal of Fluid Mechanics*, Cambridge University Press, v. 379, p. 71–104, 1999.
- [23] MUPPIDI, S.; MAHESH, K. Study of trajectories of jets in crossflow using direct numerical simulations. *Journal of Fluid Mechanics*, Cambridge University Press, v. 530, p. 81–100, 2005.
- [24] KEIMASI, M.; TAEIBI-RAHNI, M. Numerical simulation of jets in a crossflow using different turbulence models. *AIAA journal*, v. 39, n. 12, p. 2268–2277, 2001.
- [25] KARAGOZIAN, A.; CORTELEZZI, L.; SOLDATI, A. *Manipulation and Control of Jets in Crossflow*. USA: Springer, 2003.

- [26] MARGASON, R. *Fifty years of jet in cross flow research*. AGARD, *Computational and Experimental Assessment of Jets in Cross Flow*. 1993.
- [27] KARAGOZIAN, A. Transverse jets and their control. *Progress in Energy and Combustion Science*, Elsevier, v. 36, n. 5, p. 531–553, 2010.
- [28] KARAGOZIAN, A. R. The jet in crossflow). *Physics of Fluids (1994-present)*, AIP Publishing, v. 26, n. 10, p. 101303, 2014.
- [29] MAHESH, K. The interaction of jets with crossflow. *Annual Review of Fluid Mechanics*, Annual Reviews, v. 45, p. 379–407, 2013.
- [30] LIN, S. *Breakup of Liquid Sheets and Jets*. New York: Cambridge University Press, 2003.
- [31] CHANDRASEKHAR, S. *Hydrodynamic and Hydromagnetic Stability*. New York: Dover Publications, 1961.
- [32] SCHMID, P.; HENNINGSON, D. *Stability and Transition in Shear Flows*. New York: Springer, 2001.
- [33] HUERRE, P.; MONKEWITZ, P. A. Local and global instabilities in spatially developing flows. *Annual Review of Fluid Mechanics*, Annual Reviews, v. 22, n. 1, p. 473–537, 1990.
- [34] BATCHELOR, G.; GILL, A. Analysis of the stability of axisymmetric jets. *Journal of Fluid Mechanics*, Cambridge University Press, v. 14, n. 04, p. 529–551, 1962.
- [35] MICHALKE, A. Instabilitaet eines kompressiblen runden freistrahls unter beruecksichtigung des einflusses der strahigrenzschichtdicke (instability of a compressible circular jet considering the influence of the thickness of the jet boundary layer). *Zeitschrift für Flugwissenschaften*, In English: NASA TM 75190 (1977), v. 19, n. 04, p. 319–328, 1971.
- [36] MICHALKE, A. On the inviscid instability of the hyperbolic tangent velocity profile. *Journal of Fluid Mechanics*, Cambridge University Press, v. 19, n. 04, p. 543–556, 1964.
- [37] MICHALKE, A. On spatially growing disturbances in an inviscid shear layer. *J. Fluid Mech*, Cambridge University Press, v. 23, n. 3, p. 521–544, 1965.
- [38] MICHALKE, A. Vortex formation in a free boundary layer according to stability theory. *Journal of Fluid Mechanics*, Cambridge University Press, v. 22, n. 02, p. 371–383, 1965.

- [39] MORRIS, P. The spatial viscous instability of axisymmetric jets. *Journal of Fluid Mechanics*, Cambridge University Press, v. 77, n. 03, p. 511–529, 1976.
- [40] MICHALKE, A.; HERMANN, G. On the inviscid instability of a circular jet with external flow. *Journal of Fluid Mechanics*, Cambridge University Press, v. 114, p. 343–359, 1982.
- [41] MICHALKE, A. Survey on jet instability theory. *Progress in Aerospace Sciences*, Elsevier, v. 21, p. 159–199, 1984.
- [42] ALVES, L. *Transverse Jet Shear-Layer Instabilities: Linear Stability Analysis and Numerical Simulations*. Tese (Doutorado) — UCLA - University of California at Los Angeles, USA, 2006.
- [43] ALVES, L.; KELLY, R.; KARAGOZIAN, A. Local stability analysis of an inviscid transverse jet. *Journal of Fluid Mechanics*, Cambridge University Press, v. 581, p. 401–418, 2007.
- [44] MEGERIAN, S. et al. Transverse-jet shear-layer instabilities. part 1. experimental studies. *Journal of fluid Mechanics*, Cambridge University Press, v. 593, p. 93–129, 2007.
- [45] ALVES, L.; KELLY, R.; KARAGOZIAN, A. Transverse-jet shear-layer instabilities. part 2. linear analysis for large jet-to-crossflow velocity ratio. *Journal of Fluid Mechanics*, Cambridge University Press, v. 602, p. 383–401, 2008.
- [46] KELLY, R.; ALVES, L. A uniformly valid asymptotic solution for a transverse jet and its linear stability analysis. *Philosophical Transactions of the Royal Society A: Mathematical, Physical and Engineering Sciences*, The Royal Society, v. 366, n. 1876, p. 2729–2744, 2008.
- [47] BAGHERI, S. et al. Global stability of a jet in crossflow. *Journal of Fluid Mechanics*, Cambridge University Press, v. 624, p. 33–44, 2009.
- [48] DAVITIAN, J. et al. Transition to global instability in transverse-jet shear layers. *Journal of Fluid Mechanics*, Cambridge University Press, v. 661, p. 294–315, 2010.
- [49] ILAK, M. et al. Stability of a jet in crossflow. *Physics of Fluids*, Cambridge University Press, v. 23, p. 091113, 2011.
- [50] SCHLATTER, P.; BAGHERI, S.; HENNINGSON, D. Self-sustained global oscillations in a jet in crossflow. *Theoretical and Computational Fluid Dynamics*, Springer, v. 25, n. 1-4, p. 129–146, 2011.

- [51] ILAK, M. et al. Bifurcation and stability analysis of a jet in cross-flow: onset of global instability at a low velocity ratio. *Journal of Fluid Mechanics*, Cambridge University Press, v. 696, p. 94–121, 2012.
- [52] NEW, T.; LIM, T.; LUO, S. Effects of jet velocity profiles on a round jet in cross-flow. *Experiments in Fluids*, Springer, v. 40, n. 6, p. 859–875, 2006.
- [53] MUPPIDI, S.; MAHESH, K. Direct numerical simulation of round turbulent jets in cross-flow. *Journal of Fluid Mechanics*, Cambridge University Press, v. 574, p. 59–84, 2007.
- [54] MUPPIDI, S.; MAHESH, K. Direct numerical simulation of passive scalar transport in transverse jets. *Journal of Fluid Mechanics*, Cambridge University Press, v. 598, p. 335–360, 2008.
- [55] DENEV, J. et al. *Direct numerical simulation, analysis and modelling of mixing processes in a round jet in crossflow*. Berlin: Springer, 2010. 143–164 p.
- [56] MULDOON, F.; ACHARYA, S. Direct numerical simulation of pulsed jets-in-crossflow. *Computers & Fluids*, Elsevier, v. 39, n. 10, p. 1745–1773, 2010.
- [57] SAU, R.; MAHESH, K. Optimization of pulsed jets in crossflow. *Journal of Fluid Mechanics*, Cambridge University Press, v. 653, p. 365–390, 2010.
- [58] COUSSEMENT, A.; GICQUEL, O.; DEGREGZ, G. Large eddy simulation of a pulsed jet in cross-flow. *Journal of Fluid mechanics*, Cambridge University Press, v. 695, p. 1–34, 2012.
- [59] LEE, I. et al. Spray jet penetration and distribution of modulated liquid jets in subsonic cross-flows. *Journal of mechanical science and technology*, Springer, v. 24, n. 7, p. 1425–1431, 2010.
- [60] RANA, Z.; THORNBUR, B.; DRIKAKIS, D. Transverse jet injection into a supersonic turbulent cross-flow. *Physics of Fluids*, AIP Publishing, v. 23, n. 4, p. 046103, 2011.
- [61] GROUT, R. et al. Direct numerical simulation of flame stabilization downstream of a transverse fuel jet in cross-flow. *Proceedings of the Combustion Institute*, Elsevier, v. 33, n. 1, p. 1629–1637, 2011.

- [62] MARR, K.; CLEMENS, N.; EZEKOYE, O. Mixing characteristics and emissions of strongly-forced non-premixed and partially-premixed jet flames in crossflow. *Combustion and Flame*, Elsevier, v. 159, n. 2, p. 707–721, 2012.
- [63] HSU, C.; HUANG, R. Effects of acoustic excitation at resonance strouhal numbers on characteristics of an elevated transverse jet. *Experimental Thermal and Fluid Science*, Elsevier, v. 35, n. 7, p. 1370–1382, 2011.
- [64] HERRMANN, M. Detailed numerical simulations of the primary atomization of a turbulent liquid jet in crossflow. *Journal of Engineering for Gas Turbines and Power*, American Society of Mechanical Engineers, v. 132, n. 6, p. 061506, 2010.
- [65] EGGERS, J.; VILLERMAUX, E. Physics of liquid jets. *Reports on progress in physics*, IOP Publishing, v. 71, n. 3, p. 036601, 2008.
- [66] TOMOTIKA, S. On the instability of a cylindrical thread of a viscous liquid surrounded by another viscous fluid. *Proceedings of the Royal Society of London. Series A, Mathematical and Physical Sciences*, JSTOR, v. 150, n. 870, p. 322–337, 1935.
- [67] STRUTT, J.; RAYLEIGH, L. On the instability of jets. *Proc. London Math. Soc.*, v. 10, p. 4–13, 1878.
- [68] MEISTER, B. J.; SCHEELE, G. F. Drop formation from cylindrical jets in immiscible liquid systems. *AIChE Journal*, American Institute of Chemical Engineers, v. 15, n. 5, p. 700–706, 1969.
- [69] MEISTER, B. J.; SCHEELE, G. F. Prediction of jet length in immiscible liquid systems. *AIChE Journal*, American Institute of Chemical Engineers, v. 15, n. 5, p. 689–699, 1969.
- [70] KITAMURA, Y.; MISHIMA, H.; TAKAHASHI, T. Stability of jets in liquid-liquid systems. *The Canadian Journal of Chemical Engineering*, Wiley Subscription Services, Inc., A Wiley Company, v. 60, n. 6, p. 723–731, 1982.
- [71] BRIGHT, A. Minimum drop volume in liquid jet breakup. *Chemical engineering research & design*, Elsevier, v. 63, n. 1, p. 59–66, 1985.
- [72] RUSSO, M. J.; STEEN, P. H. Shear stabilization of the capillary breakup of a cylindrical interface. *Physics of Fluids A: Fluid Dynamics (1989-1993)*, AIP Publishing, v. 1, n. 12, p. 1926–1937, 1989.



- [73] WEBER, C. Disintegration of liquid jets. *Zeitschrift für Angewandte Mathematik und Mechanik*, v. 11, n. 2, p. 136–159, 1931.
- [74] LIN, S.; REITZ, R. Drop and spray formation from a liquid jet. *Annual Review of Fluid Mechanics*, Annual Reviews 4139 El Camino Way, PO Box 10139, Palo Alto, CA 94303-0139, USA, v. 30, n. 1, p. 85–105, 1998.
- [75] MOALLEMI, N. *Numerical and experimental investigations in the stability and breakup of capillary water jets*. Tese (Doutorado) — University of British Columbia, Canada, 2014.
- [76] RICHARDS, J. R.; LENHOFF, A. M.; BERIS, A. N. Dynamic breakup of liquid–liquid jets. *Physics of Fluids (1994-present)*, AIP Publishing, v. 6, n. 8, p. 2640–2655, 1994.
- [77] HOMMA, S. et al. Breakup mode of an axisymmetric liquid jet injected into another immiscible liquid. *Chemical engineering science*, Elsevier, v. 61, n. 12, p. 3986–3996, 2006.
- [78] SALLAM, K.; AALBURG, C.; FAETH, G. Breakup of round nonturbulent liquid jets in gaseous crossflow. *AIAA journal*, v. 42, n. 12, p. 2529–2540, 2004.
- [79] MAZALLON, J.; DAI, Z.; FAETH, G. Primary breakup of nonturbulent round liquid jets in gas crossflows. *Atomization and Sprays*, Begel House Inc., v. 9, n. 3, 1999.
- [80] MEYERS, R. *The Physics of Membrane Emulsification and Applications for Controlled Drug Delivery*. Tese (Doutorado) — University of Pennsylvania, USA, 2010.
- [81] VLADISAVLJEVIĆ, G.; KOBAYASHI, I.; NAKAJIMA, M. Production of uniform droplets using membrane, microchannel and microfluidic emulsification devices. *Microfluidics and nanofluidics*, Springer-Verlag, v. 13, n. 1, p. 151–178, 2012.
- [82] WEGENER, M. et al. The formation and breakup of molten oxide jets. *Chemical Engineering Science*, Elsevier, v. 105, p. 143–154, 2014.
- [83] WEGENER, M. et al. The formation and breakup of molten oxide jets under periodic excitation. *AIChE Journal*, Wiley Online Library, 2014.
- [84] PATHAK, M. Numerical simulation of membrane emulsification: Effect of flow properties in the transition from dripping to jetting. *Journal of Membrane Science*, Elsevier, v. 382, n. 1, p. 166–176, 2011.

- [85] HIRT, C.; COOK, J.; BUTLER, T. A lagrangian method for calculating the dynamics of an incompressible fluid with free surface. *Journal of Computational Physics*, Elsevier, v. 5, n. 1, p. 103–124, 1970.
- [86] CHAN, R. A generalized arbitrary lagrangian-eulerian method for incompressible flows with sharp interfaces. *Journal of Computational Physics*, Elsevier, v. 17, n. 3, p. 311–331, 1975.
- [87] LÖHNER, R. *Applied Computational Fluid Dynamics Techniques: An Introduction Based on Finite Element Methods*. [S.l.]: John Wiley and Sons: England, 2008.
- [88] DONEA, J.; HUERTA, A. *Finite element methods for flow problems*. England: John Wiley & Sons, 2003.
- [89] DONEA, J. et al. Arbitrary lagrangian–eulerian methods. *Encyclopedia of computational mechanics*, John Wiley & Sons, 2004.
- [90] HUGHES, T.; WING, K.; ZIMMERMANN, T. Lagrangian-eulerian finite element formulation for incompressible viscous flows. *Computer Methods in Applied Mechanics and Engineering*, v. 29, n. 3, p. 329–349, 1981.
- [91] SCOVAZZI, G.; HUGUES, T. *Lecture Notes on Continuum Mechanics on Arbitrary Moving Domains*. 2007.
- [92] MALVERN, L. *Introduction to the Mechanics of a Continuous Medium*. New Jersey: Prentice-Hall, 1969.
- [93] TRYGGVASON, G.; SCARDOVELLI, R.; ZALESKI, S. *Direct Numerical Simulations of Gas-Liquid Multiphase Flows*. [S.l.]: Cambridge University Press, 2011.
- [94] HOU, T.; LOWENGRUB, J.; SHELLEY, M. Boundary integral methods for multicomponent fluids and multiphase materials. *Journal of Computational Physics*, Elsevier, v. 169, n. 2, p. 302–362, 2001.
- [95] HARLOW, F.; WELCH, J. Numerical calculation of time-dependent viscous incompressible flow of fluid with free surface. *Physics of fluids*, v. 8, n. 12, p. 2182, 1965.
- [96] HIRT, C.; NICHOLS, B. Volume of fluid (vof) method for the dynamics of free boundaries. *Journal of computational physics*, Elsevier, v. 39, n. 1, p. 201–225, 1981.

- [97] BRACKBILL, J.; KOTHE, D. B.; ZEMACH, C. A continuum method for modeling surface tension. *Journal of computational physics*, Elsevier, v. 100, n. 2, p. 335–354, 1992.
- [98] LAFAURIE, B. et al. Modelling merging and fragmentation in multiphase flows with surfer. *Journal of Computational Physics*, Elsevier, v. 113, n. 1, p. 134–147, 1994.
- [99] RIDER, W. J.; KOTHE, D. B. Reconstructing volume tracking. *Journal of computational physics*, Elsevier, v. 141, n. 2, p. 112–152, 1998.
- [100] SCARDOVELLI, R.; ZALESKI, S. Analytical relations connecting linear interfaces and volume fractions in rectangular grids. *Journal of Computational Physics*, Elsevier, v. 164, n. 1, p. 228–237, 2000.
- [101] POPINET, S. An accurate adaptive solver for surface-tension-driven interfacial flows. *Journal of Computational Physics*, Elsevier, v. 228, n. 16, p. 5838–5866, 2009.
- [102] UNVERDI, S.; TRYGGVASON, G. A front-tracking method for viscous, incompressible, multi-fluid flows. *Journal of computational physics*, Elsevier, v. 100, n. 1, p. 25–37, 1992.
- [103] OSHER, S.; SETHIAN, J. Fronts propagating with curvature-dependent speed: algorithms based on hamilton-jacobi formulations. *Journal of computational physics*, Elsevier, v. 79, n. 1, p. 12–49, 1988.
- [104] OSHER, S.; FEDKIW, R. Level set methods: an overview and some recent results. *Journal of Computational physics*, Elsevier, v. 169, n. 2, p. 463–502, 2001.
- [105] SUSSMAN, M.; SMEREKA, P.; OSHER, S. A level set approach for computing solutions to incompressible two-phase flow. *Journal of Computational physics*, Elsevier, v. 114, n. 1, p. 146–159, 1994.
- [106] TAKEWAKI, H.; YABE, T. The cubic-interpolated pseudo particle (cip) method: application to nonlinear and multi-dimensional hyperbolic equations. *Journal of Computational Physics*, Elsevier, v. 70, n. 2, p. 355–372, 1987.
- [107] KOBAYASHI, R. Modeling and numerical simulations of dendritic crystal growth. *Physica D: Nonlinear Phenomena*, Elsevier, v. 63, n. 3, p. 410–423, 1993.
- [108] STEINBACH, I. et al. A phase field concept for multiphase systems. *Physica D: Nonlinear Phenomena*, Elsevier, v. 94, n. 3, p. 135–147, 1996.

- [109] KIM, J. Phase-field models for multi-component fluid flows. *Commun. Comput. Phys.*, v. 12, n. 3, p. 613–661, 2012.
- [110] ADAMSON, A.; GAST, A. *Physical chemistry of surfaces*. Great Britain: John Wiley and Sons, 1997.
- [111] LAMB, H. *Hydrodynamics*. Cambridge, U.K.: Dover Publications, 1945.
- [112] ARIS, R. *Vectors, Tensors and the Basic Equations of Fluid Mechanics*. New Jersey: Dover Publications, 2012. (Dover Books on Mathematics).
- [113] SHEWCHUK, J. R. Triangle: Engineering a 2d quality mesh generator and delaunay triangulator. Springer, p. 203–222, 1996.
- [114] SI, H. *Tetgen, a quality tetrahedral mesh generator and three-dimensional delaunay triangulator, v1.3, user's manual*. [S.l.], 2004.
- [115] GEUZAIN, C.; REMACLE, J. Gmsh: A 3d finite element mesh generator with built-in pre- and post-processing facilities. *International Journal for Numerical Methods in Fluids*, Wiley, v. 79, n. 11, p. 1309–1331, 2009.
- [116] CIARLET, P. *The Finite Element Method for Elliptic Problems*. Amsterdam, Netherlands: North-Holland Publishing Company, 1978.
- [117] ERN, A.; GUERMOND, J. *Theory and Practice of Finite Elements*. New York, USA: Springer, 2004.
- [118] TRYGGVASON, G. et al. A front-tracking method for the computations of multiphase flow. *Journal of Computational Physics*, Elsevier, v. 169, n. 2, p. 708–759, 2001.
- [119] OLIVEIRA, G. et al. Ale/finite element modeling of an unconfined bubble plume in periodic domain: bubble shape and oscillation analysis. *submitted*, 2014.
- [120] GURTIN, M. *An Introduction to Continuum Mechanics*. USA: Academic Press, 1981.
- [121] SOUSA, F. S. *Simulation of multiphase flows in unstructured meshes*. Tese (Doutorado) — USP - University of Sao Paulo, Brazil, 2005.
- [122] CHORIN, A. J. Numerical solution of the navier-stokes equations. *Mathematics of computation*, v. 22, n. 104, p. 745–762, 1968.

- [123] TEMAM, R. Sur l'approximation de la solution des équations de navier-stokes par la méthode des pas fractionnaires (i). *Archive for Rational Mechanics and Analysis*, Springer, v. 32, n. 2, p. 135–153, 1969.
- [124] DENARO, F. M. On the application of the helmholtz–hodge decomposition in projection methods for incompressible flows with general boundary conditions. *International Journal for Numerical Methods in Fluids*, Wiley Online Library, v. 43, n. 1, p. 43–69, 2003.
- [125] LADYZHENSKAYA, O. *The mathematical theory of viscous incompressible flow*. New York: Gordon and Breach, 1969.
- [126] GUERMOND, J.; P, M.; SHEN, J. An overview of projection methods for incompressible flows. *Computer Methods in Applied Mechanics and Engineering*, v. 195, n. 44, p. 6011–6045, 2006.
- [127] LEE, M. J.; BYUNG, D. O.; YOUNG, B. K. Canonical fractional-step methods and consistent boundary conditions for the incompressible navier-stokes equations. *Journal of Computational Physics*, Elsevier, v. 168, n. 1, p. 73–100, 2001.
- [128] GRESHO, P.; SANI, R. *Incompressible Flow and the Finite Element Method: Advection, Diffusion and Isothermal Laminar Flow*. Great Britain: John Wiley and Sons, 1998.
- [129] WIIN-NIELSEN, A. On the application of trajectory methods in numerical forecasting. *Tellus*, Wiley Online Library, v. 11, n. 2, p. 180–196, 1959.
- [130] SAWYER, J. A semi-lagrangian method of solving the vorticity advection equation. *Tellus*, Wiley Online Library, v. 15, n. 4, p. 336–342, 1963.
- [131] BONAVENTURA, L. An introduction to semi-lagrangian methods for geophysical scale flows. *Lecture Notes, ERCOFTAC Leonhard Euler Lectures, SAM-ETH Zurich*, 2004.
- [132] STANIFORTH, A.; CÔTÉ, J. Semi-lagrangian integration schemes for atmospheric models-a review. *Monthly Weather Review*, AMS Journals, v. 119, n. 9, p. 2206–2223, 1991.
- [133] SMOLARKIEWICZ, P. K.; PUDYKIEWICZ, J. A. A class of semi-lagrangian approximations for fluids. *Journal of the Atmospheric Sciences*, v. 49, n. 22, p. 2082–2096, 1992.
- [134] BARTELLO, P.; THOMAS, S. J. The cost-effectiveness of semi-lagrangian advection. *Monthly weather review*, v. 124, n. 12, p. 2883–2897, 1996.

- [135] PIRONNEAU, O. On the transport-diffusion algorithm and its applications to the navier-stokes equations. *Numerische Mathematik*, Springer, v. 38, n. 3, p. 309–332, 1982.
- [136] XIU, D.; KARNIADAKIS, G. E. A semi-lagrangian high-order method for navier–stokes equations. *Journal of computational physics*, Elsevier, v. 172, n. 2, p. 658–684, 2001.
- [137] EL-AMRANI, M.; SEAĪD, M. A finite element semi-lagrangian method with l2 interpolation. *International Journal for Numerical Methods in Engineering*, Wiley Online Library, v. 90, n. 12, p. 1485–1507, 2012.
- [138] FALCONE, M.; FERRETTI, R. Convergence analysis for a class of high-order semi-lagrangian advection schemes. *SIAM Journal on Numerical Analysis*, SIAM, v. 35, n. 3, p. 909–940, 1998.
- [139] KAAZEMPUR-MOFRAD, M.; ETHIER, C. An efficient characteristic galerkin scheme for the advection equation in 3-d. *Computer methods in applied mechanics and engineering*, Elsevier, v. 191, n. 46, p. 5345–5363, 2002.
- [140] BRENNER, S.; SCOTT, L. *The Mathematical Theory of Finite Element Method*. New York: Springer-Verlag, 1994.
- [141] ZIENKIEWICZ, O. *The finite element method in engineering science*. London: McGraw-Hill, 1971.
- [142] STRANG, G.; FIX, G. *An Analysis of the Finite Element Method, 2ed*. USA: Wellesley-Cambridge Press, 1973.
- [143] BABUŠKA, I.; SURI, M. The p and h-p versions of the finite element method, basic principles and properties. *SIAM review*, SIAM, v. 36, n. 4, p. 578–632, 1994.
- [144] MOËS, N.; DOLBOW, J.; BELYTSCHKO, T. A finite element method for crack growth without remeshing. *Int. J. Numer. Meth. Engng*, v. 46, n. 1, p. 131–150, 1999.
- [145] BROOKS, A.; HUGHES, T. Streamline upwind/ Petrov-galerkin formulations for convection dominated flows with particular emphasis on the incompressible navier-stokes equations. *Computer methods in applied mechanics and engineering*, Elsevier, v. 32, n. 1, p. 199–259, 1982.

- [146] HUGHES, T. J.; FRANCA, L. P.; HULBERT, G. M. A new finite element formulation for computational fluid dynamics: Viii. the galerkin/least-squares method for advective-diffusive equations. *Computer Methods in Applied Mechanics and Engineering*, Elsevier, v. 73, n. 2, p. 173–189, 1989.
- [147] MIER-TORRECILLA, M.; IDELSOHN, S.; OÑATE, E. Advances in the simulation of multi-fluid flows with the particle finite element method. application to bubble dynamics. *International Journal for Numerical Methods in Fluids*, Wiley Online Library, v. 67, n. 11, p. 1516–1539, 2011.
- [148] SEVILLA, R.; FERNÁNDEZ-MÉNDEZ, S.; HUERTA, A. 3d nurbs-enhanced finite element method (nefem). *International Journal for Numerical Methods in Engineering*, Wiley Online Library, v. 88, n. 2, p. 103–125, 2011.
- [149] TEZDUYAR, T. E. et al. Space-time finite element computation of complex fluid-structure interactions. *International Journal for Numerical Methods in Fluids*, Wiley Online Library, v. 64, n. 10-12, p. 1201–1218, 2010.
- [150] TAKIZAWA, K.; TEZDUYAR, T. E. Multiscale space–time fluid–structure interaction techniques. *Computational Mechanics*, Springer, v. 48, n. 3, p. 247–267, 2011.
- [151] HUGHES, T. J.; COTTRELL, J. A.; BAZILEVS, Y. Isogeometric analysis: Cad, finite elements, nurbs, exact geometry and mesh refinement. *Computer methods in applied mechanics and engineering*, Elsevier, v. 194, n. 39, p. 4135–4195, 2005.
- [152] DANG, T. S.; MESCHKE, G. An ale–pfem method for the numerical simulation of two-phase mixture flow. *Computer Methods in Applied Mechanics and Engineering*, Elsevier, v. 278, p. 599–620, 2014.
- [153] ANJOS, G. et al. A 3d moving mesh finite element method for two-phase flows. *Journal of Computational Physics*, Elsevier, v. 270, p. 366–377, 2014.
- [154] TEZDUYAR, T. E. Finite elements in fluids: stabilized formulations and moving boundaries and interfaces. *Computers & fluids*, Elsevier, v. 36, n. 2, p. 191–206, 2007.
- [155] BAZILEVS, Y.; TAKIZAWA, K.; TEZDUYAR, T. E. Challenges and directions in computational fluid–structure interaction. *Mathematical Models and Methods in Applied Sciences*, World Scientific, v. 23, n. 02, p. 215–221, 2013.

- [156] ZIENKIEWICZ, O.; TAYLOR, R. *The Finite Element Method: The Basis*. Oxford: Butterworth-Heinemann, 2000.
- [157] REDDY, J. *An Introduction to the Finite Element Method*. New York: McGraw-Hill, 1993.
- [158] HUGUES, T. J. R. *The Finite Element Method: Linear Static and Dynamic Finite Element Analysis*. New Jersey: McGraw-Hill, 2000.
- [159] JOHNSON, C. *Numerical Solution of Partial Differential Equations by the Finite Element Method*. New York: Cambridge University Press, 1987.
- [160] WAIT, R.; MITCHELL, A. R. *Finite Element Analysis and Applications*. Great Britain: John Wiley and Sons, 1985.
- [161] GIRAULT, V.; RAVIART, P. *Finite Element Methods for Navier-Stokes Equations - Theory and Algorithms*. Germany: Springer: Heidelberg, 1986.
- [162] BAZILEVS, Y.; TAKIZAWA, K.; TEZDUYAR, T. E. *Computational fluid-structure interaction: methods and applications*. [S.l.]: John Wiley & Sons, 2012.
- [163] BABUSKA, I. *The History of the Finite Element Method from -infinity to 1970*. 2011.
- [164] GROSS, S.; REUSKEN, A. *Numerical Methods for Two-Phase Incompressible Flows*. Heidelberg, Germany: Springer, 2011.
- [165] TEMAM, R. *Navier-Stokes Equations and Nonlinear Functional Analysis*. Philadelphia, USA: SIAM, 1995.
- [166] GANESAN, S.; TOBISKA, L. An accurate finite element scheme with moving meshes for computing 3d-axisymmetric interface flows. *International journal for numerical methods in fluids*, John Wiley & Sons, Ltd., v. 57, n. 2, p. 119–138, 2008.
- [167] GROSS, S.; REICHELT, V.; REUSKEN, A. A finite element based level set method for two-phase incompressible flows. *Computing and Visualization in Science*, v. 9, n. 4, p. 239–257, 2006.
- [168] OLIVEIRA, G. *Hydrodynamic Stability in Electrochemical Cells through the Finite Element Method*. Tese (Doutorado) — UFRJ - Federal University of Rio de Janeiro, Brazil, 2011.



- [169] ANJOS, G. R. *A 3D ALE Finite Element Method for Two-Phase Flows with Phase Change*. Tese (Doutorado) — EPFL - École Polytechnique Fédérale de Lausanne, Switzerland, 2012.
- [170] CUVELIER, C.; SEGAL, A.; STEENHOVEN, A. van. *Finite Element Method and Navier-Stokes Equations*. [S.l.]: Dordrecht, Netherlands, 1986.
- [171] ADAMS, R. *Sobolev Spaces*. Adams. Oxford: Academic Press, 1975.
- [172] CHANG, W.; GIRALDO, F.; PEROT, B. Accurate projection methods for the incompressible navier-stokes equations. *Journal of Computational Physics*, v. 180, n. 1, p. 183–199, 2002.
- [173] ARNOLD, D.; BREZZI, F.; FORTIN, M. A stable finite element for the stokes equations. *Calcolo*, v. 21, n. 4, p. 337–344, 1984.
- [174] XU, J.; ZIKATANOV, L. Some observations on babuska and brezzi theories. *Numerische Mathematik*, Springer, v. 94, n. 1, p. 195–202, 2003.
- [175] BALAY, S. et al. *PETSc Users Manual Revision 3.4*. 2013.
- [176] CAMPBELL, C.; BRENNEN, C. Chute flows of granular material: some computer simulations. *Journal of applied mechanics*, v. 52, n. 1, p. 172–178, 1985.
- [177] MAURY, B. Direct simulations of 2d fluid-particle flows in biperiodic domains. *Journal of computational physics*, Elsevier, v. 156, n. 2, p. 325–351, 1999.
- [178] ALLEN, M. P. Introduction to molecular dynamics simulation. *Computational Soft Matter: From Synthetic Polymers to Proteins*, NIC Series, v. 23, p. 1–28, 2004.
- [179] BEALE, S. Use of streamwise periodic boundary conditions for problems in heat and mass transfer. *Journal of heat transfer*, v. 129, n. 4, p. 601–605, 2007.
- [180] SAWKO, R.; THOMPSON, C. P. *Towards Multiphase Periodic Boundary Conditions with Flow Rate Constraint*. 2011. 147 p.
- [181] FRITZEN, F.; BÖHLKE, T. Influence of the type of boundary conditions on the numerical properties of unit cell problems. *Technische Mechanik*, v. 30, n. 4, p. 354–363, 2010.

- [182] MANGIAVACCHI, N. et al. Numerical simulation of a periodic array of bubbles in a channel. *Mecánica Computacional*, XX Congreso sobre Métodos Numéricos y sus Aplicaciones, Mendoza, Argentina, XXXII, n. 21, p. 1813–1824, 2013.
- [183] WANG, W. et al. Converting an unstructured quadrilateral mesh to a standard t-spline surface. *Computational Mechanics*, Springer, v. 48, n. 4, p. 477–498, 2011.
- [184] PATANKAR, S.; LIU, C.; SPARROW, E. Fully developed flow and heat transfer in ducts having streamwise-periodic variations of cross-sectional area. *Journal of Heat Transfer*, v. 99, p. 180–186, 1977.
- [185] BEALE, S. B. *On the Implementation of Stream-Wise Periodic Boundary Conditions*. San Francisco, USA, 2005. 771–777 p.
- [186] LAHBABI, A.; CHANG, H.-C. Flow in periodically constricted tubes: transition to inertial and nonsteady flows. *Chemical engineering science*, Elsevier, v. 41, n. 10, p. 2487–2505, 1986.
- [187] OLIVEIRA, G. et al. *Finite Element Analysis of Pressure-Driven Laminar Flow inside Periodically Staggered Arrays*. 2014.
- [188] HOSSEINI, S.; FENG, J. Pressure boundary conditions for computing incompressible flows with sph. *Journal of Computational physics*, Elsevier, v. 230, n. 19, p. 7473–7487, 2011.
- [189] COMINI, G.; MANZAN, M.; NONINO, C. Finite element solution of the streamfunction-vorticity equations for incompressible two-dimensional flows. *International journal for numerical methods in fluids*, Wiley Online Library, v. 19, n. 6, p. 513–525, 1994.
- [190] NGUYEN, V. D. et al. Imposing periodic boundary condition on arbitrary meshes by polynomial interpolation. *Computational Materials Science*, Elsevier, v. 55, p. 309–406, 2012.
- [191] SUKUMAR, N.; PASK, J. Classical and enriched finite element formulations for Bloch-periodic boundary conditions. *International journal for numerical methods in fluids*, Wiley, v. 77, n. 8, p. 1121–1138, 2009.
- [192] NONINO, C.; COMINI, G. Finite-element analysis of convection problems in spatially periodic domains. *Numerical Heat Transfer, Part B*, Taylor & Francis, v. 34, n. 4, p. 361–378, 1998.

- [193] SEGAL, G.; VUIK, K.; KASSELS, K. On the implementation of symmetric and antisymmetric periodic boundary conditions for incompressible flow. *International journal for numerical methods in fluids*, Wiley Online Library, v. 18, n. 12, p. 1153–1165, 1994.
- [194] MCGRATH, D.; PYATI, V. Periodic structure analysis using a hybrid finite element method. *Radio Science*, Wiley, v. 31, n. 5, p. 1173–1179, 1996.
- [195] GLOWINKSI, R. *Finite Element Methods for Incompressible Viscous Flows, Handbook of Numerical Analysis IX*. Amsterdam: North-Holland: Netherlands, 2003.
- [196] MANZAN, M.; COMINI, G.; CORTELLA, G. A streamfunction–vorticity formulation of spatially periodic flows. *Communications in numerical methods in engineering*, Wiley Online Library, v. 13, n. 11, p. 867–874, 1997.
- [197] PERALTA-FABI, R.; MANDUJANO-GARCÍA, A.; HUSSAIN, F. An exact solution for a decaying symmetric vortex. *Revista Mexicana de Física*, v. 37, n. 1, p. 8–16, 1991.
- [198] VELDHUIS, C.; BIESHEUVEL, A.; WIJNGAARDEN, L. V. Shape oscillations on bubbles rising in clean and in tap water. *Physics of Fluids*, AIP Publishing, v. 20, n. 4, p. 040705, 2008.
- [199] CLIFT, R.; GRACE, J. R.; WEBER, M. *Bubbles, Drops and Particles*. London: Academic Press, 1978.
- [200] SAFFMAN, P. On the rise of small air bubbles in water. *Journal of Fluid Mechanics*, Cambridge University Press, v. 1, n. 03, p. 249–275, 1956.
- [201] MOUGIN, G.; MAGNAUDET, J. Path instability of a rising bubble. *Physical review letters*, APS, v. 88, n. 1, p. 014502, 2001.
- [202] VRIES, A. de. *Path and wake of a rising bubble*. Tese (Doutorado) — University of Twente, Netherlands, 2001.
- [203] WICHTERLE, K.; VECER, M.; RUZICKA, M. C. Asymmetric deformation of bubble shape: cause or effect of vortex-shedding? *Chemical Papers*, Springer, v. 68, n. 1, p. 74–79, 2014.
- [204] BATEN, J. V.; KRISHNA, R. Cfd simulations of wall mass transfer for taylor flow in circular capillaries. *Chemical engineering science*, Elsevier, v. 60, n. 4, p. 1117–1126, 2005.

- [205] SHAO, N.; GAVRIILIDIS, A.; ANGELI, P. Mass transfer during Taylor flow in microchannels with and without chemical reaction. *Chemical Engineering Journal*, Elsevier, v. 160, n. 3, p. 873–881, 2010.
- [206] TALIMI, V.; MUZYCHKA, Y. S.; KOCABIYIK, S. Numerical simulation of the pressure drop and heat transfer of two phase slug flows in microtubes using moving frame of reference technique. *International Journal of Heat and Mass Transfer*, Elsevier, v. 55, p. 6463–6472, 2012.
- [207] TALIMI, V.; MUZYCHKA, Y. S.; KOCABIYIK, S. A review on numerical studies of slug flow hydrodynamics and heat transfer in microtubes and microchannels. *International Journal of Multiphase Flow*, Elsevier, v. 39, p. 88–104, 2012.
- [208] KOMRAKOVA, A.; ESKIN, D.; DERKSEN, J. Lattice Boltzmann simulations of a single n-butanol drop rising in water. *Physics of Fluids (1994-present)*, AIP Publishing, v. 25, n. 4, p. 042102, 2013.
- [209] SHEWCHUK, J. *Theoretically guaranteed delaunay mesh generation-in practice*. 2004. 99–105 p.
- [210] BLOCH, E. *A First Course in Geometric Topology and Differential Geometry*. Boston, USA: Birkhauser, 1956.
- [211] OLIVEIRA, G. et al. *Topological Remeshing and Locally Supported Smoothing for Bubble Coalescence in Two-Phase Flows*. 2013.
- [212] OBERKAMPE, W. L.; TRUCANO, T. G. Verification and validation benchmarks. *Nuclear engineering and Design*, Elsevier, v. 238, n. 3, p. 716–743, 2008.